2020

Building And Validating Next-Generation Neurodevices Using Novel Materials, Fabrication, And Analytic Strategies

Nicolette Driscoll
University of Pennsylvania

Building And Validating Next-Generation Neurodevices Using Novel Materials, Fabrication, And Analytic Strategies

Abstract

Technologies that enable scientists to record and modulate neural activity across spatial scales are advancing the way that neurological disorders are diagnosed and treated, and fueling breakthroughs in our fundamental understanding of brain function. Despite the rapid pace of technology development, significant challenges remain in realizing safe, stable, and functional interfaces between manmade electronics and soft biological tissues. Additionally, technologies that employ multimodal methods to interrogate brain function across temporal and spatial scales, from single cells to large networks, offer insights beyond what is possible with electrical monitoring alone. However, the tools and methodologies to enable these studies are still in their infancy. Recently, carbon nanomaterials have shown great promise to improve performance and multimodal capabilities of bioelectronic interfaces through their unique optical and electronic properties, flexibility, biocompatibility, and nanoscale topology. Unfortunately, their translation beyond the lab has lagged due to a lack of scalable assembly methods for incorporating such nanomaterials into functional devices. In this thesis, I leverage carbon nanomaterials to address several key limitations in the field of bioelectronic interfaces and establish scalable fabrication methods to enable their translation beyond the lab. First, I demonstrate the value of transparent, flexible electronics by analyzing simultaneous optical and electrical recordings of brain activity at the microscale using custom-fabricated graphene electronics. Second, I leverage a recently discovered 2D nanomaterial, Ti3C2 MXene, to improve the capabilities and performance of neural microelectronic devices. Third, I fabricate and validate human-scale Ti3C2 MXene epidermal electrode arrays in clinical applications. Leveraging the unique solution-processability of Ti3C2 MXene, I establish novel fabrication methods for both high-resolution microelectrode arrays and macroscale epidermal electrode arrays that are scalable and sufficiently cost-effective to allow translation of MXene bioelectronics beyond the lab and into clinical use. Thetechnologies and methodologies developed in this thesis advance bioelectronic technology for both research and clinical applications, with the goal of improving patient quality of life and illuminating complex brain dynamics across spatial scales.

Degree Type

Dissertation

Degree Name

Doctor of Philosophy (PhD)

Graduate Group

Bioengineering

First Advisor

Flavia Vitale

Second Advisor

Brian Litt

Keywords

bioelectronics, MXene, nanomaterials, neural interface

Subject Categories

Nanoscience and Nanotechnology | Neuroscience and Neurobiology

BUILDING AND VALIDATING NEXT-GENERATION NEURODEVICES USING NOVEL MATERIALS, FABRICATION, AND ANALYTIC STRATEGIES

Nicolette Driscoll

A DISSERTATION

in

Bioengineering

Presented to the Faculties of the University of Pennsylvania

in

Partial Fulfillment of the Requirements for the

Degree of Doctor of Philosophy

2021

Supervisor of Dissertation

_____

Flavia Vitale, Ph.D.
Assistant Professor of Bioengineering, Neurology, & Physical Medicine & Rehabilitation

Co-Supervisor of Dissertation

_____

Brian Litt, M.D.
Professor of Bioengineering & Neurology

Graduate Group Chairperson

_____

Yale E. Cohen, Ph.D.
Professor of Otorhinolaryngology

Dissertation Committee

D. Kacy Cullen, Ph.D., Associate Professor of Neurosurgery & Bioengineering

Yury Gogotsi, Ph.D., Professor of Materials Science & Engineering

Douglas A. Coulter, Ph.D., Professor of Pediatrics & Neuroscience

BUILDING AND VALIDATING NEXT-GENERATION NEURODEVICES USING NOVEL MATERIALS, FABRICATION, AND ANALYTIC STRATEGIES

Acknowledgments

This thesis is the culmination of years of work that would not have been possible without the support of my mentors, my peers, and my friends and family.

First, I'd like to thank Dr. Brian Litt for welcoming me into the Center for Neuroengineering and Therapeutics (CNT) and for being a remarkably caring and supportive mentor. Brian has an uncanny ability to help you see the "big picture" and to always focus on how your work can someday help patients. Brian juggles many roles, treating epilepsy patients, running a lab, teaching courses, and directing organizations, yet he always makes time for his trainees. He is a deeply caring mentor and I am very grateful.

I was remarkably lucky to have started at Penn shortly after Dr. Flavia Vitale arrived, and she immediately took me under her wing. From our early days working in the "closet lab" in Hayden Hall with little more than a soldering iron and a potentiostat, to the establishment of our new lab space at the VA Medical Center (full of *much* more equipment), I have learned more from Flavia than I can ever recount. She allowed me the freedom to explore the problems I found most interesting, and to come up with my own, sometimes unorthodox solutions. Flavia is a dedicated mentor, a brilliant scientist, and an excellent role model.

I am grateful to Dr. Hajime Takano for sharing his expertise in neuroscience and optical imaging and for being instrumental in the multimodal graphene experiments. We faced many challenges, and at times it seemed we would not succeed, but together we persevered. Thanks also to Dr. Richard Rosch, whose expertise in computational neuroscience was critical for illuminating the interesting dynamics buried in a very complex dataset.

I am also very grateful to Dr. Andrew Richardson for lending his time and support in numerous animal experiments over the years. Drew's surgical expertise and his prodigious knowledge of neural recording and stimulation paradigms were invaluable as I sought to validate the various devices I developed in this thesis.

I would also like to thank Dr. Yury Gogotsi, Dr. Babak Anasori, Dr. Kathleen Maleski and the numerous other members of the Drexel Nanomaterials Institute who have shared their time and expertise on MXenes with me. I count myself as incredibly lucky to have had the opportunity to work with the folks who literally invented MXenes, and to be a part of the

meteoric rise of this new nanomaterial. Yury is generous with his time and resources, and his dedication to his trainees is inspiring.

Thanks also to Dr. John Medaglia and Dr. Brian Erickson for being among the earliest believers in the "MXtrodes" technology, and for all the time and effort they put into experimentally validating its use for EEG. Your enthusiasm has kept me motivated and excited to keep pushing the bounds with this work.

I am incredibly thankful for all the members of the CNT who have been my friends and colleagues throughout this journey. Thanks to Carolyn Wilkinson, Everett Prince, and Ruthie Kreiger for keeping the lab running smoothly and for helping me in procuring countless orders of lab supplies (no matter how strange). Many thanks to Dr. Kate Davis for sharing her neurology expertise and many helpful insights into clinical EEG recording, and to Jacqueline Boccanfuso and Magda Wernovsky, who were incredibly helpful and patient as I learned the ropes of crafting IRBs. Thanks to Brendan Murphy, for being an incredibly supportive and helpful colleague, my sympathizer when things inevitably went wrong in the nanofabrication facility, and my lab partner in all things "jenky." Finally, thank you to all labmates, past and present, including: Hank Bink, Hoameng Ung, Steve Baldassano, Preya Shah, Lohith Kini, Peter Hadar, Heather Gatens, Ryan Archer, Arian Ashourvan, Nick Apollo, John Bernabei, Brittany Scheid, Campbell Arnold, Andy Revell, Placid Unegbu, Theodore Wang, Kayla Prezelski, and many others. They have made each day fun, both in and out of the lab. Thank you for the laughs and the memories.

Last, but certainly not least, I am infinitely grateful for the friends who have kept me happy and sane with adventures outside of research and for my incredible family, my parents, Jim, Mira, Alyssa, Nico, and Corey, who have supported and encouraged me every step of the way.

ABSTRACT

BUILDING AND VALIDATING NEXT-GENERATION NEURODEVICES USING NOVEL MATERIALS, FABRICATION, AND ANALYTIC STRATEGIES

Nicolette Driscoll

Flavia Vitale

Brian Litt

Technologies that enable scientists to record and modulate neural activity across spatial scales are advancing the way that neurological disorders are diagnosed and treated, and fueling breakthroughs in our fundamental understanding of brain function. Despite the rapid pace of technology development, significant challenges remain in realizing safe, stable, and functional interfaces between manmade electronics and soft biological tissues. Additionally, technologies that employ *multimodal* methods to interrogate brain function across temporal and spatial scales, from single cells to large networks, offer insights beyond what is possible with electrical monitoring alone. However, the tools and methodologies to enable these studies are still in their infancy. Recently, carbon nanomaterials have shown great promise to improve performance and multimodal capabilities of bioelectronic interfaces through their unique optical and electronic properties, flexibility, biocompatibility, and nanoscale topology. Unfortunately, their translation beyond the lab has lagged due to a lack of scalable assembly methods for incorporating such nanomaterials into functional devices. In this thesis, I leverage carbon nanomaterials to address several key limitations in the field of bioelectronic interfaces and establish scalable fabrication methods to enable their translation beyond the lab. First, I demonstrate the value of transparent, flexible electronics by analyzing simultaneous optical and electrical recordings of brain activity at the microscale using custom-fabricated graphene electronics. Second, I leverage a recently discovered 2D nanomaterial, Ti_3C_2 MXene, to improve the capabilities and performance of neural microelectronic devices. Third, I fabricate and validate human-scale Ti_3C_2 MXene epidermal

electrode arrays in clinical applications. Leveraging the unique solution-processability of Ti_3C_2 MXene, I establish novel fabrication methods for both high-resolution microelectrode arrays and macroscale epidermal electrode arrays that are scalable and sufficiently cost-effective to allow translation of MXene bioelectronics beyond the lab and into clinical use. The technologies and methodologies developed in this thesis advance bioelectronic technology for both research and clinical applications, with the goal of improving patient quality of life and illuminating complex brain dynamics across spatial scales.

Table of Contents

List of Tables

List of Figures

Chapter 1: Introduction

Since the first evidence of electrical activity in the nervous system was observed by Luigi Galvani in the 1790s, a host of technologies have evolved to enable recording and modulating electrical activity in excitable tissues. These technologies have enabled breakthroughs in our understanding of brain function and neuropathologies, have provided diagnostic and therapeutic tools for diseases such as epilepsy and Parkinson's disease, and have even enabled locked-in patients to control external effectors through brain computer interfaces (BCIs) to regain some independence.

Today, neurotechnologies are shedding new light on the fundamental mechanisms governing the structure and function of neural circuits, which is essential to advance diagnostics and therapies for debilitating neurological diseases and disorders. In epilepsy, for example, targeted therapies such as surgical resection, thermal ablation, or responsive neurostimulation rely on precise localization of seizure onset regions to be effective. Currently, these seizure onset regions are identified by a combination of electrophysiological recordings from mm-scale implanted electrodes, non-invasive imaging techniques such as magnetic resonance imaging (MRI) and positron emission tomography (PET), and through observing seizure semiology. These techniques offer limited spatial resolution, however, and a growing body of literature suggests that seizure activity may begin at the scale of neural microcircuits, which current clinical technologies cannot observe [1]–[3]. Thus, there is great interest in observing the cell and microcircuit level dynamics of seizure initiation and linking these to the macroscale, brain-wide activity observed with current clinical technologies. This notion of recording neural activity across spatial scales is critical for improving our understanding and targeting of therapies not only for epilepsy, but for many neurological diseases and disorders, and it was one of the primary motivations for the BRAIN Initiative launched in 2013.

There remain significant technological hurdles to achieving this goal, many of which stem from challenges associated with interfacing manmade electronics with soft biological tissues such as the brain. Recently, carbon nanomaterials such as graphene and carbon nanotubes have shown significant promise for improving the electrical properties, flexibility, biocompatibility, and multimodal capabilities of tissue-interfacing electrodes. Despite their promise, a lack of scalable assembly methods for producing devices using nanomaterials has

so far been a significant barrier to their translation and widespread adoption. The goal of this thesis is to develop new technologies for mapping and modulating neural and neuromuscular activity across spatial scales by leveraging the unique properties of carbon nanomaterials and by establishing scalable fabrication methods that will enable translating these technologies beyond the lab and into clinical and consumer use.

At one end of the spatial scale, tools and techniques have been evolving to observe brain activity at the cellular level. In particular, the rise of optogenetics has enabled optical imaging and modulation of targeted cell types in the brain to discern the functions of different cell assemblies [4]. Optical imaging techniques, such as calcium imaging, enable observing activity with high spatial resolution, however their temporal resolution is limited by the kinetics of the fluorescent reporter molecules and it remains challenging to image at high resolution across a broad field of view [5]. Electrophysiology with microelectrodes offers a complimentary approach, with high temporal resolution but sparse spatial sampling. Combining these two recording modalities presents a unique opportunity to harness the spatial resolution of optical imaging along with the temporal resolution of electrophysiology, however this requires imaging and recording simultaneously in the same location. This is not possible using conventional microelectrode arrays utilizing opaque materials, as these block optical access and suffer from photoelectric artifacts. Recently, progress in transparent microelectrode array technology, predominantly utilizing graphene, has enabled such multimodal studies [6]–[9]. However, innovation is still needed in experimental and analytical methods to fully realize their potential. So far, these multimodal studies have mainly focused on 2-photon imaging either from brain slices or from the cortical surface of anesthetized animals. This approach offers a limited field of view that may fall beneath only one or a small number of the transparent electrodes. Thus, there is a need to establish new experimental methods enabling broader area coverage to observe brain dynamics across spatial scales relevant in epilepsy. Additionally, new analytical approaches are needed to link the spatial and temporal information contained in the two modalities. In Chapter 3 of this thesis, I build upon previous work to improve the performance of transparent graphene electronics, I establish new experimental techniques for multimodal recording across a mm-scale area of cortex, and I develop a framework for combining data features from optical and

electrical domains. Taken together, these advances offer the ability to study neural circuits with unprecedented spatiotemporal resolution, making it possible to link cell-level behavior to broader network oscillations.

While graphene offers excellent optical transparency for multimodal studies, these electrodes cannot be scaled down to cellular dimensions to record individual neuron spiking activity because they are hindered by high impedance. Thus, it has not yet been possible to record one-to-one optical and electrical spiking activity of individual cells except through the use of cumbersome patch pipettes. This highlights one of the main challenges in achieving high density neural recording from microelectrodes, even setting aside optical transparency requirements. Microelectrodes suffer from a trade-off between geometric surface area and interface impedance: as electrodes are scaled down to cellular dimensions, a concurrent rise in their impedance causes a degradation in recorded signal quality [10]. This challenge is often addressed by increasing the effective surface area over which ionic species can interact with the electrode without increasing the geometric area. This can be achieved through nanopatterning [11], surface roughening [12], or electroplating with porous additives [13] and has led to significant interest in the use of nanomaterials to achieve nanoscale topology [14]–[16]. Though nanomaterials have shown great promise for improving microelectrode performance, due to their intrinsically high specific surface areas and their favorable electronic properties, incorporating these materials into flexible substrates has proven challenging. For example, graphene and carbon nanotubes must be synthesized through high-temperature chemical vapor deposition processes which are incompatible with flexible polymeric substrates, and thus require tedious manual steps to transfer and pattern films after their growth [17].

Recently, a newly discovered family of 2D nanomaterials, MXenes, have attracted interest for applications in energy storage [18], electromagnetic interface shielding [19], and supercapacitors [20] owing to their exceptional electronic, thermal, and mechanical properties. Of the dozens of MXenes that have been discovered, Ti_3C_2 has been the most extensively characterized and optimized, and it exhibits remarkably high electronic conductivity (~15,000 S/cm) [21] and volumetric capacitance (1500 F/cm^3) [22]. Ti_3C_2 also contains abundant surface-terminating functional groups, such as hydroxyl (–OH), oxygen

(–O), and fluorine (–F), which endow it with a hydrophilic nature and allow for flexible surface modification and functionalization. These unique properties make Ti_3C_2 an appealing candidate for improving neural microelectrode performance, while also enabling the use of simple and scalable solution processing methods which are more practical than those required to use other carbon nanomaterials. In Chapter 4 of this thesis, I develop a fabrication method to produce microelectrodes of Ti_3C_2 MXene, and I demonstrate their effectiveness for high-resolution neural recording, the first-ever demonstration of any MXene for *in vivo* electrophysiology. I show that Ti_3C_2 microelectrodes possess exceptionally low electrochemical impedance and improved signal quality compared to gold electrodes, thus identifying Ti_3C_2 as a promising new bioelectronic material.

While Chapters 3 and 4 of this thesis focus on microscale interrogation within the brain, macroscale electrodes deployed across the body can offer a broader view of activity and key capabilities for medical therapeutics, healthcare monitoring, and wearable devices. For example, non-invasive epidermal electronics can offer important insights into the function of the heart (via electrocardiography; ECG), muscles (via electromyography; EMG), nerves (via nerve-conduction studies), and brain (through electroencephalography; EEG). Additionally, active bioelectronic devices capable of delivering targeted electrical stimulation can be used to treat a number of conditions, including neurological diseases [23], [24], heart arrythmias [25], [26], and inflammatory disorders [27], [28]. The promise of such devices has fueled a revolution in "bioelectronic medicine", where electrical modulation of neural circuitry is used in place of pharmacotherapy [29].

In both passive recording and active stimulation devices, conventional materials and fabrication processes still remain inadequate for producing high-density multielectrode arrays that can map and modulate activity in excitable tissues at high spatiotemporal resolution and over broad areas. For example, in epidermal electronics achieving low electrode-skin interface impedance has proven a key challenge that has limited the spatial resolution of epidermal interfaces. Typically, these interfaces require a conductive gel to reduce the impedance, and these gels are problematic on many fronts: they can be irritating to the skin [30], they leave unwanted residues in the hair, they can short neighboring electrodes and thus limit high density recording, and they dry out over time, causing changing

electrode impedances and preventing practical long-term monitoring. New materials may hold the key for overcoming this and other crucial challenges.

In Chapter 5, I develop a highly scalable method for producing large-area, high-density Ti_3C_2 MXene multielectrode arrays – which we name MXtrodes – of arbitrary size and geometry for varied bioelectronic applications. I perform a comprehensive evaluation of the electrochemical properties of the MXtrodes relevant for recording and stimulation of excitable tissues, and I show that they are comparable, and in many aspects superior to, conventional bioelectronic materials, especially in the context of delivering charge for safe and effective electrical stimulation. I demonstrate MXtrodes of different scales and geometries for mapping and modulating excitable networks in different applications, including scalp electroencephalography (EEG), electromyography (EMG), electrocardiography (ECG), electrocorticography (ECoG), and neural stimulation. Notably, I show that mm-scale MXtrodes achieve low electrode-skin interface impedance without any conductive gel, enabling high-density epidermal electronics. Finally, I characterize the compatibility of MXtrodes with clinical imaging modalities and demonstrate artifact-free high-field magnetic resonance and computed tomography imaging. MXtrodes represent a new class of flexible, multichannel, high-density bioelectronic interfaces which leverage the exceptional properties of Ti_3C_2 MXene to enable human-scale, clinically-translatable neurodevices that show great promise for numerous applications in healthcare, research, and wearable electronics.

Chapter 2: Background

2.1 The promise of bioelectronics

Devices which can record and modulate electrical activity in the brain and other excitable tissues are a mainstay for medical diagnostics and monitoring and increasingly for therapeutic interventions. They are key tools in neuroscience research, allowing scientists to decipher the neural basis of movements, behaviors, and even abstract thoughts. They are enabling a revolution in at-home health and activity monitoring via wearable devices and have allowed the development of brain-computer interfaces to restore lost functions. In recent years, there has also been growing interest in the use of neuromodulation as a treatment option for a number of chronic diseases as a complementary approach to traditional pharmacotherapy, a concept known as bioelectronic medicine [29].

In the field of medical diagnostics and monitoring, the use of electrodes to monitor electrical activity in the body is not new. The first ECG was recorded by Willem Einthoven in 1902 [31], and the first EEG recordings were performed by Hans Berger in 1924 [32]. Since that time, both techniques have become mainstays of clinical care. In addition to these noninvasive recording methods, techniques in which electrical activity is recorded directly from brain tissue have become essential for informing resection surgeries for brain tumors and epilepsy treatment. Intraoperative recordings can help a surgeon distinguish between healthy and pathologic tissue during a tumor resection surgery, and long-term recordings from implanted electrocorticography electrodes in epilepsy patients can help identify seizure foci to target resection surgery. These are just a few examples of the numerous ways in which electrophysiologic recording is used in clinical medicine.

In addition to passive recording, modulating activity through electrical stimulation has also become a key therapeutic approach. The first demonstration of this notion was the invention of the cardiac pacemaker in 1952, with the earliest implants in human beings carried out between 1958 and 1960 [33]. Since then, stimulation devices have been developed for the brain and peripheral nerves to treat a variety of diseases. Deep brain stimulation (DBS), which delivers consistent electrical stimulation to focal areas within the brain, was approved in the U.S. in 2002, and it has been heralded as providing “a new life for people with Parkinson’s disease” as it can effectively eliminate debilitating tremor and other

motor symptoms [34]. While the exact mechanisms for how DBS achieves its effects are still not fully understood, this approach has shown so much promise that it is currently being evaluated for treating a number of additional disorders, including dystonia, depression, multiple sclerosis, and obsessive compulsive disorder. Stimulation of nerves can achieve similar effects, and one such example is vagus nerve stimulation (VNS), which was approved in the U.S. in 1997 for the treatment of medically refractory partial-onset seizures. Like DBS, VNS has also gained attention as a potential treatment option for numerous disorders beyond its initial indication, including depression, mood disorders, migraines, and inflammatory disorders such as rheumatoid arthritis, diabetes, and cardiovascular disease [35]. More recently, closed-loop neuromodulation systems have emerged which are capable of monitoring activity and delivering electrical stimulation only when needed, rather than constantly stimulating. These devices, which are likened to "pacemakers for the brain", have shown great promise for the treatment of medically refractory epilepsy by sensing the onset of abnormal brain activity and stimulating to inhibit seizure initiation [36].

In recent years, bioelectronics have also enabled the development of brain-computer interfaces (BCIs) which can restore lost sensory or motor functions. For example, cochlear implants have proven effective for restoring partial hearing to the deaf [37], and retinal prostheses have been developed for restoring limited vision to the blind [38]. These devices relay signals from external sensors to small, implanted electrodes which stimulate the sensory cells in the cochlea and retina, respectively. For patients suffering from paralysis or locked-in syndrome, motor BCIs capable of decoding movement intention from electrodes placed in motor areas of the brain and translating this into the movement of an external effector, such as a computer cursor or a robotic arm, offer great promise for restoring some independence and greatly enhancing quality of life [39].

Beyond their uses in clinical medicine, bioelectronics are increasingly finding their way into consumer use in the form of wearable devices. While many of these devices sense signals other than the biopotentials which are the main focus of this work, including temperature, motion, and metabolites in sweat, there are growing applications where monitoring of electrophysiologic signatures is useful. For example, heart rate monitors have been used by athletes for decades but sensors that now collect the full ECG waveform are

increasingly being incorporated into smartwatches to check for abnormal heart rhythms. There has also been increasing interest in consumer-grade EEG headsets for monitoring stress and attention, for enabling "brain training" with neurofeedback, for tracking sleep and meditation, and even for brain-controlled videogaming [40], [41]. Wearable EMG sensors have also gained attention for monitoring muscle activity during exercise to tune sports performance [42].

Finally, it is difficult to overstate the importance of devices for recording and modulating the activity of excitable tissues in neuroscience research. Such devices have contributed in profound ways to our understanding of the nervous system and other excitable tissues, from the level of individual cell behavior up to large scale network activity. To choose just one notable example, the development of microelectrodes in the 1950s allowed "micromapping": precisely mapping regions of the cortical surface that corresponded to particular sensory and motor areas on the body. Through a series of micromapping experiments in monkeys, Michael Merzenich showed that the cortical maps corresponding to individual fingers were plastic and would rearrange in response to the amputation of a finger [43]. These and other experiments using microelectrodes eventually gave rise to the concept of neuroplasticity, overturning the longstanding belief that the adult brain was static and leading to revolutionary new therapies for deficits in speech, language, memory, and reading which had been believed to be untreatable.

The numerous examples of bioelectronic interfaces outlined in this section highlight the tremendous potential of these technologies for applications across healthcare, research, and consumer electronics. At their core, such technologies all rely on an interface between manmade electronics and biological tissues. Improving the properties of this interface is one of the core themes of this thesis work.

2.2 Methods for neural recording and modulation

> "There are only a handful of tools at the neuroscientist's disposal to monitor brain activity without seriously interfering with it. Can we finish the job with these tools alone? Maybe not, but for now, we have to live with them and believe that we will not fail or falter. Each of the existing methods is a compromise between spatial and temporal resolution. The desired temporal resolution is the operation speed of neurons, that is, the millisecond scale. The desired spatial resolution depends on the goal of the investigation and expands from the global scale of the brain down to the spines of individual neurons. No current method is capable of continuously zooming from the decimeter to the micrometer scale, which is why several methods are being used, often in combination."
>
> – Gyorgy Buzsaki [44]

There are numerous methods for recording and modulating the activity of the brain and other excitable tissues, and as Gyorgy Buzsaki so nicely stated, they each offer a specific range of temporal and spatial resolution. These methods span multiple modalities, including electrical, optical, magnetic, acoustic, and chemical. The work of this thesis focuses on the electrical and optical domains, however in this section I will provide a brief overview of the numerous approaches for neural recording and modulation. I will focus on methods primarily applied to the study of the brain, however many of these approaches can be extended to the study of the peripheral nervous system. A useful schematic depicting the spatiotemporal resolution of some of these methods is shown in **Figure 2.1**.

2.2.1 Electrical

The origin of extracellular fields and currents

Activity within the nervous system is a complex interplay of electronic and chemical signaling. The primary information-encoding cells in the nervous system are neurons, though glial cells also play important roles. Neurons communicate with each other by firing action

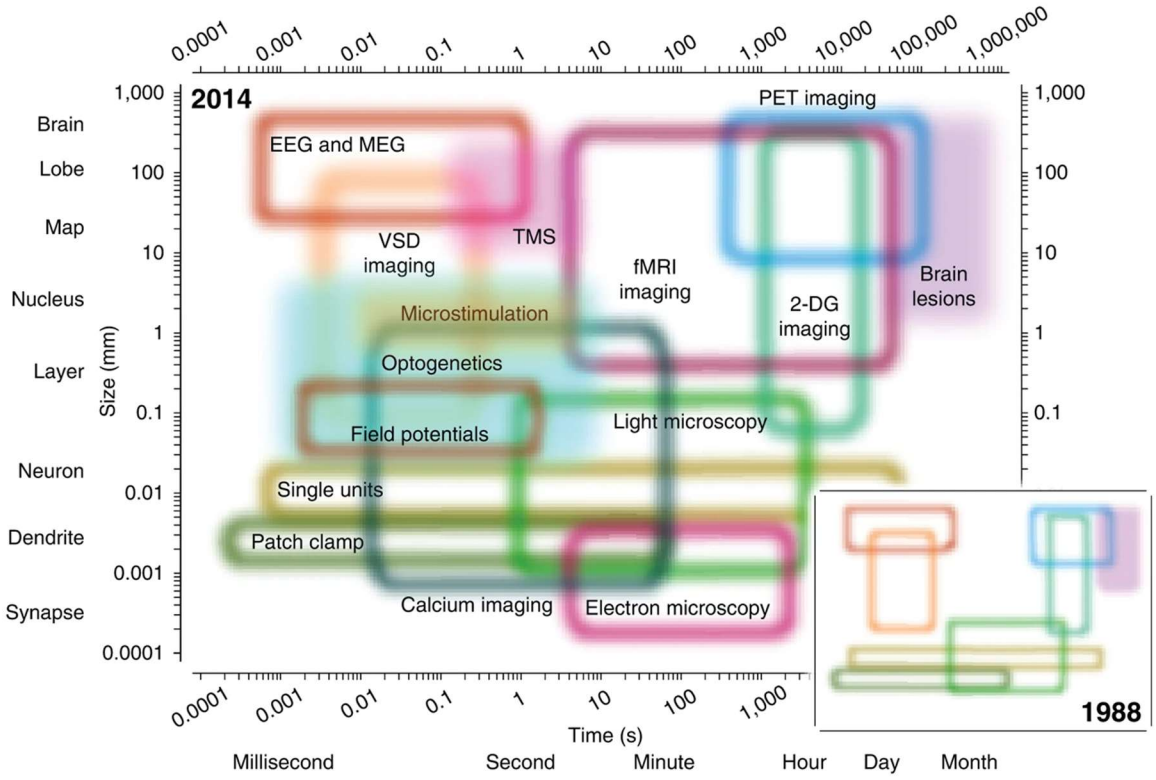

Figure 2.1 The spatiotemporal domain of neuroscience methods. Each colored region represents the useful domain of spatial and temporal resolution for one method available for the study of the brain. Open regions represent measurement techniques; filled regions represent perturbation techniques. Inset, a cartoon rendering of the methods available in 1988, notable for the large gaps where no useful method existed. Regions allocated to each domain are somewhat arbitrary and represent estimates. From [375].

potentials (APs), also called "units" or "spikes", which result in the release of chemical neurotransmitters at synapses, which in turn influence the behavior of other neurons. During an action potential, voltage-gated ion channels embedded in the cell membrane facilitate a coordinated pattern of Na^+ ion influx into the cell, followed by K^+ ion outflux, resulting in a large amplitude voltage spike ~1 ms in duration which is largest in amplitude near the soma (**Figure 2.2**). Even when neurons are not firing APs, smaller ionic currents at the postsynaptic membrane, called excitatory or inhibitory postsynaptic potentials, affect the neuron's membrane potential, causing it to deviate from its resting state of approximately -70 mV. These voltage fluctuations are much smaller than those of APs, but they last for 10s of milliseconds and contribute significantly to the extracellular field.

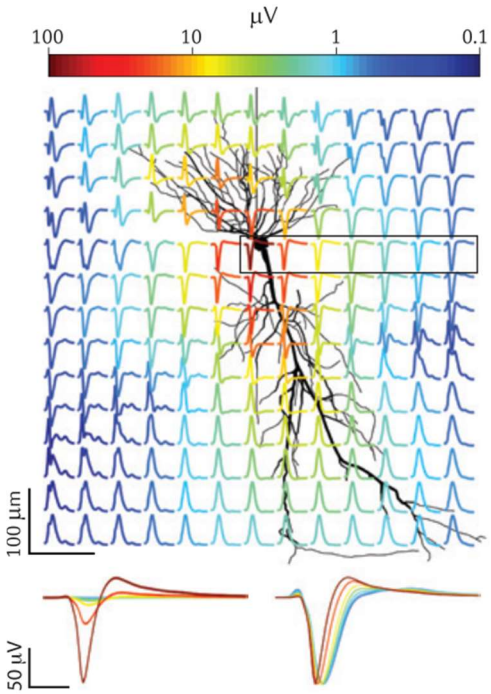

Figure 2.2 Extracellular contribution of an action potential ("spike") to the LFP. The peak-to-peak voltage range is indicated b the color of the traces. Note that the spike amplitude decreases rapidly with distance from the soma. Note the widening of the spike with distance from the soma, owing to greater contributions from dendritic currents and intrinsic filtering of high-frequency currents by the cell membrane. From [45].

At any point in the extracellular space, the measured potential V_e is the superposition of all ionic processes, from fast action potentials, to synaptic currents and Ca^{2+}-mediated spikes, to even slow fluctuations in glia. This potential is often referred to as the local field potential (LFP) when recorded on the cortical surface. The voltage arising from any transmembrane current, assuming a current dipole, decays as $1/r^2$, where r is the distance between the recording electrode and the source current [45]. Another consistent feature of extracellular potential is that the magnitude of the power (or the square of the Fourier amplitude), is inversely related to temporal frequency f. This $1/f$ power scaling relation is attributed in part to the low-pass frequency filtering properties of dendrites [46], as well as to broader network mechanisms: in a brief time window only a limited number of neurons can be recruited in a given volume, whereas in a longer time window the activity of many more neurons can contribute to the LFP, generating a larger amplitude LFP at slower frequencies [45].

In measuring extracellular potentials, it is important to keep these relations in mind as both the size of the electrode and its distance from the active neurons will affect the signal content. Importantly, the V_e that is measured by an electrode reflects a spatial average of the activity near the electrode. Thus, electrodes record a "spatiotemporally smoothed" version of the extracellular potential integrated over their surface, and a larger electrode will record less high frequency signal content corresponding to individual neuron activity. A summary of the various scales of neural recording and their frequency content is shown in **Figure 2.3**.

Macroscale recording: Scalp EEG

Scalp electroencephalography is one of the oldest and most widely used methods for investigating the electric activity of the brain. EEG electrodes are typically ~10 mm in diameter, and the signals they detect represent only the largest, most synchronous neural signals since they must travel through the brain, cerebrospinal fluid, skull, and scalp before reaching the electrode. The skull and scalp act as low-pass filters, thus the EEG typically retains little high frequency content and little relationship to the firing patterns of the

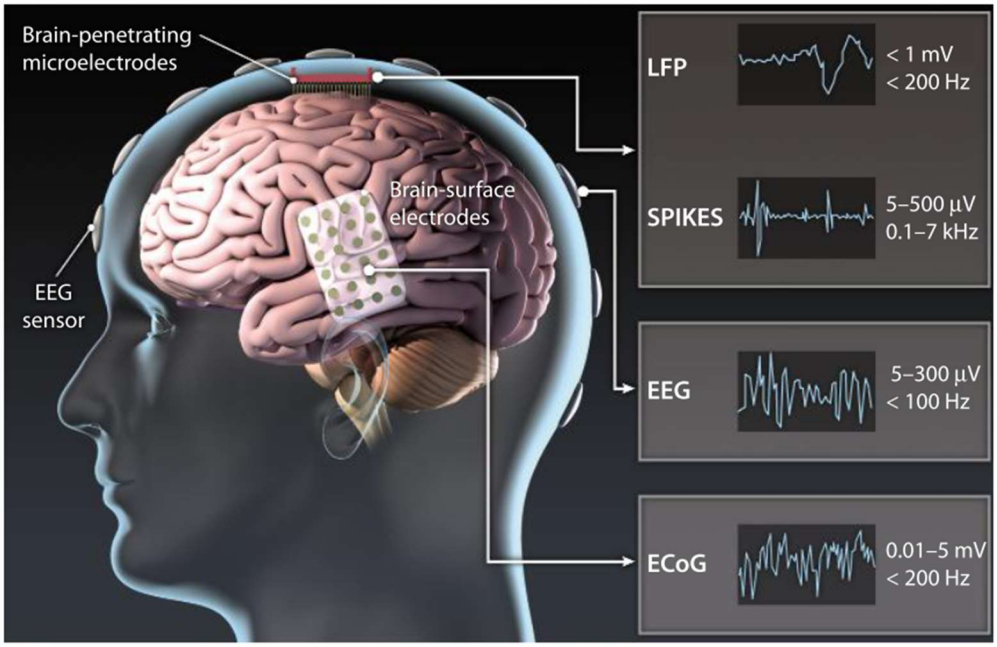

Figure 2.3 Methods for brain recording at different scales. Several types of brain signals can be recorded from noninvasive and invasive electrodes: EEG signals are recorded from the scalp, ECoG from the brain surface, and spikes from brain-penetrating electrodes. From [376].

contributing individual neurons [47]. The spatial resolution of EEG is inherently quite poor, however computational methods for source localization can give theoretical approximations for the areas of cortex responsible for the activity recorded on the scalp [48], [49].

Mesoscale recording: Intracranial EEG

When EEG recordings are obtained with intracranial electrodes, it is referred to as intracranial EEG (iEEG). This can be in the form of electrocorticography (ECoG) using grids and strips of electrodes placed subdurally onto the surface of the brain, or stereotaxic EEG (sEEG) using thin penetrating electrodes placed into deeper targets within the brain. These techniques are used in patients with drug-resistant epilepsy, for whom surgical resection of seizure foci may offer seizure freedom. Typically, these patients are implanted with a number of ECoG and sEEG electrodes, then weaned off of their antiepileptic medications and continuously monitored in the hospital with the goal of recording seizures or abnormal interictal activity that can help to localize the patient's seizure foci. iEEG recordings offer much higher resolution than EEG and they can resolve a wider range of frequency content due to their placement directly on the surface (ECoG) or within (sEEG) the brain. ECoG electrodes are typically Pt or stainless steel flat electrodes 2.3 mm in diameter with a 10 mm pitch between contacts, while sEEG electrodes are typically cylindrical contacts ~2mm in length spaced along a probe ~1 mm in diameter [50]. Using known estimates of the number of neurons per cortical area along with the size of these electrodes, it can be assumed that there are ~500,000 cells beneath or surrounding one of these electrodes [51]. Still, iEEG signals typically contain information in frequency bands ranging from delta (1-3 Hz) all the way up to high-gamma activity (60-250 Hz), which is a correlate of averaged neuronal spiking activity [52].

Microscale recording: Microelectrodes

In the electrical domain, microelectrodes offer the highest spatial and temporal resolution for recording and stimulating neural activity. They are typically <100 μm in dimension and can resolve the spiking activity of individual neurons. Microelectrodes were originally developed as research tools for academic investigation into the neural mechanisms

that regulate attention, movement, and behavior. They fall into three general categories: (1) microwire arrays, (2) microfabricated planar arrays, and (3) micromachined arrays (**Figure 2.4**). Microwire electrodes are typically conductive core wires, with an insulation layer such as glass, parylene, or polyimide coating the wire except at the very tip, where the recording contact is located. Multiple microwires can be arranged into an array, typically requiring manual assembly [53] (**Figure 2.4a**).

Planar microelectrode arrays (**Figure 2.4b**) are typically produced using microfabrication techniques drawn from the well-established methods of the semiconductor industry, and these include both surface micro-ECoG (μECoG) arrays and penetrating shank arrays. μECoG arrays typically consist of thin metal films patterned through photolithography on polymer substrates. Achieving high electrode density on a surface μECoG array to maximize spatial resolution has been quite challenging due to the need to wire out the signals from each individual electrode, however recent advances allowing the incorporation of active multiplexing electronics onto such arrays have pushed the limits of μECoG resolution [54] (**Figure 2.5a**). Additionally, surface μECoG arrays typically cannot resolve individual neuron APs because the neuronal cell bodies that generate them are located ~100s of micrometers deep in the cortex, however recent work has shown that unit activity can be recorded from

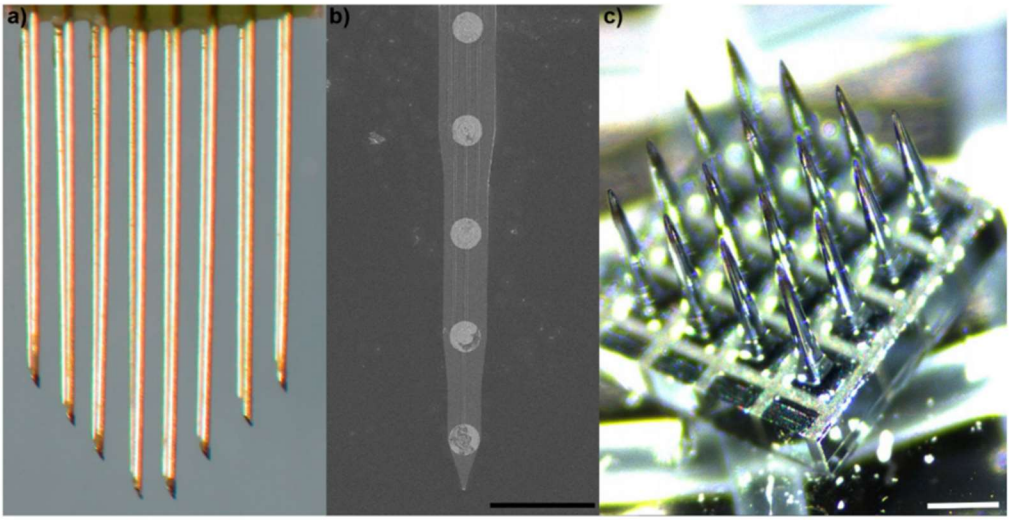

Figure 2.4 Classes of implantable microelectrodes. (a) 50 μm polyimide-insulated tungsten microwires with chiseled tips (Tucker-Davis Technologies). (b) Microfabricated silicon planar Michigan array with iridium electrode sites (NeuroNexus Technologies). Scale bar: 100 μm. (c) Micromachined boron-doped silicon array (Blackrock Microsystems). Scale bar: 400 μm. From [377].

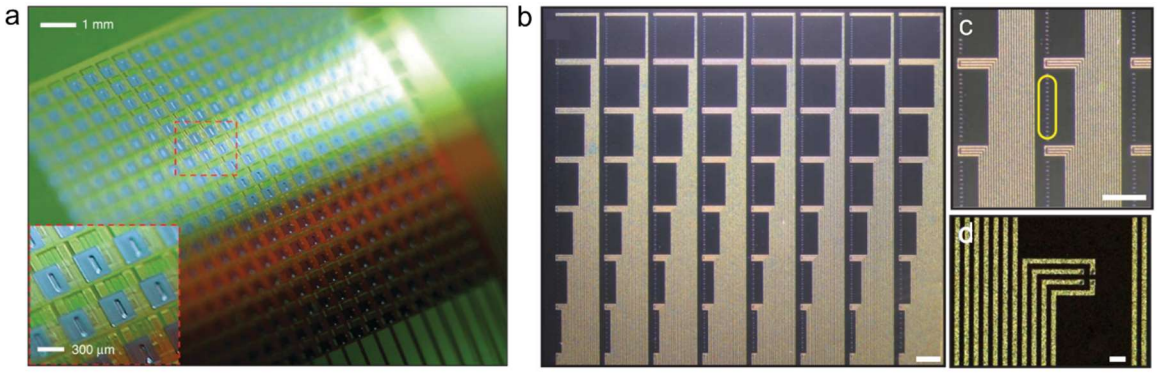

Figure 2.5 Advanced µECoG array technologies. (a) Actively multiplexed high-density µECoG array. Active transistors within the array allow for sampling from 360 electrodes with just 40 wires. From [54]. (b-c) NeuroGrid high-density µECoG array. 10 µm² electrodes are arranged in 2x2 tetrode arrangement for isolation of individual neuronal spikes from the cortical surface. Scale bars: (b) 1 mm, (c) 1 mm, (d) 20 µm. From [378].

the cortical surface with electrodes that are sufficiently small (~10 µm² in size) and low in impedance [55] (**Figure 2.5b-d**). The other class of planar microelectrode arrays are penetrating shank arrays. These are typically fabricated on rigid silicon substrates, with multiple electrode contacts along the length of the shank. This enables recording neural activity at multiple depths spanning the cortex or other brain areas with just a single probe inserted. Recently, the use of complementary metal-oxide-semiconductor (CMOS) processing has enabled pushing the bounds of electrode density on these planar depth electrodes to unprecedented new limits. The Neuropixels probe unveiled in 2017 offers 384 recording channels, programmably addressable from a selection of 960 possible recording sites along a 10 mm-long, 70 x 20 µm cross-section shank, the highest density electrode array reported to date [56].

The final main class of microelectrodes are micromachined arrays. These are similar to microwire arrays in that each "probe" contains a single electrode contact located at its tip, however they are produced by micromachining a block of silicon into an array of needle-like probes. This "bed of nails" type electrode array was introduced in the late 1990s and became known as the Utah array [57]. Today's version of the Utah array offers 100 penetrating electrode contacts within a 2 x 2 mm area, and it is the only microelectrode array that has been approved for human use in the U.S. This had made the Utah array central in human BCI

research [58], despite the fact that its rigid needle-like architecture presents significant challenges for long-term recording reliability [59].

Electrical stimulation

While recording electrodes provide insight into the activity within the nervous system, they do not allow for control over its dynamics. Electrical stimulation is one way to perturb neural activity, both for research purposes (i.e. to see how the system responds to a change in stimuli) and also for therapeutic purposes (i.e. to inhibit or alter pathologic activity). As mentioned in section 2.1, electrical stimulation in the brain and peripheral nervous system has proven an effective therapy for Parkinson's disease, depression, and many other conditions. Electrical stimulation is non-selective, meaning that any excitable cells within the vicinity of the stimulation delivery will be affected. The amount of charge that can be safely delivered for electrical stimulation depends largely a quantity known as charge injection capacity (CIC), which depends on innate electrochemical properties of the electrode material, as well as the geometry and surface roughness of the electrode [60]. CIC will be discussed further in Section 2.4. Common materials for stimulation electrodes include platinum and platinum-iridium, though coatings of iridium oxide and titanium nitride are often used to improve the CIC of electrodes [61].

2.2.2 Optical

Calcium imaging

Calcium imaging is a sensitive method for monitoring neuronal activity because most depolarizing electrical signals are associated with Ca^{2+} influx attributable to the activation of one or more of the numerous types of voltage-gated Ca^{2+} channels abundantly expressed in the nervous system [62]. These signals are often further amplified by Ca^{2+} release from intracellular Ca^{2+} stores. Fluctuations in intracellular Ca^{2+} concentration in response to cell activity can be observed using fluorescent indicators that exhibit altered fluorescent properties when bound with free Ca^{2+} ions. There are two general classes of Ca^{2+} indicators: genetically encoded fluorescent proteins and chemically engineered fluorophores [63]. Chemical Ca^{2+} indicator dyes, such as Orgeon Green BAPTA provide large signal-to-noise

ratios, but they can be difficult to load into cells in intact tissue, they can compartmentalize into cellular organelles, and they leak out of cells over longer recording periods, making chronic imaging infeasible [64]. Genetically encoded Ca^{2+} indicators (GECIs), such as the GCaMP family, have the advantage of genetic targeting so that imaging can be performed with only specific cell types containing the Ca^{2+} indicator. They also do not suffer from the challenges that prevent chronic imaging with synthetic dyes. There have been many types of Ca^{2+} indicators developed over the years, and they each have slightly different Ca^{2+} binding affinity, excitation/emission wavelengths, and signal-to-noise ratios [62]. A few key limitations of calcium imaging techniques include: (i) their temporal resolution is limited by the kinetics of Ca^{2+} binding and unbinding from the fluorescent indicators, as well as by the speed of the imaging instrumentation such that neuronal action potentials cannot be clearly resolved [5], (ii) it is challenging to image at high resolution across a broad field of view [65], (iii) due to light scattering in tissue, it is difficult to image deep structures, although new implantable GRIN lens scopes have improved these capabilities [66], and (iv) calcium transients are an indirect measure of neuronal activity.

Voltage imaging

Another technique for observing neural activity is the use of voltage-sensitive fluorescent indicators. These enable direct imaging of voltage, which is an attractive method for studying neural circuits [67]. Small molecule voltage-sensitive fluorescent indicators generally fall into two classes: electrochromic-type dyes which posses fast response speeds sufficient to track action potentials but with low sensitivity, and oxonols, which have larger fluorescent responses to voltage but respond too slowly to visualize discrete action potentials [68]. Voltage imaging offers a direct measure of neural activity, in contrast to the indirect measure of calcium transients in Ca^{2+} imaging, and it is capable of resolving the fast dynamics of individual action potentials. However, voltage imaging has several inherent challenges which have limited its widespread adoption. First, to resolve action potentials the speed of image acquisition must be fast, on the order of 1000 Hz to accurately sample action potentials, while acquisition speeds for Ca^{2+} imaging can be in the range of 1-10 Hz [68]. This means that voltage indicators have less time to deliver photons to the imaging detector, making each

measurement inherently noisier. Achieving fast acquisition speeds while maintaining a large field of view is also a significant challenge for imaging instrumentation. Also, voltage indicators must localize to the plasma membrane to properly sense voltage, in contrast to Ca^{2+} indicators which are localized to the cytosol. This makes it challenging to segment adjacent cells in the image processing to resolve activity from individual cells [68]. Finally, voltage imaging is hindered by background autofluorescence and signal decay by photobleaching [69]. A comparison of voltage imaging to Ca^{2+} imaging is shown in **Figure 2.6**.

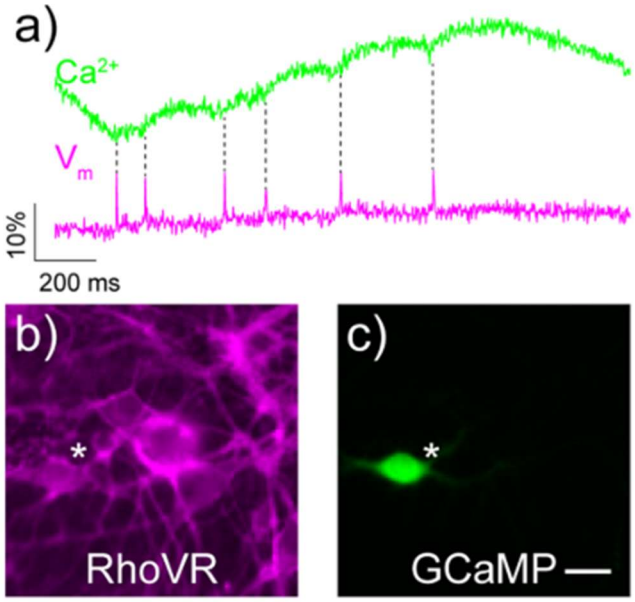

Figure 2.6 Comparison of voltage and Ca^{2+} imaging in neurons. (a) Ca^{2+} (green) and voltage (magenta) responses to single, spontaneous action potentials in the same rat hippocampal neuron, as recorded by GCaMP6s (green) and the voltage-sensitive dye RhoVR 1 (magenta). Panels (b) and (c) depict the neuron (white star) analyzed in panel (a). Scale bar: 20 μm. Adapted from [379].

Optogenetics

Optogenetics is a powerful technique that enables modulating the activity of genetically-targeted cell types with light. It involves manipulating neurons so that they express genes taken from algae that encode light-sensitive ion channels and pumps, called opsins. In the first key demonstration in 2005, the gene encoding channelrhodopsin-2 (ChR2) was delivered to neurons via a lentivirus vector, and subsequently these neurons could be induced to fire action potentials upon delivery of millisecond-timescale pulses of blue light [70]. Since that initial demonstration, the optogenetics toolkit has been expanded to include

opsins that mediate neural activation with green and red light, and light-sensitive chloride pumps that act as inhibitory opsins, among others [71]. Optogenetics has made it possible to causally probe the contributions of specific cell types to neural circuits, since activation and silencing of those specific cells can reveal the impact they have on the generation of behaviors and pathologies. The ability to selectively perturb the activity of specific cell types is a key advantage for optogenetics over electrical stimulation, which is nonspecific.

One of the primary challenges in optogenetics is that the visible light needed for opsin activation is scattered and absorbed by neural tissue. The mean scattering length for visible light in biological tissues is on the order of 100s of micrometers, though it is slightly higher for infrared light [72]. Thus, methods of light delivery to the brain have become a key research area. Approaches include implantable optical fibers [73], implantable probes with integrated optical waveguides [74] or micro-LEDs [75], and more exotic methods such as ultrasonic guiding of light [76]. Even more recently, methods have been evolving for finely directing light stimulation using spatial light modulation to enable studies with single-cell targeting precision [77].

Optogenetics has proven a powerful technique in neuroscience research, and it is still in the early years of its adoption. An open question that remains is how optogenetic tools might someday be used clinically. It is still too early to know whether the opsin genes will be well tolerated in the human body, especially over long timescales. Even so, one promising candidate for optogenetics-based treatment in humans is retinitis pigmentosa, which is attractive because the retina is both immune-privileged and allows simple light delivery through the eye [78].

2.2.3 Magnetic

Imaging

Magnetic fields are perhaps the only modality that can access arbitrarily deep tissues with little signal attenuation, due to the low magnetic susceptibility of biological tissues [79]. Functional magnetic resonance imaging (fMRI) exploits the differences between the magnetic properties of oxygenated and deoxygenated hemoglobin to measure local increases in blood flow that accompanies neural activity [80]. It is a noninvasive method that allows whole-brain

imaging, however it has limited spatial and temporal resolution and it an indirect metabolic correlate of neural activity. The spatial resolution is primarily defined by the voxel size, which is on the order of ~1 mm^3 or larger, and the signal-to-noise ratio of the acquired data [81]. The temporal resolution is on the order of ~1 s, and it is limited both by the image sampling rate and the inherently slow hemodynamic response time [82]. Despite its relatively poor spatiotemporal resolution, fMRI has enabled many insights into the functions of specific regions in the human brain and their contributions to different cognitive processes.

Modulation

In addition to enabling non-invasive, whole brain imaging, magnetic fields can be leveraged to modulate activity in the brain. Transcranial magnetic stimulation (TMS) is a technique in which magnetic fields with frequencies <1 kHz and amplitudes >1 T can inductively evoke ionic currents it order to non-invasively modulate brain activity through the skull [83]. TMS pulses are produced by sending a brief, high-current pulse through a coil of wire, which produces a transient magnetic field with lines of flux passing perpendicularly to the plane of the coil. This magnetic field in turn induces an electric field in the tissue, perpendicular to the magnetic field, which can excite neurons and induce currents [83]. Different coil geometries have been engineered to target the TMS stimulation area, however the spatial resolution is still limited to ~1 cm. TMS is most frequently used as a research tool to probe brain physiology, however it has also shown potential as a therapeutic option for treating depression and other psychiatric disorders [84].

Another method for exploiting magnetic fields to achieve neuromodulation is the use of magnetic nanoparticles (MNPs) as transducers. There are two primary mechanisms by which MNPs can transduce magnetic fields into neural activation: magnetothermal and magnetomechanical. In the first, MNPs exposed to an alternating magnetic field generate heat through hysteresis, which in turn activates heat-sensitive cation channels in neurons to trigger action potentials [85]. In the second, iron-containing MNPs tethered to the cell membrane produce a torque on the membrane in the presence of magnetic fields, which triggers mechanosensitive cation channels in neurons to achieve neuromodulation [86]. In

contrast to neuromodulation using DBS or TMS, the use of these magnetic transducers allows modulation on the microscale, as well as cell-type specific targeting.

2.2.4 Acoustic

Ultrasound (US) is a form of acoustic energy that easily penetrates soft tissues at wavelengths on the order of ~100 μm. This allows US-based methods to deliver focused energy several centimeters deep into tissue, and with spatial precision corresponding to the wavelength [87]. Furthermore, sound waves propagate at speeds of ~1.5 km/s in soft tissue, which allows US to operate with temporal precision below 1 ms. These properties have made US a widely used technology in clinical medicine, and more recently have drawn attention in the neuroscience research community.

Imaging

US has long been used as a tool for imaging soft tissues throughout the body. US imaging is a pulse-echo technique involving the transmission of brief pulses of US into tissue and recording the backscattered echoes from objects and interfaces in the tissue [87]. Scattering arises from materials with different density or compressibility relative to the surrounding medium, including tissue interfaces and blood cells. Although US is strongly attenuated by bone, brain imaging is possible through the intact skull in mice, and through cranial windows in other species. Recently, methods using ultrafast US have been demonstrated for visualizing hemodynamic correlates of neural activity in behaving animals with brain-wide coverage. The technique, known as functional US imaging (fUSI) can image cerebral blood flow with greatly enhanced temporal resolution compared to fMRI, and it has the added advantage that it can be used to image awake, behaving subjects (including during locomotion) by fixing a miniaturized US probe onto the skull [88].

Modulation

The same properties that make US attractive for neural imaging also make it appealing for neuromodulation, including the ability of sound waves to penetrate deep into tissues and achieve high spatiotemporal precision. For neuromodulation, US waves only need

to travel in one direction (backscattering is no longer important), which allows lower frequencies to be used which more easily travel through the intact skull, including the human skull [87]. In awake nonhuman primates and humans, focused ultrasound (FUS) applied to the brain has been shown to modify perception, behavior, and other neurophysiological responses [89]. The exact mechanisms by which FUS achieves its neuromodulatory effects are not fully understood, but it is believed to act through mechanical force on neurons, transduced by mechanosensitive ion channels [90]. More work is needed to explore the safety and efficacy of FUS for neuromodulation, but it offers great promise as a non-invasive method that can target cm-deep brain areas with higher spatial precision that TMS.

The list of neural recording and modulation methods outlined in this section is by no means exhaustive, but it gives an overview of some of the primary modalities for interacting with the nervous system, as well as their pros and cons, in order to provide context for the methods explored in this thesis.

2.3 Challenges for bio-interfacing electrodes

The design and fabrication of bioelectronic interfaces are guided by some universal principles, including low interfacial impedance and intimate integration with soft and curvilinear tissues. The inherent mismatch between biological tissues and manmade electronics cannot be ignored, it and has required significant innovation to realize electronics which can intimately and safely interact with tissues. At epidermal interfaces, human skin is both stretchable and breathable, but electronics are typically non-stretchable and require impermeable encapsulation for prolonged lifetimes. At implanted interfaces, tissues are soft and ionically conductive while conventional electronics are rigid and electronically conductive. These and other inherent mismatches between tissues and electronics pose significant challenges.

2.3.1 Implantable interfaces

Electrodes that are implanted inside the body face the challenge of long-term exposure to a warm, aqueous, saline environment and must contend with the body's innate

immune response. Decades of investigations into the long-term performance of implanted neural electrodes have established that the quality of signals transduced across this interface considerably decays over time [91], [92]. One of the primary factors that limits the functional lifespan of implanted bioelectronics is the mismatch in mechanical properties between the materials composing the device and the surrounding soft tissues. Numerous studies have shown that chronic implantation of stiff, penetrating microelectrode probes into brain tissue triggers a cascade of biological responses that are detrimental to the recording performance of the electrode [93], [94]. There is an acute wound-healing response triggered by the initial probe insertion, characterized by the migration of activated microglia, reactive astrocytes, and blood-borne macrophages to the cite as well as the secretion of inflammatory cytokines, reactive oxygen species, and other neurotoxic factors [95], [96]. If the probe remains in the tissue, this acute response transforms into a chronic foreign body response. This response is characterized by the formation of an insulating glial scar around the implant, composed of fibroblasts, reactive astrocytes, and activated microglia, as well as the formation of a neurodegenerative zone around the implant where neurons die or migrate away from the site [92], [97]. The acute and chronic phases of the biological response to a stiff implant are shown in **Figure 2.7**. The glial scar limits ionic exchange between the electrode and surrounding tissue, effectively insulating it from the neural signals, and the death and migration of neurons away from the implant means that there are fewer signals to record.

Several strategies have proven effective for minimizing the biological response to implanted electrodes. For instance, the addition of coatings which elute anti-inflammatory drugs can significantly reduce the inflammatory response [98]. The most effective approaches for improving the long-term performance of implanted electrodes, however, center on making electrodes smaller and softer. Neural tissues are soft (<10 kPa), compliant, and constantly undergoing micro and macroscopic motions caused by pulsatile blood flow and motions of the human body [99]. Conventional electronic materials, notably noble metals and silicon, have Young's moduli orders of magnitudes higher than that of the neural tissue (~100 GPa), which means that rigid electronics in these tissues are constantly undergoing micromotions with respect to the surrounding tissue, exacerbating the inflammatory response. To combat this challenge, new ultrasoft and flexible probes have been developed,

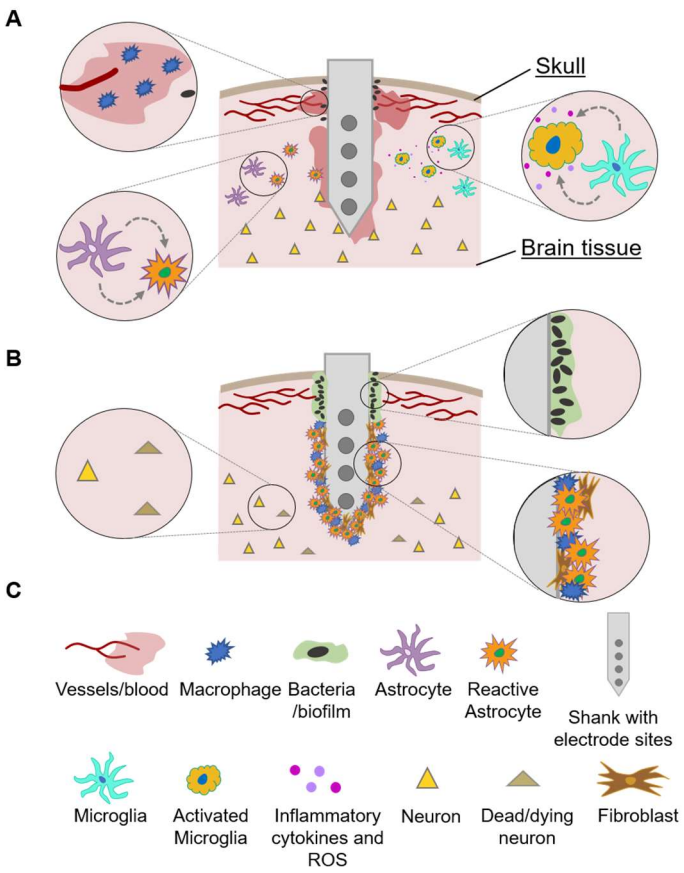

Figure 2.7 Biological response to implantation of a stiff probe. Illustration of the (A) acute, and (B) chronic phases of the biological response to stiff microelectrodes implanted into brain tissue. (C) Legend of symbols used in (A) and (B).

which can move with the tissue and have been shown to elicit a significantly reduced biological response [100]. In addition to using soft, compliant materials, reducing the size of the electronics can also reduce the inflammatory response by reducing the tissue compression forces and damage to capillaries and vasculature during insertion [101].

This poses another significant challenge for implantable electrodes: while making them ultra-compliant and reducing their dimensions can greatly improve their long-term recording functionality, implanting such devices into neural tissues becomes challenging because they may be too compliant to bear the necessary insertion forces to enter the tissue, and instead buckle. Numerous strategies have emerged for implanting soft probes into neural tissue, including the use of temporary rigid insertion shuttles [100], dissolvable coatings [102], shape memory polymers [103], and microfluidic actuation [104], among others [105].

Another key challenge for implantable interfaces is the durability of the electrode and insulation materials in the warm, wet, oxidizing environment of the body. The electrode material must be corrosion-resistant over the planned life of the implant, which is one reason noble metals, such as Pt and its alloys, have been widely used in clinical devices such ECoG and sEEG. If the electrode will be used to deliver electrical stimulation, avoiding electrochemical corrosion during charge injection cycles also becomes an important consideration. The insulation materials must also withstand cracking and delamination, as this leads to current leakage and potential shorts, parasitic capacitances, fluctuations in electrode impedance, and accelerated degradation of the underlying conductive layers [106].

Finally, minimizing electrode impedance is an important consideration for any implantable interface, and it becomes a significant challenge when electrodes are miniaturized to achieve high spatial resolution recording or microstimulation. Electrode impedance will be discussed in more detail in Section 2.4, however a key relation is that impedance rises as the size of an electrode is reduced. Achieving a low interface impedance is key for recording high-fidelity signals, as well as for safely and efficiently delivering charge for stimulation. Thus, choosing electrode materials that effectively minimize impedance is a primary consideration for implantable interfaces.

2.3.2 Epidermal interfaces

Epidermal electrode interfaces face a different set of challenges compared to implantable devices, however there are many areas of overlap. Like implantable interfaces, mismatch in mechanical properties between electronics and the soft, flexible skin is one important challenge. Human skin has a Young's modulus of ~20-100 kPa, and can sustain up to 15% tensile strain during normal motions [107], [108]. Thus, achieving compliant and conformal contact between an epidermal sensor and the skin requires using soft, flexible, and even stretchable materials. Insulating elastomeric substrates can meet these requirements, however this is a more challenging problem for the conductive materials used for the electrodes and interconnects. One common strategy for enabling deformable electronics is to pattern thin metallic films into serpentine or fractal mesh geometries to minimize local

strains [108], however other strategies incorporating stretchable hydrogels [109], liquid metals [110], and carbon nanotube composites [111] have been demonstrated.

In epidermal interfaces, the electrode-tissue interface impedance is an even bigger challenge than it is for implantable interfaces. The epidermis is essentially an "information barrier", insulting external electronics from the signals coming from deeper muscle or nerve tissues [112]. The topmost layer, the stratum corneum, consists of dead skin cells and intercellular lipids and it is electrically insulating, with a resistance that is significantly higher than that of the underlying layers of the epidermis [112]. This layer dominates the electrode-skin interface impedance, which can be variable depending on skin hydration.

There are two main classes of epidermal interfaces: "wet" electrodes that use a conductive hydrogel at the interface, and "dry" electrodes which do not have a hydrogel. Wet electrodes typically achieve lower impedance because they hydrate the stratum corneum and facilitate ionic exchange, and they are the preferred type for clinical ECG and EEG monitoring. The hydrogels employed in these wet interfaces can pose significant problems for long-term use, however, including skin irritation, and impedance variability as the gels dry out [113], [114]. For scenarios where long-term wear, repeated placement and removal of the device, or easy at-home use are desired, a dry electrode format may be more suitable. Achieving low electrode-skin interface impedance is even more challenging for dry interfaces: they do not offer direct skin-hydrating effects, and the roughness of the skin may introduce air pockets between the skin and sensor, causing increased resistance [112]. Artifacts induced by motion of the electrode relative to the skin are also typically more pronounced in dry electrodes [115]. To overcome these challenges, new dry electrode technologies have focused on ultra-thin, ultra-conformable architectures in order to ensure robust, gap-free contact [116] and some have utilized microneedles capable of penetrating through the stratum corneum layer [117].

Another important challenge for epidermal electronics, particularly in long-term wear applications, is that most plastics and elastomers have poor gas permeability which blocks perspiration and can induce skin irritation and inflammation [118]. Strategies to address this challenge include using breathable textile-based electronics [119] and engineering pores into soft silicone substrates [120]. These strategies must ensure

appropriate insulation of conductive components while still allowing gas and moisture to escape from the skin surface.

2.4 Properties at the electrode-tissue interface

2.4.1 Electrode impedance

One of the most important properties of the interface between an electrode, whether intended for sensing or for stimulation, and a biological tissue is the electrochemical impedance. Electrochemical impedance spectroscopy (EIS) measures the response of an electrode to a small sinusoidal input signal, usually between 10 and 100 mV in amplitude. By comparing the amplitude and phase of the input signal with the recorded output signal, the electrochemical impedance, Z, can be deduced. Impedance is frequency-dependent, so the measurement is typically repeated over a range of frequencies to result in a spectrum. It is often plotted in two separate parts: the magnitude of Z in logarithmic scale,

$$|Z| = \sqrt{Re\{Z\}^2 + Im\{Z\}^2} \quad (1)$$

and the phase shift of Z,

$$\varphi = \arctan\left(Im\{Z\}/Re\{Z\}\right) \quad (2)$$

in linear scale at each frequency tested. This representation is known as the Bode plot, and it represents the 'transfer function' of the electrode interface, or how well signal content at various frequencies is transferred over the electrode-electrolyte boundary. EIS is typically measured in a phosphate buffered saline (PBS) solution approximating the ionic liquid environment of the body, however it can also be measured on the skin.

A typical Bode plot for a metal electrode in PBS shows high-pass filtering behavior, with high frequency signal content being authentically transferred while low-frequency signal content is attenuated (**Figure 2.8a**) [121]. The mechanisms underlying this behavior can be understood by modeling the electrode interface with an equivalent circuit model, which describes the physical processes contributing to charge transfer (**Figure 2.8b**). The ionic medium separating the working electrode and the counter electrode contributes a frequency-independent attenuation, the access resistance, R_A. At the boundary between the working electrode and the ionic medium, the behavior is more complex and several

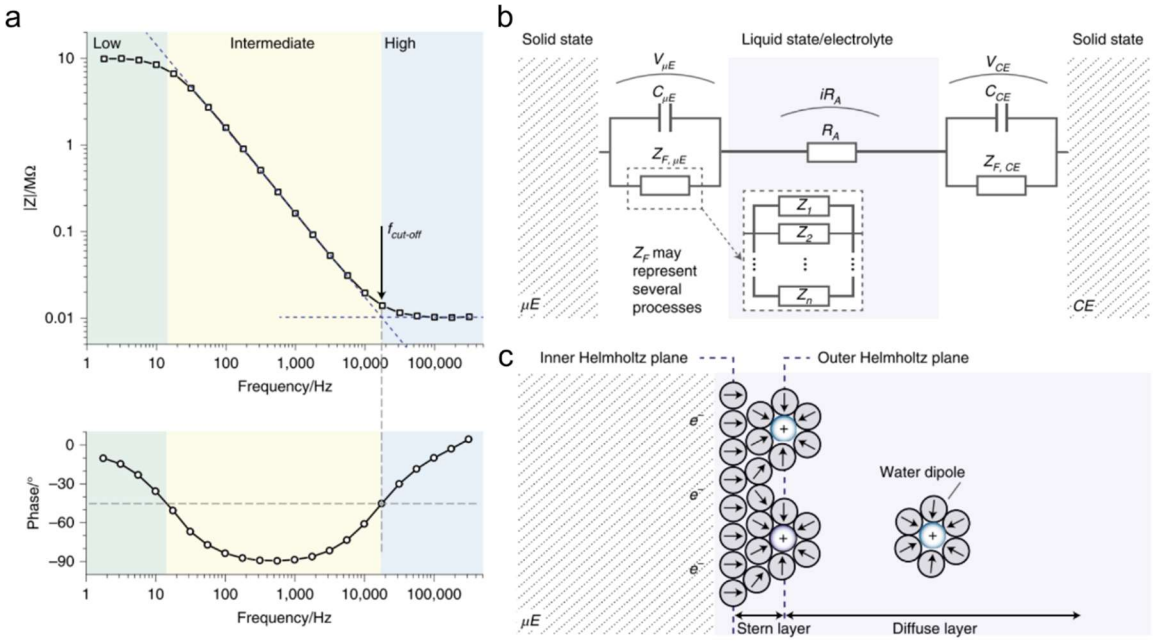

Figure 2.8 EIS at the electrode-tissue interface. (a) Example Bode plot for a smooth metal electrode in PBS. The top plot shows the magnitude and the bottom plot shows the phase of the impedance. The colored zones indicate typical behavior in low (green), intermediate (yellow), and high (blue) frequency ranges. (b) An equivalent circuit model outlining the different contributors to the overall impedance between two electrodes. Here μE is referring to a microelectrode as the working electrode, and CE refers to the counter electrode. At the interfaces, each electrode contributes a double-layer capacitance, *C*, in parallel to an impedance, *Z*, representing all additional charge transfer mechanisms available at the surface. The electrolyte between the two comprises the resistive contribution, R_A. (c) The double-layer capacitance at the electrode-electrolyte interface. Adapted from [121].

mechanisms acting in parallel contribute, which strongly depend on the material characteristics of the surface. One mechanism that contributes is the double-layer capacitance, or Helmholtz capacitance, that forms at the interface between a solid electrode and surrounding electrolyte medium. Two layers of charge with opposing polarity form, one at the surface of the electrode in the form of electrons, and one in the electrolyte consisting of solubilized ions which self-organize into a layer (**Figure 2.8c**). This capacitance contributes more at low frequencies, introducing a phase shift and attenuating the signal [121].

The effect of the double-layer capacitance is directly proportional to the contact area of the electrode with the electrolyte solution. This is one reason why rough or porous electrode interfaces have lower interface impedance: the full three-dimensional contact area

of the electrode surface can contribute to charge transfer, enhancing the capacitance of the surface (**Figure 2.9**).

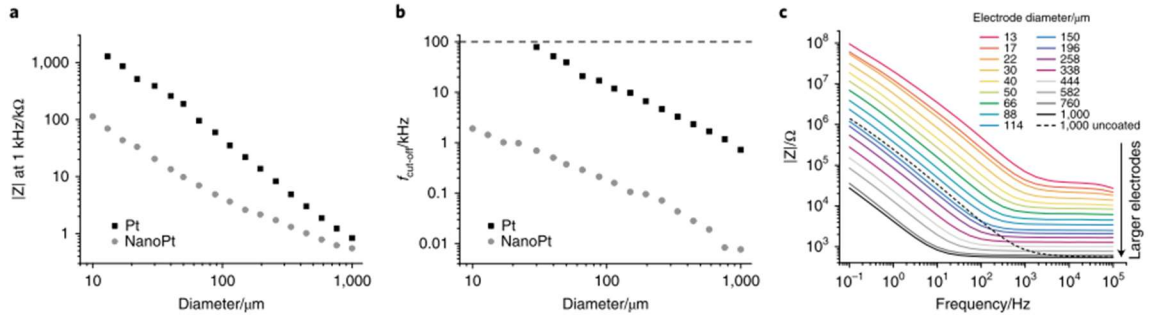

Figure 2.9 Impedance in relation to electrode size. (a) Impedance comparison between smooth Pt electrodes and nano-roughened Pt electrodes at 1 kHz for different electrode diameters. (b) Increased electrode roughness leads to a reduction in cutoff frequency in addition to the reduction in overall impedance. (c) Impedance magnitude for different electrode diameters. The high-frequency impedance is dominated by the access resistance, R_A. From [121].

EIS is used broadly for benchmarking the performance of recording and stimulating electrodes. For neural electrodes, it is common to report the impedance magnitude at 1 kHz, as this is around the frequency where the information content in an action potential occurs. It is important to note, however, that in many bioelectronic applications the primary biosignals have much lower frequency content. EEG, for example, typically contains useful information only below 100 Hz. In many epidermal sensing applications, therefore, it has become more common to report the impedance magnitude at 10 Hz, although there is not yet standardization across the field.

One reason the electrochemical impedance is used so broadly as a performance measure is that it is believed to correlate with signal-to-noise ratio (SNR). The theoretical basis for this notion is that Johnson or thermal noise, v_n, scales with impedance according to equation (3), where k is the Boltzmann constant, T is the temperature, and Δf is the bandwidth of the amplifier:

$$v_n = \sqrt{4kT\Delta f Re\{Z\}} \tag{3}$$

Because of this relation, a lower impedance electrode is expected to collect less thermal noise and thus provide a higher SNR. Thus, signal losses at the interface will be smaller when low-impedance electrodes are used [121].

2.4.2 Charge injection capacity

Stimulating electrodes allow current to be driven over the solid-liquid boundary by exchanging electronic charge carriers in the solid state to ionic charge carriers in the biological medium. For bio-stimulating electrodes, it is important that this process does not induce irreversible reactions that alter the electrode material. This means that the charge injection mechanisms should allow for equal charge transfer in the opposite direction to restore the original state of the electrode. In most bio-stimulation paradigms, charge is delivered in the form of biphasic, charge-balanced pulses, meaning that the current injected in the first half-phase is immediately compensated for by reversing the polarity over the second half-phase such that the net charge transfer over the interface is zero.

There are several mechanisms which can contribute to charge injection. Capacitive charging and discharging over the Helmholtz double-layer often contributes significantly, a non-faradaic process in which no species are exchanged. Electrochemical reactions at the electrode surface may also contribute to charge injection, such as the formation of an oxide at the surface of a metal electrode when metal atoms react with oxygen in the electrolyte. Here electrons are exchanged to ions in a faradaic reaction, which changes the chemical composition of the electrode and the surrounding electrolyte. Over time, faradaic reactions at the electrode interface can corrode or degrade the electrode, however this is not always the case. Reactions where the products remain bound to the surface have a high degree of reversibility, and these can be important contributors to charge injection. While capacitive charge injection is preferable for safe and stable stimulation electrodes, in practice most electrodes have mixed charge injection.

One irreversible faradaic reaction that can be generated by any electrode, regardless of its material properties, is the electrolysis of water:

$$2H_2O + 2e^- \rightarrow H_2 + 2OH^- \quad \text{(reduction)} \tag{4}$$

$$2H_2O \rightarrow O_2 + 4H^+ + 4e^- \quad \text{(oxidation)} \tag{5}$$

This reaction results in the formation of oxygen or hydrogen gas and local pH changes, which may damage the electrode and are harmful to the surrounding tissue. Thus, stimulation electrodes are often characterized by their ‘water window’, or the outer voltage boundaries

which are safe to apply to the electrode and will not induce electrolysis. These voltage boundaries are material-dependent. Using these limits, stimulation electrodes are then further characterized by their 'maximally safe charge injection capacity', CIC, which is defined as the maximum charge per pulse that can be injected before water splitting occurs under either the cathodic or anodic phase. In bio-stimulation, it is more common to lead with the cathodic pulse to depolarize cell membranes, so the CIC in the cathodic phase, CIC_C, is often the value reported for performance benchmarking.

To measure the CIC experimentally, biphasic, charge-balanced current pulses are delivered through the working electrode in PBS while the voltage at the electrode interface is monitored (**Figure 2.10**). Several key parameters can then be deduced from the observed voltage excursion, or 'voltage transient'. The access voltage, V_a, is the instantaneous voltage change when the current pulse is applied or removed, and it is related to the interface impedance. The maximum cathodic voltage or excursion potential, E_{mc}, is measured at the termination of the access voltage in the cathodic phase, where the transient potential begins to decay asymptotically towards the open circuit voltage. The CIC_C is then defined as the total injected charge (current × pulse width) at which E_{mc} reaches the reduction potential for water, or the water window limit.

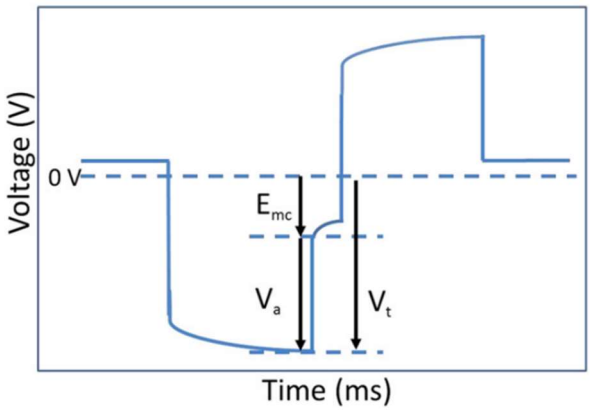

Figure 2.10 Schematic of a biphasic voltage transient potential. The metrics used in assessing the charge injection limit include V_a, the access voltage, and E_{mc}, the maximum cathodic voltage, found at the termination of V_a. From [122].

The voltage produced across an electrode for a particular charge density is inversely proportional to the surface area, meaning that in general larger electrodes are able to inject more charge before exceeding the electrochemically safe limits [122]. However, this

relationship is complicated by the fact that higher field and current densities are typically reached at edges or corners, which means that reactions may be inhomogeneously distributed over the surface. Thus, increasing the surface roughness of an electrode is one way to improve the CIC because this increases the charge transfer area [123].

In addition to the CIC, another empirical relation has been established for determining the safe limit of stimulation charge density: the Shannon limit. The limit derives from histological evaluation of electrical stimulation-induced tissue damage observed in the brains of animal models, and it is a useful relation for determining the boundary between damaging and non-damaging levels of stimulation [124]. Shannon described the boundary between tissue damaging and non-damaging levels of stimulation on a log charge density (D) versus log charge per phase (Q) plot as a line with the equation:

$$\log(D) = k - \log(Q) \tag{6}$$

where the adjustable parameter k is typically chosen between 1.5 and 2.0, with a more conservative estimate of damage thresholds using a lower k. While this empirical relation is useful, studies have shown that it is less accurate for microelectrodes and that the limit for damage also varies significantly with both pulse width and pulse frequency [125].

2.4.3 Charge storage capacity

Another useful characterization of stimulation electrodes is the charge storage capacity, CSC, which is evaluated using slow-scan-rate cyclic voltammetry (CV) in PBS over a potential range that is just within the water electrolysis window for the given electrode. CSC is a measure of the total charge available from an electrode for delivering stimulation. It has become common practice to characterize stimulation electrodes by their cathodic CSC, CSC_C, which is the time integral of the cathodic current during the CV scan (**Figure 2.11**). It is important to note, however, that only a fraction of the charge enclosed by the CV is typically available in practice for injection during a short pulse. Thus, while some electrode materials can offer enhanced CSC due to internal pseudocapacitance, it is misleading to interpret this as if the full internal surface area of the electrode is available for stimulation. In practice, only the most superficial layers of the electrode will be actively involved in charge transfer during a short stimulation pulses, and the CSC therefore overestimates the charge available [121].

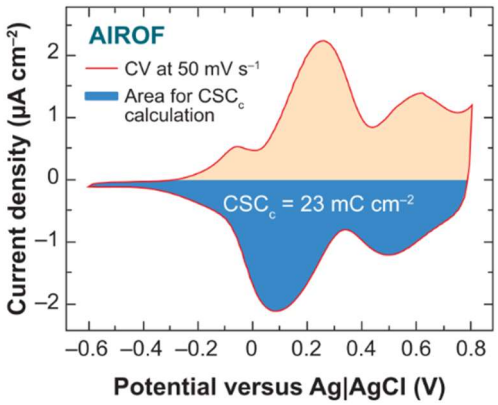

Figure 2.11 CV of activated iridium oxide film (AIROF). The cathodic CIC is shown by the blue area of the voltammogram. From [60].

2.5 Carbon nanomaterials for bioelectronics

In recent years, a variety of carbon-based nanomaterials have emerged as promising candidates for addressing some of the primary challenges of bioelectronic interfaces. These nanocarbons exhibit a wide variety of structures, morphologies, and physical and chemical properties which can be leveraged for different applications (**Figure 2.12**). They offer a combination of mechanical flexibility, nanoscale topology, oxidation stability, and biocompatibility which are advantageous for bioelectronics. Furthermore, their electrical, physical, and chemical properties can be tuned through covalent or non-covalent functionalization. In this thesis work, I leverage some of these key properties to build new bioelectronic technologies based on graphene, and Ti_3C_2 MXene. To provide context for the work in this thesis, in this section I will briefly summarize the current state of research into using carbon nanomaterials for bioelectronics.

2.5.1 Carbon nanotubes

Carbon nanotubes (CNTs) are cylindrical nanostructures of carbon, structured as seamlessly rolled-up sheets of graphene, which is an atomic layer of two-dimensional (2D) sp^2-hybridized carbon lattice. CNTs can be single-walled (SWCNTs), composed of one layer of carbon lattice, or they can consist of multiple nested single-walled CNTs to form multi-

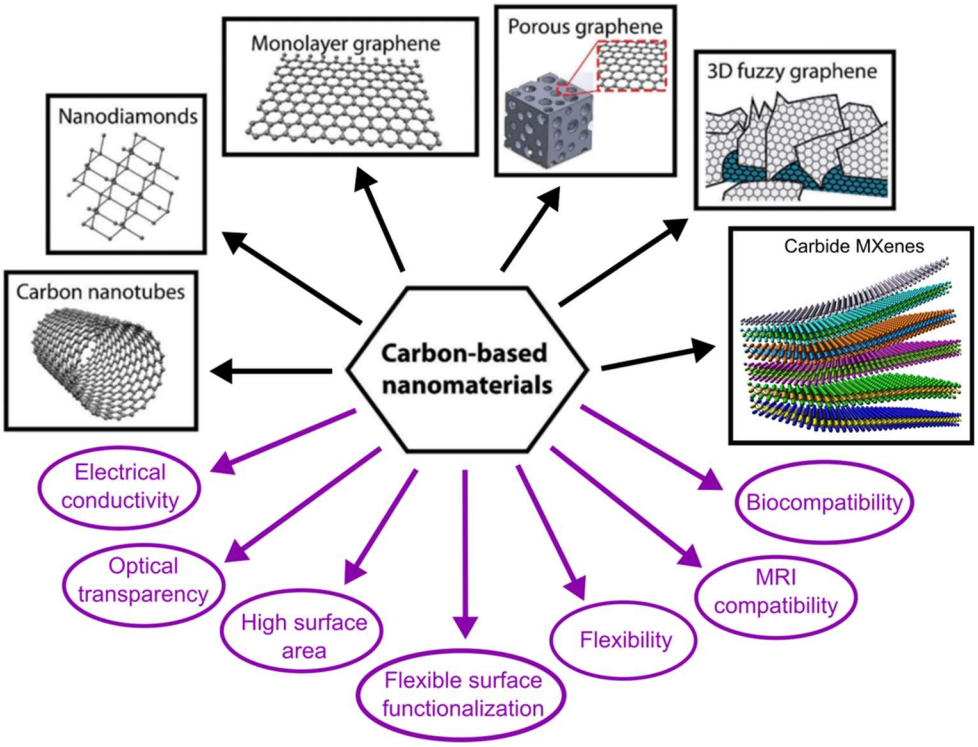

Figure 2.12 Various carbon nanomaterials and their key advantages in bioelectronic interfaces. Materials are shown in black boxes across the top, and their properties are shown in purple ovals across the bottom. Modified from [380].

walled CNTs (MWCNTs). CNTs have been explored in bioelectronics due to their high intrinsic surface area, conductivity, mechanical flexibility, and wide electrochemical water window which contributes to a high charge injection capacity.

In neural recording applications, both CNT coatings on metallic microelectrodes and electrodes entirely composed of vertically-aligned CNTs have shown significantly reduced interface impedance and improved SNR compared to metallic controls of the same geometric area [126], [127]. These improvements are attributed to their high specific surface area and high conductivity. In stimulation applications, CNTs and CNT-coated surfaces have also been shown to exhibit increased capacitance, and a wide water window [128]. Together with their low interface impedance, these properties contribute to enhanced charge injection capacity, and they have been demonstrated in several studies for effective neural stimulation [129]. CNT films are also quite mechanically flexible, and this property has been used to generate flexible and even stretchable electrode arrays with all-carbon circuitry [14], [130]. The

unique properties of CNTs on the nanoscale have also been harnessed at the macroscale by combining aligned CNTs to form carbon nanotube fibers (CNTfs) through a wet-spinning process [131], [132]. These CNTfs have been used for chronic neural recording and stimulation *in vivo*, and their advantages include mechanical flexibility, low impedance, high SNR, and resistance to biofouling [133].

In terms of biocompatibility, the safety of CNTs is a topic of some debate. Pristine CNTs are highly hydrophobic, and thus they tend to aggregate in physiologic medium. When freely circulating in the body, CNTs can aggregate in tissues and cause toxicity in the kidney, liver, and spleen [134]. When CNTs are bound to an electrode interface, however, a more important consideration is their cytotoxicity to the cell types with which the electrode will directly interface. Several studies have demonstrated that neurons cultured on CNT substrates actually exhibit increased neurite outgrowth, synapse formation, and activity compared to neurons cultured on planar conductive controls [135], [136]. It is believed that the nanoscale topology and positive surface charge of CNTs promote neuronal adhesion and encourage growth [137].

2.5.2 Nanocrystalline diamond

Nanocrystalline diamond (NCD) refers to diamond films with grains smaller than 100 nm. NCD has been gaining interest for bio-interfacing microelectrodes due to its chemical stability, biocompatibility, wide water potential window, optical transparency, and tunable electrical conductivity [138]–[140]. When doped with boron, NCD can exhibit high conductivity and excellent stability in physiologic medium, in addition to tunable optical transparency [138]. The optical transparency can be utilized for combining optical imaging and electrophysiological recording, however as the boron doping concentration increases to improve conductivity, the optical transparency decreases [141]. NCD has been used as a coating on microelectrodes and has shown promise for neural recording, though it has not been as widely studied as CNTs and graphene derivatives.

2.5.3 Graphene

Graphene is a one-atom thick 2D lattice structure of sp^2-hybridized carbon. Graphene and its derivatives have gained attention for bioelectronics due to their exceptional physical and chemical properties, including high electrical conductivity, mechanical strength and flexibility, high surface area, high chemical stability, and high optical transparency. Beyond these properties, a number of studies have demonstrated a favorable biocompatibility profile of graphene, though the material preparation (i.e. the synthesis and subsequent processing) can influence its purity and surface chemistry to negatively affect biocompatibility [142]. In this section, I will discuss three different forms of graphene that have gained attention: 2D planar graphene, porous graphene, and out-of-plane/fuzzy graphene.

2D planar graphene

Planar monolayer graphene has attracted attention for enabling transparent bioelectronics that allow studies combining electrophysiology with optical methods such as optogenetics, Ca2+ imaging, optical coherence tomography imaging, or monitoring biochemical activity of cells using fluorescent dyes. Similar transparent electronic platforms have been demonstrated using indium tin oxide (ITO), however its brittle nature has made integrating the electronics with soft tissues challenging. Thus graphene, with its high optical transparency and conductivity along with its excellent mechanical flexibility, has largely dominated this space and has enabled fabrication on flexible polymeric substrates. A number of studies have demonstrated successful neural recording with graphene microelectrodes, and several have also combined optical methods [6], [7], [143], [144]. Transparent graphene microelectrodes have high impedance, though chemical doping methods have been shown to reduce the impedance somewhat [6]. Planar graphene has also been shown to exhibit good corrosion resistance, and thus it has also been explored as a coating material on metallic electrodes to improve stability [145].

Porous graphene

3D porous graphene structures can be synthesized by various methods, including hydrothermal treatment of graphene oxide nanosheet suspensions [146], template-directed

CVD synthesis on Ni foam [147], and by laser pyrolysis of polymer substrates [16]. The high accessible surface area of porous graphene has made it an attractive material for electrochemical biosensing platforms and for bioelectronic devices. In one notable demonstration, porous graphene microelectrodes were fabricated by laser pyrolysis of polyimide films and used for neural recording and cortical microstimulation. The electrode arrays showed good mechanical flexibility, low impedance, high charge storage and charge injection capacity, and good long-term stability in a PBS environment [16].

Out-of-plane graphene

An alternative approach to forming 3D graphene structures is to perform out-of-plane or vertical growth of graphene on a 3D Si nanowire mesh template, an approach which was developed just in the past few years [148]. This produces so-called "fuzzy graphene" with a different morphology and an even larger surface-to-volume ratio than the porous graphene forms discussed above. The exceptionally high surface area of fuzzy graphene makes it an attractive candidate for bioelectronics platforms. While this form of graphene is still quite new, one study reported recordings of neuronal activity for neurons cultured on a fuzzy graphene microelectrode array with high SNR [149]. The electrodes also showed significantly reduced impedance and enhanced charge storage capacity compared to size-matched gold electrodes [149].

Carbon nanomaterials show excellent promise for bioelectronic interfaces due to their unique properties, and new devices incorporating various forms of nanocarbons may soon gain more widespread adoption.

Chapter 3: Multimodal seizure mapping with transparent graphene electronics

Neurological disorders such as epilepsy arise from disrupted brain networks. Our capacity to treat these disorders is limited by our inability to map these networks at sufficient temporal and spatial scales to target interventions. Current best techniques either sample broad areas at low temporal resolution (e.g. calcium imaging) or record from discrete regions at high temporal resolution (e.g. electrophysiology). This limitation hampers our ability to understand and intervene in aberrations of network dynamics. In this chapter, I develop transparent graphene microelectrode arrays, and establish experimental techniques to map the onset and spatiotemporal spread of acute epileptic seizures *in vivo* by simultaneously recording high bandwidth microelectrocorticography and calcium fluorescence. I then integrate dynamic data features from both modalities using non-negative matrix factorization to identify sequential spatiotemporal patterns of seizure onset and evolution, revealing how the temporal progression of ictal electrophysiology is linked to the spatial evolution of the recruited seizure core. This integrated analysis of multimodal data reveals otherwise hidden state transitions in the spatial and temporal progression of acute seizures. The techniques demonstrated here may enable future targeted therapeutic interventions and novel spatially embedded models of local circuit dynamics during seizure onset and evolution.

3.1 Introduction

Understanding the dynamics underlying seizure generation and spread at the scale of neural microcircuits is critical for improving epilepsy therapies and enabling more efficient seizure control. For example, targeted epilepsy treatments such as surgical resection, thermal ablation, or responsive neurostimulation rely on precisely localizing seizure onset regions to be effective. Currently, clinicians localize these regions by observing seizure semiology, identifying electrophysiological signatures from millimeter-scale implanted electrodes, and combining these features with non-invasive imaging techniques such as magnetic resonance imaging (MRI) and positron emission tomography (PET). Unfortunately, the spatial and temporal resolution of these techniques is limited to collective, region-wide network oscillations, which hampers the development of precision therapy approaches. A growing

body of literature indicates that seizures, in fact, begin at the scale of neural microcircuits, which current clinical technologies cannot observe [1], [3], [150], [151]. Thus, there is great interest in observing cellular and microcircuit level dynamics as seizures begin and spread, and in linking these to the macroscale, brain-wide activity recorded by current clinical technologies.

Recently, microelectrode array recordings in humans have opened a window into complex, microscale ictal dynamics within the cortical area usually covered by a single clinical electrocorticography (ECoG) electrode. Similarly, microarray and microwire studies have revealed spatially distinct territories near the seizure onset zone [152], characterized by heterogeneous firing of single cells [153] and associated with different states of excitation-inhibition balance [154]. Observing seizures at this new scale has led to the idea that the cortical areas involved can be divided into a core territory of recruited neurons (the 'ictal core'), surrounded by areas that receive intense synaptic input but do not show hypersynchrony and pathologically high firing rates (the 'ictal penumbra'). Observations at the microscale have also revealed previously unobserved temporal phenomena at play during epileptic seizures: individual ictal and interictal epileptiform discharges observed on intracranial EEG (iEEG) can spread near-synchronously across macroscopic brain areas [155], [156]. In contrast, microscale neurophysiological markers of the so-called 'ictal wavefront' spread locally at much slower speeds, typically not exceeding ~5 mm/s [157]. It has now become apparent that macroscale signatures of these microscale dynamics are present in particular frequency bands of clinical iEEG, but were only identified with the benefit of concurrent microelectrode recordings [158], [159].

Although microelectrode array recordings are significantly advancing our understanding of microscale epileptic dynamics, these electrode arrays still cannot offer a complete picture of neural circuits due to their limited spatial sampling. Recordings with the Utah array (96 electrodes in a 4 x 4 mm area), for example, typically detect the activity from several dozen up to ~180 neurons, at most, from patches of cortex that are just a few millimeters across, and which contain hundreds of thousands of neurons [153]. Evolving alongside implantable microelectrode technologies, optical tools and techniques enable investigators to observe neural activity at cellular and even sub-cellular spatial scales [65],

[160], [161]. Optogenetics gives these techniques tremendous power to image and modulate the function of specific, genetically-targeted cell types in the brain to discern the roles of different cell assemblies [4]. Calcium fluorescence imaging has provided insights into the role of inhibitory interneurons in seizure initiation and spread [162], and in the microstructure of synchronous neuronal assemblies in epileptic networks [163]–[165]. However, such imaging studies typically suffer from low temporal resolution limited by the kinetics of the fluorescent reporter molecules as well as the speed of currently available imaging systems [5], [160], [166].

Combining electrophysiological and optical recording modalities presents a unique opportunity to harness the spatial resolution of optical imaging along with the temporal resolution of electrophysiology. However, such a combination requires imaging and recording simultaneously in the same location, which is not possible with conventional microelectrode arrays composed of opaque metallic materials, as these block optical access and suffer from photoelectric artifacts [167]. Recently, progress in transparent microelectrode array technology, predominantly utilizing graphene, has enabled such multimodal studies [6]–[9]. However, innovation is still needed in experimental and analytical methods to fully realize the potential of these multimodal mapping techniques. Notably, there is currently a lack of analytical methods to combine high density optical and neurophysiology datasets, while accounting for their differences in temporal and spatial sampling.

In this work, we demonstrate a novel experimental and methodological paradigm which combines mapping of microscale local network dynamics at high spatiotemporal resolution with a quantitative analysis framework to distill the dynamics underlying seizure generation and evolution *in vivo*. Specifically, we utilize custom-made, transparent graphene microelectrode arrays to simultaneously record electrophysiology and optical signals of microscale brain activity in a rodent model of acutely induced epileptic seizures. We combine dynamic data features from both modalities in a sparsity-constrained non-negative matrix factorization (NMF) approach in order to identify spatiotemporal patterns across these acquisition modalities. NMF is used for dimensionality reduction, similar to principal component analysis, but yields sparser and potentially more interpretable factors due to the

non-negativity constraints on both the original feature matrix and the resultant factors. Such an approach has previously been used to decompose dynamic functional connectivity into sets of variably expressed subnetworks and track their temporal evolution in human neuroimaging [168]–[170].

This analysis reveals how the temporal progression of ictal electrophysiology is linked to the spatial evolution of the recruited seizure core. We show that locally synchronous increases in broadband micro-ECoG (μECoG) power are associated with a progressive expansion of the ictal core at seizure onset, and that state transitions occur during an established seizure that are accompanied by subtle changes in ictal discharge morphology. These microscale spatiotemporal dynamics are not apparent from electrophysiology alone, and highlight the unique advantages of multimodal recording enabled by transparent electronics. The analytical framework presented here serves as a proof of concept for future studies combining data from multiple modalities, with the potential to illuminate mechanisms underlying seizure initiation, spread, and microscale network interactions that may characterize other types of brain disorders.

3.2 Development of transparent graphene microelectrode array technology

3.2.1 Prior work

The first demonstrations of transparent graphene electronics for multimodal neural recording were published simultaneously in 2014 by two separate groups. Dong-Wook Park et al. developed a transparent array of 250 μm-diameter graphene electrodes encapsulated in a flexible parylene C substrate and demonstrated the ability to optogenetically stimulate neurons through the array while simultaneously recording local field potentials (LFPs), as well as to image cortical vasculature through the array (**Figure 3.1a**) [7]. In that work, the graphene arrays were fabricated by stacking 4 layers of CVD-grown graphene by coating each graphene layer with PMMA, chemically etching the copper foil substrate, transferring the PMMA/graphene to the wafer substrate, and subsequently dissolving the PMMA. This transfer process is known to induce cracking defects in the graphene monolayers as well as

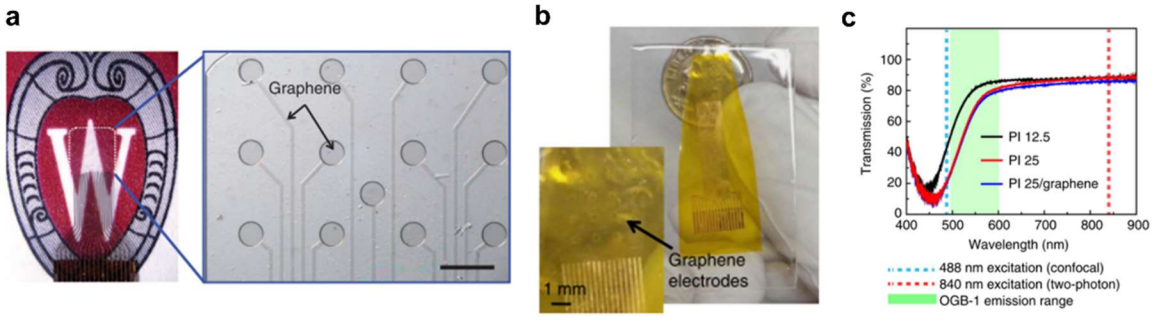

Figure 3.1 Early demonstrations of transparent graphene microelectrodes. (a) CLEAR graphene device from Dong-Wook Park et al. in parylene C substrate. Scale bar 500 μm. (b) Graphene electrode array from Duygu Kuzum et al. in polyimide substrate. (c) Optical transmission of the device in (b), showing reduced optical transparency within the OGB-1 emission range. (a) from [7], (b) and (c) from [6].

to leave PMMA and Cu residues on the graphene film [171]. Thus, while Park et al. showed functional devices, the 1 kHz impedance of their graphene electrodes was quite high at 244 ± 6 kΩ for 250 μm-diameter electrodes, likely due to defects and residues present on the graphene films.

The second group, led by Duygu Kuzum, developed an array of 50x50 μm^2 graphene electrodes encapsulated in a polyimide (PI) substrate, and demonstrated simultaneous two-photon calcium fluorescence imaging and low-noise electrophysiology (**Figure 3.1b**) [6]. The recordings were performed in brain slices *ex vivo*. Kuzum et al. achieved superior impedance performance compared to Park et al. by utilizing a cleaner graphene transfer method which eliminated the copper etching step, and subsequently using nitric acid chemical doping to reduce electrode impedance (541 kΩ for 50x50 μm^2 electrodes). However, the choice of PI substrate resulted in electrode arrays with inferior optical transparency. While parylene C is highly transparent across the visible spectrum, PI absorbs light at wavelengths below 550 nm, which is within the emission range of common optical reporter molecules such as Oregon Green BAPTA-1 (OGB-1) (**Figure 3.1c**).

Since these initial demonstrations, some progress has been made toward improving transparent electrode technology. Kuzum's group showed that electrodepositing Pt nanoparticles onto graphene electrodes could significantly lower the impedance, however this approach sacrifices optical transparency [144]. Another group took a different approach, developing a transparent electrode array based on a nanomesh of Au coated with PEDOT:PSS, rather than using graphene [9]. These Au nanomesh electrodes achieved far lower impedance

than their graphene counterparts, however they had reduced optical transparency and were more prone to light-induced artifacts than graphene electrodes are.

Here, we sought to build upon this foundational work, and to further optimize the fabrication of transparent graphene microelectrodes to offer an improved combination of high optical transparency and low electrochemical impedance. By optimizing the properties of the graphene microelectrode array, we can improve the quality of data which can be obtained during *in vivo* multimodal recording.

3.2.2 Fabrication optimization

To fabricate transparent graphene devices, we began with the protocol outlined by Park et al. and made several important modifications to improve the graphene quality and reduce electrode impedance [172]. We initially designed a μECoG array of nine 50 x 50 μm^2 electrodes in a parylene C substrate and used this device design to test and optimize the graphene processing conditions.

As the first modification, we used a bubble transfer method similar to that described by Gao et. al. [173] to transfer monolayers of graphene grown on copper foils via chemical vapor deposition (CVD) to the wafer substrate. While conventional graphene transfer methods rely on complete etching of metal substrates (typically copper) in suitable etchants, which causes damage to the graphene and leaves metal residues, bubble transfer using electrolysis of water enables transferring large-area graphene films with high purity and without inducing cracking or damage. Using this improved transfer method, we sought to determine an optimal number of stacked monolayers of graphene. We fabricated devices with either one or two stacked monolayers of graphene and assessed the relationship between number of graphene layers and electrochemical impedance (**Figure 3.2a**). While we found that adding a second layer of graphene reduced the impedance (2.16 ± 0.23 MΩ for 2-layer vs. 2.75 ± 0.26 MΩ for 1-layer graphene at 1 kHz), we sought to reduce the impedance further without adding additional graphene layers, as these would reduce the optical transparency of our devices and also add significant time to the fabrication process, as each graphene transfer is performed sequentially. To this end, we next explored chemical doping methods

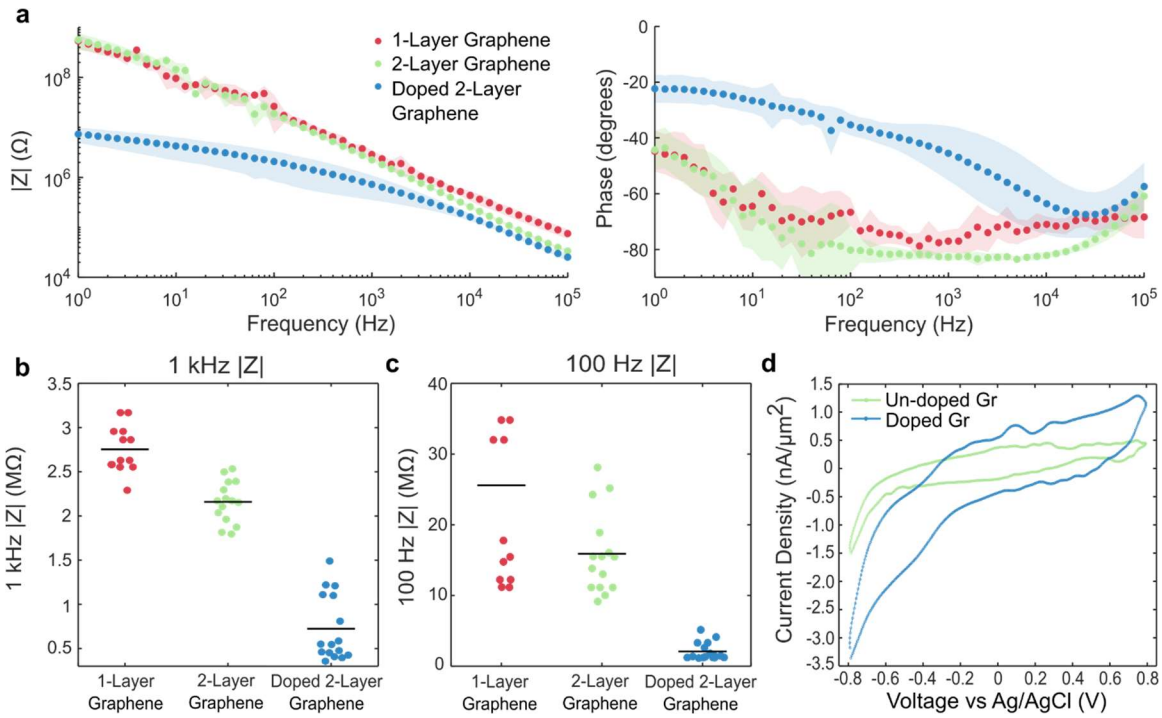

Figure 3.2 Optimization of graphene processing. (a) Electrochemical impedance spectra for 50 μm x 50 μm graphene μECoG electrodes of three preparations: 1-layer graphene, 2-layer graphene, and HNO3-doped 2-layer graphene. Impedance magnitude significantly decreased with doping, particularly at frequencies below 1 kHz. Noise in the low-frequency range for the un-doped graphene samples is attributed to the high impedance modulus. Shaded bounds represent standard deviations. (b) Impedance magnitude at 1 kHz for the three device preparations. Horizontal black bars indicate means. (c) Impedance magnitude at 100 Hz for the three device preparations. Horizontal bars indicate means. (d) Cyclic voltammograms showing superior CSC_C in an HNO_3-doped 2-layer graphene electrode, as compared to an un-doped 2-layer graphene electrode (CSC_C is 22.4 μC/cm2 and 15.9 μC/cm2, respectively). The scan rate was 500 mV/s.

for enhancing the out-of-plane conductivity of graphene, similar to those described by Kuzum et al [6].

Exposing graphene to nitric acid (HNO_3) results in the adsorption of electropositive NO_3^- groups onto the graphene surface. Specifically, the HNO_3 molecule physisorbs onto the graphene sheet, without breaking any C-C bonds, and then dissociates into three groups: two radicals NO_2^0 and NO_3^0, and a water molecule: $2HNO3 = NO_2^0 + NO_3^0 + H_2O$. The two radicals have a singly occupied state below the Fermi energy of the graphene layer, which allows two electrons to transfer from graphene into these states, creating two holes and causing p-type doping [174]. This p-type or hole doping has been shown to reduce electrochemical impedance and improve the noise characteristics of graphene electrodes [174]–[176].

Additionally, layer-by-layer doping has been shown to produce doped graphene sheets with reduced and more stable sheet resistance values compared to doping after stacking of graphene monolayers, where only the topmost layer experiences doping [175], [177]. We optimized a process for HNO_3 doping of graphene and performed this doping layer-by-layer after the transfer of each graphene sheet to the wafer substrate. We tested various HNO_3 exposure times and temperatures, and found that exposing the graphene to 75% HNO_3 for 15 minutes at room temperature produced the largest and most stable impedance reduction. We used these doping conditions for all subsequent device fabrication.

A summary of the results of these optimization procedures is shown in **Figure 3.2**, in which we compare impedance values both at the commonly-used 1 kHz reference frequency, and at the lower frequency of 100 Hz (**Figure 3.2b,c**). We show the values at 100 Hz because many physiologic signals of interest in the brain are of lower frequency content than the typical 1 kHz reference frequency. We find that the impedance relationships between 1-layer, 2-layer, and doped 2-layer graphene devices are similar at 1 kHz and 100 Hz, with the advantage of chemical doping being more pronounced at lower frequencies: the 100 Hz impedance of 1-layer devices is 25.6 ± 11 MΩ, 2-layer devices is 15.9 ± 5.5 MΩ, and HNO_3-doped devices is 2.07 ± 0.65 MΩ. The significant spread of 100 Hz impedance values for the un-doped device preparations can be attributed to their high impedance in this lower frequency range, which limits the accuracy of the EIS measurement. As a low electrode

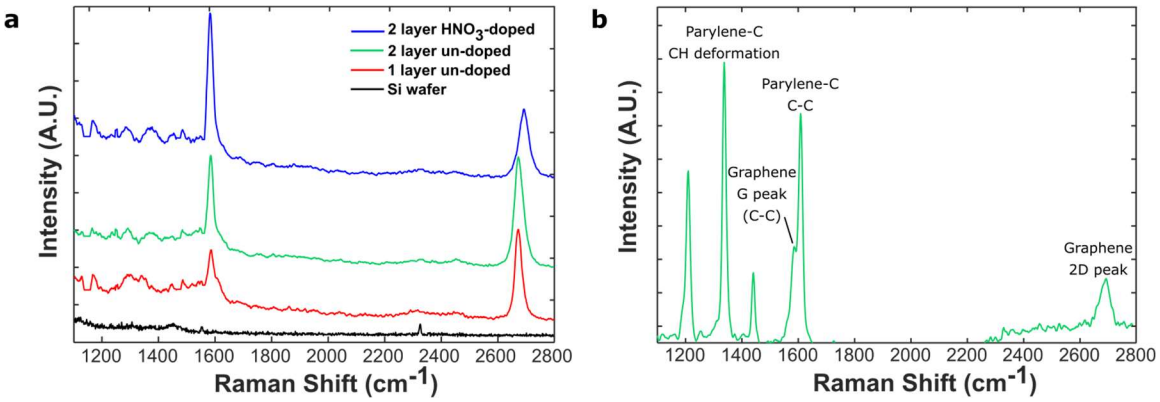

Figure 3.3 Raman spectroscopy. (a) Raman spectra of monolayer un-doped (red), bilayer un-doped (green), and bilayer HNO_3-doped (blue) graphene on Si wafer. The spectrum for the Si wafer substrate (black) is included as a reference. (b) Raman spectrum of doped bilayer graphene between parylene C layers in a completed device.

Table 3.1 Raman spectroscopy analysis. Summary of results from Raman analysis of graphene preparations on Si wafer

	1 layer un-doped	2 layer un-doped	2 layer HNO_3-doped
FWHM(G)	27.42 cm^{-1}	19.88 cm^{-1}	20.57 cm^{-1}
FWHM(2D)	28.13 cm^{-1}	37.40 cm^{-1}	42.40 cm^{-1}
Pos(2D)	2673.20 cm^{-1}	2676.39 cm^{-1}	2694.39 cm^{-1}
I_{2D}/I_G	2.29	1.30	0.50
I_D/I_G	0.65	0.097	0.031

impedance is essential for obtaining recordings with high signal-to-noise ratio (SNR) [10], [126], these results indicate that HNO_3 doping is a useful approach for improving the performance of graphene microelectrodes, especially at lower frequencies where most physiologic signals of interest occur. In addition to EIS measurements, cyclic voltammetry (CV) measurements were taken to assess the effect of HNO_3 doping on the charge storage capacity of graphene electrodes. Doping with nitric acid increased the charge storage capacity from 22.87 $\mu C/cm^2$ to 64.44 $\mu C/cm^2$, indicating that this method of doping may also improve the performance of graphene electrodes for neural stimulation applications (**Figure 3.2d**).

In addition to electrochemical characterization, we also performed Raman spectroscopy to assess the quality of the graphene films and confirm successful p-type doping after exposure to HNO_3 (**Figure 3.3a**). First, Raman spectra for monolayer un-doped, bilayer un-doped, and bilayer doped graphene films on an Si wafer substrate were evaluated. Monolayer un-doped graphene exhibited a D peak at 1309.3 cm^{-1}, a G peak at 1583.1 cm^{-1}, and a 2D peak at 2673.2 cm^{-1}. The average I_D/I_G ratio, which is an indicator of defect concentration, was 0.65. The fact that this ratio is less than unity indicates that our graphene films are of high crystalline quality [178]. The addition of a second layer of un-doped graphene resulted in a narrowing of the G peak, a broadening of the 2D peak, and an upshift in position of the 2D peak, which agrees with previously reported results [178], [179]. In the doped bilayer preparation, further broadening and upshift of the 2D peak was observed, and the I_{2D}/I_G ratio was decreased significantly. These results indicate successful p-type doping of our graphene films after HNO_3 exposure [178], [180]. Values for FWHM(G), FWHM(2D), Pos(2D), I_{2D}/I_G, and I_D/I_G for each of the three graphene preparations can be found in **Table**

3.1. Next, Raman spectra for a doped graphene electrode in a fully-fabricated μECoG array was evaluated to confirm that the doped graphene remained of high quality following device fabrication (**Figure 3.3b**). The G and 2D peaks retained similar intensity and width as those seen in the doped graphene on Si preparation, indicating that device fabrication does not significantly alter the graphene properties. The peaks at 1210, 1340, 1440, and 1610 cm^{-1} are attributed to parylene-C, and the graphene D peak is obscured by the parylene peak at 1340.

Using the optimal graphene processing conditions determined here, we proceeded with device fabrication for *in vivo* testing. A schematic of the electrode fabrication process is shown in **Figure 3.4**, and a detailed description of the process is provided in the methods at the end of this chapter.

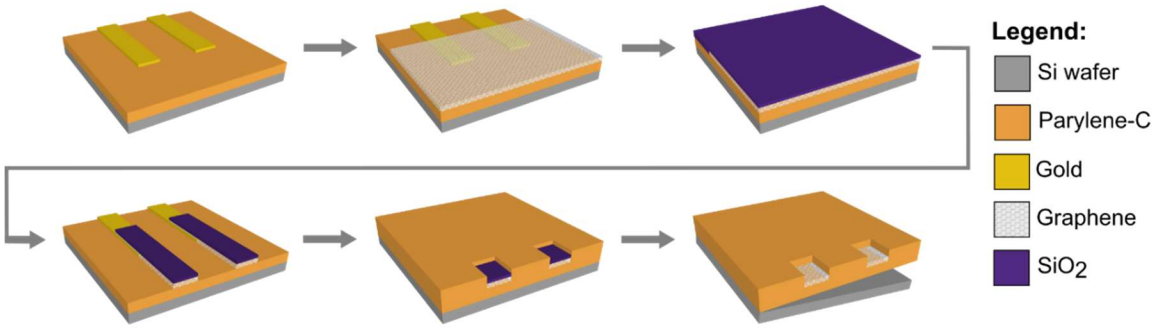

Figure 3.4 Fabrication of transparent graphene μECoG devices. Details of the fabrication are given in the Methods section. Briefly, parylene C is deposited onto a Si wafer and Ti/Au traces are patterned on the parylene C. CVD-grown graphene is transferred to this substrate using a bubble transfer method. An SiO2 layer is deposited to protect the graphene during later processing steps, then the graphene and SiO2 layers are patterned and etched. A top layer of parylene C is deposited to encapsulate the device, then VIAs are etched to open the graphene electrode contacts as well as open the Ti/Au bonding pads at the back end of the device. Finally, the SiO2 covering the graphene electrode contacts is chemically etched away and the devices are removed from the wafer.

3.2.3 Electrode characterization

For *in vivo* experiments, we designed an μECoG electrode array consisting of a 4 x 4 grid of 50 μm x 50 μm square electrode contacts with 500 μm pitch (total recording area of 1.55 mm x 1.55 mm and total array footprint 2.75 mm x 2.75 mm). In each device, graphene forms the electrodes and conductive traces in the distal end of the array, and overlaps with Ti/Au conductive traces outside of the array, such that the entire recording area of the device is fully-transparent (**Figure 3.5a**). The graphene electrodes and Ti/Au traces were patterned

on a 4 μm-thick bottom parylene C substrate and encapsulated by another 4 μm-thick

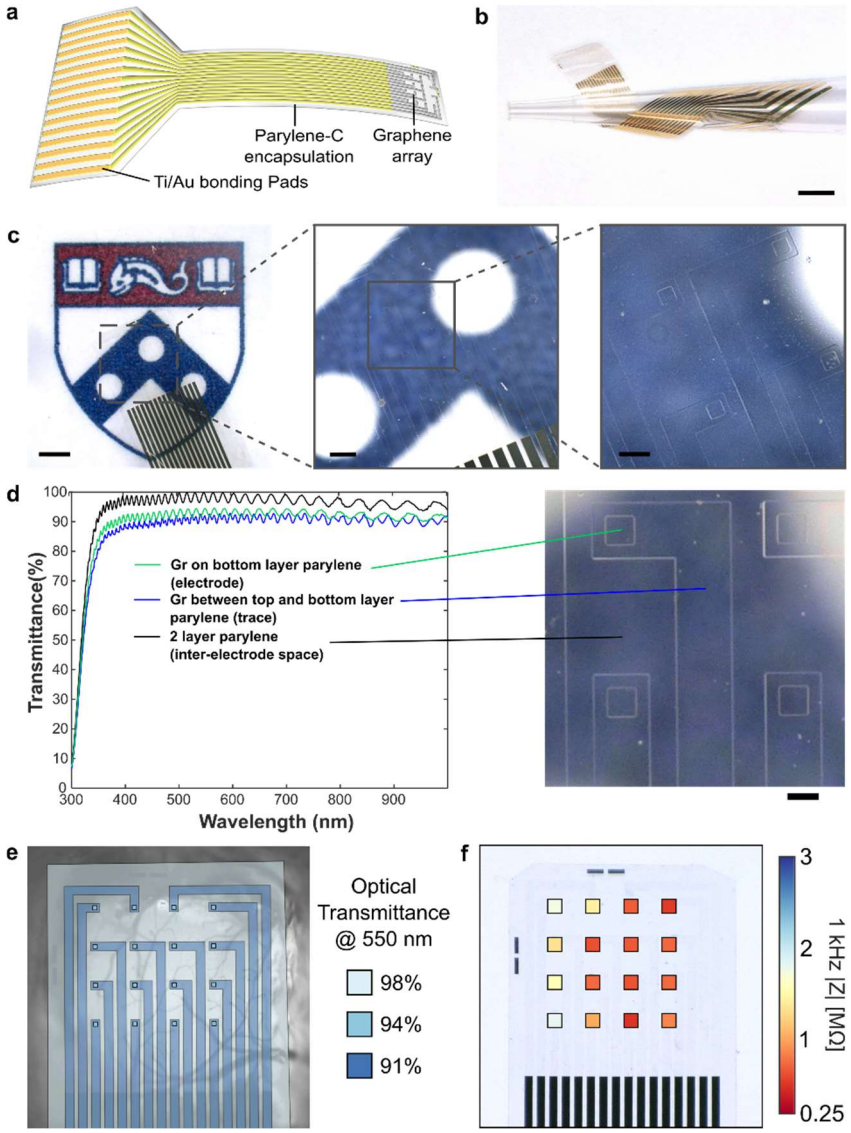

Figure 3.5 Optically transparent graphene μECoG arrays. (a) Schematic of graphene μECoG device: A fully transparent array of graphene microelectrodes and traces connects to gold traces in a flexible cable which can be interfaced with a data acquisition system through a ZIF connector. (b) A graphene μECoG device wrapped around a pipette tip to demonstrate its flexibility. Scale bar: 2 mm. (c) Images of the graphene electrode array overlaid on the Penn logo to demonstrate optical transparency. Scale bars, left to right: 1 mm, 250 μm, 100 μm. (d) Optical transmission spectra for different locations in the graphene μECoG array. Overall, the device is > 90% transparent across the visible to near infrared spectrum. The ringing behavior in the spectra is attributed to parylene C. Scale bar: 50 μm. (d) Mapping of optical transmittance at 550 nm for the locations shown in (d). (e) 1 kHz impedance magnitude for each 50 μm x 50 μm transparent graphene electrode in the array, averaged over 4 devices. Values are overlaid in the corresponding electrode locations on a light microscopy image of a single device. For clarity, electrodes are not shown to scale.

parylene C layer to yield devices with a total thickness of 8 μm. The combination of the thin profile of the device, the low Young's modulus of parylene C and the extreme broadband optical transmittance of both parylene-C and graphene endow the device with high flexibility (**Figure 3.5b**) and optical transparency (**Figure 3.5c**). We found that the devices showed on average >90% optical transparency across the visible spectrum (**Figure 3.5d,e**). The average impedance over 4 such devices (n=64 channels) was 908 ± 488 kΩ at the 1 kHz reference frequency (**Figure 3.5f**), which corresponds to an area-normalized impedance of 22.7 ± 12.2 Ω·cm2.

3.3 Acute, multimodal recording of pharmacologically-induced seizures on the cortex

3.3.1 Experimental overview

We utilized our transparent graphene arrays to perform simultaneous calcium epifluorescence imaging of neurons and electrophysiology recording *in vivo* in an acute murine model of epilepsy. GCaMP6-expressing mice were anesthetized, and the graphene μECoG arrays were placed on the cortical surface following craniotomy. Electrode arrays were connected to a NeuroNexus amplifier/digitizer through a custom interface connector for electrophysiological recording, and wide-field epifluorescence microscopy was used to simultaneously capture GCaMP6 activity at low magnification at a frame acquisition rate of 10 Hz. Several previous studies combining electrophysiology and neuroimaging with transparent microelectrodes have utilized two-photon imaging [181], [182], which offers high spatial resolution but a limited field of view, thus providing detailed information for only a small population of cells lying beneath one or a small number of individual electrodes. For this study, we instead used wide-field epifluorescence imaging to observe the calcium dynamics across the entire millimeter-scale cortical region covered by the array in order to maximally leverage data features from each modality. This choice also allowed us to observe the spatial dynamics of seizure spread across a millimeter-scale cortical area. The flexible electrode arrays readily conformed to the cortical surface and their high broad-band optical transparency allowed penetration of the excitation light (470 nm) and fluorescence emission

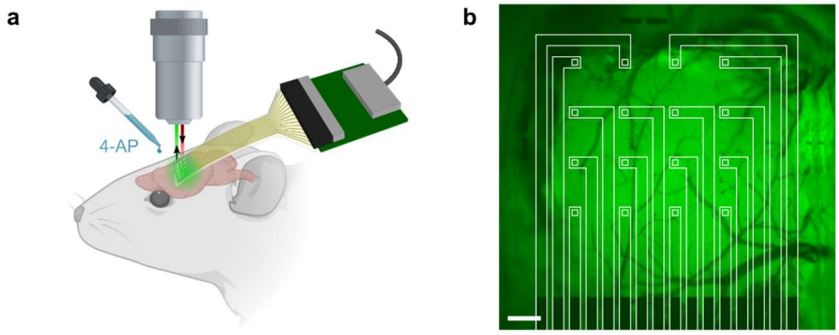

Figure 3.6 Multimodal recording setup. (a) Schematic of the in vivo recording and imaging setup. (b) Image of the graphene electrode array placed over barrel cortex, with baseline calcium epifluorescence visible in green, and array outlined in white to show locations of the electrodes. Scale bar: 300 μm.

light (500-550 nm). A potassium channel blocker, 4-aminopyridine (4-AP), was bath-applied to induce epileptiform activity. A schematic of the recording and imaging setup is shown in **Figure 3.6a**, and an image of the graphene electrode array on the cortex, outlined in white to show the locations of the transparent electrodes is shown in **Figure 3.6b**. Seizure events were recorded on the graphene array and were visible in epifluorescence imaging through the electrodes as changes in normalized fluorescence, where each imaging pixel was normalized by the amplitude and standard deviation of fluorescence changes observed in the baseline, pre-seizure condition.

3.3.2 Multimodal data

The advantages of our experimental setup are underscored in **Figure 3.7**. With the high-density graphene μECoG arrays, we obtained high temporal resolution recordings of seizure activity, including the fast dynamics of seizure onset as well as discrete high frequency oscillations (HFOs). HFOs are of particular interest because of their potential role in ictogenesis and their use as a biomarker to identify seizure onset regions [183]–[185]. Throughout our study, we observed 200-300 Hz "fast-ripple" HFOs consistent with a pathologic, seizure-prone state as determined by a clinician trained in EEG marking (**Figure 3.7a**). These oscillations are too brief and high frequency to be observed with calcium imaging alone.

While electrophysiological recordings offer the high temporal resolution necessary to observe fast activity such as pathologic HFOs, the spatial resolution of these recordings is limited by the minimum size and spacing achievable for microelectrodes in an array. Despite recent advances in the development of ultra-high-density microelectrode arrays [54], imaging modalities still offer superior spatial resolution for observing the spatial spreading dynamics of neural activity, albeit with limited temporal resolution. Using calcium fluorescence imaging, we observed complex, non-stereotyped spatial patterns of seizure

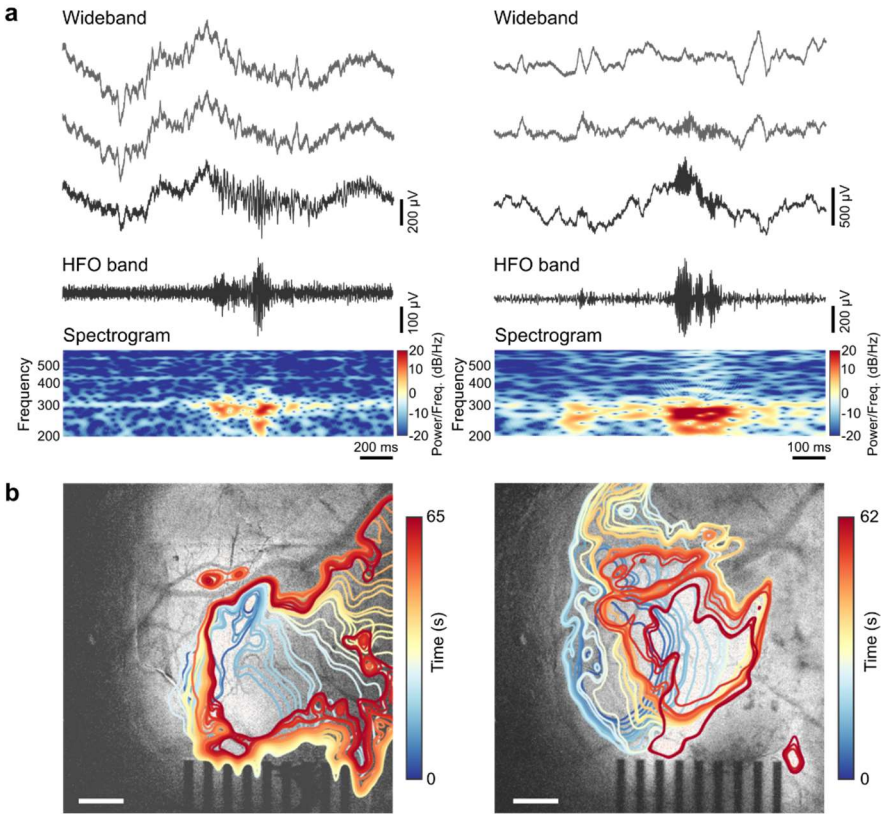

Figure 3.7 Simultaneous electrophysiology and calcium imaging of 4-AP-induced seizure activity in an anesthetized mouse. (a) Examples of two clinician-validated high frequency oscillations (HFOs) recorded on graphene electrodes. Raw, wideband signal from 3 adjacent electrodes highlights the localized nature of the HFOs. Below these, the 80-600 Hz bandpass-filtered signal and the spectrogram, which reveals 200-300 Hz power consistent with fast ripple HFOs, are shown for the bottom-most wideband signal trace. (b) Two representative examples of ictal wavefront onset and propagation patterns observed in the calcium epifluorescence imaging for different seizure events, showing complex non-stereotyped spatial patterns of activation and spread. Ictal wavefront progression is overlaid on images of baseline fluorescence. Scale bars: 500 µm.

initiation and spread, which we illustrate by plotting the putative ictal wavefront evolution over time for two different seizure events (**Figure 3.7b**).

It is important to note that our transparent graphene electrodes recorded seizure activity with high signal-to-noise ratio (SNR). Despite some variability in electrode impedance across the array during *in vivo* recordings, we found that all electrodes had SNR >5, and that SNR was not in fact correlated with electrode impedance (**Figure 3.8a,b**). Instead, the SNR values across the electrode array mapped more closely to the seizure onset pattern, with electrodes closer to the seizure focus showing larger amplitude ictal spikes and thus higher SNR (**Figure 3.8c**). While higher impedance electrodes do pick up more 60 Hz noise interference, this artifact is removed in the data filtering step such that electrode impedance does not affect the results of our analysis.

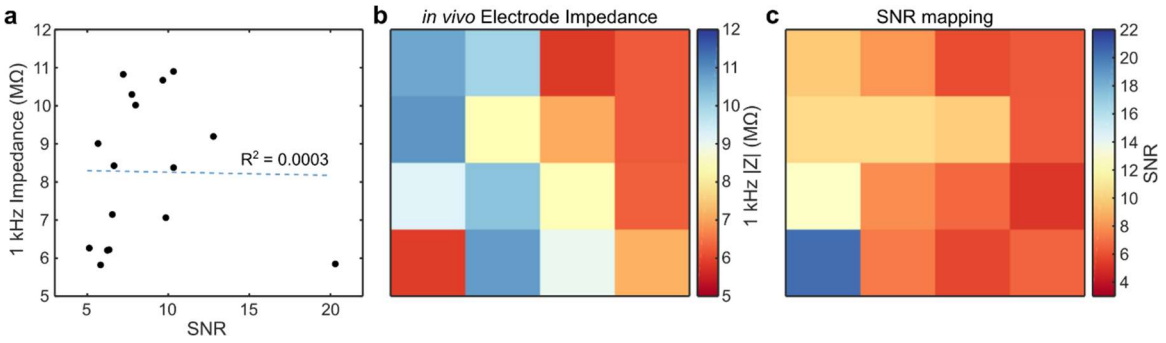

Figure 3.8 SNR vs. electrode impedance. (a) SNR vs. 1 kHz impedance magnitude for each electrode during the *in vivo* recording analyzed in this work. No correlation between SNR and impedance was found, as evidenced by the poor linear fit shown. Note that while the impedance magnitudes measured *in vivo* are significantly higher than those measured in saline, these electrodes still achieve high SNR >5. (b) Map of *in vivo* electrode impedances across the 16 ch graphene array. (c) Map of SNR values across the 16 ch graphene array.

We performed our analysis on the data recorded during the first acute seizure onset in one animal. While the animal experienced multiple seizure events following the drug application, we were primarily interested in the dynamics at play during the brain's initial transition into the ictal state. Because it was not clear that the brain returned to a normal baseline state in between seizures, we chose to focus solely on the initial seizure onset. The multimodal data recorded during this seizure onset are shown in **Figure 3.9**. The locations of the graphene electrodes on the cortex, and their position relative to the 4-AP application site, are shown in **Figure 3.9a**. Upon visual inspection of the ECoG time series, we determined

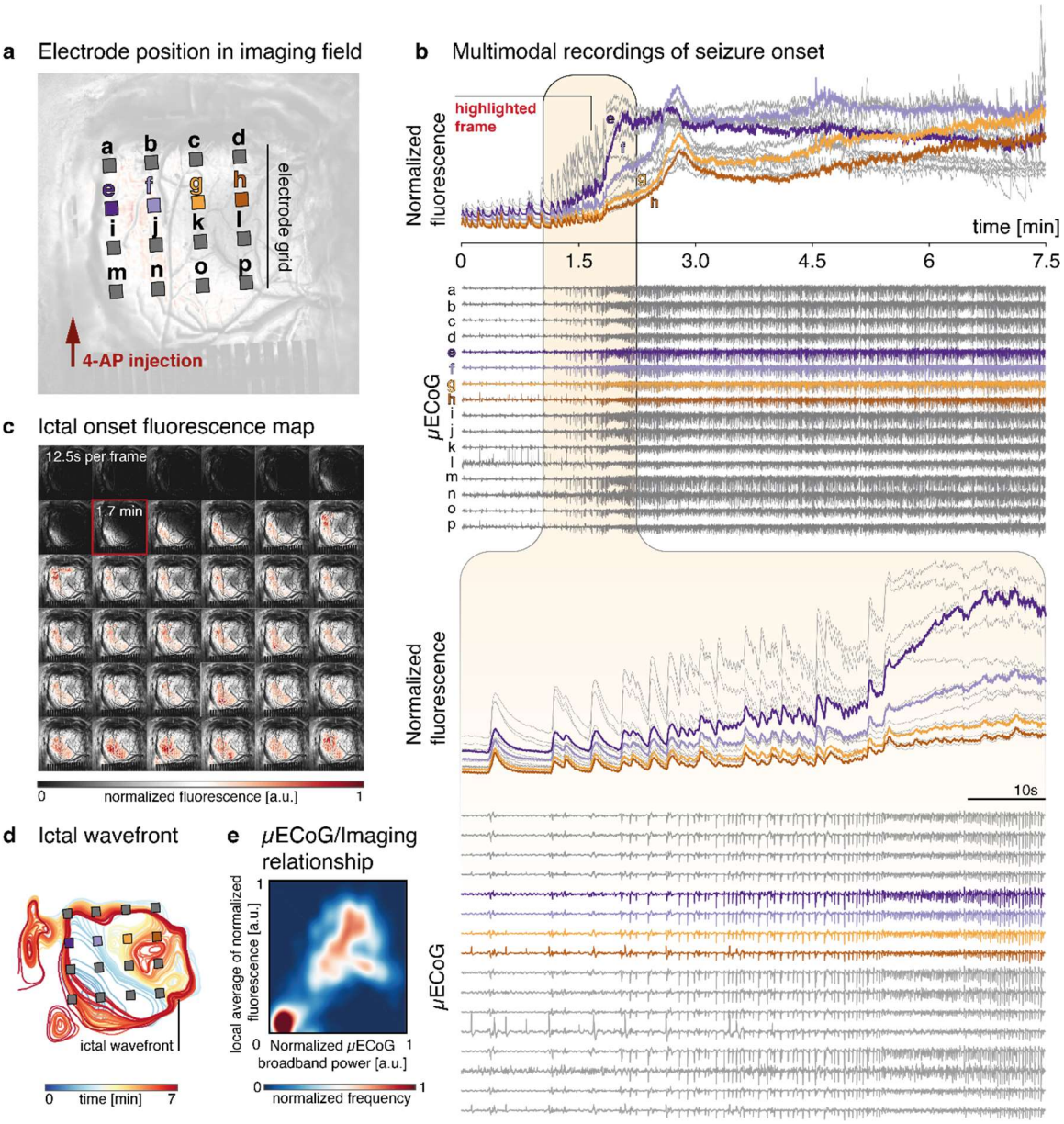

Figure 3.9 Concurrent multimodal data obtained during a single seizure onset. (a) Relative positions of the graphene contacts on the cortex (individual electrodes not shown to scale) and the location of 4-AP drug application. Electrodes labeled e, f, g, and h are highlighted and shown as example data. (b) Fluorescence intensity (normalized to baseline mean and variance) beneath each individual electrode and simultaneous μECoG recordings from the graphene array. The period of acute seizure onset is magnified in the bottom panel. (c) Series of image frames corresponding to the seizure onset shown in panel b. (d) Ictal wavefront evolution over time for the seizure shown in b. Note particularly the early recruitment of channel e and the comparatively late recruitment of channel h. (e) Density plot indicating the significant relationship between μECoG broadband power and local calcium fluorescence averages. The colormap indicates the density, or normalized observed frequency of values distributed along the two dimensions (μECoG broadband power, calcium fluorescence).

the time of ictal onset by identifying changes in rhythmic background activity that evolve in time and space; the determination was validated by a board certified epileptologist. In the recording event shown here, μECoG traces first show an increasing frequency of epileptiform discharges which appear near-synchronously across the whole electrode array, followed by a higher frequency, evolving rhythm that changes in amplitude and frequency for the duration of the seizure (**Figure 3.9b**).

Associated with these changes in the electrophysiological activity, we observe an increase in high amplitude calcium transients, followed by a transition of the global calcium-fluorescence to a higher overall amplitude. When fluorescence is instead measured at the location of individual μECoG contacts, we further see a separation in the temporal dynamics of this progression of seizure-associated calcium activity. While individual calcium transients beneath each electrode appear to be timed nearly synchronously, channels to the left of the array (nearer the location of chemoconvulsant drug application) show an earlier and higher amplitude transition into the seizure state overall. This spatial evolution of the seizure is apparent in the sequence of normalized calcium images (**Figure 3.9c**), where high amplitude calcium fluorescence indicates that ictal activity evolves slowly from the bottom left corner of the image to reach maximum amplitude near the end of the recorded segment shown here. High amplitude fluorescence corresponds to temporal summation of very fast neuronal firing, indicative of recruitment into the seizure. This intense, hypersynchronous activity in the recruited 'ictal core' stands in stark contrast to the less synchronous and lower frequency firing behavior of surrounding cortical areas, commonly referred to as the 'ictal penumbra'. The distinct neuronal dynamics of these areas are separated by a slowly traveling 'ictal wavefront' that gradually expands throughout the recording to ultimately engulf nearly the entire field of view (**Figure 3.9c,d**). Features of this core-penumbra organization of epileptic activity have previously been described both in human microelectrode recordings in chronic epilepsy, and *in vitro* using optical imaging of acutely induced seizures in cortical slices, where these dynamics unfold across temporal and spatial scales comparable to the ones reported here [154]. Similar to previous reports [154], [186], individual ictal discharges may spread near-synchronously across the whole μECoG recording array, while calcium fluorescence, and to some extent signal amplitude on the μECoG array, expands slowly across

the recorded surface. We treat this slow spatial evolution of the seizure as a traveling wave phenomenon [156], where we consider the boundary between significantly increased calcium fluorescence and activity nearer the resting state background level to be the edge of the ictal core (**Figure 3.9d**).

Despite the apparently synchronous onset of ictal features across individual channels in the μECoG, there is a clear relationship between the spatial distribution of the calcium signal, and local features of the electrophysiological recording. Specifically, we observe a correlation between normalized μECoG broadband power (Pearson's correlation coefficient $r = 0.71$, $p < 0.001$ for linear fit), and local average normalized calcium fluorescence (**Figure 3.9e**). While less obvious in the μECoG signal alone, this observation indicates that both calcium imaging and electrophysiology capture related, local spatiotemporal phenomena of ictal onset.

3.4 Non-negative matrix factorization identifies sequences of state transitions during seizure onset and evolution

3.4.1 Low dimensional representation of seizure dynamics

We next aim to describe the spatiotemporal profile of ictal onset across multimodal data in a lower dimensional representation. We make the assumption that the high dimensional dynamics of seizure onset and early ictal evolution can be well captured through time varying expression of latent spatial factors and subnetworks, whose individual makeup does not change with time, but fluctuates in its relative expression. First, we calculate features previously identified as dynamic markers of ictal territories [152] using temporal windows matching the calcium imaging frame acquisition speed: phase locked high gamma, high gamma power, and local network synchrony. This choice enables us to downsample the μECoG data while preserving the information afforded by its high temporal resolution, and align in time with the calcium fluorescence images. To detect latent spatial factors and subnetworks that best explain the temporal variation in key data features, we use a sparsity constrained non-negative matrix factorization (NMF) [187], [188] with the number of factors chosen to optimize the variance explained per factor for a limited total number of factors used

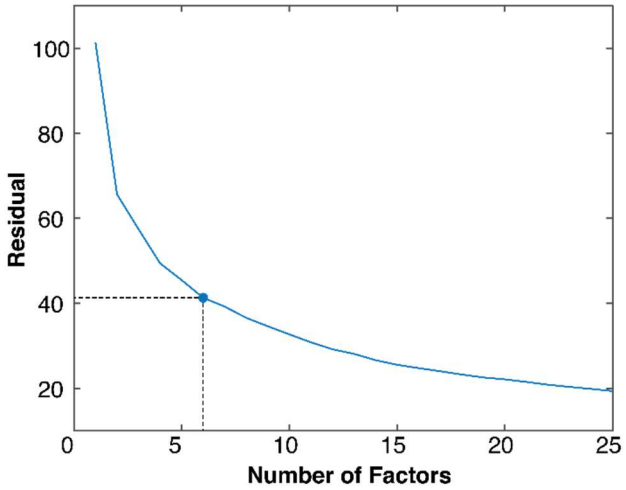

Figure 3.10 Variance explained by number of factors. Residuals for NMF fits after optimization for preset factor numbers ranging from 1 to 25. The final number of factors (k = 6) was selected as a trade-off between maintaining a low number of factors and achieving a low residual variance.

for dimensionality reduction (**Figure 3.10**). This method yields interpretable and sparse individual factors while remaining computationally tractable (**Figure 3.11a**). With this approach, we are able to integrate insights across different recording modalities, and to include many data features to trace latent dynamics that might not otherwise be easily discernible from single data features alone [189].

The spatial evolution of the ictal core is apparent both in the calcium imaging- and electrophysiology-derived components of the factors obtained with NMF. For example, as we move from factor 1 to factor 6, we observe an increase in both μECoG broadband power and calcium fluorescence amplitude (**Figure 3.11b**), which at the time of seizure onset is maximal at the bottom left corner of the array, closest to the drug application site. Similar to these univariate measures, NMF also yields μECoG-derived pairwise dynamic functional connectivity factors, or 'subgraphs' (**Figure 3.11c**). These are modules of functional connectivity whose variable expression over time approximates the full scale original dynamic connectivity matrix in linear supposition [190]. Their temporal progression also tracks transition into the seizure, and further evolution. For example, high gamma connectivity is lowest for factors expressed during seizure onset; and higher for factors expressed in the established seizure, when the ictal core occupies the majority of the electrode grid (**Figure 3.11c**).

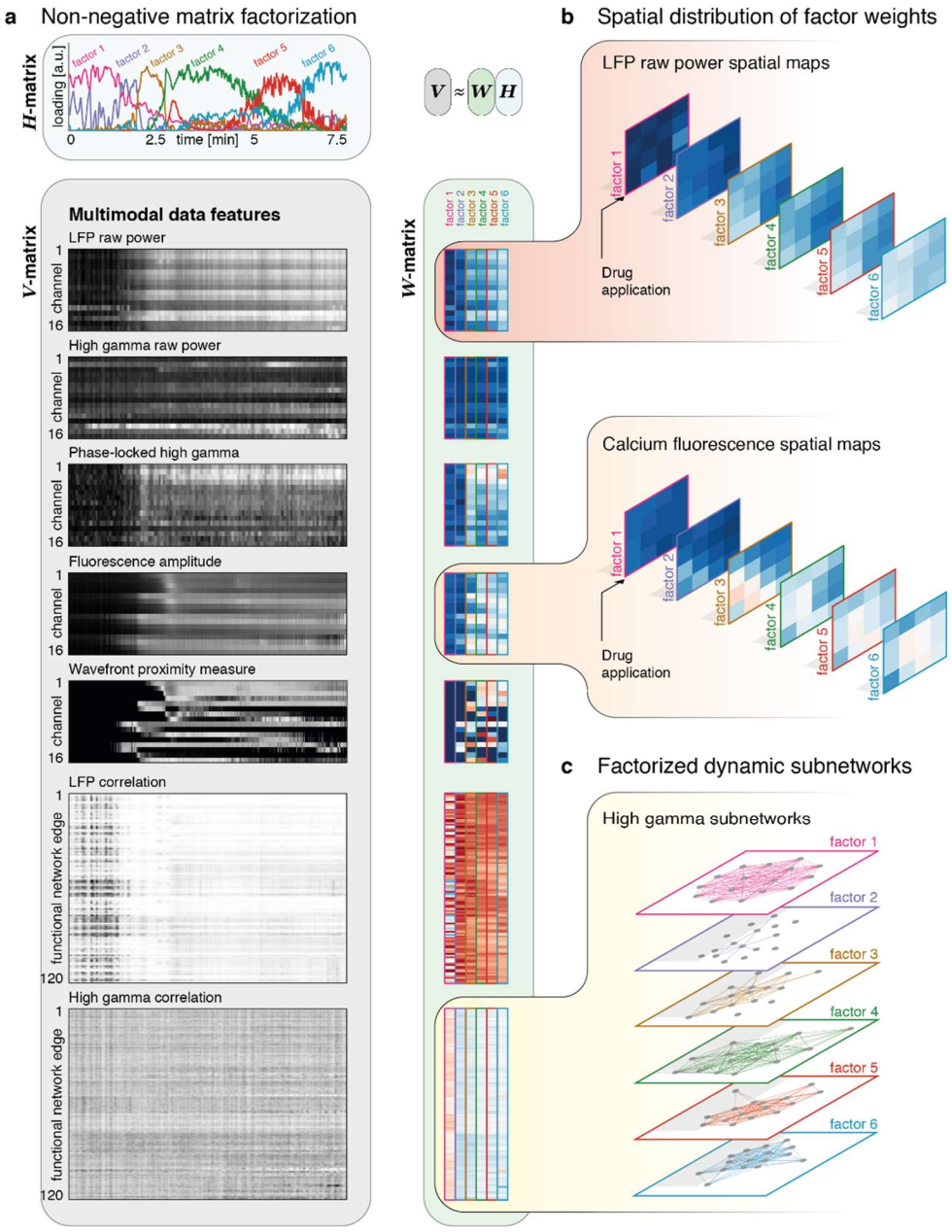

Figure 3.11 Non-negative matrix factorization (NMF) of time varying feature matrix. (a) The feature matrices supplied to the NMF (V matrix), and the resultant factorized matrices (H matrix showing temporal expression of six factors; W matrix showing factor weights for six factors). The ictal onset transition can be seen in most of the feature matrices, and occurs around the time factor 2 is expressed most highly. (b) Example factor weights are illustrated for LFP raw power, and calcium fluorescence in the sequence in which they are most highly expressed. Both show sequential increases in combined overall weights, with a maximum in the bottom left quadrant of the matrix, corresponding to the contact nearest the drug application site. (c) Factorized edge-weights can be used to reconstruct frequency-band specific subnetworks of which the high gamma derived subnetworks are shown here. These show a decoupling at seizure onset, with subsequent increases in coupling.

The time varying expression of the six factors further identifies a sequence of state transitions: periods that are characterized by expression of just a single factor alternate with periods characterized by mixed expression of multiple factors, indicating a gradual transition between states (**Figure 3.11a**). Thus, the factor loadings allow us to track transitions through a reduced dimensionality feature space, and to identify key transitions between transiently expressed states. It is of interest to determine whether these state transitions could be identified without the calcium imaging data, which captures a clearer spatial evolution of activity at slower time scales than the electrophysiology. To address this question, we perform the same analysis separately with calcium imaging features, or with electrophysiological data features alone. We observe that the state transitions are not detectable in the electrophysiology-only analysis. The timing of state changes appears to be preserved in the calcium-only analysis, although the dynamics of individual factor expression differs from the combined analysis (**Figure 3.12**). These findings indicate that identifying the sequential latent factors reported here requires the inclusion of calcium imaging data.

Using NMF, we derive a low-dimensional state space representing ictal onset. We depict this state space as a 3-D plot for the three factors that are predominantly expressed

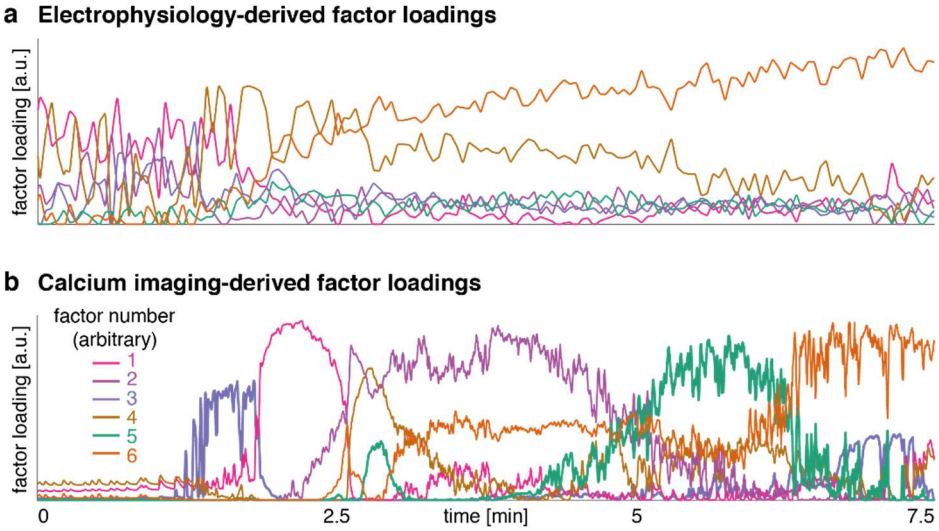

Figure 3.12 Factor loadings (i.e. *H*-matrix) derived from non-negative matrix factorization. (a) Results derived from matrices containing electrophysiology-derived data features only show transition into seizure and some progressive changes, but no clear sequential states. (b) Factor loadings derived from calcium imaging features only shows sequential states similar to those of the combined analysis.

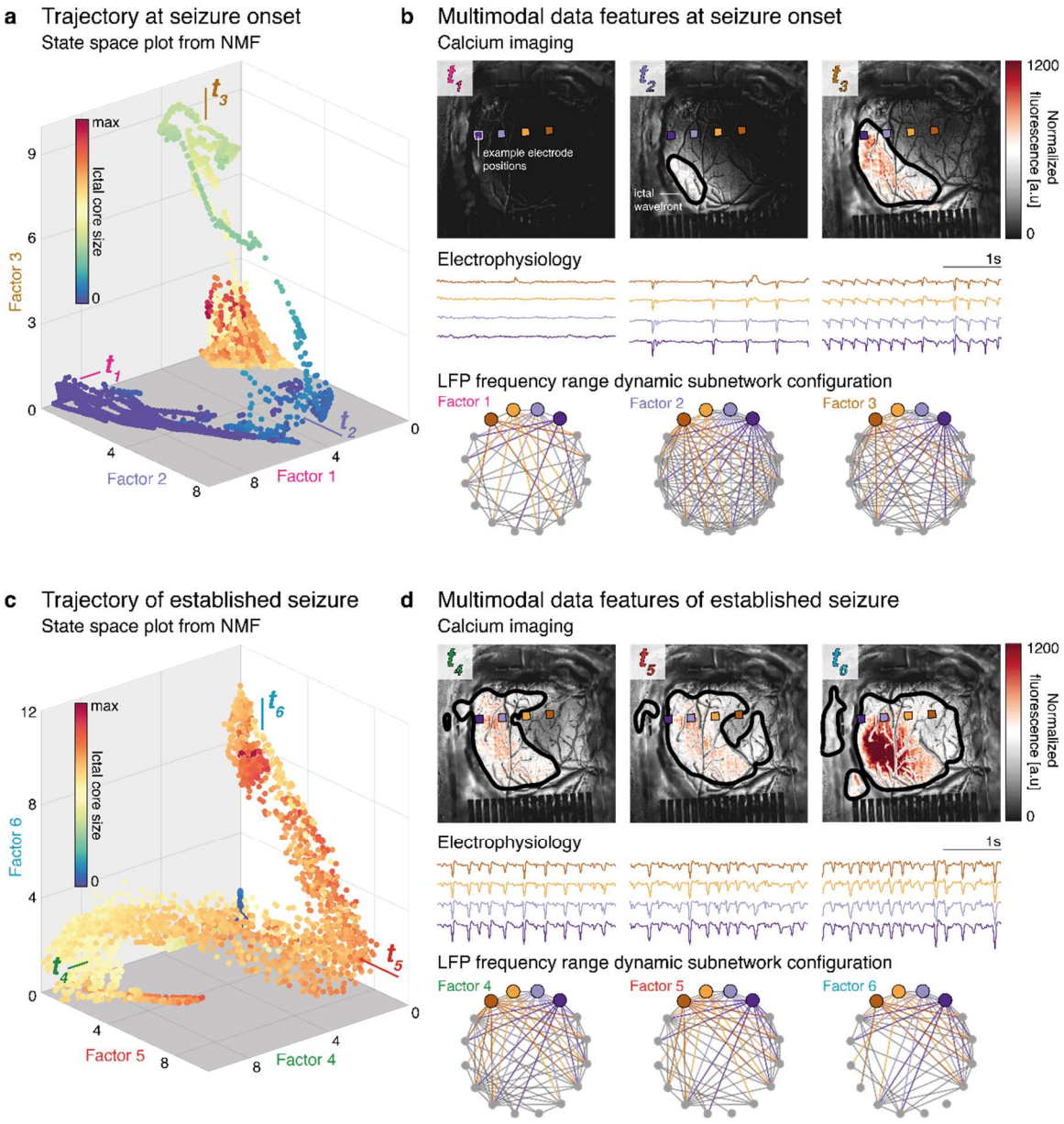

Figure 3.13 Spatiotemporal trajectories during induced epileptic seizure. (a) Weighting along three factors showing high loadings early during the seizure, with each point colored by the cortical surface area recruited to the size of the ictal core estimated from the number of suprathreshold pixels on calcium imaging. Seizure onset is associated with a smooth trajectory through this state space. (b) Three time points are sampled based on the extrema of the state-space trajectory, showing normalized calcium fluorescence, raw electrophysiology, and dynamic subnetwork configuration. (c) Analogous to the seizure onset, this plot illustrates the transition through state space based on three factors with maximum activation late in the seizure. (d) Data for three time points late in the seizure are shown, and are associated with gradual μECoG desynchronization along with continuing spatial increase of the seizure core on calcium imaging.

early in the seizure (**Figure 3.13a,b**). Next, we depict the 3-D state space of three factors that are predominantly expressed later during the established seizure (**Figure 3.13c,d**). Throughout the recording, transitions between factors are accompanied by smooth slow increases in the spatial extent of the recruited seizure core as defined by imaging features. In **Figure 3.13b,d** we show data segments that most closely correspond to each factor, by selecting time windows around the maximum expression of a given factor. These segments show distinctive patterns of specific dynamic features: a gradual increase in the spatial distribution of the calcium signal, changes in ictal discharge morphology and frequency, and strong initial synchronization with subsequent desynchronization in the between-channel functional network.

3.4.2 State transitions are associated with changes in ictal discharge electrophysiology

Next, we explore whether features which are in principle measurable in clinical ECoG recordings change quantitatively between seizure states identified from the multimodal NMF analysis. The most prominent features of abnormal cortical dynamics observed in clinical seizure recordings are often ictal epileptiform discharges, which are present in our μECoG recordings (**Figure 3.14a**). For this analysis, we were interested in quantifiable features of ictal discharges that (i) do not depend on the spatial resolution afforded by μECoG (e.g. excluding between-electrode correlation measures), and (ii) were not already included in the NMF analysis (e.g. excluding discharge amplitude). We identify two features that fulfil these criteria, which we hypothesize could act as indicators for ictal state transitions: ictal discharge frequency and ictal discharge stereotypy. We evaluate both features in 3s non-overlapping sliding time windows that are labelled according to the factors maximally expressed during that time window. We then compare median values of discharge frequency and between-discharge correlation, as a measure of discharge stereotypy, for temporally adjacent states (**Figure 3.14b,c**).

This analysis reveals contrasting changes in discharge frequency and discharge stereotypy. Discharge frequency monotonically increases from ictal onset, with increasing frequency at each state transition, and reaches a maximum at the end of the recording. However, discharges are most stereotyped early in the seizure, and become most variable in the established seizure around the time windows characterized by high expression of factor 5, before returning to a more stereotyped state towards the end of the recording.

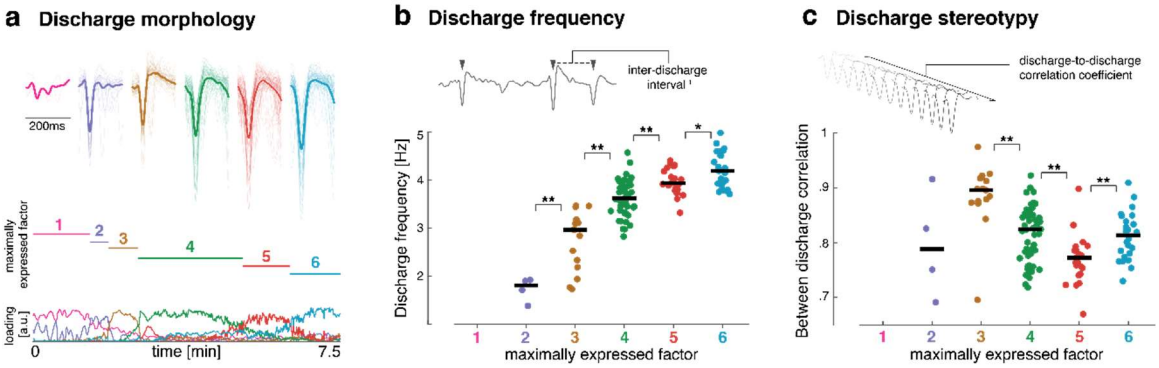

Figure 3.14 Electrophysiological changes associated with ictal state transitions. (a) Peak-centered averages of ictal discharges are shown for all discharges detected in a 10 s time window around the peak expression of each of the six sequential factors derived from NMF. Note that for visualization purposes we show averages at a lower detection threshold, meaning that some fluctuations in the baseline are shown for comparison. For subsequent panels, thresholds were selected to not include baseline fluctuations in the detected discharges. (b) Ictal discharge frequency was estimated for non-overlapping 3s sliding windows labelled according to the factor that was maximally expressed during the time window. This shows progressive increases in ictal discharge frequency for the duration of the seizure. (c) Stereotypy of ictal discharges was measured by calculating for each channel the between-discharge correlation for all discharges identified within a 3s sliding window. This shows that discharges are very stereotyped early in the seizure and become most heterogeneous around the expression of factor 5.

3.5 Discussion

3.5.1 Transparent graphene electrode arrays enable multimodal seizure mapping

To truly harness the combined advantages of electrophysiology and optical imaging, it is necessary to record and image in the same locations simultaneously. While insights have been gained by utilizing single micropipette local field potential (LFP) recordings in locations proximal to the imaging region [162], these studies do not offer spatial information about the propagation of high frequency ictal activity, which requires the use of multi-electrode arrays. In recent years, marked progress has been made in realizing transparent microelectrode array technology, initially using graphene and more recently utilizing other materials [9]. One of the key challenges in developing transparent microelectrodes has been a trade-off between optical transparency and electrode impedance. For example, the impedance of graphene electrodes, which are subject to graphene's fundamental quantum capacitance limit [144], can be reduced by electrodeposition of platinum nanoparticles on the surface [191], although at the expense of optical transparency. In this study, we have optimized the process for fabricating transparent graphene microelectrodes by utilizing a bubble transfer method to deposit clean and defect-free graphene layers [171], a layer-by-layer HNO_3 doping procedure [192], and sequentially stacked layers of graphene [193]. This optimization resulted in electrodes with a combination of high optical transparency and low impedance which is the best reported so far for graphene-based transparent electrodes of this size.

Electrophysiological signals detected with μECoG are extracellular in origin, and this allows mixing of signals from different spatial origins and cell types through volume conduction. Thus, even with the most advanced high-density surface μECoG arrays, the effective spatial resolution is limited not only by the electrode spacing, but also by the contributions of volume conduction and the unknown cellular origins of the recorded signal. In contrast, calcium imaging relies on intracellular changes in calcium concentrations which can be more precisely localized to their cellular origins. Furthermore, calcium indicators can be genetically targeted to provide access to precisely isolated signals from specific neuronal subpopulations in a way that is not currently achievable by electrophysiology [194], [195].

Here, we used widefield calcium epifluorescence imaging to offer a broad field of view encompassing the entire area covered by the 16-channel graphene array. Widefield imaging combined with somatically expressed calcium indicators is more sensitive to dendritic synaptic currents than individual action potentials, giving a readout of population activity rather than individual neuronal firing. For epileptic seizures, which emerge at the population level, this resolution is an appropriate spatial scale for subsequent analysis. However, some phenomena that characterize seizure activity (e.g. HFOs) cannot be captured with calcium-based methods at all, given the slow dynamics of both calcium transients and the fluorescent calcium indicators. Therefore, our approach allowed us to analyze the complex spatial patterns of ictal wavefront progression over a millimeter-scale cortical area in combination with spatially distributed measures of electrophysiology. In contrast to previous multimodal studies which have utilized cellular resolution multiphoton imaging, our approach also offers a much larger field of view.

To observe the contributions of excitatory neurons to ictal dynamics, in this study we utilized an animal model expressing GCaMP6s in excitatory pyramidal neurons. In the future, our approach can be extended to study the contributions of inhibitory interneurons. This direction would be particularly valuable for shedding light on the delicate balance between excitation and inhibition, and its role in seizure propagation, which is currently a subject of much debate [152], [154].

3.5.2 Ictal dynamics unfold on multiple temporal scales

Seizures are characterized by abnormalities in neuronal dynamics spanning across spatial and temporal scales. There is an extensive body of literature mapping these phenomena using a variety of recording setups in a range of different model systems [152], [196]. Convergent evidence from these studies suggests that at the onset of a focal seizure, the cortical sheet organizes into distinct territories characterized by particular dynamics signatures [156]. The recruited, intensely active ictal core is separated by an ictal wavefront from the surrounding cortex (the ictal penumbra*)* that may be propagating ictal discharges but lacks intense single neuron firing [1], [154]. These distinct seizure territories are best characterized by microelectrode arrays that can record invasively from electrodes piercing

pial layers and recording within cortical lamina, but evidence has also arisen from imaging acute seizure-like events *in vitro* [154].

In our analysis, we quantitatively combine surface μECoG recording of ictal onset with more spatially resolved calcium mesoscopic imaging, and find that we can identify signatures of these distinct seizure territories in our acute *in vivo* model of epileptic seizures. We further replicate previous observations of ictal dynamics unfolding on multiple temporal scales: we observe fast spread of individual ictal discharges in both calcium imaging and electrophysiology, as well as the slow, wave-like recruitment of the cortical surface into an ictal core. Similar findings have previously been described based on a variety of electrophysiological features (including multi-unit activity [197]), as well as demonstrated in neural field models of cortical physiology [198].

While previous studies have demonstrated simultaneous electrophysiology and imaging, none has so far addressed the challenges that arise in combining and interpreting quantitative features from multiple modalities that operate on different spatial and temporal scales. Dimensionality reduction techniques, such as NMF, are frequently applied to neurophysiological data to extract low-dimensional information from high-dimensional signals, and are thus relevant for the multimodal data on which we report in this study [189]. NMF provides linear representations of non-negative data, and the algorithm applied here contains a sparsity constraint, allowing us to identify low-dimensional factorizations of the data that contain only a limited number of active contributors to each factor [199]. To apply NMF to multimodal data, modality-specific data matrices are concatenated into a single matrix and aligned in time. This procedure allows us to utilize the high temporal resolution of electrophysiological data by calculating key quantitative features that have been associated with distinct ictal territories – such as phase-locked high gamma. Such features, while requiring high temporal resolution to detect, evolve slowly enough in time to be related to the slower dynamics identified from calcium imaging. The NMF analysis then provides us with temporal loadings on sparse factors that span multiple imaging and electrophysiological features, fully leveraging the strengths of both recording modalities.

Using this approach, we demonstrate that the ictal onset transition – defined by changes in the ongoing oscillatory dynamics of electrophysiological recordings – can be

factorized using a data-driven approach into a sequence of states that evolve on the time scale of minutes. Identification of these spatiotemporal patterns is made possible by the combination of recent advances in both transparent electrode fabrication and analytical techniques for processing neuronal data. The framework demonstrated here, enabled by our transparent graphene array technology, allows characterization of ictal phenomena observed with multimodal experimental setups, and helps quantitatively integrate information from concurrent calcium imaging and μECoG recordings.

3.5.3 Data driven multimodal analysis can identify new hypotheses for clinical translation

Recording seizures with multimodal combined μECoG and calcium imaging will not be achievable in human patients in the near future. However, there is already evidence that experimental high-resolution recordings can aid in the identification of novel biomarkers with translational potential. For example, microelectrode mapping of seizure territories has led to the identification of phase-locked high gamma as a potential biomarker for the ictal core and the seizure onset zone, even on intracranial macro-electrodes [152], [200].

In our analysis, we similarly illustrate how high-resolution mapping only achievable in experimental settings might be used to provide new hypotheses that could be testable in clinically achievable recordings. We show that calcium imaging provides data features that separate distinct states within a single seizure, even where aggregate electrophysiological features suggest only a monotonic, gradual change. We harness information on the putative timing of state-changes identified as changes in expression of NMF factors. We achieve this by exploring complementary features in the electrophysiological recordings, through which we can identify putative electrophysiological correlates of ictal state changes. One example of such a putative correlate is a gradual loss of local synchrony with progressive enlargement of the seizure core, which can be seen in the changes to the dynamic subnetwork graphs moving from factor 2 to factor 6 (**Figure 3.13b,d**). Similarly, the increasing variability of ictal discharges during the established seizure (**Figure 3.14c**) may be a marker of a specific ictal state which is potentially measurable with macroscopic clinical ECoG electrodes.

Such changes may be quantitatively subtle, but informative with regard to the underlying dynamical system generating ictal dynamics. If seizures are considered a pathological stable oscillation around a limit cycle [201]–[203], reductions in stereotypy of discharges may indicate that the system is approaching points of instability where closed-loop interventions may be most successful. These neurophysiological changes, while important, may not themselves be quantitatively sufficient to allow separation into states from dimensionality reduction approaches as presented here in neurophysiological data alone. However, as demonstrated through our analysis, they may be identifiable from combined analysis with modalities that are more sensitive to dynamics of distinct seizure territories, such as calcium imaging.

Characterizing individual seizures in such detail is important for several reasons: markers associated with distinct spatial territories may guide resective epilepsy surgery and identifying dynamically distinct states within a seizure may enable effective targeting of stimulation for seizure abatement, harnessing novel closed-loop stimulation approaches for the treatment of seizures. Thus, deriving candidate biomarkers from experimental animal studies is an essential step in identifying novel treatment strategies for currently untreatable epilepsies.

3.5.4 Methodological considerations and limitations

While the graphene electrode technology presented here enables recording of fast ictal dynamics, we were not able to resolve multi-unit activity (MUA) in this study due both to the size of the electrodes (50 μm x 50 μm) and their placement on the cortical surface (relatively distant from the cell bodies which lie in deeper cortical layers). Previous studies have reported successful recording of MUA from the cortical surface [55], when the electrodes are scaled down to cellular dimensions (i.e. ≤ 30 μm in diameter), however the high impedance of current transparent microelectrodes has largely prevented the realization of functional electrodes at these cellular spatial dimensions. Further progress in transparent electrode technology may enable high-fidelity recording from electrodes at this scale in the future. Such progress may be achievable by exploring other materials systems which have shown promise for optoelectronics and may offer higher conductivity than graphene, such as

MXenes [21], [204]. Access to MUA activity can also be achieved by considering alternative implantation strategies that place the graphene electrodes closer to cell bodies. Such strategies could include brain slice studies or approaches where the array is implanted over deep brain structures, such as the hippocampus, utilizing an implanted cranial window [205].

The seizure model used in this study is a bath-application of 4-AP, which offers experimental control and the ability to reliably induce acute seizures for validating our methodology and analytical methods. Yet, the model also has some limitations that are worth noting. In particular, it is challenging to discern the effects of drug diffusion on the spatial propagation of ictal activity, and the pharmacologically-induced seizure model may not replicate ictal dynamics that occur in spontaneous seizures. While offering less experimental control, a chronic seizure model in which mice experience spontaneous seizures following drug-induced status epilepticus may offer a more naturalistic view of ictal dynamics [206].

In terms of analysis, the methodological choices make certain assumptions. Applying dimensionality reduction techniques (such as NMF) to high-dimensional neuronal data assumes that key information is contained in large signal changes affecting a high proportion of recording channels. The representational accuracy of the low-dimensional approximation of the full dataset can be arbitrarily increased by increasing the number of factors or components, and a trade-off between accuracy and interpretability must be made. Furthermore, NMF assumes that the dynamics emerge from variable expression of spatially invariant factors, rather than changes in the spatial factors themselves. Other conceptual approaches or interpretations may prove more useful for specific cases.

3.5.4 Conclusion

Novel recording and analysis methods such as the ones introduced here improve our ability to quantify and ultimately understand the dynamics of epileptic activity in local microcircuits, and brain-wide epileptogenic networks. Concurrently recorded multimodal data may be used to address novel biological questions that are not tractable with a single method approach. For example, genetically-targeted calcium imaging of inhibitory neuron activity during concurrent measurement of the µECoG may enable separating the contributions of excitatory and inhibitory cell types to the ECoG signal. Combining µECoG

with imaging of cortical vasculature using injected fluorescent probes may also enable linking neural activity patterns to changes in blood flow, offering a direct proxy for fMRI studies [207].

Increasingly, through resective epilepsy surgery and laser ablation for example, patients are being offered interventions that aim to disrupt epileptogenic networks in order to reduce or stop their seizures. These therapies are currently driven by a crude understanding of cortical dynamics at the scale of ECoG signals. This understanding is based on coarse physical models, such as mesoscale neural masses representing large homogeneous populations of different neuronal subtypes [208] and equivalent current dipoles representing the electromagnetic spread of single source signals [209]. The sequence of spatiotemporal patterns constituting distinct states in the ictal onset reported here all occur at a spatial scale that would classically be regarded as a single source in most ECoG models. We now have the technological ability to acquire data at unprecedented temporal and spatial resolutions, and have the computing power and analysis methods at hand to identify from these complex data the key features that capture the dynamics at play. Through high fidelity recordings in experimental systems we will be able to inform the development of new hypotheses and models that may more accurately explain the phenomena observed in clinical recordings in human patients.

There is an urgent unmet need for novel therapies for patients who cannot currently benefit from resective surgery or antiepileptic medication. Novel treatment approaches such as responsive neuromodulation using electrically stimulating devices [210], [211], or novel optogenetic closed-loop control strategies [212] are currently already in clinical use or in development. Yet such modulation-based treatments require a detailed characterization of state transitions in local epileptogenic circuits as well as models of how interventions may disrupt these transitions. The integrated recording and analysis approach presented here is one strategy to quantify these state transitions utilizing optical and electrophysiological measurements. As such, we provide essential tools for epilepsy research to explore novel treatments in experimental systems.

3.6 Materials and methods

Graphene device fabrication

Three inch silicon wafers were coated with 4 μm parylene-C using a CVD process (SCS Labcoter 2 Parylene Deposition System). Following photolithography, 10 nm titanium (Ti) and 100 nm gold (Au) were evaporated onto the wafer using an electron-beam deposition process, and lift-off techniques were used to pattern the metal to form traces and connection pads. Monolayer graphene was transferred from a copper foil to the wafer using a wet bubble-transfer method consisting of the following steps: spin-coat 950 PMMA A4 on graphene/copper foil; bake at 100°C for 2 min; apply 20V potential between tweezers gripping copper foil and stainless steel counter electrode placed in 1 mM NaOH solution, and grip copper foil in tweezers while slowly submerging into NaOH, releasing graphene/PMMA from foil; transfer graphene/PMMA to three water baths for cleaning; transfer graphene/PMMA onto wafer substrate and let air dry for 2 hrs; bake wafer at 150°C for 2 min, then remove PMMA with acetone, IPA (soak for 20 min), and deionized (DI) water rinse. Following each graphene transfer to the wafer, the graphene was doped by soaking the wafer in 75% HNO_3 in DI water at room temperature for 15 minutes and subsequently dried with an N_2 gun. SiO_2 (30 nm) was then deposited onto the wafer using e-beam deposition to protect the graphene from damage during subsequent reactive ion etching (RIE) steps. The SiO_2 and graphene were patterned using photolithography and RIE to form the electrode array and traces, such that graphene traces overlapped Ti/Au traces. A second 4 μm layer of parylene-C was deposited through CVD and subsequently patterned through photolithography and RIE to form the outline of the device and to open the graphene electrode sites and Ti/Au contact pads. The protective SiO_2 layer was removed from the graphene electrode contacts by immersing the wafer in 1:6 buffered oxide etchant (BOE) for 30 s. Devices were released from the wafer and Kapton tape was applied to the back of the Ti/Au bond pad region to ensure proper thickness and stiffness for insertion into a zero insertion force (ZIF) connector and connection to the recording amplifier.

Electrochemical characterization

Electrochemical impedance spectroscopy (EIS) measurements were made using a Gamry Reference 600 potentiostat/galvanostat/ZRA in standard three-electrode configuration in 10 mM phosphate buffered saline (PBS) solution (pH 7.4). A graphitic carbon rod was used as the counter electrode, and an aqueous (3 M KCl) Ag/AgCl electrode was used as the reference. EIS measurements were taken between 1 Hz and 1 MHz using a 20 mV rms AC voltage. Cyclic voltammetry measurements were also taken using the Gamry Reference 600 from -0.8 to 0.8 V, with scan rates of 200, 300, 400, and 500 mV/s and a potential step of 5 mV. The cathodal charge storage capacity (CSC_C) was calculated by integrating the area under the average CV curve and dividing by the sweep rate (50 mV/s).

Ultraviolet-visible spectroscopy

Transmission mode UV-vis spectroscopy was obtained using a Perkin-Elmer Lambda-950 spectrophotometer over wavelengths from 300 to 1000 nm. Spectra were taken for the inter-electrode space (consisting of top and bottom parylene-C layers only), for a graphene electrode contact (consisting of the bottom layer parylene-C and the graphene layer), and for a graphene trace (consisting of top and bottom parylene-C layers and graphene layer).

***In vivo* imaging and electrophysiological recording**

All experiments were performed under a protocol approved by the Children's Hospital of Philadelphia Institutional Animal Care and Use Committee. Briefly, 6 to 8-week-old Thy1-GCaMP6 (Jax #025776, Jackson Laboratory) mice were anesthetized with isoflurane (0.5%-1.5%) in oxygen. Using a micro-drill, a hole was made for inserting a stainless steel skull screw with a silver- ground wire. A metal headplate with 6x6 mm^2 square imaging well (Narishige USA) was fixed to the skull overlying the somatosensory cortex with dental acrylic (Ortho-Jet). A rectangular craniotomy was drilled (right hemisphere, center at 2 mm posterior and 2 mm lateral of bregma). The exposed cortical surface was kept wet by ACSF containing the following (in mM): 155 NaCl, 3 KCl, 1 $MgCl_2$, 3 $CaCl_2$, and 10 HEPES. After the craniotomy surgery, aesthetic was switched to ketamine/xylazine (100/10 mg /kg) and the headplate was attached to a small imaging platform (Narishige USA) and mounted on an x,y-

translational stage of an upright microscope (Olympus BX-61). The graphene electrode array, a custom-connector, and the headstage (SmartLink16, NeuroNexus) were attached to a stainless steel bar, which was then attached to a micro-manipulator. The graphene electrode array was gently placed on the cortical surface. Signals from the graphene electrode array were sampled at 5 kHz via the headstage and the controller (SmartBox, Neuronexus), and the data was saved to a PC. The microscope was equipped with blue LED (470nm, Thorlabs), a filter cube (49002, Chroma) and sCMOS camera (Orca Flash 4 V2, Hamamatsu). The imaging data was captured in TIF format on another PC, and timing of electrophysiological recording and imaging was synched by a TTL signal. For epifluorescence imaging, excitation light was continuously illuminated and fluorescence images were captured at a constant acquisition rate of 10 Hz. Baseline activity was recorded for 20 min prior to seizure induction. Local seizure induction was achieved via bath-application of 100 µL of 4-amino pyridine (4-AP) in ACSF (30 mM) on the exposed cortical surface adjacent to the graphene electrode array.

SNR calculations

To compute SNR on each electrode, the mean amplitude of 8 ictal spikes that occurred during a 4-second window during seizure onset was divided by the RMS of the signal during a 3-second window of pre-seizure baseline activity.

Dynamic feature extraction

Quantitative analysis was performed on custom scripts on MATLAB R2019a; all scripts to reproduce analysis figures are available online on https://github.com/BassettLab/Graphene-Electrode-Seizures.

Features from µECoG

For this analysis, we extracted quantitative features that dynamically evolve at a time scale similar to that evident in the features of calcium imaging. Specifically, we estimated time-varying phase locked high gamma amplitude, frequency-band specific power in two frequency bands, and sliding-window dynamic functional connectivity.

Phase-locked high gamma: We estimated phase-locked high gamma amplitude $\hat{a}_{high}^{\Phi}$ following prior work[152]. Briefly, we applied the Hilbert transform separately to the data recorded at each microelectrode contact, after filtering each into two distinct frequency bands: a low frequency band (1-40 Hz) and a high frequency gamma band (80-250 Hz). From the Hilbert transform we were then able to calculate low frequency instantaneous phase Φ_{low}, and high frequency instantaneous amplitude normalized by the average band-passed amplitudes at baseline a_{high}. From a second Hilbert transform, we derived the instantaneous phase of the slowly time-varying instantaneous amplitude of the high frequency content $\Phi_{a_{\text{high}}}$. From these values, we calculated the phase locked high gamma amplitude as a measure of normalized high frequency amplitude weighted by the mean cross-frequency band phase correlation. Specifically, we calculated this variable within the sliding window ranging from sample $n = 1$ to sample $n = N$:

$$\hat{a}_{high}^{\Phi} = \left| \frac{1}{N} \sum_{n=1}^{N} a_{high} exp(i(\Phi_{low}^{n} - \Phi_{a_{\text{high}}}^{n})) \right|$$

We calculated this variable through sliding windows of length 3s and then then interpolated linearly to a full sampling frequency of 10Hz to enable cross modality analysis with the imaging features.

Frequency band-specific power: We calculated frequency band-specific power using the Hilbert transform on time series filtered into low (1-40 Hz), and high (80-250 Hz) frequency components, tracking evolution of most of the classically visible frequency ranges, and of high frequency oscillations separately. We estimated band-specific power in 3 second non-overlapping sliding windows, before interpolating to the 10 Hz sampling frequency of the calcium imaging in order to track slow modulations of frequency power.

Functional connectivity: To estimate functional networks, we calculated pair-wise correlations between individual microelectrode contacts. Full correlation matrices were estimated for sliding 3 second windows, edges with correlation values of < 0 were reset to 0, and edge-wise temporal evolution was interpolated to the sampling frequency of the calcium imaging at 10 Hz.

Features from calcium imaging

For our analysis we derived normalized measures of fluorescence intensity during the seizure, as well as a measure of each pixel's proximity to a putative ictal wave front. Imaging yielded raw epifluorescence image sequences for the baseline period, and from the period following the application of the chemoconvulsant 4-AP. We used the baseline period to quantify pixel-wise mean fluorescence, and fluorescence intensity variability (estimated as the standard error of the mean). From the baseline mean and standard error maps, we then calculated a t-statistic map for each image in the sequence following chemoconvulsant exposure, where $t = (x - \mu_{BL})/\sigma_{\bar{x}_{BL}}$, with x being the sample value, μ_{BL} the baseline mean, and $\sigma_{\bar{x}_{BL}}$ the baseline standard error of the mean.

In order to coarse-grain the data, we applied a 2-dimensional gaussian filter with a width of 15 pixels to each t-map in the sequence, and binarized the resultant images at a manually selected threshold that would first be crossed at the time of visually apparent electrographic seizure onset. We detected the edge of these binarized maps at each time point and convolved the edges with a two-dimensional Gaussian kernel with a width of 15 pixels, which yielded a measure of proximity of each imaging pixel to the putative ictal wave front.

Finally, we sampled both raw fluorescence, and proximity to the putative wavefront from the imaging pixels underlying each of the 16 microarray contacts, generating 16 time series for both measure, which were then used in the subsequent analysis.

Non-negative matrix factorization

We used non-negative matrix factorization on a multimodal feature matrix containing the time varying features estimated above in order to identify a subset of composite factors, whose time-varying expression could recapitulate the multi-modal feature evolution observed in the data. NMF will decompose any $n * t$ feature matrix V (where n is the number of features, and t is the number of temporal samples) into a set of k factors (i.e., sets of features encoded in the W matrix) and their temporal evolution (encoded in the H matrix), so that the full matrix V can be approximately reconstructed from these factors (i.e. $V \simeq WH$).

In terms of network analysis, these approaches have been previously used to decompose dynamic functional connectivity into sets of variably expressed subnetworks and track their temporal evolution in human neuroimaging [168]–[170]. Here, we extend the application of the approach to integrate data features across modalities and feature types. In contrast to the original formulation of the method, the algorithm applied here uses additional sparsity constraints and has been previously described elsewhere [187], [188]. The full feature matrix V was concatenated from channel-specific time series of broadband LFP (1-40 Hz), and high gamma (80-250 Hz) band power, normalized fluorescence amplitude, and wave front proximity estimates, as well as the $n_c(n_c-1)/2$ unique edge-weights unfolded from the symmetrical correlation-based n_c^2 functional connectivity matrix, where n_c is the number of channels.

Ictal discharge analysis

We quantified between-state differences in features of ictal discharge. For this we divided the whole seizure recording included in the NMF analysis into 3s long non-overlapping time windows, labelled according to the factor that was maximally expressed during each window. We z-transformed data for each time window using baseline data to calculate normalizing mean and standard deviations individually for each channel. In the resultant z-normalized time series, we identified putative ictal discharges as negative deviations of an amplitude of z > 3.9 and a width of at least ~30ms. These parameters were identified by a clinician with training in epilepsy (RER) visually confirming that the detected events were ictal in nature, and no baseline events were detected (for visualization purposes in Fig 6a, the thresholds were slightly relaxed in order to allow inclusion of some baseline detections – but those were not included in subsequent statistical analysis).

We calculated the average inter-discharge interval for each time window as an inverse measure of spike frequency. We also estimated the correlation of all ictal discharges within a time window. For this we segmented out ictal discharges from 50ms prior to the peak amplitude to 150ms after peak amplitude, and calculated Pearson's correlation coefficient between each pair of these segments within time windows and channels. We then averaged all correlation coefficients to estimate a single mean correlation value per 3s window,

representing ictal discharge stereotypy. We compared each pair of sequential states (defined by their factor expression) by Wilcoxon ranksum comparison of discharge frequency and stereotypy for each group of time window associated with either state.

Chapter 4: High-resolution neural interfaces using Ti_3C_2 MXene

High-resolution neural interfaces are essential tools for studying and modulating neural circuits underlying brain function and disease. As we saw in the previous chapter, they can enable new insights into brain dynamics at the microscale that underly phenomena such as epileptic seizures. To achieve high spatial resolution and channel count, however, electrodes must be miniaturized, even down to the scale of individual neuronal processes (~10s of μm). At these scales, maintaining low electrode impedance and high signal quality becomes a significant challenge. Nanostructured materials can address this challenge, as they can combine high electrical conductivity with mechanical flexibility and can interact with biological systems on a molecular scale. Unfortunately, fabricating high-resolution neural interfaces from nanostructured materials is typically expensive, time consuming, and does not scale, which precludes translation beyond the benchtop. Two-dimensional (2D) Ti_3C_2 MXene possesses a combination of remarkably high volumetric capacitance, electrical conductivity, surface functionality, and processability in aqueous dispersions distinct among carbon-based nanomaterials. In this chapter, I develop a high-throughput microfabrication process for constructing Ti_3C_2 microelectrodes and I demonstrate their superior impedance and *in vivo* neural recording performance in comparison to standard metal microelectrodes. Specifically, when compared to gold microelectrodes of the same size, Ti_3C_2 electrodes exhibit a 4-fold reduction in interface impedance. Furthermore, intraoperative *in vivo* recordings from the brains of anesthetized rats at multiple spatial and temporal scales demonstrate that Ti_3C_2 electrodes exhibit lower baseline noise, higher signal to noise ratio (SNR), and reduced susceptibility to 60 Hz interference than gold electrodes. Finally, I present a neuronal biocompatibility study showing that neurons cultured on Ti_3C_2 are as viable as those in control cultures, and they proliferate, grow axonal process, and form functional networks. Overall, these results indicate that Ti_3C_2 MXene microelectrodes have the potential to become a powerful platform technology for high-resolution bioelectronic interfaces.

4.1 Introduction

Understanding the fundamental mechanisms governing the structure and function of neural circuits is critical for treating neurological disorders like epilepsy, depression, and Parkinson's disease. Microelectrode technologies are widely used to elucidate neural dynamics on fine spatial and temporal scales (~10-100 μm, 1 ms). However, recording stable neural signals with high signal-to-noise ratio (SNR) from micro-scale electrodes remains a significant challenge. Current microelectrode arrays are stiff, invasive, and limited in their ability to provide high fidelity long-term recordings because conventional electrode materials, including metals and silicon, are inadequate for interfacing with biological tissues. The significant mechanical mismatch between conventional electrode materials and the soft brain tissue elicits an inflammatory response that eventually results in the formation of an insulating glial scar around the implant [213]. Additionally, as the geometric area of an electrode is decreased to approximate the size of individual neuronal processes, a corresponding rise in the electrochemical interface impedance leads to an increased susceptibility to noise sources, including thermal noise, mains interference, and signal loss to shunt pathways, which ultimately degrade signal quality [10]. Solving these issues to achieve seamless, stable, long-term integration between man-made devices and neuronal structures requires innovation in bioelectronic materials.

One strategy commonly adopted to overcome the trade-off between electrode footprint and interface impedance is to increase the effective surface area over which ionic species in the extracellular space can interact with the electrode. This is achieved through nanopatterning [11], surface roughening [12], or electroplating with porous additives[10], [13]. Nanomaterials such as graphene [16], carbon nanotubes [126], [133], and nanowires [214] show great promise for high-resolution neural interfaces because they offer high specific surface areas, and desirable thermal, electronic and mechanical properties, including flexibility and high conductivity [215]. However, the lack of scalable assembly methods is a key barrier to their widespread adoption for neural interfaces. For example, carbon-based nanomaterials are typically hydrophobic and require the use of surfactants [216], superacids [217], or surface functionalization [218] to allow fluid-phase assembly from aqueous dispersions. Residues from surfactants or superacids used in assembly are difficult to remove

completely and can be detrimental to electrode performance [219] or toxic to biological tissues [220], respectively. Surface functionalization induces defects and reduces the conductivity and strength of the resulting structures [218]. Besides solution processing methods, chemical vapor deposition (CVD) can also be used to assemble carbon-based nanomaterials into thin films for neural electrodes. However these processes are conducted at high temperatures that are incompatible with many flexible, biocompatible polymeric substrates [221], and thus require tedious subsequent steps to align and transfer the films from the catalyst layer to the polymeric substrate [222].

MXenes are a large class of 2D nanomaterials, composed of early transition metal carbides, nitrides, and carbonitrides that present an exceptional combination of high electrical conductivity, strength, flexibility and volumetric capacitance [18]. MXenes contain abundant surface terminating functional groups, such as hydroxyl (–OH), oxygen (–O) or fluorine (–F), which make them hydrophilic and also allow for flexible surface modification or functionalization. MXenes' hydrophilicity enables the use of high-throughput solution processing methods without the need for surfactants, superacids, or surface functionalization, and may also provide opportunity for creating functionalized platforms for drug delivery or electrochemical sensing. While much of the early research on MXenes focused on applications in energy storage [18], [22], more recent work has shown that MXenes hold great promise for biomedical applications as well. In the following section, **4.2**, I will expand upon the synthesis, properties, and biomedical applications of MXenes to provide additional context for this chapter.

Of the dozens of MXenes that have been discovered, the first MXene, Ti_3C_2, has been the most extensively studied, characterized, and optimized [223]–[225]. Ti_3C_2 demonstrates remarkably high volumetric capacitance (1,500 F/cm^3) [22] and electronic conductivity (~20,000 S/cm) [226]. The volumetric capacitance of Ti_3C_2 exceeds that of activated graphene (~60–100 F/cm^3) [227], carbide-derived carbons (180 F/cm^3) [228], and graphene gel films (~260 F/cm^3) [229]. The outstanding electrical properties of Ti_3C_2, coupled with its processability and high specific surface area make it an extremely promising material for neural interfaces, particularly for overcoming the trade-off between geometric surface area and electrochemical interface impedance, which is a primary limitation to achieving high-

fidelity recording from micro-scale electrodes. The high capacitance of Ti_3C_2 films is also a significant advantage for biosensing and stimulation applications, where capacitive electrode interfaces are preferable as they avoid harmful Faradaic reactions. Finally, the hydrophilic nature of Ti_3C_2, an uncommon attribute among carbon-based nanomaterials, allows the use of simple, scalable, high-throughput solution processing methods.

Prompted by its outstanding properties, in this study we investigate the suitability of Ti_3C_2 MXene for high-resolution, implantable electrodes for neural signal sensing. First, we describe a high-throughput fabrication process which combines standard photolithographic patterning with an *ad-hoc* method for forming precise, micropatterned MXene films from a colloidal solution on flexible polymeric substrates. Using this custom approach, we demonstrate the feasibility of producing implantable, multichannel neural electrode arrays comprised of Ti_3C_2, developing different geometries for recording both from the cortical surface and from deeper brain regions. We show that Ti_3C_2 electrodes exhibit markedly reduced impedance compared to gold (Au) electrodes of the same size, and that this impedance reduction is accompanied by significant improvement in neural recording signal quality *in vivo*. In particular, when used *in vivo* for high-fidelity recording of neural spiking activity, Ti_3C_2 electrodes show significantly improved sensitivity, reduced noise, and the ability to detect a larger number of spikes compared to Au electrodes. Finally, we demonstrate that Ti_3C_2 MXene is biocompatible with neuronal cultures and does not affect cell viability, proliferation or synapse formation, though neurons are known to be highly sensitive to their local environment and surface interactions.

4.2 MXenes: background and prior work

4.2.1 Synthesis and properties

MXenes, which are a large family of early transition metal carbides, nitrides, and carbonitrides, were first discovered in 2011 by Drexel University scientists [223]. They are produced by selectively etching out the A layers from MAX phases, which are so-called because of their composition: $M_{n+1}AX_n$, where M is an early transition metal, A is a group 13 or 14 element of the periodic table, X is carbon and/or nitrogen, and n = 1, 2, or 3. Single-layer MXene flakes are generally produced by first etching the A element from the MAX phase using

acid and salt mixtures, such as pure hydrofluoric acid (HF), HCl + LiF (forming HF in situ), or HF + HCl, and subsequently delaminating the sheets from each other through intercalation with organic molecules, such as dimethyl sulfoxide (DMSO), or with solvated Li^+ ions [230] (**Figure 4.1**). This top-down selective etching procedure is far more scalable than bottom-up approaches, such as chemical vapor deposition (CVD) or physical vapor deposition (PVD), which are required for producing many other 2D materials [231].

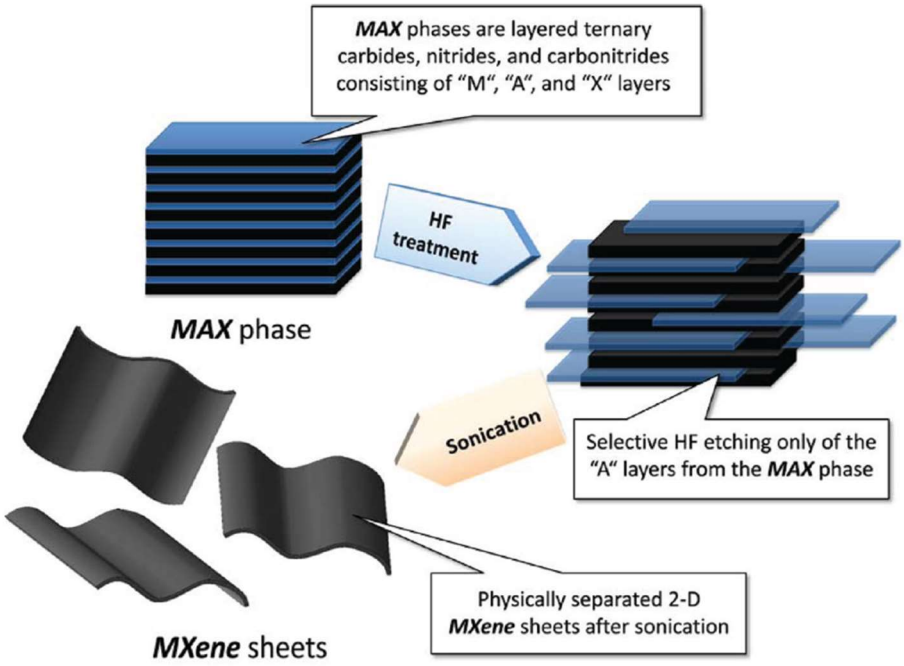

Figure 4.1 Schematic for the exfoliation process of MAX phases and formation of MXenes. Note that there are now many variations on this method, not all using HF and not all requiring sonication to separate the 2D MXene sheets. From [373].

Methods for synthesizing single-layer MXene flakes are still evolving and undergoing optimization, and the synthesis conditions have a large effect on the properties of the resulting MXene material [231]–[233]. For example, early methods of producing single-layer Ti_3C_2 required sonication to complete the delamination, however more recently a method called the minimally intensive layer delamination (MILD) method was developed which made it possible to isolate single flakes of MXene using manual shaking rather than sonication. This resulted in larger single flakes, which could produce films with higher conductivity [233]. Another very recent advance has been the development of methods for synthesizing fluorine-

free MXenes without using HF-containing or HF-forming chemicals, offering improved safety [234].

MXenes have a number of interesting physical, chemical, and electrical properties which make them attractive for a wide range of applications. The presence of surface terminating functional groups, such as hydroxyl (–OH), oxygen (–O) or fluorine (–F) (the composition of the surface terminations can be tuned by varying the processing conditions [235]), renders MXenes hydrophilic, which is unusual among 2D materials. This means that MXenes are stable in surfactant-free water-based colloidal solutions and can be processed using highly scalable solution processing methods. The surface terminations, along with the high specific surface area of the 2D sheets, also provide opportunity for flexible functionalization of the surfaces of MXene flakes, such as with antibodies or drugs [236]–[238]. Furthermore, the ultrathin layered structure gives MXenes interesting physiochemical properties (e.g. photothermal conversion [239], [240], X-ray attenuation [241], [242], and localized surface plasmon resonance [243], [244]) and biological behaviors (e.g. biodegradation [239], [245] and cellular endocytosis [241]). Regarding their electrical properties, MXenes show metallic electronic conductivity of up to 15,000 – 20,000 S/cm, which is higher than all other solution-processed 2D materials [226], [246]. In fact, the unique combination of hydrophilicity and metallic conductivity is a key advantage for MXenes over graphene and its derivatives. MXenes also have extremely high volumetric capacitance (~1,500 F/cm3) [22], which led early research efforts to predominantly focus on energy storage [18].

Since their initial discovery, more than 30 MXene compositions have been synthesized and dozens more have been theoretically predicted. Each composition offers a unique combination of properties, and potentially even a way to tune the properties by varying ratios of M or X elements. To date, the first MXene, Ti_3C_2, has been the most extensively studied and optimized, with more than 70% of all MXene research focusing on this single composition [247]. In this thesis, Ti_3C_2 is the MXene composition of choice because at the time of these studies it was the most well-optimized, well-studied, and considered to be the most electrically conductive. It is quite possible that other compositions of MXene may in time prove even more optimal for biomedical applications such as the ones presented in

this thesis work, and even open the doors to new areas of research which have not yet been explored.

4.2.2 Biomedical applications

As noted above, much of the early research on MXenes focused on energy storage, and it is still the dominant area of MXene research. In just the past few years, however, the number of applications which have been explored using MXenes has rapidly expanded (**Figure 4.2**). The use of MXenes in the biomedical field first gained traction in 2017, and since then there

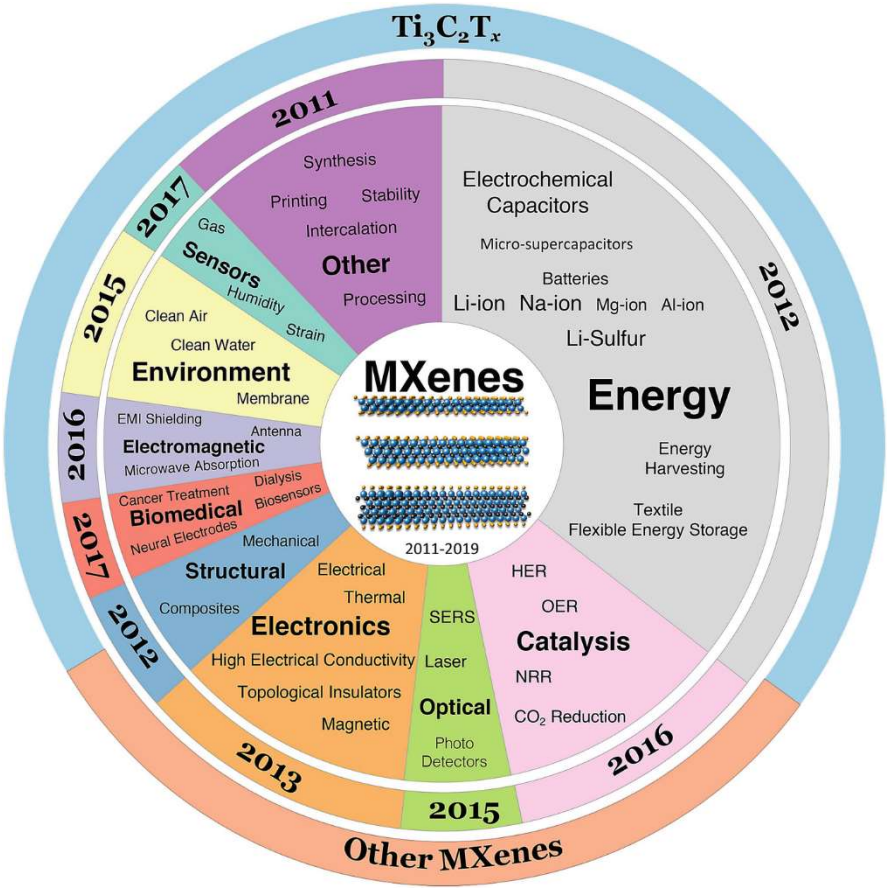

Figure 4.2 Explored applications of MXenes to date. The center pie chart shows the ratio of publications in each explored application/property of MXenes with respect to the total number of publications on MXenes. The middle pie chart ring, with the same colors, shows the starting year for exploration of each application/property of MXenes. NB: although there may be one or two papers published prior to the mentioned year, we considered a year with several significant publications as the starting (breakthrough) year for each slice. The outer ring shows the ratio of publications on $Ti_3C_2T_x$ MXene versus all other MXene compositions (M_2XT_x, $M_3X_2T_x$, and $M_4X_3T_x$). From [374].

has been an explosion of interest. The earliest biomedical-related research using MXenes focused on biosensors for small molecule detection, using the nanolayered structure and surface functional groups of Ti_3C_2 to immobilize enzymes for electrochemical detection of small molecules such as H_2O_2 [248] and glucose [249]. Next, MXene was demonstrated for cancer theranostics, both as a photothermal conversion agent for in photothermal therapy [240], and as a contrast agent for diagnostic imaging techniques such as computed tomography (CT), photoacoustic (PA), and magnetic resonance imaging (MRI) (when Ti_3C_2 is decorated with magnetic nanoparticles) [250]. In photothermal therapy, the characteristic 800 nm absorption peak of Ti_3C_2 enables efficient conversion of near infrared (NIR) radiation to heat in order to ablate tumor cells [240]. The nanosheets preferentially accumulate in tumor tissue due to the characteristic high permeability of tumor blood vessels, which allows targeted ablation, diagnostic imaging, and also chemotherapeutic drug delivery [251]. Of the biomedical applications of MXenes shown to date, cancer theranostics has emerged as one of the most promising and well-studied [242], [252]–[254].

Another interesting application of MXenes in biomedicine has been in dialysis. It has been shown that Ti_3C_2 can selectively adsorb urea from dialysate through binding at the surface terminations on the MXene flakes, offering great potential for the realization of a wearable artificial kidney [255]. Yet another promising area of research has been in wearable mechanical sensors based on MXene. These have predominantly been strain gauge or pressure sensors which can be used for tracking limb movement [256] or even decoding facial expressions [257] or speech [258]. Beyond these applications, MXenes have been explored for pH sensing [259], detection of metabolites in sweat [260], and as antimicrobial agents [261], [262].

Given the high electrical conductivity of MXenes, it seemed natural that they might perform well as electrodes for electrophysiological recording from excitable tissues such as the brain, muscles, and heart. When I began working on developing MXene electrodes for electrophysiology in 2017, however, no other group had yet reported this. The closest predicate was a single report from 2016 describing a Ti_3C_2-based field-effect transistor (FET) that could detect the spiking activity of neurons in culture, though it did so by electrochemical detection of dopamine rather than by directly recording the extracellular voltage fluctuations

[263]. In this chapter and the next, I detail how our group pioneered the use of MXenes for recording and stimulating electrodes that directly interface with excitable tissues, thus opening a new field of MXene bioelectronics.

As interest in using MXenes for biomedical applications has grown, so too has evidence showing their excellent biocompatibility, which is always an important concern whenever nanomaterials are used to interface with biology. One study showed that intravenous injection of Ti_3C_2 into healthy mice at doses up to 20 mg kg^{-1} did not produce any measurable behavioral change, weight loss, change in blood indexes, change in liver or kidney function, or toxicology in any major organ [250]. A similar study evaluating the biocompatibility of intravenously administered Nb_2C MXene also found no measurable toxicity in mice [239]. One factor contributing to the lack of toxicity when MXenes are administered intravenously is the fact that MXenes have been shown to be biodegradable [239], [245], [264]. Thus, they do not accumulate in tissues as micron-sized particles, but rather break down into small molecules such as TiO_2 (from Ti_3C_2 MXene) which can be cleared from the body. In addition to the intravenous studies, a series of acute toxicity, locomotion, and neurotoxicity assays performed in a zebrafish embryo model indicated that Ti_3C_2 could be classified within the "practically nontoxic" group according to the Acute Toxicity Rating Scale by the Fish and Wildlife Service [265]. Several studies have also found little evidence of cytotoxicity for cells cultured with MXenes [251], [263], [266]. While more systematic evaluations are needed, these and other studies indicate that MXenes are safe and biocompatible.

Finally, it is important to note here that MXenes suffer from limited stability in physiologic conditions, where oxidation causes degradation of the MXene flakes [267], [268]. This is advantageous in applications where biodegradation is desired, but it becomes a challenge when the MXene is instead part of a system or device where long-term function inside the body is preferable, such as for chronically implanted neural electrodes. In just the past few years, however, significant progress has been made toward improving the oxidation stability of MXenes [226], [269]–[271]. Thus, it is possible that MXenes may be viable for use in long-term implantable devices in the near future.

4.2.3 Patterning methods

Interest in using MXenes in electronic devices has exploded in the past few years. One of the primary challenges of incorporating MXene into devices has been achieving reliable patterning of the material with high resolution. This challenge is mainly relevant when devices require sub-millimeter spatial resolution. For example, in this thesis chapter I sought to develop microscale neural electrodes using MXene, which required patterning the material with spatial precision of ~5 μm. At the time, no method had yet been developed to allow precise patterning of MXene at these resolutions. Thus, in this chapter I describe a method I developed, which uses a selective lift-off process combining photolithography and reactive ion etching (RIE) to form a polymeric shadow mask. In the years since, many advances have been made and new methods for patterning MXene have been described, however the method described in this thesis chapter still appears to offer the highest spatial resolution to date.

One of the most common methods of patterning MXene is ink-jet printing. Several studies have focused on tuning the rheological properties of MXene-based ink to push the limits of ink-jet printing resolution [272]–[274]. Of these, the highest resolution reported is ~40 μm [272]. Another interesting patterning method demonstrated by B. Lyu et al. is the use of UV/ozone treatment of a substrate with an overlaid shadow mask to render the substrate selectively hydrophilic [275]. Subsequent dip-coating in MXene ink resulted in selective wetting in the patterns exposed through the shadow mask in order to form organic field-effect transistors (OFETs) with MXene source and drain electrodes sized 1000 x 200 μm. Another high-resolution patterning method which has been described is micro-contact printing using PDMS stamps with 20 μm-wide alternating grooves and ridges [263].

A few other interesting approaches which have been demonstrated for patterning MXene include automated scalpel patterning, which can engrave thin MXene films with an interspace resolution of 0.1-0.2 mm [276], laser cutting [277], and direct writing [278]. These approaches give somewhat lower spatial resolution than those listed above, however they represent highly scalable methods suitable for producing devices where micron-scale resolution is not needed.

4.3 Preparation and characterization of Ti_3C_2 MXene for neural electrodes

We synthesized Ti_3C_2 MXene by selectively etching the aluminum atomic layers from its ternary carbide MAX phase precursor (Ti_3AlC_2) in aqueous hydrofluoric (–HF)/ hydrochloric (HCl) solution for 24 hours. After washing, intercalation and delamination was performed using LiCl and several steps of centrifugation and re-suspension. After collecting the supernatant containing well-dispersed single-layer Ti_3C_2 flakes, the solution was Argon bubbled, and packaged in an Argon-sealed headspace vial to ensure longevity. This process is outlined in **Figure 4.3**. This Ti_3C_2 solution could be used to spin-coat Si wafers on which devices are fabricated. An overview of the process flow from Ti_3C_2 synthesis, through device fabrication, to final application in neural signal recording is shown in **Figure 4.4a**, along with the atomic structure of Ti_3C_2. The atomic model shows the –OH termination for simplicity, however the MXenes produced for this study have a distribution of –F, –OH, and –O terminations. We characterized the Ti_3C_2 MXene by scanning electron microscopy (SEM), dynamic light scattering, and UV-vis spectroscopy. SEM of Ti_3C_2 flakes deposited on a porous

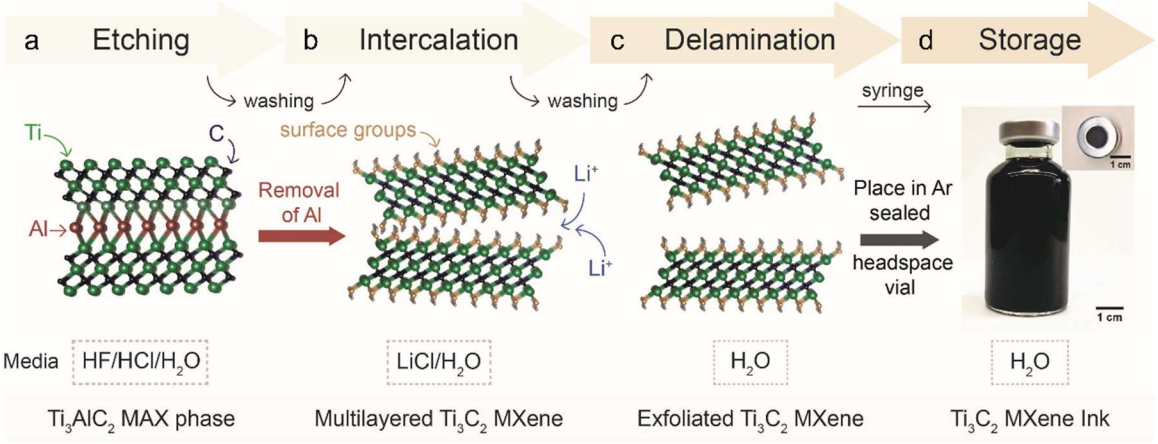

Figure 4.3 Schematic depicting MXene synthesis procedure. (a) Ti3AlC2 MAX is added to a selective etchant solution (HF, HCl, and DI H2O), resulting in the removal of aluminum (Al). (b) After washing the etching solution to neutral pH using DI H2O, multilayered Ti3C2 is obtained. Multilayered Ti3C2 is intercalated with Li+ from an aqueous solution of lithium chloride (LiCl). (c) After washing the intercalation reaction, sediment swelling is observed representing the exchange of Li+ with H2O. Agitation of the swollen sediment results in exfoliated (or delaminated) single- to few-layer flakes of Ti3C2 MXene in H2O. Size selection and separation of delaminated Ti3C2 MXene from multilayered Ti3C2 and Ti3AlC2 MAX phase occurs at this stage. (d) Ti3C2 MXene ink is transferred via syringe to an Argon sealed headspace vial for long-term storage.

alumina membrane from the MXene colloidal solution reveals flake-like morphology and µm-scale lateral size (**Figure 4.4b**). Single-layer MXene flakes have a thickness of ~ 1 nm and lateral sizes in the range of a few hundred nm to few microns, depending on the synthesis

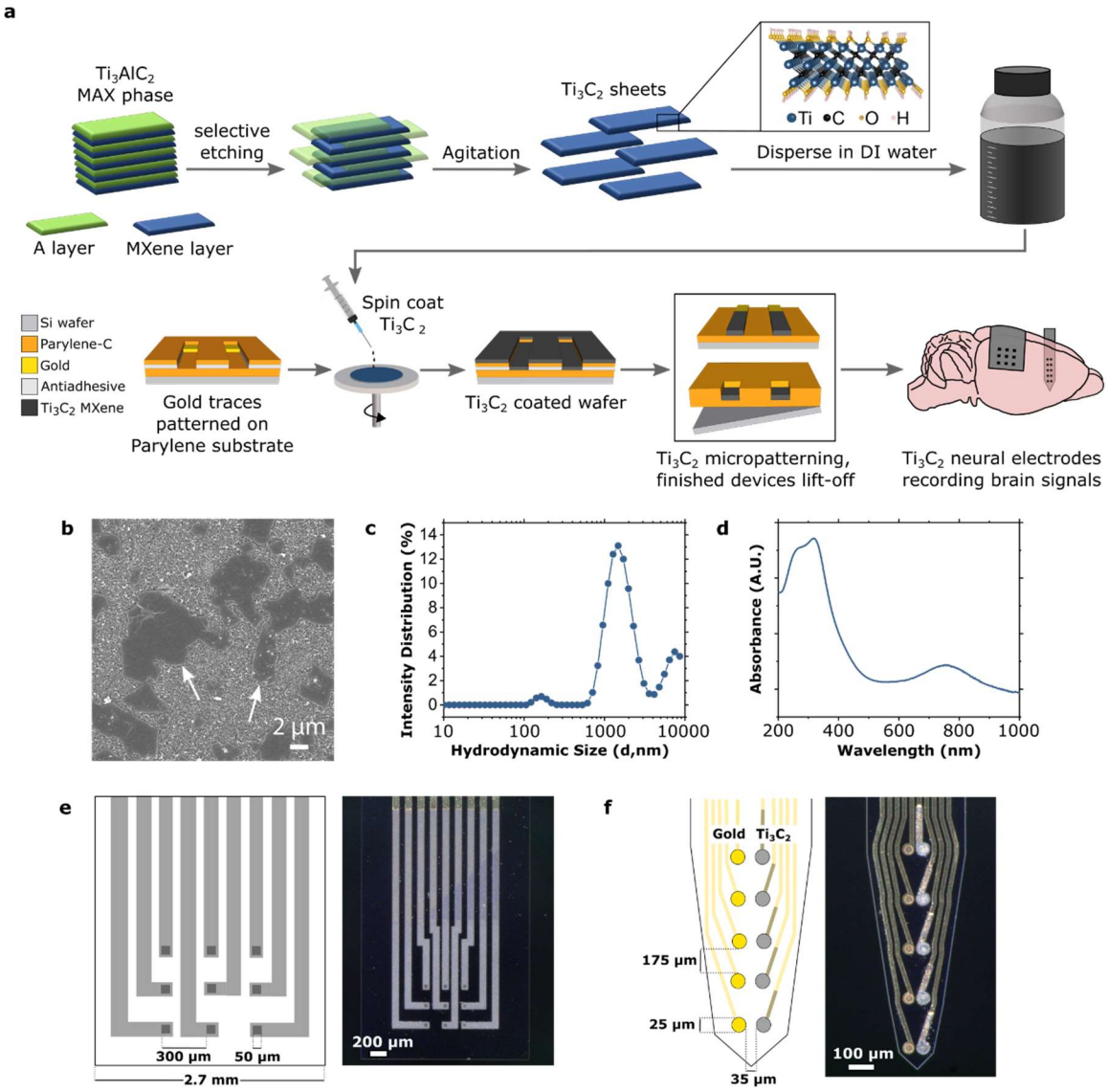

Figure 4.4 Synthesis, characterization, and application of Ti3C2 for neural recording. (a) Schematics illustrating synthesis and atomic structure of Ti3C2, fabrication of Ti3C2 neural microelectrode arrays, and application of Ti3C2 arrays for recording brain activity at different locations in the rat brain. (b) SEM image of Ti3C2 flakes deposited onto an alumina membrane. The arrows point to Ti3C2 flakes on the membrane. (c) Dynamic light scattering particle size intensity distribution (percent) of the Ti3C2 solution in terms of hydrodynamic size (d, nanometer) (d) UV–vis absorption spectra of the Ti3C2 aqueous solution diluted 1000×. (e, f) Schematics and bright-field microscopy image of (e) Ti3C2 micro-ECoG array and (f) Ti3C2/Au intracortical electrode array.

process [224]. For application to neural electrodes, flakes with large lateral size are preferable because they produce films with higher conductivity [224]. Thus, we disperse the Ti_3C_2 flakes in solution by manual agitation rather than sonication, as it is gentler and produces samples with larger flakes. To determine the distribution of flake sizes in our sample, we performed dynamic light scattering on a dilute Ti_3C_2 solution. The intensity distribution reveals a Z-average of 1406 ± 77 nm, a polydispersity index of 0.390, with three noticeable peaks located at 1.6 μm (81.1%), 6.8 μm (16.8%) and 164 nm (2.1%), indicating the percent intensity of different sized flakes (**Figure 4.4c**). Finally, to confirm the composition of the Ti_3C_2 aqueous dispersion, we performed UV-vis spectroscopy from 200-1000 nm. The material in solution absorbed light at the characteristic UV-vis-NIR wavelengths for Ti_3C_2, showing high UV absorption and a broad peak from 760-800 nm (**Figure 4.4d**).

4.4 Development of Ti_3C_2 MXene neural electrode arrays

4.4.1 Fabrication optimization

To evaluate the performance of Ti_3C_2 as a bioelectronic material for recording neural activity at different spatiotemporal scales, we designed two different electrode array geometries. The first electrode array is a 3x3 micro-electrocorticography (micro-ECoG) array consisting of 50 μm x 50 μm square electrode contacts with 300 μm pitch, covering a total recording area of 750 μm x 750 μm, for recording field potentials from the cortical surface (**Figure 4.4e**). We fabricated micro-ECoG arrays of both gold and Ti_3C_2 contacts for comparison. The second electrode array is a 10-channel laminar array with pairs of 25 μm-diameter Ti_3C_2 and Au contacts arranged in a side-by-side "stereotrode" configuration (*i.e.* close enough that each electrode in a pair could plausibly record from the same neurons) (**Figure 4.4f**) [279]. This configuration enables recording the spiking activity of individual neurons within deeper brain structures and allows direct comparison of the signals recorded by the two types of electrode materials.

Unlike most carbon-based nanomaterials, the surface of Ti_3C_2 is inherently hydrophilic due to the surface terminations present, thus enabling dispersion in aqueous solution without the need for surfactants or strong acids. This property is particularly

favorable for developing high-throughput microfabrication processes and patterning high-quality Ti_3C_2 films onto flexible, biocompatible polymeric substrates. To precisely and reliably micropattern Ti_3C_2 recording contacts and interconnects on flexible parylene-C substrates, we developed and optimized an *ad-hoc* spin-coat and dry lift-off technique, similar to previously-reported techniques for micropatterning thin films of organic polymers such as PEDOT:PSS [280]. Briefly, we applied an antiadhesive layer to the wafer, followed by a sacrificial parylene-C layer. Patterns in this sacrificial layer were defined by photolithography and etched by oxygen plasma reactive ion etching (RIE). Then, we spin-coated the Ti_3C_2 colloidal solution onto the wafer, thoroughly dried it, and peeled up the sacrificial parylene layer to leave Ti_3C_2 films behind only in the patterns that had been etched through the sacrificial layer. Using this technique, we were able to pattern Ti_3C_2 features with high fidelity and reproducibility. A detailed description of the fabrication procedure outlined in the Methods section of this chapter (Section **4.8**), and a schematic of the procedure is shown in **Figure 4.5**.

It is worth noting that we designed the devices such that Ti_3C_2 contacts and traces overlapped with gold traces outside of the electrode array, so that Ti_3C_2 was the sole material comprising the electrode contact and exclusively responsible for the device's impedance and

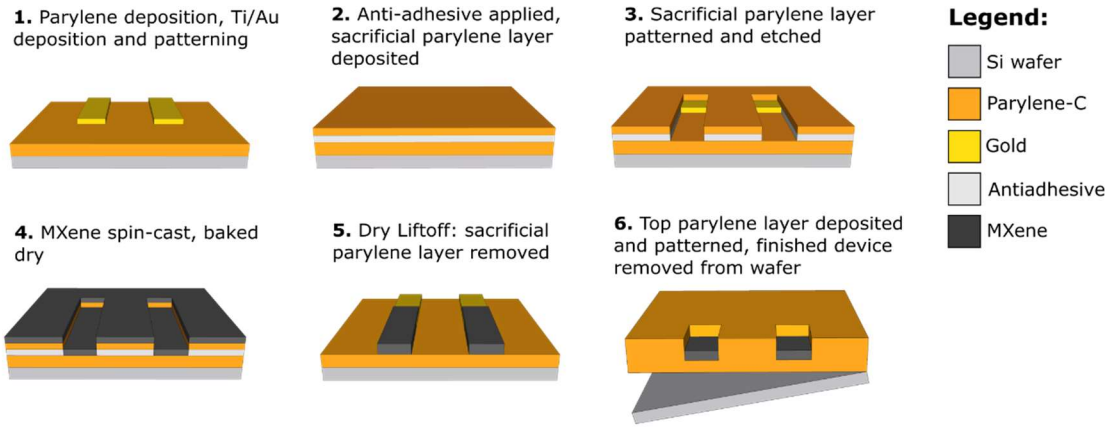

Figure 4.5 Fabrication of multi-channel Ti_3C_2 neural electrodes. Fabrication process: pattern metal traces and connection pads on bottom parylene-C layer; deposit an anti-adhesive layer (1% Micro 90) and a sacrificial parylene-C layer; use photolithography and oxygen plasma RIE to pattern the sacrificial parylene-C layer; spin coat Ti_3C_2 and thoroughly dry the film; peel up the sacrificial layer, leaving Ti_3C_2 patterns behind; deposit top parylene-C layer; use photolithography and oxygen plasma RIE to pattern and etch open electrode and Au bonding pad contacts; release completed device from wafer.

recording performance. To provide adequate mechanical strength for precise insertion of the intracortical arrays into the brain along a straight trajectory, we manually aligned and affixed micromachined steel backings to the parylene substrate with a thin layer of polydimethylsiloxane (PDMS). Finally, for interfacing the devices with the data acquisition systems, we connected the assembled devices to custom printed circuit boards (PCBs) *via* zero insertion force (ZIF) connectors.

4.4.2 Characterization of Ti_3C_2 neural electrodes

We used electrochemical impedance spectroscopy (EIS) in a three-electrode configuration to characterize the electrochemical behavior of the electrode-electrolyte interface (**Figure 4.6a**). At the 1 kHz reference frequency, the 50 μm x 50 μm Ti_3C_2 and Au micro-ECoG electrodes show impedance values of 52 ± 25 kΩ and 206 ± 31 kΩ, respectively, while the impedance of 25 μm diameter Ti_3C_2 and Au intracortical electrodes is 219 ± 60 kΩ and 865 ± 125 kΩ, respectively (**Figure 4.6b**) (Student's t-test, $p < .001$). In both cases, Ti_3C_2 electrodes exhibit roughly 4-fold lower impedance than comparable Au contacts, showing an advantage in utilizing Ti_3C_2 as the active material. The Ti_3C_2 electrodes exhibit a more complex phase behavior than the Au electrodes, which display predominantly capacitive behavior (**Figure 4.6a**). It has been well established that Ti_3C_2 exhibits mainly capacitive charge transfer mechanisms [281], [282], and the roughness and porosity of the film contributes to its behavior as a non-ideal capacitor, as shown by the higher values of the impedance phase. Furthermore, the functional groups on the surface of the Ti_3C_2 flakes can interact with the ionic species in the electrolyte, possibly leading to mixed charge-transfer mechanisms.

One attribute that can reduce electrode impedance is the overall surface roughness or porosity, which produces an increase in the effective surface area without impacting the device footprint. We evaluated the surface morphology of the Ti_3C_2 electrodes with SEM and atomic force microscopy (AFM) and found that the electrode surface is comprised of a dense network of overlapping Ti_3C_2 flakes (**Figure 4.6c**) of nanoscale thickness and several μm in lateral size. AFM mapping of the surface further elucidates the rough and wrinkled morphology and reveals an average surface roughness of 32 nm (**Figure 4.6d**). The thickness

of the Ti_3C_2 films forming the electrodes, as measured by a profilometer following lift-off patterning, is 200 ± 30 nm. The rough surface morphology we observe suggests that ions can interact with the Ti_3C_2 electrodes over a large effective surface area, likely contributing to their remarkably low impedance compared to metal electrodes.

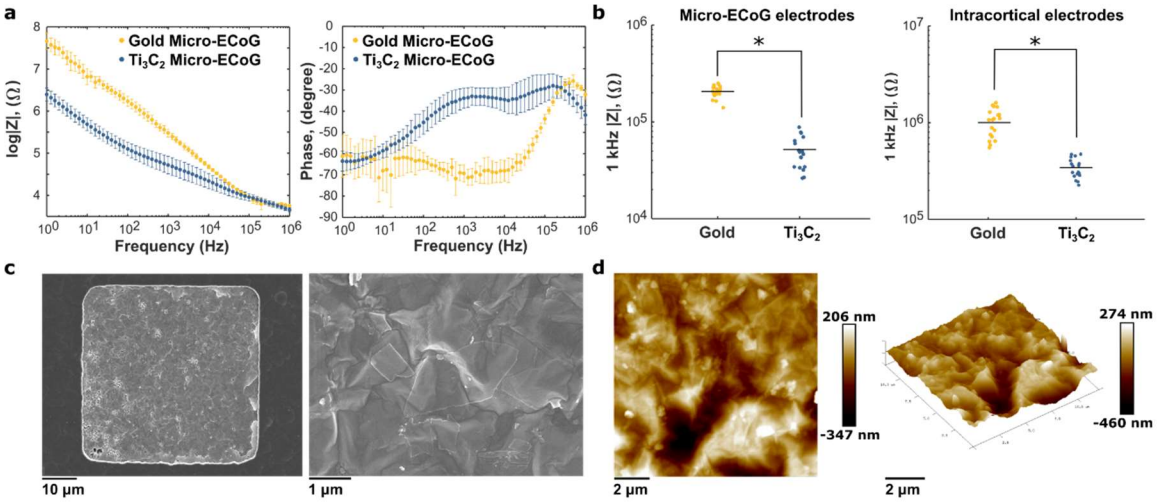

Figure 4.6 Characterization of Ti_3C_2 neural electrodes. (a) Bode plots of impedance magnitude and phase for comparable Ti_3C_2 and Au micro-ECoG electrodes. Points represent means, and bars show standard deviations; Ti_3C_2 n = 10 and Au n = 10. (b) Scatter plots of 1 kHz impedance values for Ti_3C_2 and Au electrodes in micro-ECoG and intracortical electrode arrays. Micro-ECoG electrodes are 50 µm × 50 µm, and intracortical electrodes are 25 µm in diameter. For both types of electrode arrays, Ti_3C_2 shows a ~4× reduction in impedance compared to Au. Black bars indicate means. Micro-ECoG: Ti_3C_2 n = 18 and Au n = 18. Intracortical: Ti_3C_2 n = 19 and Au n = 19. Single asterisks indicate $p < 0.001$ (c) SEM images of Ti_3C_2 electrodes. Individual Ti_3C_2 flakes are visible on the electrode surface. (d) AFM surface mapping showing the rough surface morphology of a Ti_3C_2 electrode.

4.5 *In vivo* neural recording with Ti_3C_2 MXene neural electrode arrays

4.5.1 Cortical surface recording

To assess the functionality of Ti_3C_2 neural electrodes *in vivo*, we performed acute recording experiments in rats under ketamine-dexmedetomidine anesthesia. Schematic of the recording setup for both the brain surface (micro-ECoG) and the brain-penetrating (intracortical) arrays are shown in **Figure 4.7a**. First, we tested Ti_3C_2 and Au micro-ECoG devices placed over sensorimotor cortex (**Figure 4.7a**, left). On both electrodes, we detected

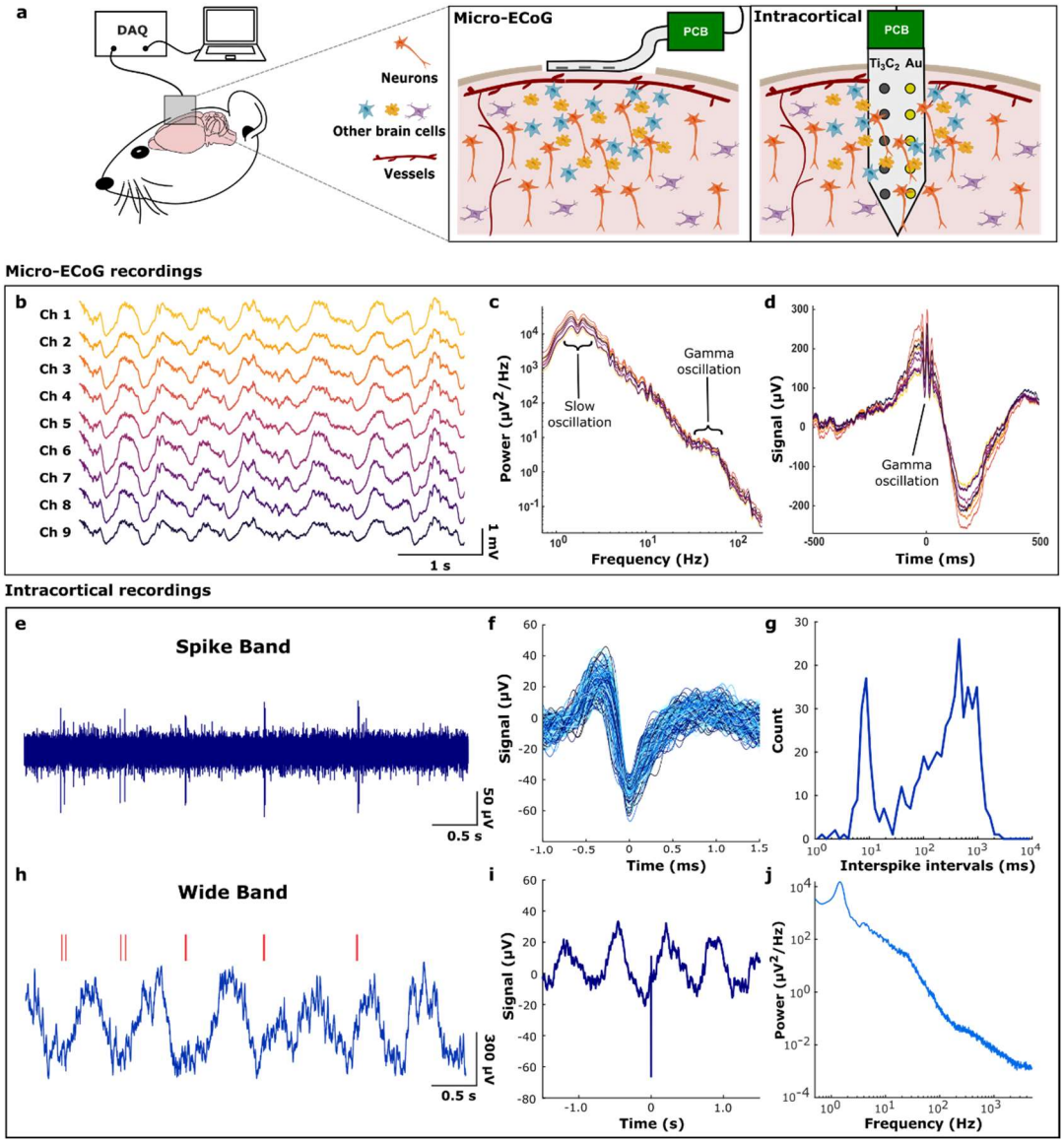

Figure 4.7 *In vivo* neural recordings with Ti_3C_2 MXene electrodes. (a) Schematic of *in vivo* neural recording with Ti_3C_2 electrode arrays. (b) Raw signals obtained from a Ti_3C_2 micro-ECoG device. (c) Power spectral density of micro-ECoG signals showing physiologic peaks for 1–2Hz slow oscillations and 40–70 Hz γ oscillations. (d) γ-triggered average showing γ oscillations coupled to the up phase of the slow oscillation. (e) Action potentials (spikes) recorded extracellularly in rat hippocampus. Noise in the spike frequency band (500–5000 Hz) was 4.67 μVrms. (f) Overlaid spike waveforms (N = 580) from a 200 s recording. (g) Interspike intervals had a bimodal distribution. The neuron tended to fire rhythmically at 1 to 2 Hz with bursts of 2 spikes separated by about 10 ms. (h) The full bandwidth (0.5–5000 Hz) recording revealed that the rhythmic spiking was related to a slow oscillation in the field potential. Red lines indicate spike times corresponding to E. (i) Spike-triggered average showing that the spikes were locked to the rising phase of the slow oscillation. (j) Power spectrum of the full bandwidth recording with a physiological peak at 1.5 Hz.

clear physiological signals (**Figure 4.7b**). However, the background noise level in the spike band (500 – 5000 Hz) was lower in the Ti_3C_2 recordings than in the Au recordings: 3.7 ± 0.3 μVrms vs. 6.6 ± 2.0 μVrms, respectively. The power spectral density (PSD) of the recorded signals confirmed the presence of two brain rhythms commonly observed in rats under this type of anesthesia: slow oscillations at 1-2 Hz and gamma oscillations at 40-70 Hz (**Figure 4.7c**). These two rhythms were, in fact, coupled, as revealed by computing the signal average in a window centered on gamma oscillation events (**Figure 4.7d**). Gamma bursts occurred on average at a specific phase, namely the peak, of the slow oscillation as reported previously with traditional metal electrode recordings [283], [284]. Thus, the Ti_3C_2 electrode surface recordings reproduced known physiology in this brain state and with lower noise than Au electrodes.

4.5.1 Intracortical recording

Next, we inserted electrode arrays intracortically to record neuronal action potentials (spikes). The 10-channel intracortical arrays were composed of both Ti_3C_2 and Au electrodes (**Figure 4.7a**, right). Examples of the neural activity recorded from a Ti_3C_2 contact are shown in **Figure 4.7e,f**. The neuron recorded on this Ti_3C_2 electrode tended to fire rhythmically at a low frequency (<5 Hz), but with bursts of spikes in each cycle (**Figure 4.7e,g**). The full bandwidth recording revealed that the rhythmic spiking of this cell was related to the slow oscillation in the field potential (**Figure 4.7h**). As with gamma oscillations recorded at the brain surface, spikes from this neuron were biased to occur at a particular phase of the rhythm (**Figure 4.7i**), which again had a frequency of 1-2 Hz (**Figure 4.7j**). Although these results demonstrate the functionality of intracortical Ti_3C_2 electrodes, we next pursued the more critical question of how they perform relative to the Au electrodes.

The intracortical array was designed such that each pair of Ti_3C_2 and Au electrodes was arranged as a stereotrode, with contacts separated by 35 μm. This configuration allows the direct comparison of the signal recorded with the two types of electrodes at different depths in the sensorimotor cortex (**Figure 4.8a**). Spiking activity was observed predominantly on the distal three pairs of electrodes (**Figure 4.8b**). Spikes that occurred simultaneously on adjacent Ti_3C_2 and Au electrodes in a pair were considered to be generated

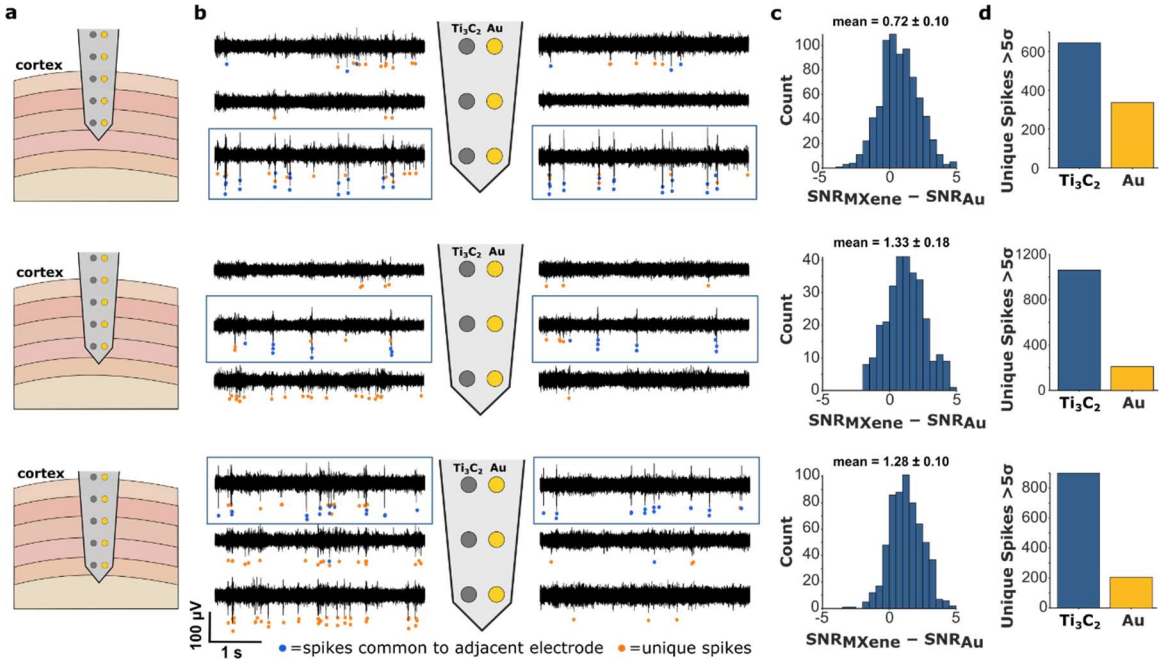

Figure 4.8 Comparison of *in vivo* signal recorded on Ti_3C_2 and Au electrodes intracortically. (a) Schematics of an intracortical electrode array with five Ti_3C_2/Au stereotrode pairs. The array was inserted into the cortex and advanced in approximately 500 µm steps to a depth of 2 mm while recording. (b) Multiunit spiking activity observed on the distal three pairs of electrodes in the array at three different recording depths. Spikes that were observed simultaneously on adjacent Ti_3C_2 and Au contacts are indicated by blue dots. Spikes unique to a given electrode are indicated by orange dots. (c) Histogram of $SNR_{MXene} - SNR_{Au}$ for the common spikes on the adjacent electrodes outlined in blue boxes in (b). In all cases the distribution mean was significantly greater than zero (permutation tests, $p < 0.001$), indicating higher SNR on Ti_3C_2 contacts compared to Au. (d) Number of unique spikes seen on adjacent Ti_3C_2 and Au electrodes. In all cases, more unique spikes were observed on Ti_3C_2 contacts, indicating these electrodes were more sensitive for recording unit activity than Au electrodes.

by the same neuron. For each of these "common spikes," we computed the SNR from each electrode. The mean of the distribution of $SNR_{MXene} - SNR_{Au}$ was, at all three depths, greater than zero (permutation test, $p < .001$), indicating that spikes recorded on the Ti_3C_2 electrodes had higher SNR than those on the Au electrodes (**Figure 4.8c**). Additionally, Ti_3C_2 electrodes recorded more "unique spikes", or spikes that occurred only on one electrode in the pair (**Figure 4.8d**). These unique spikes had lower amplitudes than the common spikes and therefore may have arisen from neurons located further from the electrode sites. This result suggests that, due to their lower impedance, the Ti_3C_2 electrodes have a larger "seeing distance", allowing them to resolve spiking activity from a larger volume of tissue.

Finally, we quantified the power spectrum of the wideband neural signal recorded on representative Ti_3C_2 and Au electrodes in the array (**Figure 4.9**). The Ti_3C_2 electrode recorded higher overall power across a wide range of frequencies. Additionally, a significant peak at 60 Hz was observed on the Au electrode, while this peak is completely absent on the adjacent Ti_3C_2 contact, which indicates that the higher impedance Au electrodes are more susceptible to mains interference.

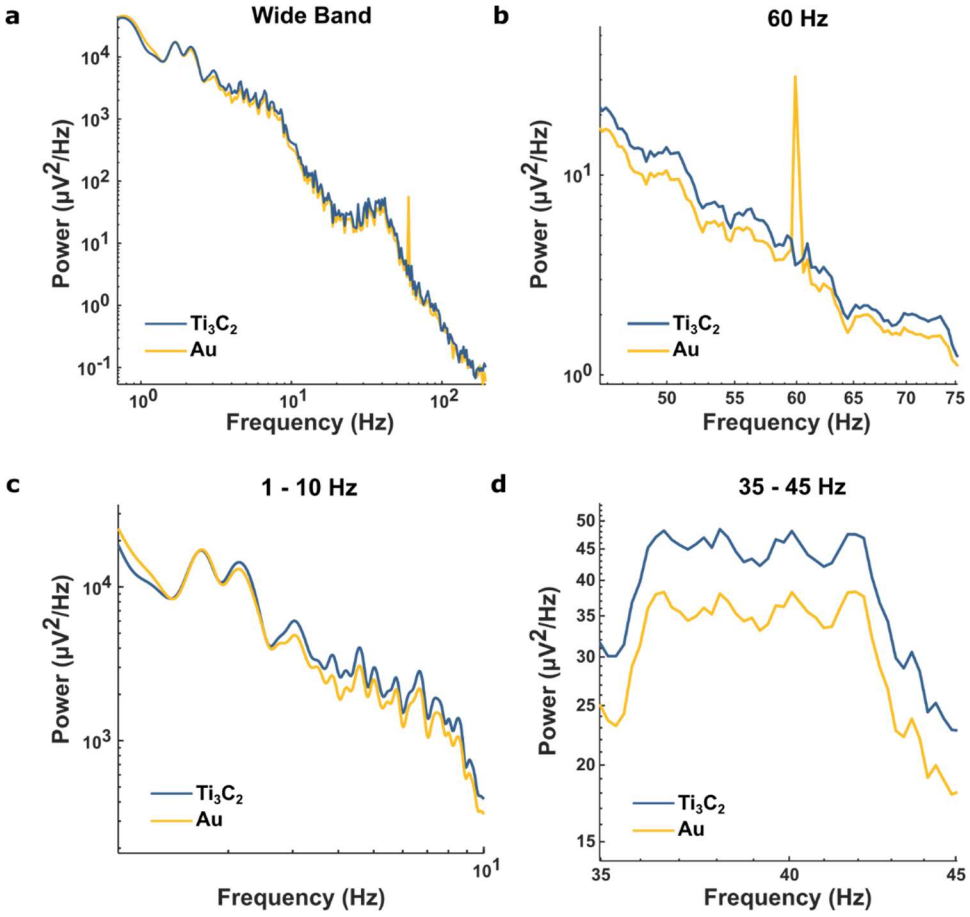

Figure 4.9 ***In vivo*** **noise characteristics.** (a) Wide band power spectral density from representative Ti3C2 and Au electrodes from the intracortical array. (b) A significant peak in power at 60 Hz, attributed to mains noise, was seen on Au electrodes but was not observed on Ti3C2 electrodes. (c,d) Ti3C2 electrodes recorded higher power across a broadf range of frequencies, including 1-10 Hz delta and theta rhythms (c) and 35-45 Hz gamma rhythms (d).

4.6 Neuronal biocompatibility of Ti_3C_2 MXene

MXenes have shown great promise in a number of biomedical applications including cancer theranostics [242], diagnostic imaging [285], and biosensing [249]. Recent studies report that MXenes are biocompatible to immortalized tumor cell lines *in vitro* and at the systemic level when injected intravenously *in vivo* [236], [250]. However, very little is known about the safety and compatibility of MXenes to neuronal cells. Thus, we performed

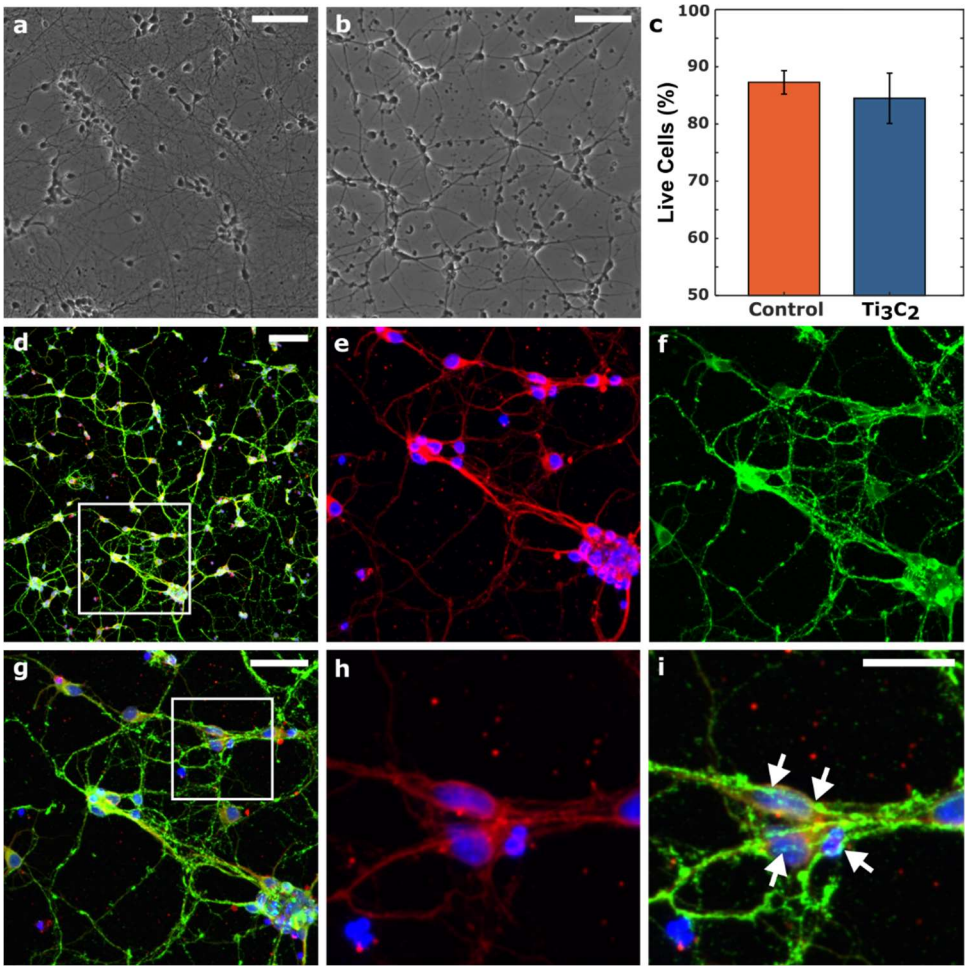

Figure 4.10 Biocompatibility of Ti_3C_2 MXene films. Representative phase images of primary cortical neurons cultured on (a) polystyrene and (b) 200 nm-thick Ti_3C_2 films at 7 DIV. (c) Quantitative comparison shows no significant difference in neuronal survival on Ti_3C_2 or polystyrene ($p>0.6$). (d-i) Representative multiphoton images of neurons cultured on Ti_3C_2 at 7 DIV stained for nuclei (blue), axons (red), and synapses (green). Outlined region in (d) is shown in (e-g); outlined region in (g) is shown in (h-i), highlighting network formation as confirmed by the presence of synapsin-positive puncta along axons and cell bodies (arrows). Scale bars: 100 µm (a, b, d), 50 µm (g), 25 µm (i).

cytotoxicity studies *in vitro* on primary cortical neurons grown on Ti_3C_2 films. At 7 days *in vitro* (DIV), quantification of the percent viable neurons showed no significant difference in cell survival between Ti_3C_2 and control polystyrene cultures (Ti_3C_2: 84.4 ± 4.40%, polystyrene: 87.3 ± 2.05%; $p > 0.64$) (**Figure 4.10a-c**). Cell densities on Ti_3C_2 at 7 DIV were significantly sparser than those on polystyrene (Ti_3C_2: 650 ± 155 neurons/mm^2, polystyrene: 1132 ± 132 neurons/mm^2; $p < 0.05$), suggesting additional surface treatments may be required to promote neuronal adhesion. Although there was also a reduction in overall neurite density on the Ti_3C_2 cultures, there were no significant differences in neurite outgrowth per neuron (Ti_3C_2: 5.73 ± 1.05 neurites per neuron, polystyrene: 6.00 ± 0.737 neurites per neuron; $p > 0.8$). Immunocytochemistry revealed widespread network formation on both substrates (**Figure 4.10d-i**), with neurons extending branching neurites (**Figure 4.10e,h**) and synapsin-positive puncta present surrounding cell bodies and at axon-soma junctions (**Figure 4.10f,i**).

Overall, neurons reproducibly adhered, grew, and formed neuronal networks on both Ti_3C_2 and polystyrene, with both substrates yielding equivalent neuronal viability and neurite outgrowth per neuron out to at least 7 DIV. These results indicate that Ti_3C_2 is capable of supporting neuronal growth and network formation with negligible cytotoxicity relative to established cell culture substrates. While both cultures exhibited similar neurite counts per neuron and axonal/synaptic presence at 7 DIV, Ti_3C_2 cultures had a reduction in both neuron density and a commensurate reduction in neurite outgrowth compared to polystyrene. These results suggest decreased neuronal adhesion on Ti_3C_2 compared to polystyrene, which indicates further optimization of the pre-treatment protocol used to culture neurons and promote neuronal adhesion and neurite growth on Ti_3C_2 films is necessary.

4.7 Discussion

In this study, we developed a protocol for fabricating high-resolution Ti_3C_2 MXene neural electrode arrays using simple, scalable solution processing methods. The methodology described here can easily be extended to create other types of MXene sensors, and the extraordinary processability of MXenes highlights the potential for cost-effective production of MXene biosensors at industrial scales, which is not currently possible for devices based on

other carbon nanomaterials. The high conductivity of Ti_3C_2, coupled with the high effective surface area of MXene films, endows Ti_3C_2 neural electrodes with remarkably low impedance, which improves their sensitivity for recording neural activity at fine spatial scales. Recordings from Ti_3C_2 micro-ECoG devices showed known physiologic signatures with lower baseline noise than control Au electrodes. Using high-resolution intracortical arrays, we demonstrated that Ti_3C_2 electrodes record multiunit neuronal spiking activity with improved SNR compared to gold electrodes. Additionally, our observation that Ti_3C_2 electrodes recorded overall a larger number of spikes, many of which were low-amplitude, suggests that these electrodes are capable of recording from a larger volume of brain tissue. Thus, Ti_3C_2 micro-electrodes may represent a significant advance for the sensitive detection of neuronal spiking activity compared to conventional silicon or metal-based micro-electrodes. Furthermore, our observations suggest that Ti_3C_2 could be useful for a range of implantable sensors beyond neural recording applications, such as cardiac monitoring, and it may be a candidate to replace expensive electrode materials, such as platinum, currently used in many implantable devices. Finally, though the biocompatibility of Ti_3C_2 has been demonstrated following systemic injection for cancer theranostic applications, the compatibility of this material to neurons and brain cells has so far remained largely untested. Our work shows that not only do neurons remain viable in contact with Ti_3C_2, but that they also extend neurites and form functional networks when cultured on Ti_3C_2 films. While more work needs to be done, our experiments indicate that Ti_3C_2, and possibly other MXenes, have significant potential to transform the field of implantable sensors in both research and clinical applications. The promising bioelectronic properties and versatility in fabrication of Ti_3C_2 MXene may both reduce cost and improve performance in current and future medical devices.

4.8 Materials and methods

Preparation of Ti_3C_2 colloidal solution

Ti_3AlC_2 MAX phase carbide powder synthesis has been explained elsewhere [232]. 5 g of Ti_3AlC_2 was added slowly to a chemical etchant (50 mL, 12 M HCl (Alfa Aesar), deionized (DI) water, 49 % HF (Sigma-Aldrich), 6:3:1 ratio) while it was in an ice bath and was agitated on

a stir plate (24 h, 500 rpm, 25 °C, Teflon stir bar) in an unsealed container to make multi-layer Ti_3C_2 MXene (ML-MXene). The solution was then centrifuged (2 minutes, 3500 rpm, ~6 cycles) in 2 large tubes (175 mL) to reach ~6 pH. An intercalant was used to delaminate Ti_3C_2 into single flakes by mixing 10 grams lithium chloride (LiCl, Alfa Aesar) and 100 mL DI water in an ice bath 30 minutes prior to adding the ML-MXene. After adding Ti_3C_2, the solution was manually shaken until small bubbles appeared on the side of the container (~15 min) and the solution was stirred on a stir plate (at least 4 h at 300 rpm). The solution was then centrifuged (3500 rpm, 2 cycles, 2 min) in 2 large tubes to cause the sediment to swell. Next, the sediment was evenly dispersed and centrifuged (3500 rpm, 1 hr, 2 cycles) in 4 150-mL tubes, Finally, to remove insoluble contaminates from the single flake and ML-MXene, the sediment was dispersed (10 minutes manual hand shaking) in 300 mL DI water in 2 150-mL tubes and centrifuged (500 rpm, 2 minutes). The resulting supernatant was centrifuged at 10000 rpm for 15 minutes in 6 small tubes (50 mL) and the sediment (with concentration of 10 mg/mL) was collected. Prior to spin coating, the Ti_3C_2 solution was dispersed for centrifugation (3500 rpm, 2 minutes) in 2 small tubes and the supernatant was collected to be used for spin coating. The concentration of Ti_3C_2 in the supernatant was measured (~10 mg/mL) by vacuum filtration of the solution (1 mL) on a hydrophobic Celgard membrane.

Characterization of Ti_3C_2 flakes

As-prepared Ti_3C_2 was characterized by SEM, dynamic light scattering, and UV-vis spectroscopy. Scanning electron microscopy was performed using a Zeiss Supra 50 VP (Zeiss, Germany) at an accelerating voltage of 5 kV by vacuum filtering a dilute (~0.01 mg/mL) solution over a porous alumina membrane (Anodisc, 0.1 μm pore size, Whatman). Dynamic light scattering was performed using a dilute Ti_3C_2 solution (<0.1 mg/mL) in a polystyrene disposable cuvette (Malvern Instruments, Zetasizer, NanoZS). The measurement was repeated 5 times and an average was reported (Figure 1C). UV-vis spectroscopy was conducted from 200-1000 nm on a Ti_3C_2 solution diluted 1000x (ThermoScientific Evolution 201).

Device Fabrication and Assembly

A silicon wafer was coated with a 4 μm-thick layer of parylene-C. Metal traces and pads (Ti/Au = 10/100 nm) were patterned using standard photolithography and lift-off processes. The wafer was coated with an anti-adhesive layer (1% Micro-90), then a second, 3 μm thick sacrificial layer of parylene-C was deposited. Patterns for MXene traces and electrode contacts were defined by photolithography with the negative resist NR71-3000p and subsequent oxygen plasma reactive-ion etching (RIE) to etch through the sacrificial parylene-C layer. A Ti_3C_2 colloidal solution was spin-coated on the wafer and the wafer was subsequently baked at 130 °C for 3 hrs to ensure that the resulting Ti_3C_2 film was fully dried. A 50 nm-thick layer of SiO_2 was deposited by e-beam evaporation to serve as a protective mask on the Ti_3C_2 patterns during subsequent fabrication steps. The sacrificial parylene-C layer was then manually peeled up with tweezers, leaving behind Ti_3C_2/SiO_2 only on the Ti_3C_2 contacts and traces previously defined. After deposition of a top 4 μm-thick parylene-C encapsulation layer, an etch mask was defined through photolithography, e-beam deposition of aluminum (100 nm), and lift-off to define the outline of the devices, and openings over Au bonding pads and electrode contacts. The exposed parylene-C was etched with oxygen RIE, and the Al etch mask was subsequently removed *via* wet etching. The SiO_2 protective layer covering the Ti_3C_2 contacts was etched with 1:6 buffered oxide etchant (BOE: 6 parts 40% NH_4F, 1 part 49% HF, Sigma-Aldrich) to expose the Ti_3C_2 electrode sites. Finally, the completed devices were released from the silicon wafer. Both micro-ECoG and intracortical electrode arrays were fabricated using this procedure, with different photomasks to define the geometries. Steel backings (2.5 μm thick) were laser-micromachined (IPG IX280-DXF Green Laser Micromachining, 532 nm) to provide mechanical support for insertion of the intracortical arrays. Devices were carefully aligned and manually fixed to these steel backings using polydimethylsiloxane (PDMS) as an adhesive. Both micro-ECoG devices and steel-backed intracortical array devices were inserted into zero-insertion force (ZIF) connectors on custom printed circuit boards for connection to the data acquisition systems for *in vitro* characterization or *in vivo* neural recording.

Electrochemical Impedance Spectroscopy

EIS of Ti_3C_2 and Au microelectrodes was performed with a Gamry Reference 600 potentiostat (Gamry Instruments) in a phosphate buffered saline (PBS) bath pH 7.4 at room temperature. EIS measurements were collected using a three-electrode configuration with Ti_3C_2 or Au microelectrodes as the working electrode, a graphite rod (Bio-Rad Laboratories, Inc.) as the counter electrode, and a Ag/AgCl (Sigma Aldrich) electrode as the reference electrode. Measurements were acquired by applying a 20 mV rms sinusoidal voltage input in the 1 Hz – 1 MHz range.

Electrode Surface Morphology Characterization

SEM images (Zeiss Supra 50VP) were taken with an accelerating voltage of 5 kV. AFM surface mapping (Bruker Dimension Icon AFM) was performed in tapping mode in air and data were analyzed in NanoScope Analysis software (Bruker).

Animal Surgery and *In Vivo* Recording

In vivo neural recordings were collected from n = 3 Sprague-Dawley rats during acute, sterile procedures. Rats were anesthetized with a solution of ketamine (60 mg/kg) and dexmedetomidine (0.25 mg/kg) and placed in a stereotaxic frame. The right somatosensory cortex was exposed with a craniectomy and durotomy. Skull screws were placed in the left parietal and frontal bones around which Ag wires were wrapped to serve as the reference and ground for the recordings. The electrode arrays were mounted on a stereotaxic manipulator, positioned over the exposed cortex, and lowered. Ti_3C_2 and Au micro-ECoG arrays were placed over barrel cortex successively and recordings from each were collected in 5-minute segments. For intracortical Ti_3C_2 /Au arrays, recordings were made at a number of depths throughout the cortex to sample neural activity. The wideband neural signals (1 Hz to 7.5 kHz) were acquired at 30,000 sample/s by an electrophysiology system (Intan RHS2000 Stimulation/Recording System, Intan Technologies). All procedures were approved by the Institutional Animal Care and Use Committees at the University of Pennsylvania and adhered to the guidelines set forth in the NIH Public Health Service Policy on Humane Care and Use of Laboratory Animals (2015).

In Vivo Data Analysis and Statistical Methods

For multiunit analysis, signals were band-pass filtered from 300-6000 Hz (2nd order Butterworth). The standard deviation of the background noise for each channel was estimated as

$$\sigma_n = median\left\{\frac{|x|}{0.6745}\right\}$$

and spikes were detected by setting a threshold of $5\sigma_n$ [286]. Spikes observed on both the Ti_3C_2 and Au electrode in a stereotrode pair were assumed to have been generated by the same neuron, and classified as "common spikes", if they occurred within 0.1 ms of each other. All remaining spikes were classified as "unique spikes". To compare signal quality, the SNRs for each common spike were computed from the signals observed on the Ti_3C_2 and Au electrodes in the stereotrode pair and subtracted. A permutation test was then performed to test if the mean of the resulting distribution was centered around zero.

Cell Culture Substrate Preparation

Glass slides coated with Ti_3C_2 were soaked in 70% ethanol for 20 minutes. Slides were then rinsed in sterile cell culture water before exposing each side to UV light for 30 minutes (1 hr total exposure). Post-UV, slides were immersed in Poly-L-lysine (PLL) (0.05 mg/mL in sterile cell culture water) overnight. Slides were then rinsed in sterile cell culture water before being immersed in laminin (20 μg/mL in sterile cell culture water) overnight prior to neuronal plating. For control cultures, polystyrene petri dishes were coated in PLL and laminin using the same protocol.

Cortical Neuron Isolation and Culture

All procedures were approved by the Institutional Animal Care and Use Committees at the University of Pennsylvania and the Michael J. Crescenz Veterans Affairs Medical Center and adhered to the guidelines set forth in the NIH Public Health Service Policy on Humane Care and Use of Laboratory Animals (2015). Neural cell isolation and culture were performed following protocols previously published [287]. Briefly, timed-pregnant rats were

euthanized, and embryonic day 18 fetuses were removed from the uterus and transferred to cold Hank's balanced salt solution (HBSS). Post-removal, the fetus brains were extracted and the cerebral cortical hemispheres isolated under a stereoscope *via* microdissection. Cortical tissue was dissociated in 0.25% trypsin + 1mM Ethylenediaminetetraacetic acid (EDTA) at 37˚C, after which the trypsin/EDTA was removed and replaced with 0.15 mg/ml DNase in HBSS. Dissociated tissue + DNase was centrifuged for 3 min at 3000 RPM before the DNase was removed and the cells re-suspended in neuronal culture media, composed of Neurobasal® + B27® + Glutamax™ (ThermoFisher) and 1% penicillin-streptomycin. Neurons were diluted to ~1.5 x 10^6 neurons/ml. 200 µL from the primary cortical neuronal suspensions were plated on each of the Ti_3C_2 slides and control dishes within 2 mL of neuronal culture media and grown under standard cell culture conditions (37˚C, 5% CO_2). Half-media changes were performed every 2 days, with phase images taken using a Nikon Eclipse Ti-S microscope paired with a QIClick camera and NIS Elements BR 4.13.00.

Neuronal Viability Assessment

To assess culture viability, phase images of Ti_3C_2 slides (n = 6) and control cultures (n = 6) were taken at 7 days *in vitro* (DIV). Neurons within a randomly identified 0.5 mm^2 area were manually scored as either live or dead, depending on their morphology (*i.e.* presence and integrity of neurites; cell body). Neuronal survival was quantified as the proportion of live neurons to total (live + dead) neurons, while cell density was calculated as the total number of neurons per mm^2. Each metric was averaged across Ti_3C_2 and polystyrene controls and compared *via* unpaired t-test, with statistical significance identified as a p-value less than 0.05. All data presented as mean ± s.e.m.

Immunocytochemistry

At 7 DIV, Ti_3C_2 slides (n = 6) and control cultures (n = 6) were fixed in 4% formaldehyde for 35 min. Fixed cultures were rinsed in 1x PBS and permeabilized with 0.3% Triton X100 + 4% horse serum in PBS for 60 min before being incubated with primary antibodies overnight at 4˚C. Primary antibodies were Tuj-1/beta-III tubulin (T8578, 1:500, Sigma-Aldrich) to label axons and synapsin-1 (A6442, 1:500, Invitrogen) to label pre-synaptic specializations. Post-

incubation, cultures were rinsed in PBS before being incubated with fluorescently-labeled secondary antibodies (1:500; sourced from Life Technologies & Invitrogen) for 2h at 18˚-24˚C. Finally, Hoechst (33342, 1:10,000, ThermoFisher) was added for 10 min at 18˚-24˚C before rinsing in PBS. Cultures were imaged on a Nikon A1RMP+ multiphoton confocal microscope paired with NIS Elements AR 4.60.00 and a 16x immersion objective. Sequential slices of 1-1.2 μm in the z-plane (n_{slices} = 20) were acquired for each fluorescent channel. All confocal images presented are maximum intensity projections of the confocal z-slices.

Neurite Measurement & Data Analysis

Multiphoton images from the immunocytochemistry performed above were imported into ImageJ and processed using the open-source NeuriteQuant plugin. NeuriteQuant provided quantitative estimates of neurites per cell from the multiphoton images. Neurites per cell were averaged for both polystyrene and Ti_3C_2 cultures, with unpaired t-tests used to compare measurements. All data is presented as mean ± s.e.m.

Chapter 5: Human-scale, translational neurodevices using Ti_3C_2 MXene

Technologies enabling the seamless integration of electronics with soft biological tissues for mapping and modulating excitable networks at high resolution and at large scale can enable paradigm-shifting diagnostics, monitoring, and treatment strategies. Realizing such technologies has required significant innovation in both materials and fabrication strategies to develop bioelectronic interfaces which are soft, biocompatible, and highly conformable to the tissue of interest. Many of the most successful advances in this realm so far have leveraged traditional metal and silicon materials along with thin-film microfabrication strategies to create highly flexible and conformable bioelectronic interfaces. While these thin-film technologies can achieve exquisite tissue conformability, they have largely failed to translate into clinical and consumer markets because the materials and fabrication schemes are expensive, do not scale, and they critically limit the maximum attainable resolution and coverage. Solution processing is a cost-effective manufacturing alternative, however biocompatible conductive inks matching the performance of conventional metals have been lacking. In the previous chapter, I introduced Ti_3C_2 MXene as a solution-processable 2D material that showed excellent performance for neural recording when incorporated into microelectrodes. Driven by the success of those MXene microelectrodes, I next sought to expand Ti_3C_2 to human-scale translational neurodevices. In this chapter, I introduce MXtrodes, a novel class of soft, high-resolution, large-scale bioelectronic interfaces enabled by Ti_3C_2 MXene and scalable solution processing. I show that the electrochemical properties of MXtrodes exceed those of conventional materials in both epidermal and implantable use cases. In fact, MXtrodes do not require conductive gels for epidermal sensing due to their exceptionally low interface impedance. I then validate MXtrodes in a number of applications ranging from mapping large scale neuromuscular networks in humans to delivering cortical microstimulation in small animal models. Finally, I demonstrate that MXtrodes are compatible with standard clinical neuroimaging modalities.

5.1 Introduction

Recent advances in soft materials and electronics have fueled a new generation of bioelectronic technologies for medical diagnostics and therapeutics, healthcare monitoring, and wearable devices [29], [112], [288], [289]. Soft and flexible bioelectronic devices designed to safely and intimately interface with multiscale networks in the human body offer paradigm-shifting opportunities for monitoring brain activity, cardiac health, and muscle function, as well as for facilitating human-machine interactions, such as myoelectric control of advanced prostheses [290]–[292] or non-invasive brain-computer interfaces [293]. Active bioelectronic devices can also implement intelligent control strategies based on electrical stimulation of excitable circuits for treating neurological diseases [23], [24], heart arrhythmias [25], [26], and inflammatory disorders [27], [28], as well as for rehabilitation therapies [294]–[296].

Despite significant progress in the field of soft, ultra-thin, and conformable bioelectronics [54], [108], [120], [297], [298], conventional materials and fabrication processes remain largely inadequate for producing large-scale, high-density multielectrode arrays that can map and modulate activity in excitable tissues with high spatiotemporal resolution over broad areas. For example, thin-film processing has enabled advances in ultra-thin and flexible electronics; however, such processes rely on wafer-scale microfabrication conducted in a cleanroom facility, which is time consuming, expensive, and typically limits the maximum attainable area coverage to a few square centimeters [112]. Recent work has demonstrated the possibility to overcome this size limit by implementing the fabrication process on large-diameter wafers [120], but microfabrication techniques remain difficult to scale and are still not cost-effective. Contributing to the manufacturing challenges is the fact that flexible polymeric encapsulation materials require low-temperature processing below their glass transition points and can also be incompatible with certain chemicals and solvents commonly used in microfabrication. In addition to the processing constraints, conventional bioelectronic materials – such as gold (Au), platinum (Pt), iridium (Ir), and silver/silver-chloride (Ag/AgCl) – are both costly and intrinsically limited in their electronic, mechanical, and chemical compatibility with biological tissues. For example, they present challenges in achieving low electrode-tissue interface impedance, which is essential for high-fidelity

recording and for safe, effective delivery of electrical stimulation. As a result, in applications such as epidermal electronics, conventional Ag/AgCl electrodes typically require a conductive gel at the skin interface to lower the impedance enough to acquire good quality signal. The conductive gels pose a host of issues including skin irritation and impedance instability as they dry out [115], [299]. Metal-based devices are also inadequate for coupling with clinical imaging modalities such as magnetic resonance imaging (MRI), often causing artifacts in the images even if they are considered MR safe. To realize the next generation of soft, large-scale, high-density bioelectronic interfaces for human applications, innovation in both materials and fabrication is needed.

Solution processing techniques, such as inkjet or screen printing, offer a scalable and low-cost route for fabricating large-area multielectrode arrays unencumbered by the size constraints of wafer-level methods. Despite these advantages, widespread adoption of such techniques has so far been limited by the lack of conductive inks that can produce electrodes with biocompatibility, flexibility, electronic conductivity, and electrochemical properties comparable to those made with conventional materials. High conductivity can be achieved by printing ink formulations based on metal nanoparticles, however, they typically require high annealing temperatures which are not compatible with soft polymeric substrates [300], [301]. Furthermore, metal inks raise concerns about potential toxicity [302]. Conducting polymer-based inks, notably those using poly(3,4-ethylenedioxythiophene) doped with poly(styrene sulfonate) (PEDOT:PSS), can be processed at ambient temperatures to generate flexible, biocompatible films, but their conductivity is generally significantly lower than metal films [303], [304]. Finally, graphene oxide (GO) inks require an additional reduction step to be converted to the conductive reduced graphene oxide (rGO) form, which poses materials and safety issues due to the high temperatures and toxic chemicals employed in the reduction process [305]. Furthermore, the conductivity of rGO is still far inferior to that of pristine graphene [306] and PEDOT:PSS films.

Transition metal carbides, nitrides, and carbonitrides (MXenes) have emerged as a new class of two-dimensional (2D) nanomaterials that enable low-cost, additive-free, solution processing and can produce biocompatible films with metallic conductivity. MXenes are 2D flakes ~1 nm in thickness and up to 10s of μm in lateral size which contain abundant

surface-terminating functional groups, including hydroxyl (-OH), oxygen (-O), or fluorine (-F), which make them hydrophilic and also allow for versatile surface modification and functionalization. The unique hydrophilic nature of MXenes enables a wide range of safe, high-throughput, and scalable processing methods using simple water-based inks, including spray [307], spin [308], and dip coating [309], direct writing [278], and inkjet printing [274], [278]. Of the large variety of MXenes that have been synthesized to date, Ti_3C_2 (the chemical formula is often written as $Ti_3C_2T_x$ to account for the surface terminations, T_x) has been the most widely studied and optimized MXene. It is made of Earth-abundant elements and no cytotoxicity has been observed in previous studies [250]. In the past few years, Ti_3C_2 has attracted great attention for a number of biomedical applications [310], including cancer theranostics [236], hemodialysis [255], and wearable mechanical sensors [256], [311]. Our group has pioneered the use of Ti_3C_2 for implantable neural microelectrodes [312], [313] and skin-conformable, thin-film wearable sensors [314]. Ti_3C_2 has metallic behavior exhibiting electronic conductivity of up to 15,000 – 20,000 S/cm, higher than all other solution-processed 2D materials [226], [246]. Additionally, MXenes are produced using a top-down selective etching procedure which is highly scalable compared to the bottom-up techniques such as physical and chemical vapor deposition required to synthesize many other nanomaterials [231]. Additional background on MXenes can be found in Section **4.2** of this thesis.

In this work, we demonstrate a new class of flexible, multichannel, high-density bioelectronic interfaces – which we have named "MXtrodes" – that are capable of both high-fidelity recording and effective stimulation of neural and neuromuscular circuits at multiple scales. The key value of the work presented here rests on a series of advances: first, we leverage the excellent processability of Ti_3C_2 MXene to develop a rapid, low-cost, and highly scalable method for fabricating multichannel electrode arrays of arbitrary size and geometry. This process is conducive to industrial manufacturing, and paves the way for translating MXene bioelectronics into clinical and consumer markets. Second, we report the first comprehensive study of the electrochemical properties of Ti_3C_2 relevant for recording and stimulation of bioelectric circuits. We show that the electrochemical behavior of Ti_3C_2 is comparable, and in many aspects superior to, conventional bioelectronic materials, especially

in the context of delivering charge for safe and effective electrical stimulation. Third, we demonstrate the utility of MXtrodes for mapping and modulating excitable networks at scales ranging from large neural and muscular circuits in humans to small animal models. In particular, we show gel-free multichannel arrays for large-scale human epidermal recording with electrode-skin interface impedance and recording quality comparable to larger, commercially available pre-gelled Ag/AgCl single contact electrodes. Furthermore, we demonstrate the ability of MXtrodes to finely map clinically relevant neural and neuromuscular activation patterns at high spatial and temporal resolution – which is elusive for conventional epidermal sensors – and to deliver effective electrical stimulation. Fourth, we experimentally characterize the compatibility of Ti_3C_2 with clinical imaging modalities and we demonstrate that MXtrodes minimally interact with magnetic fields and X-rays, resulting in artifact-free high-field MRI and computed tomography (CT) imaging. This finding opens up new and exciting opportunities for future research and clinical paradigms combining high temporal resolution electrophysiology with advanced functional imaging. Propelled by the unique properties of Ti_3C_2 and the high-throughput, scalable, and cost-effective fabrication process developed here, MXtrodes show great promise for numerous applications in healthcare, research, and wearable electronics.

5.2 Rapid, low-cost manufacturing of MXtrodes

We developed a simple method for producing the MXtrode arrays involving 1) laser-patterning a porous absorbent substrate, 2) infusing it with a water-based Ti_3C_2 MXene ink, and 3) encapsulating the resulting conductive composite in flexible elastomeric films. For the various applications demonstrated in this work, we fabricated two types of electrodes by slightly varying the same basic process: 1) flat or planar electrodes for gel-free epidermal sensing and for epicortical brain recording and stimulation, and 2) 3D “mini-pillar” electrodes for gel-free electroencephalography (EEG). The versatility of our fabrication process allows addressing application-specific requirements and customizing the electrodes to the structures of interest: while for epidermal and cortical recording flat planar electrodes achieve adequate tissue coupling, gel-free EEG requires 3D components to overcome the hair barrier and make contact with the scalp. The fabrication process, with both variations, is

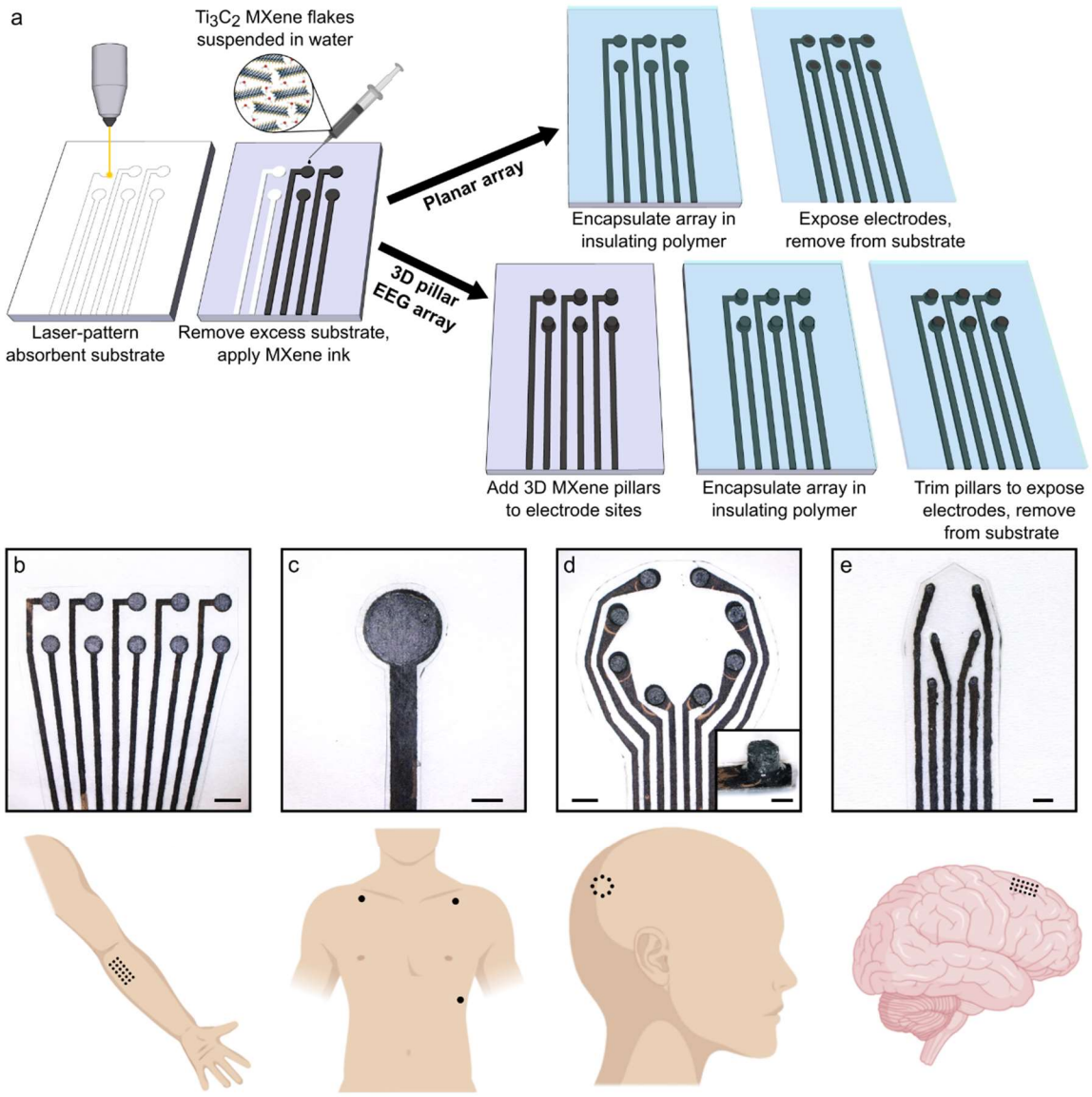

Figure 5.1 Rapid, high-throughput manufacturing of MXene ink-infused bioelectronics: MXtrodes. (a) Schematic of the fabrication method for laser-patterned planar and 3D mini-pillar MXene electrode arrays. (b)-(e) Photographs of different electrode array geometries (top) with their intended bioelectronic applications (bottom): (b) EMG, (c) ECG, (d) EEG, and (e) ECoG monitoring. Scale bars: (b)-(d) 5 mm; inset in (d) and (e) 2 mm.

depicted in **Figure 5.1a**. Briefly, we used a CO_2 laser to pattern a nonwoven, hydroentangled cellulose-polyester blend substrate into the desired electrode array geometry. This served as a scaffold for the MXene flakes, with the laser patterning process allowing for rapid prototyping and customization of the array geometry. Next, we infused the cellulose-

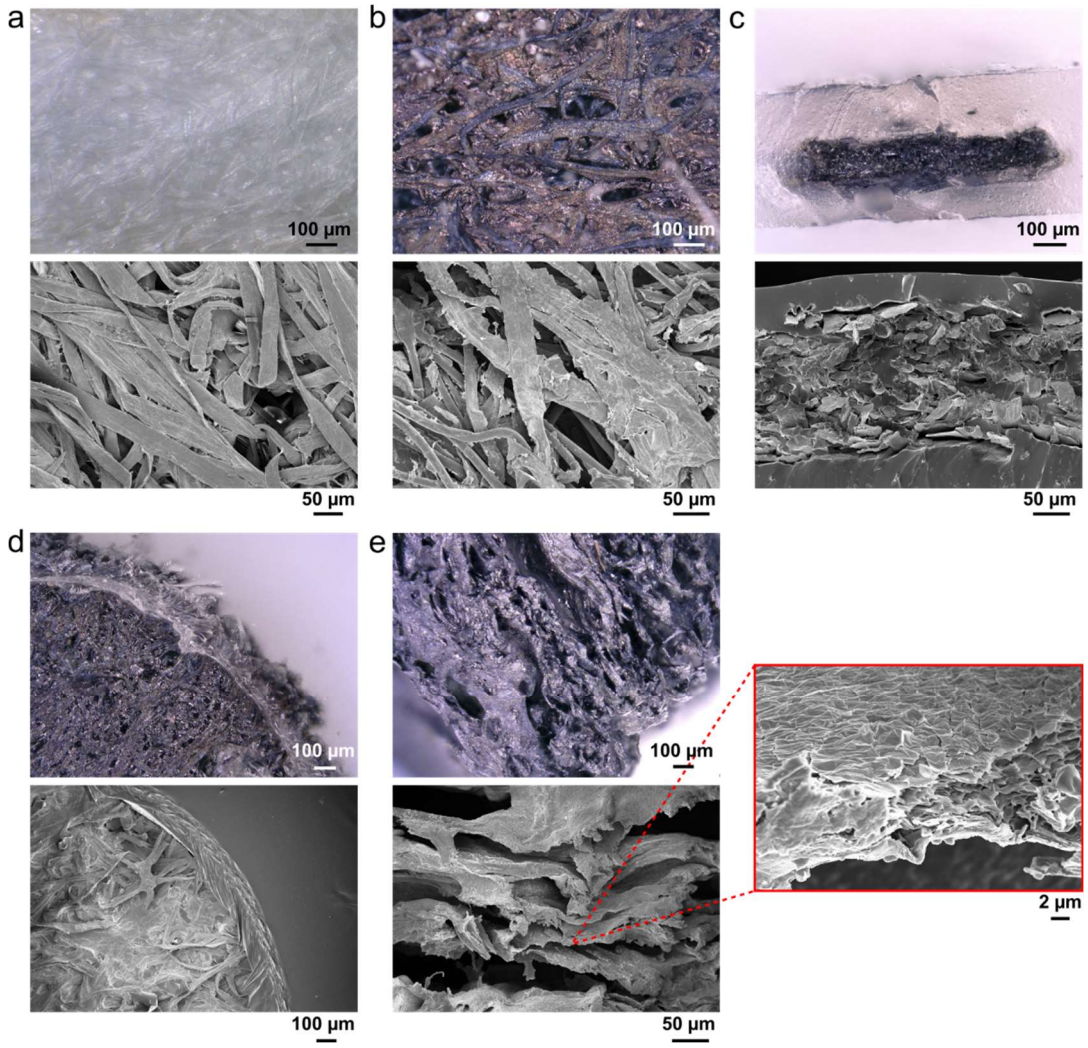

Figure 5.2 Optical and SEM images of MXtrode composites. Optical microscopy images (top panel) and corresponding SEM images (bottom panel) for: (a) pristine cellulose/polyester blend substrate, (b) the same substrate after infusing with MXene ink, (c) cross-section of MXene composite trace embedded in PDMS, (d) edge of planar electrode contact, (e) side of MXene-infused cellulose foam in 3D mini-pillar MXtrode.

polyester substrate with MXene ink, which was prepared by a minimally intensive layer delamination (MILD) method[232] to produce a water-based MXene ink with a concentration of 30 mg/mL. The ink quickly wicked into the absorbent substrate, coating all the fibers. The ink-infused substrates were then thoroughly dried in a vacuum oven for 1 h at 70°C and 60 mmHg. The resulting structure was a rough, macro-porous conductive composite, with MXene flakes coating the individual fibers in the textile matrix (**Figure 5.2a,b**). For the planar

MXtrode arrays, the MXene conductive composite was then encapsulated in ~1 mm-thick layers of polydimethylsiloxane (PDMS), with a thorough degassing step prior to curing that allows the PDMS to infiltrate into the conductive matrix (**Figure 5.2c**). Electrode contacts were defined by cutting through the top encapsulation layer with a biopsy punch of the desired electrode diameter and peeling up the resulting PDMS disk to expose the conductive MXene composite beneath (**Figure 5.2d**). In the planar MXtrode arrays for cortical recording and stimulation, an additional 1 μm-thick layer of parylene-C was deposited prior to opening

Figure 5.3 Scalable fabrication of MXtrode arrays. (a) Photo of laser-patterned array substrates for various device and array geometries. (b) The same batch of devices shown in a after infiltrating with MXene ink. In the top left are shown the EEG ring MXtrode arrays after addition of the 3D mini-pillars. (c) Photographs of completed devices (from left to right) designed for ECG, ECoG, EMG, and EEG sensing.

the electrode contacts to serve as an additional barrier to moisture. To fabricate 3D MXtrode arrays for gel-free EEG recording, "mini-pillars" of MXene-infused cellulose foam were deposited onto the electrode locations prior to PDMS encapsulation. Similar to the absorbent cellulose-polyester substrate, the cellulose foam readily absorbed the MXene ink, which thoroughly coated all surfaces to form a porous conductive composite after vacuum drying (**Figure 5.2e**). It is worth noting that no adhesive was required to affix the 3D mini-pillars to the underlying laser-patterned substrate: inking the two structures simultaneously with MXene and vacuum drying them while in contact resulted in the formation of a continuous conductive network fusing the laser-patterned substrate and the cellulose foam together. The final steps of the 3D MXtrode array fabrication involved PDMS encapsulation and manual trimming of the mini-pillars to expose the conductive MXene-cellulose foam composite. The versatility, simplicity, scalability, and low cost of this process enabled parallel fabrication of MXtrodes in a variety of geometries for diverse bioelectronic applications, even within the same batch (**Figure 5.1b-e**, **Figure 5.3**).

5.2 Electrical and electrochemical properties of MXtrodes

5.2.1 DC conductivity

In the MXtrode arrays, the MXene-cellulose-polyester conductive composite forms the wires which carry the signal out to the recording amplifier. Thus, it is important that this composite is highly conductive in order to reduce Ohmic losses, minimize noise, and acquire high-quality signals. We measured the bulk conductivity of the MXene composites and determined it to be 3015 ± 333 S/m (**Figure 5.4**) which is in agreement with previously reported values for MXene-coated cellulose fibers [315]. To highlight the conductivity advantage of Ti_3C_2 MXene compared to other conductive inks – which could in principle be used in our fabrication process – we also fabricated conductive composites using PEDOT:PSS and rGO inks with the same cellulose-polyester absorbent substrate. The bulk conductivity of

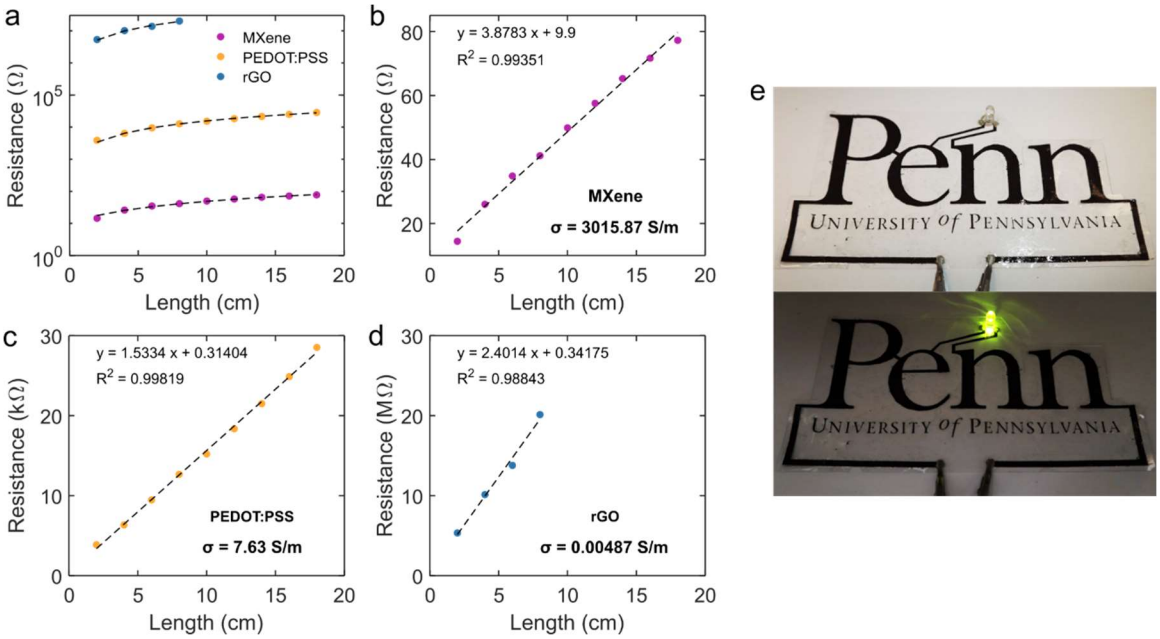

Figure 5.4 DC conductivity of ink-infused composites. (a) Plot of length vs. DC resistance for composites made using MXene, PEDOT:PSS, and rGO as the conductive ink. Test structures were 20 cm x 3 mm x 285 µm (L x W x H) strips. (b)-(d) Individual plots of DC resistance vs. length for (b) MXene, (c) PEDOT:PSS, and (d) rGO, with linear fitting curves shown as dashed lines. The linear relation of resistance vs. length, along with the cross-sectional area of the test structure, is used to compute the bulk conductivity, σ, of the composites. DC resistance of the rGO composite could only be measured out to 8 cm due to high resistance. (e) Demonstration of exceptional conductivity of the MXene composite here used as conductive trace to power an LED.

PEDOT:PSS and rGO composites was 7.6 ± 0.4 S/m and 0.005 ± 0.002 S/m, respectively, both significantly lower than MXene.

5.2.2 Electrochemical properties in saline and their scaling relations

To evaluate the impedance and charge transfer properties of MXene electrodes and compare them with other common bioelectronic materials, we conducted electrochemical measurements on MXtrodes with diameters ranging from 500 μm to 3 mm and compared them to 2.3 mm-diameter clinical Pt electrodes. Specifically, we performed electrochemical impedance spectroscopy (EIS), cyclic voltammetry (CV) and voltage transient (chronopotentiometry) experiments to measure the impedance magnitude, charge storage capacity (CSC), safe voltage window, and charge injection capacity (CIC) of each electrode, and to determine how these properties scale with electrode diameter.

Data are shown in **Table 5.1**, along with additional comparisons to other common electrode materials from literature. EIS revealed that the MXtrodes of all diameters tested showed significantly reduced impedance compared to the Pt electrodes at frequencies below 500 Hz – where impedance is dominated by the electrochemical properties of the electrode interface [321] and where most physiologic signals of interest lie (**Figure 5.5a**). At 10 Hz, the impedance of the MXtrodes ranging from 500 μm to 3 mm was 1343.3 ± 81.6 Ω (500 μm), 644.2 ± 97.3 Ω (1 mm), 451.2 ± 35.4 Ω (2 mm), and 241.4 ± 14.7 Ω (3 mm), while the impedance of the Pt electrodes was 8838.3 ± 1154.2 Ω (2.3 mm). At the reference frequency of 1 kHz – where the interface impedance is controlled by the solution resistance and electrode size [321] – the impedance of similar-sized MXtrodes is comparable to, and in some cases lower than, Pt and other bioelectronic materials like PEDOT:PSS (**Figure 5.5a** and **Table 5.1**). The 1 kHz impedance values can be found in **Table 5.1**. We attribute the exceptionally low impedance of the MXtrodes to the highly porous and rough morphology of the electrodes, which endows the interface with a high effective surface area.

The safe voltage window for MXtrodes determined from wide-scan CVs is −1.8 – +0.6 V (**Figure 5.6a,b**), showing that MXene is exceptionally stable in the cathodic region, with hydrolysis beginning at −1.9 V. This wide safe potential range is advantageous for therapeutic electrical stimulation applications, and while the safe anodic potential limit (+0.6 V) is slightly

Table 5.1 Electrochemical properties in saline. Summary of electrochemical properties of MXtrode planar electrodes of varying diameters, compared to a 2.3 mm-diameter Pt electrode and to literature values for other electrode materials.

Material	Geometric Surface Area (mm^2)	1 kHz |Z| (Ω)	Potential Limits vs. Ag/AgCl (V)	CSC_C ($mC\ cm^{-2}$)	CIC_C ($mC\ cm^{-2}$)	Source
MXtrode (Ti_3C_2 composite)	7.069	205.6 ± 11.1	-1.8 – 0.6	233.1 ± 19.6	0.55 ± 0.10	This work
	3.142	369.2 ± 40.2	-1.8 – 0.6	392.3 ± 9.8	0.69 ± 0.03	This work
	0.7854	430.2 ± 86.1	-1.8 – 0.6	604.8 ± 61.4	1.07 ± 0.07	This work
	0.1963	729.2 ± 71.2	-1.8 – 0.6	1024.1 ± 3.0	2.12 ± 0.48	This work
Pt	4.155	287.3 ± 7.8	-0.6 – 0.8	4.3 ± 0.2	0.07 ± 0.003	This work
Pt	3.142	1910 [a]	-0.6 – 0.8	3.6 [a]	0.17 [a]	[316], [317]
Au	3.142	470 [a]	-0.9 – 0.6	0.3 [a]	0.21 [a]	[316], [317]
PEDOT:PSS on Pt	3.142	1690 [a]	-0.9 – 0.6	2.3 [a]	0.18 [a]	[316], [317]
PEDOT: PSS on Au	3.142	430 [a]	-0.9 – 0.6	1.0 [a]	0.86 [a]	[316], [317]
Pt	0.1963	7790 [a]	-0.6 – 0.8	5.1 [a]	0.50 [a]	[316], [317]
Au	0.1963	4430 [a]	-0.9 – 0.6	0.3 [a]	0.21 [a]	[316], [317]
PEDOT:PSS on Pt	0.1963	2110 [a]	-0.9 – 0.6	3.7 [a]	0.66 [a]	[316], [317]
PEDOT:PSS on Au	0.1963	990 [a]	-0.9 – 0.6	1.5 [a]	1.35 [a]	[316], [317]
laser-roughened Pt	0.7854	760 [a]	-0.6 – 0.8	2.1 ± 0.1	0.026 [a]	[123]
PEDOT/CNT coating on Pt	0.0314	2100 [a]	-0.6 – 0.7	70	2.5 ± 0.1 [a]	[318]
Porous graphene (doped)	0.09	519	-1.3 – 0.8	50	3.1	[16]
CNT fiber	0.00145	11.2 ± 7.6 $x10^3$	-1.5 – 1.5	372 ± 56 [b]	6.52	[133]
TiN	0.004	11.5 $x10^3$ [a]	-0.9 – 0.9	2.47	0.55	[319]
IrOx	0.004	7.1 $x10^3$ [a]	-0.6 – 0.8	11	4	[319]
PtIr	5.985	125	-0.7 – 0.7	5.0	–	[320]

[a] Represents values extracted from plots from the respective references.
[b] CSC calculated from CV in Pt window, -0.6 – 0.8 V at 100 mV/s.

lower than that of Pt, PtIr, or IrOx (+0.8 V), stimulation waveforms can be engineered to minimize voltage excursions in the anodic range while taking advantage of the large cathodic limit [60], [322], [323]. While previous studies have reported anodic oxidation of Ti_3C_2 films at +430 mV [324], we observed no oxidation peak and negligible current loss when MXtrodes were cycled within the range of −1.8 – +0.6 V. We attribute the improved anodic stability to the rough surface morphology of the MXtrodes, resulting in decreased current density. In the

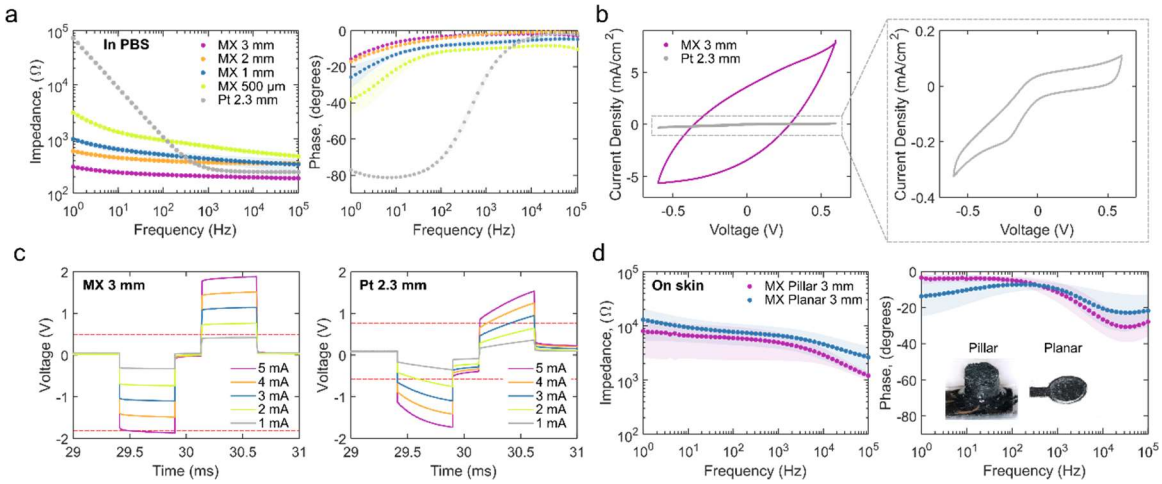

Figure 5.5 Electrochemical properties of MXtrodes. (a) EIS spectra measured in 1X PBS for 3 mm, 2 mm, 1 mm, and 500 µm planar MXene electrodes compared to 2.3 mm Pt electrodes. (b) CVs for 3 mm planar MXtrode and 2.3 mm Pt electrodes scanned from −0.6 – +0.6 V at 50 mV/s. (c) Voltage transients in response to biphasic current pulses, with t_c = t_a = 500 µs and t_{ip} = 250 µs, current amplitudes ranging from 1 to 5 mA for 3 mm planar MXtrode and 2.3 mm Pt electrodes. Anodic and cathodic voltage limits for MXene and Pt are displayed on their respective plots as dashed red lines. (d) EIS spectra measured on skin for 3 mm MXtrode 3D pillar and planar electrodes.

cathodic region, the 1 mm, 2 mm, and 3 mm MXtrodes showed stable capacitive behavior down to −1.8 V, however the 500 µm-diameter MXtrode showed initial evidence of faradaic current near this negative limit (**Figure 5.6c**) likely due to size effects. Still, the 500 µm-diameter MXtrode showed stable behavior through repeated CV cycles and no evidence of hydrolysis, confirming −1.8 V as a reasonable cathodic limit.

Analysis of cathodal CSC (CSC_C) for MXtrodes and Pt electrodes from CVs at 50 mV/s within their respective water windows reveals enhanced capacitive charging and charge delivery properties for MXtrodes with ~100 times larger CSC_C than Pt electrodes and other common materials such as PtIr and PEDOT:PSS (**Figure 5.6c,d**, **Table 5.1**). To enable a more direct comparison of CSC_C values between MXtrodes and Pt electrodes, we also ran CV scans in the intersection of the MXene and Pt voltage windows, −0.6 – +0.6 V (**Figure 5.5b**, **Figure 5.6d**, and **Table 5.2**). Even in this more constrained voltage range, the MXtrodes showed more than 20 times enhanced CSC_C compared to Pt, which we attribute both to the exceptionally high intrinsic capacitance of Ti_3C_2 MXene [18], [21], [325] and to the high effective surface area of the MXtrode surface. The scaling dependency of CSC_C on the electrode diameter for the MXtrodes is shown in **Figure 5.6e**. The non-linear relationship between CSC_C

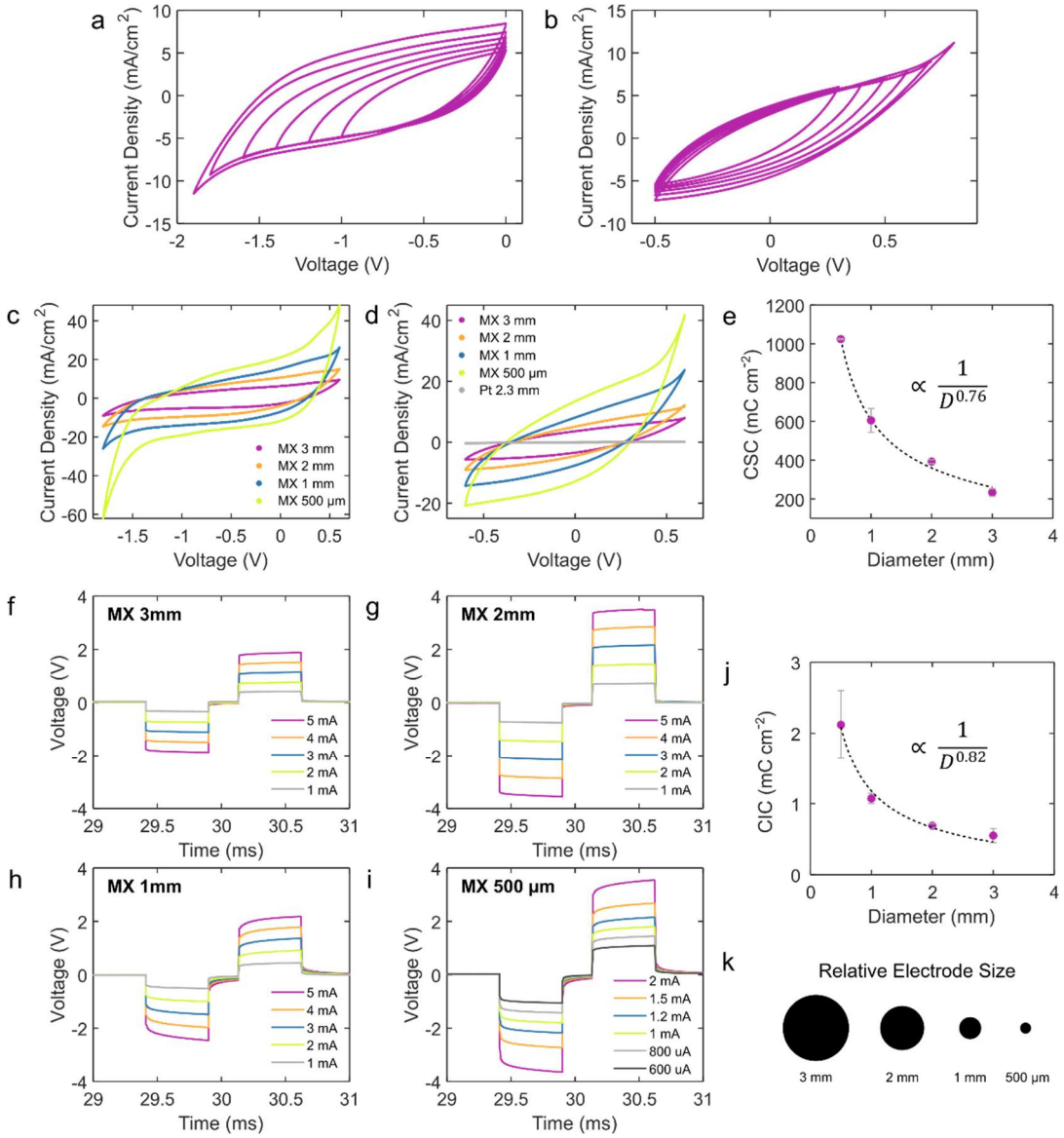

Figure 5.6 Scaling of electrochemical properties in saline. (a) CVs probing the negative voltage limit for MXene at 50 mV/s. Hydrolysis of water begins at −1.9 V. (b) CVs probing the positive voltage limit for MXene. Current loss and evidence of faradaic current begins at +0.7 V. Test electrode for (a) and (b) was 3 mm-diameter planar MXene. (c) CVs in MXene safe voltage window, −1.8– +0.6 V, for 3 mm, 2 mm, 1 mm, and 500 µm-diameter MXtrodes. (d) CVs in MXene-Pt intersection window, −0.6 to +0.6 V, for 3 mm, 2 mm, 1 mm, and 500 µm-diameter planar MXtrodes and 2.3 mm-diameter Pt electrode. (e) Charge storage capacity of scaled planar MXtrodes as a function of diameter, highlighting the CSC scaling dependence on the electrode diameter, due to edge effects. CSC values were calculated for CVs in MXene water window. (f)-(i) Voltage transients for biphasic current pulses, with $t_c = t_a = 500$ µs and $t_{ip} = 250$ µs, for currents ranging from 1 to 5 mA for (f) 3 mm, (g) 2 mm, (h) 1 mm, and (i) 500 µm-diameter planar MXene electrodes. (j) Charge injection capacity of scaled planar MXtrodes as a function of diameter, highlighting the CIC scaling dependence on the electrode diameter, due to edge effects. (k) Schematic demonstrating the relative electrode sizes used in the study.

Table 5.2 CSCc values in different voltage windows. CSC_C values for planar MXtrodes of varying diameters and the comparison clinical Pt ECoG electrode. CV scans were performed at 50 mV/s for each electrode in both its safe voltage window and the intersection of the MXene and Pt voltage windows.

Material	Electrode diameter	CSC_C (mC cm^{-2}) MXene window: -1.8 – 0.6 V	CSC_C (mC cm^{-2}) Intersection: -0.6 – 0.6 V	CSC_C (mC cm^{-2}) Pt window: -0.6 – 0.8 V
MXtrode (Ti_3C_2 composite)	3 mm	233.1 ± 19.6	80.9 ± 8.9	N/A
	2 mm	392.3 ± 9.8	118.6 ± 10.1	N/A
	1 mm	604.8 ± 61.4	188.5 ± 28.4	N/A
	500 µm	1024.1 ± 3.0	288.7 ± 1.7	N/A
Pt	2.3 mm	N/A	4.0 ± 0.2	4.3 ± 0.2

and electrode diameter is expected, and reflects the known phenomenon of electrochemical charge exchange happening predominantly at the edge of the electrode [60], [317].

Finally, we measured the voltage transients evolved on each electrode when used to deliver charge-balanced, cathodal-first biphasic current pulses ranging from 1 to 5 mA with a duration of 500 µs in both phases (t_c, t_a) and an interpulse interval (t_{ip}) of 250 µs (**Figure 5.5c** and **Figure 5.6f-i**). For the 500 µm-diameter MXtrode, the current amplitude range was restricted to 600 µA – 2 mA. The maximum cathodal excursion potential, E_{mc}, was taken 10 µs after the cathodal pulse end and CIC_C was defined as the injected charge at which E_{mc} would reach the water reduction potential. The resulting CIC_C values, shown in **Table 5.1**, reveal that the MXtrodes significantly outperform Pt electrodes, with MXtrodes showing ~10 times larger CIC_C than the Pt electrodes. Furthermore, we found a similar ~10 times improvement in CIC_C when we compared MXtrodes to other common electrode materials (**Table 5.1**). This result has significant implications for stimulation applications, and suggests that MXtrodes may offer more efficient charge transfer than current state-of-the-art Pt electrodes. This could potentially prolong battery life for implantable simulation systems such as deep brain stimulation (DBS), vagal nerve stimulation (VNS), and cardiac pacemakers. The scaling dependency of CIC_C on electrode diameter for the MXtrodes is shown in **Figure 5.6j**, again revealing the expected non-linear scaling dependency resulting from edge effects. A schematic depicting the relative sizes of the MXtrodes included in the analysis is shown in **Figure 5.6k**.

5.2.3 Electrode-skin interface impedance

While measurements in saline allow comparing the properties of MXtrodes to current standard electrode materials such as Pt, for epidermal sensing applications it is also essential to evaluate the impedance at the interface with human skin. Specifically, achieving low electrode-skin impedance is key for recording high-fidelity signals [326], [327] and becomes particularly challenging in gel-free structures like MXtrodes. Thus, we measured EIS for 3 mm-diameter MXtrodes, both in planar and 3D configurations, on clean human skin following standard preparation with an alcohol swab and light abrasion with 3M Trace Prep tape. At 1 kHz, the planar and 3D MXtrodes showed impedances of 6.6 ± 2.9 kΩ and 4.9 ± 2.6 kΩ, respectively, with the lower impedance of the 3D electrodes attributable to the improved contact from the protruding mini-pillars pressing into the skin (**Figure 5.5d**). When normalized by their geometric surface area (GSA) of 0.071 cm^2, the impedance is 0.47 ± 0.20 kΩ·cm^2 for planar and 0.35 ± 0.12 kΩ·cm^2 for 3D MXtrodes, which are among the best values reported so far for dry, gel-free epidermal electrodes [111], [112], [328] and ~100 times lower than those of commercially available gelled Ag/AgCl electrodes commonly used for electrodiagnostics and monitoring [314].

5.3 Gel-free epidermal sensing in humans

5.3.1 Scalp electroencephalography (EEG)

Motivated by the exceptionally low electrode-skin interface impedance of the dry MXtrodes, we investigated their use in a variety of human epidermal sensing applications, with custom geometries specifically designed for each application. First, we acquired scalp EEG on a healthy human subject using high resolution gel-free MXtrodes and standard gelled Ag/AgCl EEG electrodes for comparison. We designed an 8-channel MXtrode, with 3 mm-diameter 3D mini-pillar electrodes arranged in a ring around a central opening, where we placed a standard 1 cm-diameter gelled Ag/AgCl EEG electrode for side-by-side comparison of simultaneously acquired EEG (**Figure 5.7a**). In the first EEG task, we placed the MXtrode array over the parietal region near EEG site P1 (as defined in the EEG 10-20 system, located over inferior parietal cortex to the immediate left of the midline). The gelled Ag/AgCl EEG

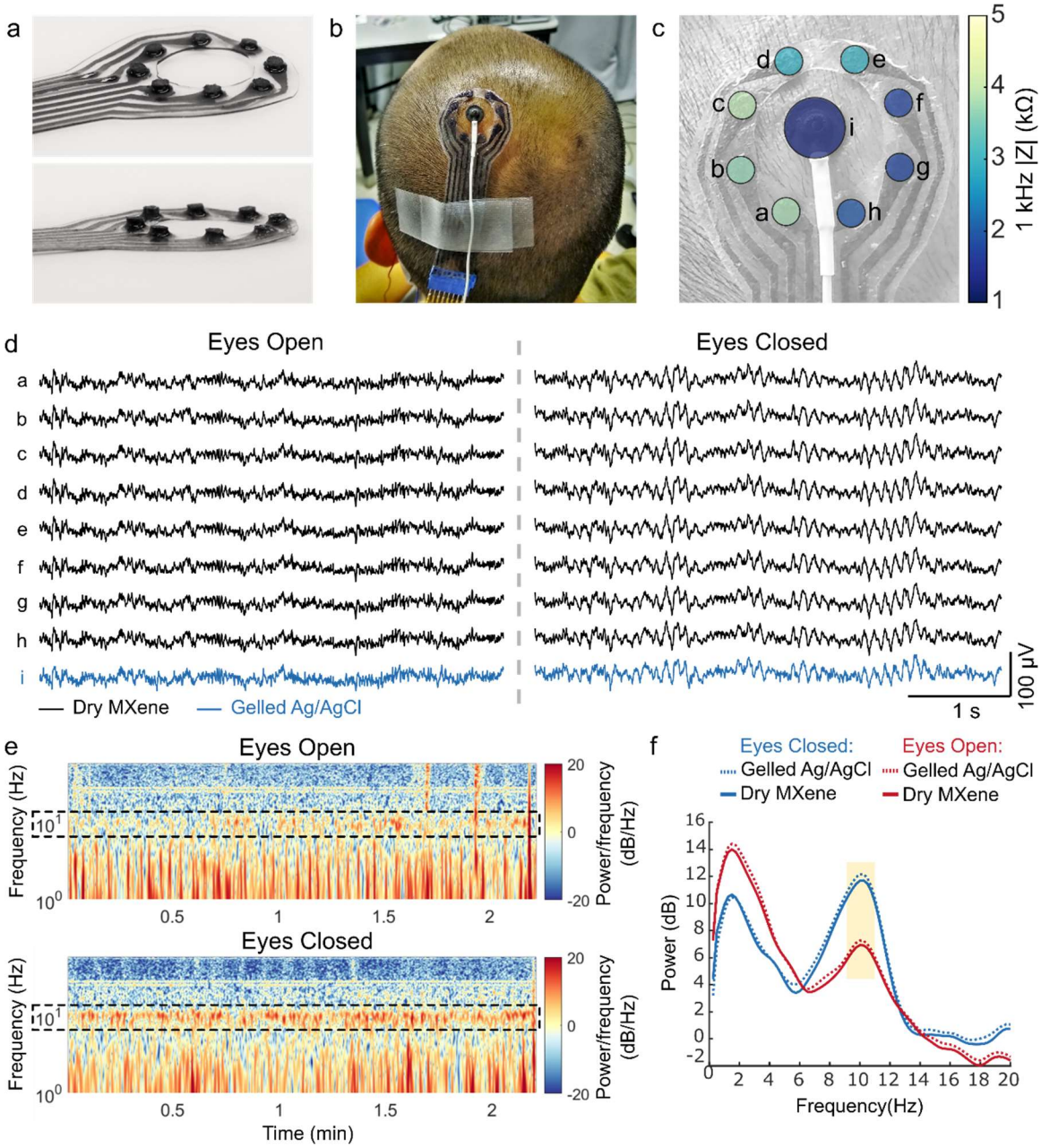

Figure 5.7 Dry EEG recording enabled by 3D pillar MXtrodes. (a) Images of a MXtrode 3D EEG array with eight 3 mm-diameter MXene electrodes in a circular arrangement around a central opening. (b) Image of MXtrode electrode array and standard gelled Ag/AgCl cup electrode placed on head of human subject. (c) Map of 1 kHz impedance values for all electrodes on the subject's head. (d) Segments of recorded EEG signal from all electrodes during the eyes open (left) and eyes closed (right) tasks at resting state. (e) Spectrograms of the EEG signal recorded on MXene electrode b in the eyes open (top) and eyes closed (bottom) conditions. Alpha frequency band is enclosed in dashed box to highlight differences between eyes open and eyes closed states. (f) Power spectral density during eyes open and eyes closed EEG recordings. The 8-12 Hz alpha band is highlighted.

electrode was placed in the center of the MXtrode ring (**Figure 5.7b**). Ground and reference for all EEG recordings were gelled Ag/AgCl electrodes placed at the center forehead and left mastoid, respectively. The slightly lateralized recording position was chosen because the subject had the shortest hair at that location (~5 mm). Before placing the electrodes on the skin, the entire recording area was cleaned with an alcohol swab and lightly abraded with 3M Trace Prep tape. Notably, we found that the electrode-skin interface impedance at 1 kHz for the dry MXtrodes was 2.8 ± 0.9 kΩ, while the impedance of the larger gelled Ag/AgCl electrode during the same experiment was 1.2 kΩ at 1 kHz (**Figure 5.7c**). Given the critical role of the electrode-skin interface impedance in determining the quality of scalp EEG signals [329], most standard EEG electrodes require conductive gels at this interface, as well as a large contact area of at least ~1 cm^2 to achieve suitably low impedance (e.g., less than 5 kΩ) [330]. Due to their enhanced material and surface area properties, our mm-scale, gel-free MXtrodes can achieve strikingly low impedance, which enables high-resolution EEG recording. We recorded EEG in 2 min sessions, with the subject alternating between a resting state with the eyes closed and a resting state with the eyes open and fixating on a target. In both tasks, the EEG signal recorded on the dry MXtrodes was indistinguishable from the signal recorded on the gelled Ag/AgCl electrode (**Figure 5.7d**). Additionally, a clear 10 Hz alpha rhythm emerged in the eyes closed state with a significantly higher amplitude than in the eyes open condition (**Figure 5.7e-f**). This alpha signature is one of the most reliable and widely studied behaviorally-linked EEG signatures in human subjects research [331], and arises from endogenous thalamic input to the visual cortex in the absence of visual input (i.e. when the eyes are closed) [332]. During the recording session, there was no significant difference between the alpha bandpower on the gelled Ag/AgCl electrode and any individual dry MXtrode, confirming that the signals were comparable between the electrode types (**Figure 5.8**). Interestingly, when alpha bandpower values were calculated in 1 s windows with 0.5 s of overlap and observed sequentially, distinct spatiotemporal patterns of alpha activation emerged even across the small sampled scalp area. MXtrodes could be spaced much closer than they were in the ring configuration we used in this experiment, however the density we tested already approximates or exceeds the densest configurations of traditional Ag/AgCl

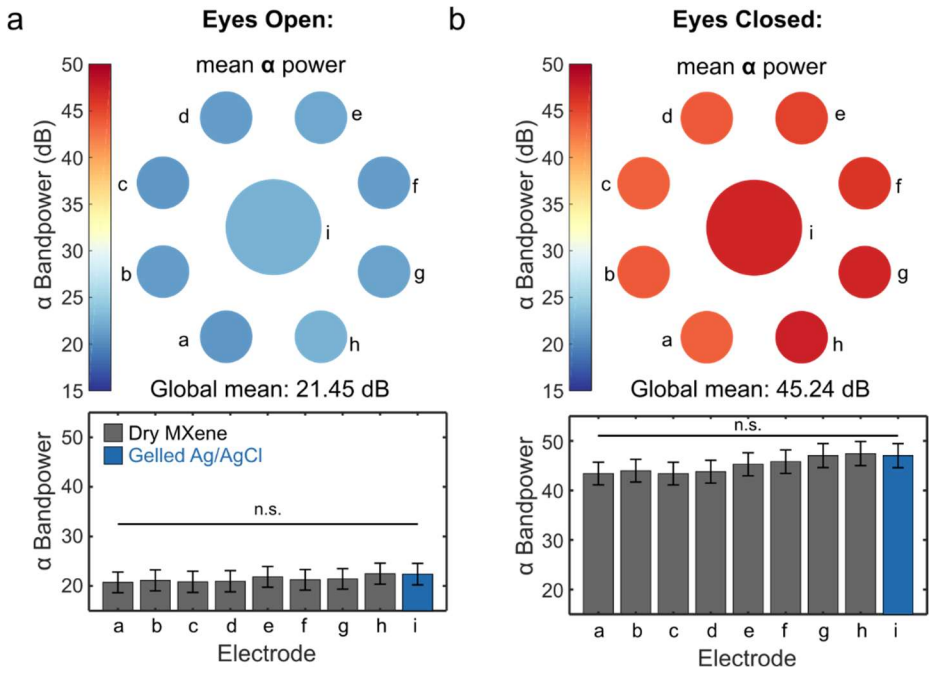

Figure 5.8 EEG alpha bandpower mapping. (a) 8-12 Hz alpha bandpower across the 2 min recording in the eyes open state. Color plot (top) shows average alpha power for each electrode, mapped to its corresponding location on the scalp. Bar plot (bottom) shows average alpha power, with error bars corresponding to standard error of the mean across all time windows. No significant difference was detected between the gelled Ag/AgCl electrode (labelled i) and the dry MXtrode electrodes (labelled a-h). (b) The same alpha bandpower analysis shown in (a), for the eyes closed task.

electrodes in common use today (the 10-5 system). This highlights the potential of mm-scale, gel-free MXtrodes to enable ultra high-density EEG mapping.

For the second EEG task, the electrodes were removed and replaced at site C3 near the hand motor area. The precise location of the hand motor area was determined using single pulses of transcranial magnetic stimulation (TMS) to evoke lateral finger movements, and the electrodes were centered over this location (**Figure 5.9a**). The subject performed 2 min periods of imagined and actual hand flexion while the EEG was recorded simultaneously with the co-located MXtrodes and gelled Ag/AgCl electrode. During this motor task, we also found that the EEG signal was indistinguishable between the two electrode types. Furthermore, we observed a suppression of the 8–12 Hz motor mu rhythm during the actual hand flexion relative to the imagined hand flexion (**Figure 5.9b**). The mu suppression signature during imagined hand movement is an important EEG feature which has been successfully used as a control signal for EEG-based brain-computer interfaces (BCIs) [333],

[334]. Together, the results of these EEG experiments confirm that mm-scale, gel-free MXtrodes can record EEG signal at least as well as standard gelled Ag/AgCl EEG electrodes, while also improving spatiotemporal resolution for high-density EEG applications. Furthermore, the application of MXtrodes to the scalp is faster and easier than standard Ag/AgCl electrodes and leaves no residue on the head. This positions MXtrodes to dramatically lower the effort of conducting EEG experiments, and to expand the use of high-fidelity EEG to environments outside the laboratory.

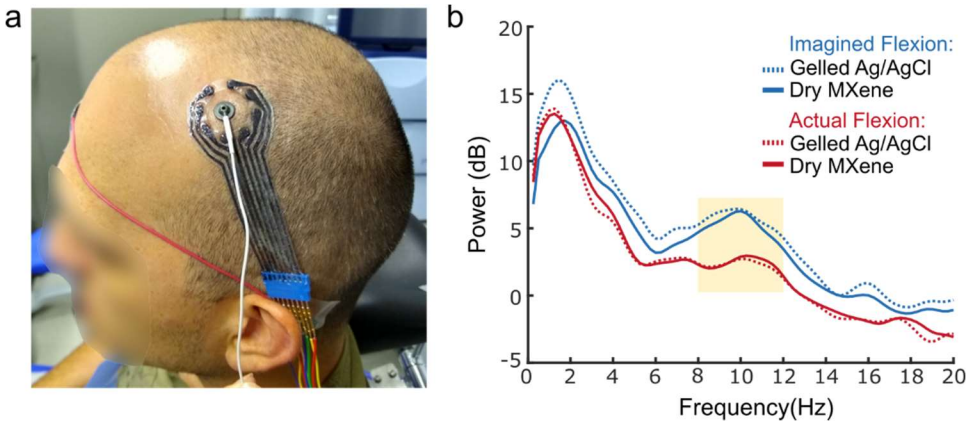

Figure 5.9 Motor EEG recording. (a) Photograph of the EEG recording setup with electrodes centered over the hand motor region, as localized with single TMS pulses. (b) PSDs of the recorded EEG signal reveal a suppression of the 8-12 Hz motor mu rhythm during actual hand flexion as compared to imagined hand flexion.

5.3.2 High-density surface electromyography (HDsEMG)

Next, we evaluated MXtrodes for high-density surface electromyography (HDsEMG) recording, muscle activation mapping and localization of the of innervation zones (IZs). HDsEMG is attracting growing interest for a number of applications in neuromuscular diagnostics and rehabilitation, including control of multifunctional prostheses [120], studies of muscle activation and coordination [335], peripheral nerve/muscle fiber conduction velocity measurements [336], and for accurate localization of neuromuscular junctions (NMJs) to target chemodenervation therapies for muscle spasticity [337], [338]. HDsEMG recordings require flexible, large-area, and high-density electrode arrays capable of covering the wide range of muscle sizes. To demonstrate the versatility of the MXtrode fabrication process, we created custom HDsEMG arrays to map muscle activation and localize IZs in two

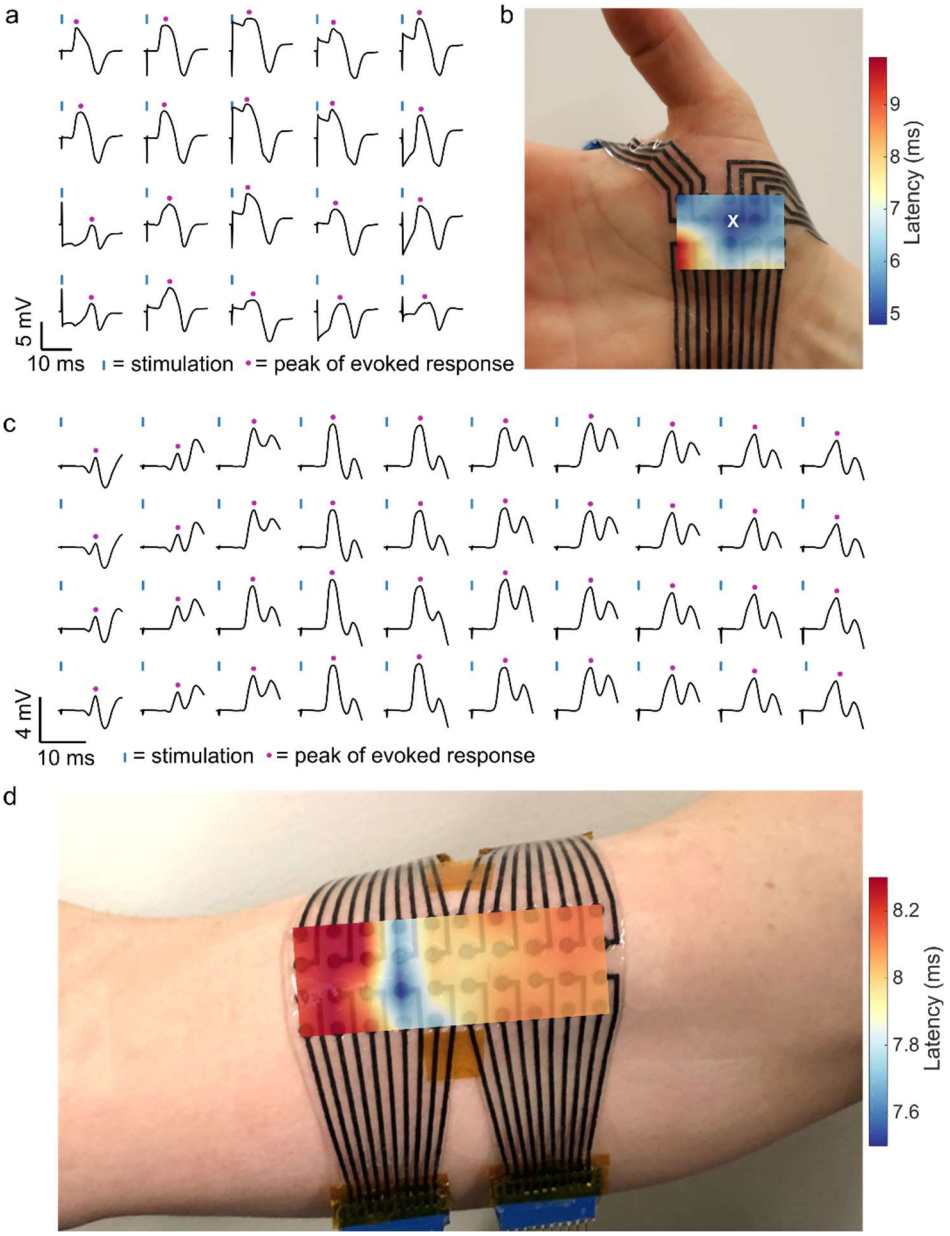

Figure 5.10 High density surface EMG mapping with MXtrode arrays. (a)-(b) EMG recordings from the APB muscle. (a) Average evoked response following N=10 median nerve stimulation epochs recorded on 20-ch MXtrode array placed over APB. Blue ticks indicate time of nerve stimulation, and purple dots indicate time of peak evoked response. (b) Latency map of peak response overlaid on photo of the MXtrode array on the APB. White "x" indicates the channel with shortest latency, corresponding to the IZ. c-d EMG recordings from the biceps muscle. (c) Average evoked response following N=10 supraclavicular nerve stimulation epochs recorded on 40-ch MXtrode array placed over the biceps. Blue ticks indicate time of nerve stimulation, and purple dots indicate time of peak evoked response. (d) Latency map of peak response overlaid on photo of the MXtrode array on the subject's biceps. Distributed IZ running perpendicular to the muscle is apparent as the band with the shortest latency.

muscle groups of different sizes (**Figure 5.10**). First, we used a 20-ch planar MXtrode array placed over the *abductor pollicis brevis* (APB) at the base of the thumb. In this experiment, the 3 mm-diameter dry MXtrodes had an average electrode-skin interface impedance of 54.6 ± 28.4 kΩ at 1 kHz (**Figure 5.11a**). We then stimulated the median nerve with a handheld bipolar stimulator to evoke APB contractions and recorded the EMG on the MXtrode array. We calculated the mean evoked muscle response across stimulation trials (**Figure 5.10a**) and constructed a latency map of the peak of the evoked response. The location with the shortest latency indicates the location of the IZ, which can be seen overlaid on the subject's hand in

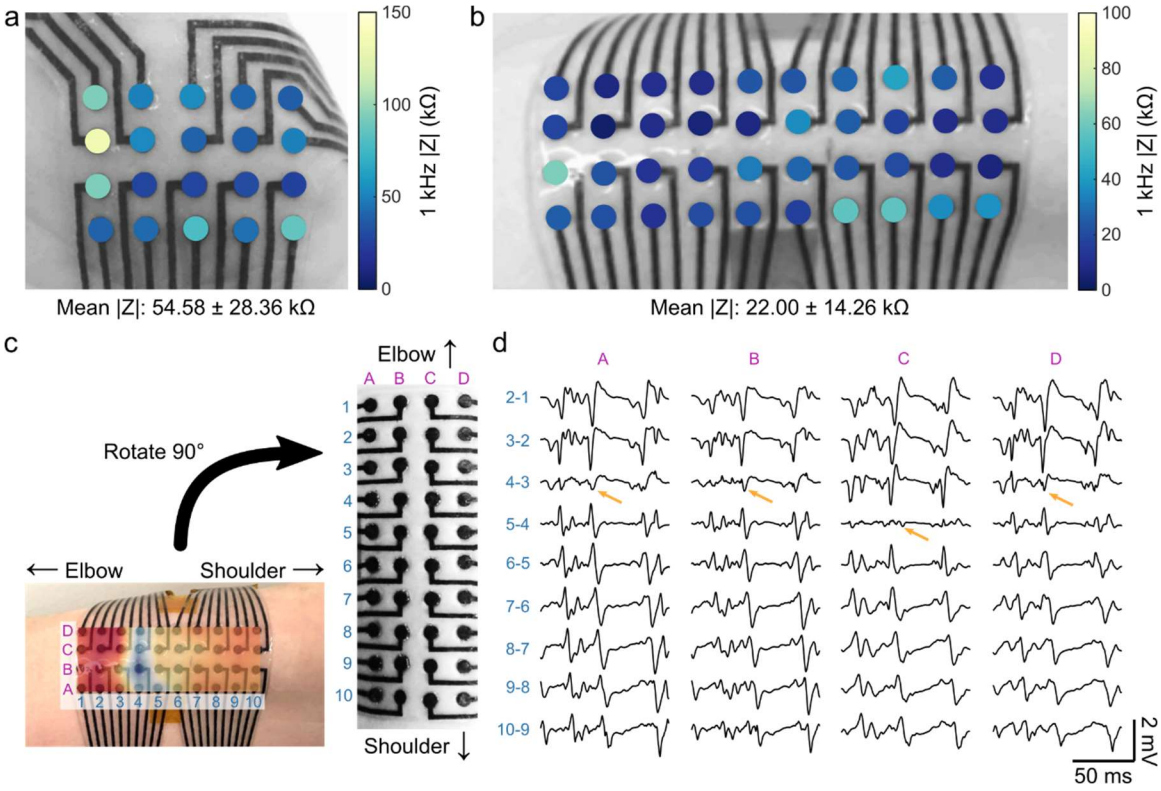

Figure 5.11 Impedance and bipolar subtraction EMG experiment. (a), (b) 1 kHz impedance magnitude maps for the (a) 20-ch planar MXtrode array used to map the APB muscle and the (b) 40-ch planar MXtrode array used to map the biceps, overlaid on images of the arrays on the subject during the experiment. (c) Schematic showing the arrangement for bipolar signal subtraction shown in (d) for resisted flexion EMG recordings on the biceps. The latency map obtained from the supraclavicular stimulation experiment is shown overlaid on the bottom image. (d) Bipolar EMG signals recorded during resisted flexion on the biceps. The location of the innervation zone is indicated by the arrows, and is clear from the propagation of the EMG signal outward from this region with some delay, as well as the inversion of the spikes on either side. The innervation zone determined from this analysis is in agreement with the region identified by the electrical stimulation-derived latency map shown in (c).

Figure 5.10b, and it is in good agreement with expectations based on anatomical landmarks [339].

Following the APB mapping experiment, we mapped the activation of the larger *biceps brachii* with a 40-ch planar MXtrode array. Here, the 3 mm-diameter dry MXtrodes had an average electrode-skin interface impedance of 22.0 ± 14.3 kΩ at 1 kHz (**Figure 5.11b**). Unlike the smaller APB muscle, which has a small and spatially confined IZ corresponding to a single NMJ, the larger *biceps brachii* has distributed NMJs in IZ regions that run perpendicular to the muscle and are typically located near the center [340]. To further confirm the validity of our approach, we used two different methods to localize these IZs in the biceps: first we stimulated the supraclavicular nerve and constructed a latency map of the peak evoked response, similar to the methods described for the APB (**Figure 5.10c,d**). This produced a clear mapping of the IZ location as the region with the shortest latency, running across the short head of the *biceps brachii*. Second, we recorded motor unit action potentials (MUAPs) as the subject performed isometric contractions of the biceps (**Figure 5.11c,d**). In these recordings, bipolar subtraction of the raw EMG signal along the length of the biceps muscle revealed MUAPs that propagated outward in both directions from the IZ, with signal inversion and a clear latency as the MUAP traveled away from the IZ (**Figure 5.11d**). Localization of the biceps IZ obtained from both methods were in excellent agreement with each other, and with previous reports [340]. These results demonstrate that dry, high-resolution MXtrode arrays are capable of mapping muscle activation with high accuracy in order to precisely localize IZs in both small and large muscle groups.

5.3.3 Electrocardiography (ECG)

To demonstrate the applicability of MXtrodes to electrocardiogram (ECG), we acquired ECG recordings on a healthy human subject with 1.3 cm-diameter MXtrodes in a simplified 3-electrode montage as shown in **Figure 5.12a**. For validation and signal comparison, we recorded sequentially from the MXtrodes and from 1 cm-diameter pre-gelled Ag/AgCl electrodes, placed in the same locations. The dry MXtrodes and pre-gelled electrodes had average 1 kHz skin-electrode impedances of 1.29 kΩ and 1.38 kΩ, respectively. On both types of electrodes, characteristic ECG features were clearly visible, with the P wave followed

by the QRS complex and the T wave (**Figure 5.12b,c**). Mean R peak amplitude, however, was slightly higher on the MXtrodes compared to the commercial electrodes: 2.55 ± 0.06 mV vs. 2.47 ± 0.30 mV. Thus, we confirmed that dry MXtrodes can record the ECG with comparable signal quality compared to standard clinical gelled electrodes.

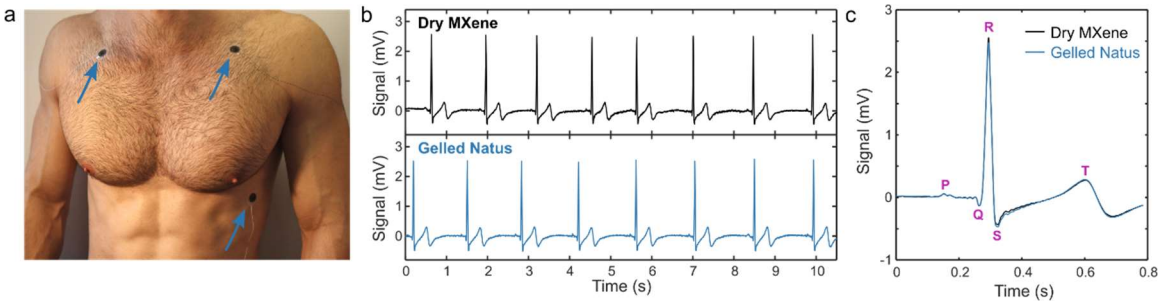

Figure 5.12 Electrocardiography with MXtrodes. (a) Photo of ECG recording setup on human subject. Electrodes were interchanged in the same locations to obtain sequential recordings from either dry MXene or pre-gelled commercial electrodes. (b) Ten seconds of ECG recordings on the dry MXtrodes (top) and the pre-gelled commercial electrodes (bottom). (c) Average ECG waveforms recorded on the two electrode types, marked with salient ECG features.

5.3.4 Electrooculography (EOG)

As a final demonstration of MXtrodes for human epidermal sensing, we acquired electrooculography (EOG), which has applications in ophthalmological diagnosis, BCIs, and for monitoring attention and fatigue [341], [342]. The EOG signal arises from the standing dipole potential between the positively charged cornea and the negatively charged retina, which enables tracking eye movements as this dipole is rotated. With the same 1.3 cm-diameter dry MXtrode geometry used in ECGs, we recorded the EOG in two configurations to track up-down and left-right eye movements (**Figure 5.13**). By placing MXtrodes above and below the eye, recorded voltage fluctuations could be decoded to track the up and down movements of the eye (**Figure 5.13a,b**). Similarly, placing MXtrodes on both sides of the eyes enabled decoding the left-right movements (**Figure 5.13c,d**).

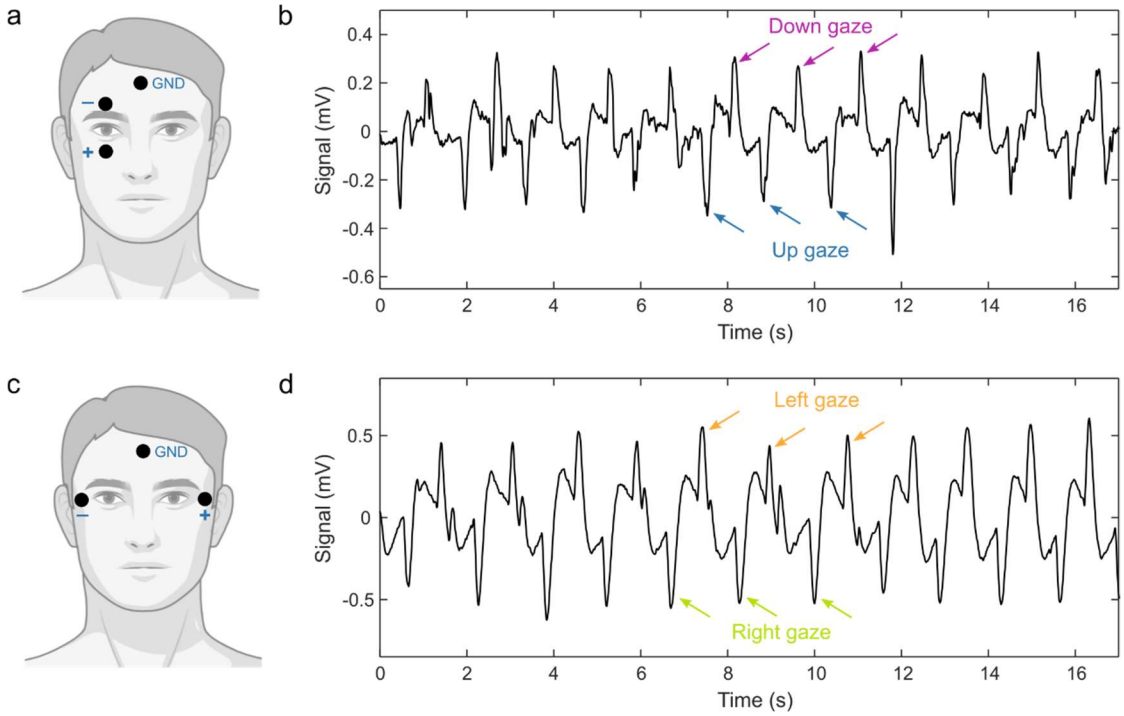

Figure 5.13 Electrooculography with MXtrodes. (a) Schematic of EOG recording for monitoring up-down eye movements. (b) EOG data recorded on MXtrodes, showing distinct up and down eye movements. (c) Schematic of EOG recording for monitoring left-right eye movements. (d) EOG data recorded on MXtrodes, showing distinct left and right eye movements.

5.4 Cortical neural recording and microstimulation in animal models

5.4.1 Intraoperative electrocorticography (ECoG)

Beyond epidermal sensing modalities, the favorable electrochemical interface of the MXtrodes also supports their use for implantable sensing and stimulation applications. One such application is intraoperative electrocorticography (ECoG), a common mapping technique used in resective brain surgery for epilepsy or tumors. We acquired ECoG recordings in an anesthetized swine, a relevant animal model in neuroscience given the gyrencephalic structure and neuro-anatomical similarity of the swine brain to the human brain. In this experiment we inserted a 6-ch array of 500 μm-diameter planar MXtrodes through an 8 mm craniotomy/durotomy and placed MXtrodes in direct contact with the

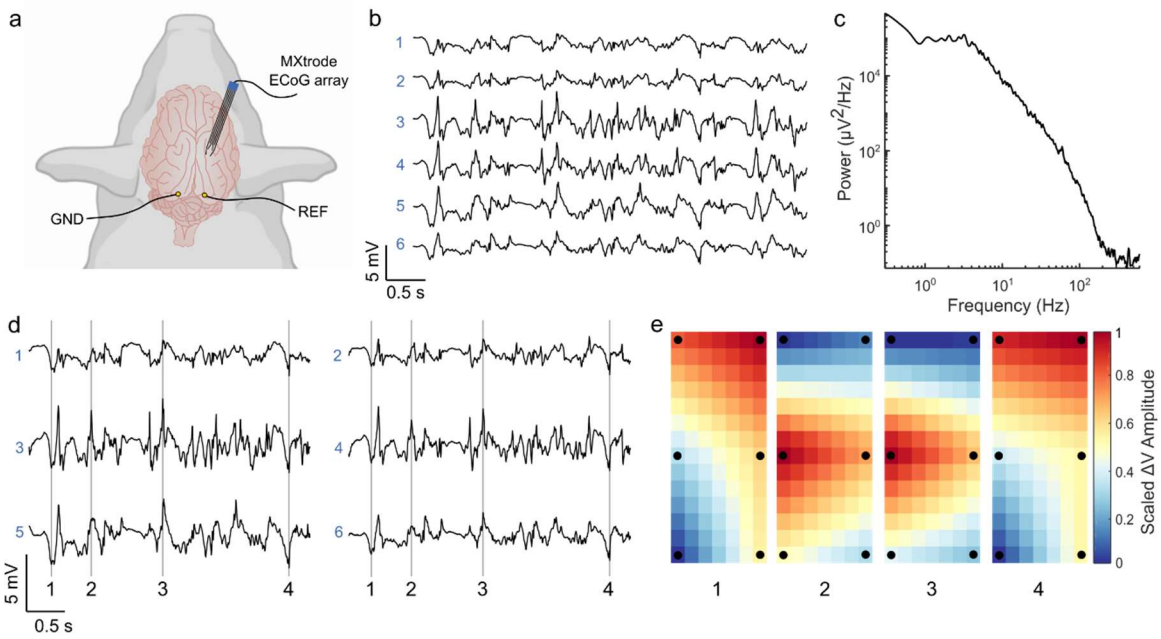

Figure 5.14 ECoG recording with MXtrode arrays in swine brain. (a) Schematic depicting ECoG recording setup with the 6-ch array of 500 μm-diameter MXtrodes placed subdurally on somatosensory cortex. (b) A few seconds of representative ECoG data recorded on the MXtrode array. (c) Power spectral density of the ECoG recording, illustrating the low-noise quality of the ECoG signals obtained, evidenced by the lack of a 60 Hz noise peak. (d) Segment of ECoG data, displayed according to the spatial arrangement of the 6 MXtrodes. (e) Instantaneous snapshots of the voltage mapping recorded across the 6 MXtrodes reveals stereotyped patterns during down states (panels 1 and 4) and up states (panels 2 and 3). The timing of these voltage snapshots is indicated in (e) by the vertical lines. Voltage was interpolated across the array and normalized, with black dots indicating location of the 6 MXtrode contacts.

cortical surface (**Figure 5.14a**). The array configuration consisted of 3 rows of electrode pairs with 5 mm inter-row spacing and 4.5 mm pitch, so that the rows of electrodes spanned several cortical gyri. A few seconds of representative raw ECoG signal are shown in **Figure 5.14b**. The signals were large in amplitude with negligible 60 Hz noise interference, as evidenced by the power spectra (**Figure 5.14c**). Furthermore, maps of interpolated voltage across the MXtrode array revealed stereotyped spatial patterns emerging during the "up" and "down" states in the ECoG signal (**Figure 5.14d,e**), highlighting the advantages and opportunities offered by high-density cortical brain mapping with MXtrodes.

5.4.2 Cortical microstimulation

In addition to ECoG recording, direct stimulation of the cortical surface is used clinically for intraoperative cortical mapping [343] and neuromodulation therapies [344], as well as for closed-loop BCIs [345]. Given that the MXtrodes showed superior CSC and CIC compared to Pt, a material commonly used in stimulating electrodes, we sought to demonstrate the effectiveness of MXtrodes for electrical stimulation by evoking motor responses via intraoperative stimulation in rat brain. Specifically, we placed a 500 µm-diameter planar MXtrode subdurally onto the whisker motor cortex of an anesthetized rat. Contralateral to the MXtrode, an optical micrometer was positioned to track whisker displacement, with one whisker placed into a plastic tube to maximize detection sensitivity

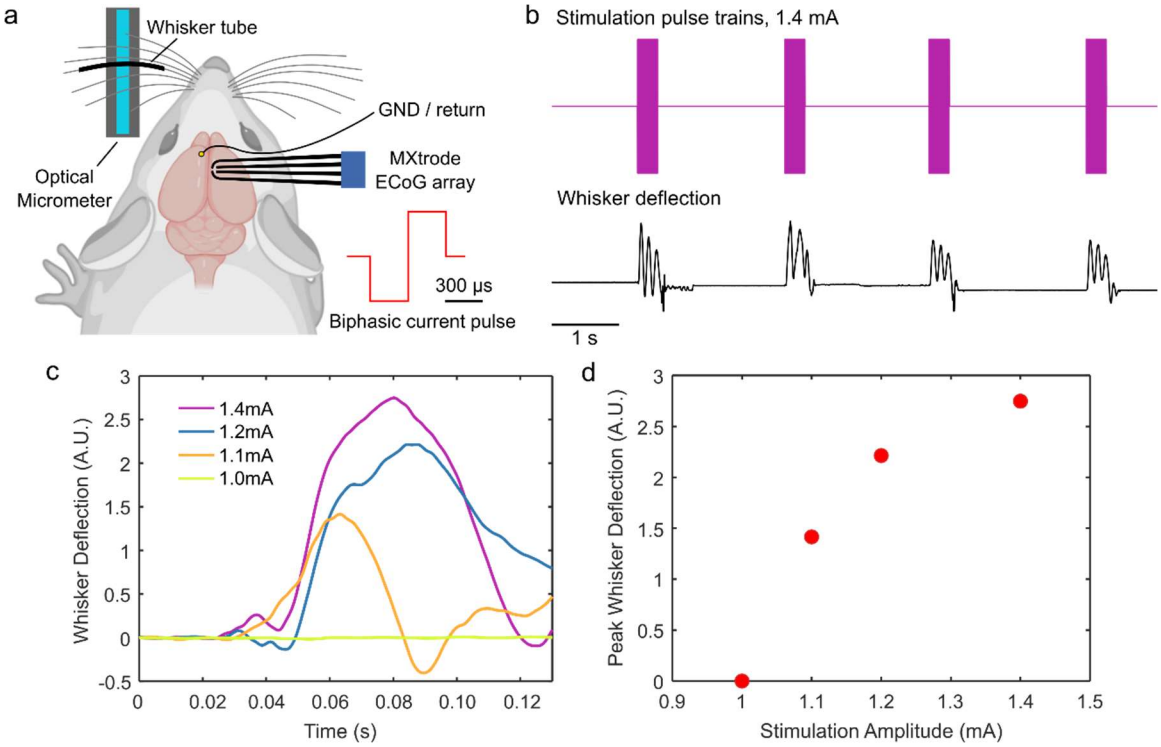

Figure 5.15 Cortical stimulation with MXtrode arrays in rat brain. (a) Schematic of the cortical stimulation setup, with the 4-ch array of 500 µm-diameter MXtrodes placed over barrel cortex, and the optical micrometer used to detect and amplify the whisker deflection signal. (b) Whisker deflection data recorded by the optical micrometer during a series of stimulation pulse trains delivered at 1.4 mA. (c) Average first whisker deflection for each stimulation pulse amplitude, time-aligned by the stimulation onset. (d) Whisker deflection amplitude scales with stimulation amplitude, with stimulation at 1.0 mA falling below the threshold required to evoke whisker movement.

(**Figure 5.15a**). Trains of charge-balanced, cathodal-first stimulation pulses with amplitudes ranging from 1.0 to 1.4 mA were delivered through the MXtrode. We observed stimulation-evoked whisker movements for amplitudes greater than 1.0 mA, with the whisker deflection amplitude scaling with the stimulation intensity (**Figure 5.15b-d**). Whisker movements registered as oscillatory deflections on the micrometer, with the first deflection peak always being the largest in amplitude. To compare whisker deflection across stimulation current amplitudes, we computed the mean amplitude of the first whisker deflection peak for each stimulation trial at each current level. These results confirm that MXtrodes are capable of delivering electrical stimulation to effectively modulate neural activity.

5.5 Compatibility of MXtrodes with clinical imaging

With the widespread adoption of bioelectronic technologies, compatibility with clinical imaging has become increasingly important. MRI and CT are the two most common imaging techniques used in the diagnosis of injury and disease, as well as in image-guided interventions. However, many of the conductive materials traditionally used in bioelectronic devices are incompatible with the challenging MRI environment and can produce heating or exert forces on the tissues. Even devices considered MR-safe often produce imaging artifacts that shadow the surrounding anatomical structures because of the mismatch in magnetic susceptibility between the device materials and the tissue [346]. These challenges are compounded at high field strengths, which are increasingly being used for high resolution imaging, as well as for novel functional and metabolic imaging techniques [347], [348]. While the magnetic susceptibility of Ti_3C_2 MXene had not been previously characterized, we hypothesized from the weak dia- and paramagnetic properties of C and Ti, respectively, that Ti_3C_2 may have a low magnetic susceptibility and thus prove compatible with the MR environment. To verify our hypotheses, we performed MRI scans of MXtrodes and measured the magnetic properties of Ti_3C_2 at body temperature. First, we imaged cross-sections of 3 mm-diameter planar MXtrodes and 2.3 mm-diameter commercial Pt electrodes embedded in conductive agarose phantoms in a 9.4T high-field research MRI system (**Figure 5.16a,b**). In the MR images, we found significant shadowing around the Pt electrodes, while no artifact was visible around the MXtrode (**Figure 5.16b**). In fact, the MXene composite forming the

conductive electrode was almost completely indistinguishable from the surrounding PDMS encapsulation. To further explore the MRI compatibility of the MXtrodes, we next imaged an array of 3 mm-diameter 3D mini-pillar MXtrodes – the same array used for EEG recording in this work – in a 3T clinical MRI scanner. The MXtrodes were placed atop a tissue phantom and imaged using a battery of scan sequences typical of structural and functional MRI. Regardless of the scan sequence, the MXtrodes showed no artifact and were nearly invisible in the images (**Figure 5.17a**). Thermal IR images of the MXtrode array immediately following a 10 min scan sequence also showed no evidence of RF heating (**Figure 5.17b**). Finally, we measured the magnetic susceptibility of a Ti_3C_2 free-standing film at 310 K, and found it to be 2.08 x 10^{-7} (**Figure 5.17c**), indicating that Ti_3C_2 is weakly paramagnetic with magnetic susceptibility very close to that of human tissues (−11.0 to −7.0 x 10^{-6}). This innate property

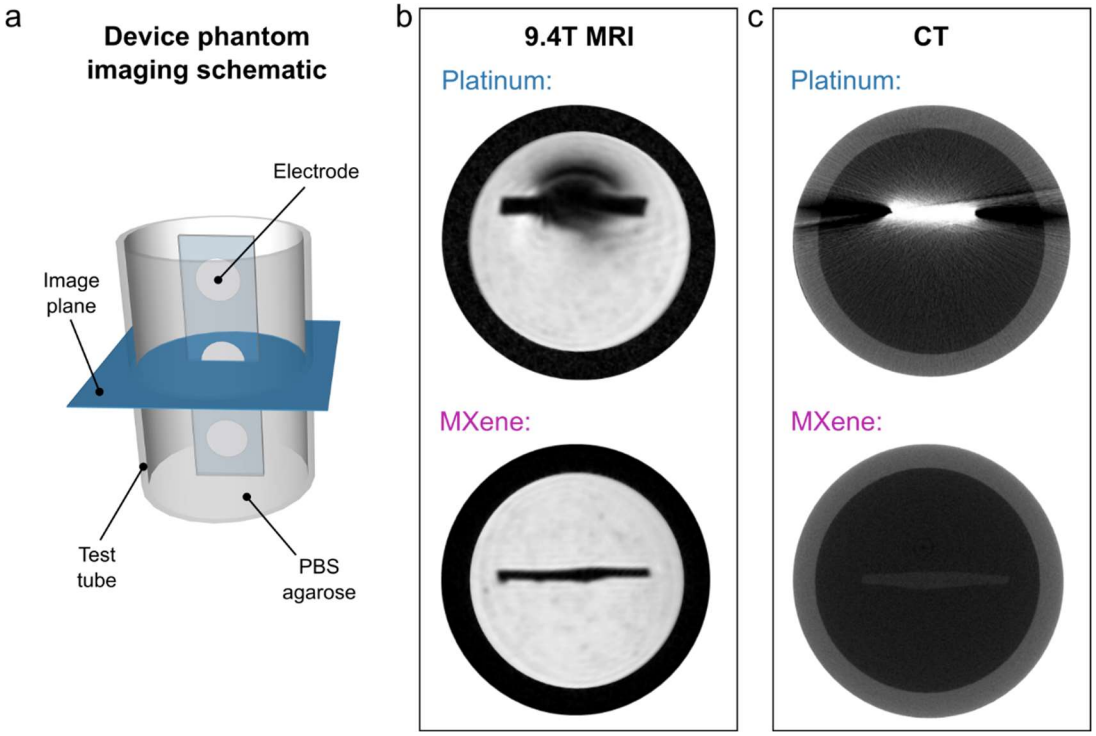

Figure 5.16 MRI and CT compatibility of MXtrodes. (a) Schematic of the phantom imaging setup for MRI and CT imaging. Strips of disk electrodes (3 mm-diameter MXtrodes or 2.3 mm-diameter clinical Pt ECoG strip electrodes) were embedded in a conductive agarose phantom and imaged in the transverse plane. (b) A high-field 9.4T MRI scan showing significant shadow artifact and image distortion around the Pt electrode (top), but no visible artifact from MXtrodes (bottom). The MXene contact is indistinguishable from the PDMS encapsulation in the device. (c) High-resolution CT scans with Pt electrodes (top) showing significant x-ray scattering artifacts, while no artifact is visible from the MXtrodes (bottom).

of Ti_3C_2, which has not been reported previously, leads directly to the excellent compatibility of the MXtrodes with MRI imaging. For comparison, the magnetic susceptibility of Pt is 2.79 x 10^{-4}, several orders of magnitude larger than the susceptibility of human tissues [346]. In situations where it might be important for implanted electrodes to be visible in MRI images, such as in epilepsy seizure foci localization relative to electrode locations, a marker such as iron oxide nanoparticles could in principle be incorporated into the electrode contacts to aid in their visualization [349].

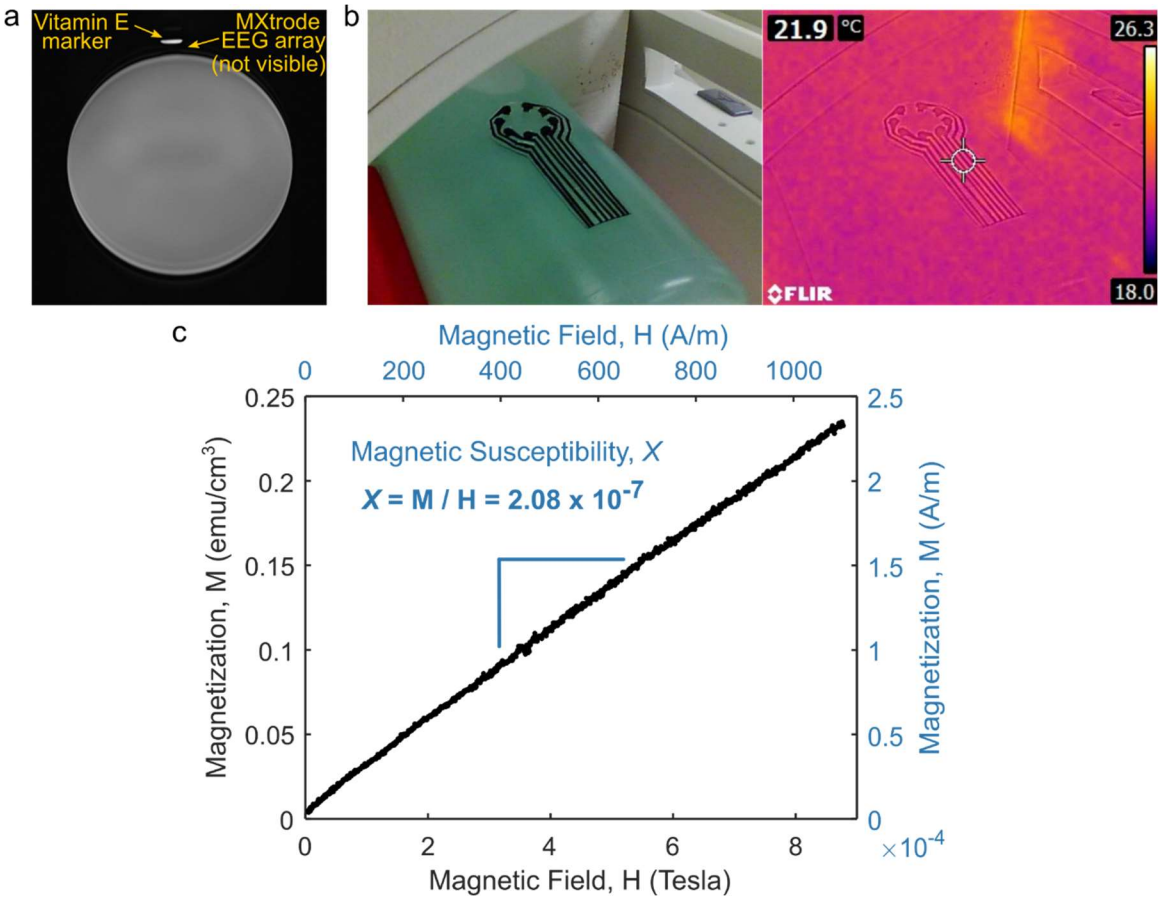

Figure 5.17 3T MRI compatibility and magnetic susceptibility of MXene. (a) MXtrode EEG array, imaged in a 3T clinical MRI with a T2 weighted sequence. The array was placed atop an MRI phantom and a Vitamin E marker was placed on top of the MXtrode array. The Vitamin E marker is visible, while the MXtrode array is not. (b) Thermal IR image of MXtrode EEG array captured immediately after a 10 min MRI sequence, showing no sign of heating. Left image shows MXtrode array atop the MRI phantom, and right image shows the thermal image overlay. (c) Magnetic susceptibility of Ti3C2 MXene measured at body temperature (i.e., 310 K) for applied magnetic field up to 9T. For calculation of the magnetic susceptibility value, X, magnetization and field strength were both converted to units of A/m such that X is unitless.

As for CT compatibility, the X-ray attenuation characteristics resulting from the high density and large atomic mass of metals in conventional electrodes poses challenges for CT imaging with bioelectronic devices [350]. Multilayer Ti_3C_2 MXene has a density of about 4 g/cm^3, which is ~5 times lower than Pt. Thus, we hypothesized that Ti_3C_2 could minimize attenuation and scattering artifacts in CT [351]. To test our hypothesis, we imaged 3 mm-diameter planar MXtrodes and 2.3 mm-diameter commercial Pt electrodes embedded in conductive agarose phantoms in a microCT scanner. As expected from the density matching considerations, we observed significant X-ray scattering artifacts around the Pt electrodes, but not around the MXtrodes (**Figure 5.16c**).

5.6 Discussion

In this work we developed a new class of MXene-based bioelectronic interfaces and demonstrated their use for high-fidelity recording and effective stimulation of neural and neuromuscular circuits across multiple scales. The simple fabrication method reported here offers a scalable and low-cost means of producing large-area, multichannel electrode arrays from high performance, solution processable 2D materials. The method is conducive to large-scale manufacturing, a key aspect for translation beyond the lab and into clinical and consumer markets. It also enables rapid customization of array geometries for various applications as well as for patient- or subject-specific fit where desired. The exceptional properties of Ti_3C_2 endow MXtrodes with impedance and charge delivery properties that meet and even exceed current state-of-the-art noble metal electrode materials in both epidermal and implantable use cases. In epidermal sensing applications, the remarkably low electrode-skin interface impedance of gel-free MXtrodes opens exciting new possibilities for high-resolution EMG and EEG, while eliminating the challenges associated with wet conductive gels. In HDsEMG mapping, MXtrode arrays hold promise for accurately localizing NMJs for use with neurolytic procedures for the treatment of spasticity and excessive muscle tone. In the future, this may eliminate the need for intramuscular needle EMG stimulation in search of the NMJ – the optimal place for injecting medications (e.g. botulinum toxin and phenol) for denervation. Furthermore, such HDsEMG arrays can also be integrated within an active prosthesis system where EMG from the residual limb serves as input signal for the

prosthesis control [352], [353]. In EEG applications, a dry electrode system enabled by MXtrodes may offer a route toward minimizing skin breakdown and alleviating many of the key logistical challenges associated with current gelled EEG systems, such as the time required to apply each electrode and impedance fluctuations over time as the gels dry out. These advantages, coupled with the possibility for obtaining high density EEG recording with mm-scaled MXtrodes, also make this technology attractive for neuroscience research [354], [355], non-invasive BCI systems [356], [357], neuro-rehabilitation [358], and brain-controlled videogaming [41]. The compatibility of MXtrodes with both CT and MRI imaging enables accurate, artifact-free imaging without the need for removing electrodes from the subject before the scan, thus opening exciting possibilities for multimodal studies in both clinical diagnostics and neuroscience research, such as those combining simultaneous EEG with functional MRI or GluCEST imaging [348], [359]. In addition to the low interface impedance, the extensive characterization of the electrochemical behavior of MXtrodes presented in this work demonstrates for the first time the advantages of Ti_3C_2 for electrical stimulation, as highlighted by remarkably high CSC and CIC compared to many commonly adopted bioelectronic materials. This finding suggests that MXtrodes may represent a suitable alternative for stimulation electrodes with enhanced safety, charge transfer efficiency, and reduced power consumption. While the technology presented here already shows great potential for translation, ongoing efforts include evaluating and improving the stability of Ti_3C_2 for long-term use [226], [269], [360], optimizing the MXene infusion process to maximize the MXene loading and conductivity of the resulting composite [315], and exploring alternative encapsulation materials to further improve the flexibility and breathability of the electrode arrays [120]. Overall, our results indicate that MXene-based bioelectronics have tremendous potential for enabling the next generation of soft interfaces for advanced healthcare diagnostics, monitoring and therapy, as well as for research and consumer electronics.

5.7 Materials and methods

Synthesis of Ti_3C_2 MXene

Ti_3C_2 MXene was provided by Murata Manufacturing Co., Ltd. It was produced using the MILD synthesis method [232] to create an ink of 30 mg/mL Ti_3C_2 in deionized water, which was placed in a vial and sealed under Argon atmosphere for long term storage.

Fabrication of MXtrode devices

Devices were fabricated by first laser-patterning absorbent nonwoven textile substrates comprised of hydroentangled 55% cellulose / 45% polyester blend (Texwipe TechniCloth) using a CO_2 laser (Universal Laser Systems PLS 4.75) such that electrode array patterns were easily separable from the surrounding textile, but could still be lifted and handled as one sheet. These were transferred to a thin and slightly tacky bottom layer of 1:10 PDMS (Sylgard 184) on a flat acrylic sheet, and the excess textile surrounding the array patterns was then peeled up. The textile patterns were then inked with 30 mg/mL Ti_3C_2 MXene, allowed to air dry for 15 min, then placed in a vacuum oven (Across International) at 70 °C and 60 mmHg for 1 h to remove all remaining water. For devices incorporating 3D mini-pillar electrodes, 3 mm circles were cut from absorbent cellulose sponges (EyeTec Cellulose Eye Spears) using a 3 mm biopsy punch and these circular sponges were inked with MXene and placed onto the electrode locations of the MXene-textile constructs at the same time that the laser-patterned textile was inked. The subsequent drying steps were identical. No adhesive was necessary at this interface, as the dried MXene and the subsequent PDMS encapsulation was sufficient to hold the 3D mini-pillars firmly in place. For multichannel arrays, connectors (FCI/Amphenol FFC&FPC clincher connectors) were then attached by screen printing silver conductive epoxy (CircuitWorks CW2400) onto the ends of the dried MXene constructs, inserting these into the connectors, and clinching shut. The devices were baked at 70 °C for 30 min to cure the silver epoxy. Next, 1:10 PDMS was layered over the devices to form the top insulation layer, thoroughly degassed at 60 mmHg for 15 min – which forced PDMS to infiltrate into the MXene composite matrix – and subsequently cured at 70 °C for 1 h. Finally, devices were cut out with a razor blade, and peeled up from the acrylic substrate. For planar electrodes, electrode

contacts were exposed by cutting circular holes though the top PDMS layer using a biopsy punch (diameters ranging from 500 μm – 3 mm) and carefully peeling up the disk of PDMS to expose the MXene composite electrode below. For 3D mini-pillar electrodes, contacts were exposed by trimming the tops of the mini-pillars with a flat razor blade, exposing the MXene-sponge composite electrode. Slight variations on this method were utilized for MXtrode arrays designed for different applications: for EMG arrays, a thin layer of silicone medical adhesive spray (Hollister Adapt 7730) was applied to the skin-facing side of the array prior to opening the electrode contacts to enhance skin adhesion; for single-channel ECG and EOG MXtrodes, EcoFlex (Smooth-on Ecoflex 00-30) in a 1:2 ratio (part A:part B) was used as the encapsulation rather than PDMS to offer enhanced skin adhesion and comfort; for the ECoG electrodes, arrays were fabricated in PDMS as described above, but were additionally coated in a 1 μm-thick layer of Parylene-C prior to opening electrode contacts to enhance the moisture barrier properties of the encapsulation.

Imaging of MXtrode devices

Optical images of MXtrodes and their constituent parts were taken with a Keyence VHX6000 digital microscope. Scanning electron microscopy (SEM) images were captured using a Zeiss Supra 50VP scanning electron microscope with an accelerating voltage of 5 kV.

DC conductivity of ink-infused composites

DC conductivity measurements were made on laser-cut test structures 20 cm long x 3 mm wide x 285 μm thick comprising 55% cellulose / 45% polyester blend (Texwipe TechniCloth) infused with either: (1) 30 mg/mL Ti_3C_2 MXene in DI, (2) 1.1% high conductivity grade PEDOT:PSS in H_2O (Sigma Aldrich), or (3) 18 mg/mL highly concentrated single-layer graphene oxide (Graphene Supermarket) which was subsequently reduced using a vitamin-C reduction method[361]. Measurements were taken with a handheld multimeter with flat alligator clip terminations, where the negative lead was fixed at the end of the construct and the positive lead was moved in 2 cm increments for each measurement.

Electrochemical characterization

For cutaneous EIS measurements, the skin of the inner forearm was prepared with an alcohol swab followed by light abrasion (3M TracePrep abrasive tape) before placing 3 mm planar and 3D mini-pillar MXtrodes and measuring EIS from 1 – 10^5 Hz with a 10 mV_{pp} driving voltage using a Gamry Reference 600 potentiostat. Reference was placed on the inner wrist and ground was placed on the elbow (Natus disposable disk electrodes). Electrochemical measurements in saline, including EIS, CV, and current pulsing, were performed for planar MXtrodes with diameters of 3 mm, 2 mm, 1 mm, and 500 μm, and Pt electrodes with a diameter of 2.3 mm (Adtec epilepsy subdural grid TG48G-SP10X-000) in 10 mM phosphate buffered saline (Quality Biological, pH 7.4) using a Gamry Reference 600 potentiostat. All electrochemical measurements were done in a 3 electrode configuration with a graphite rod counter electrode (Bio-Rad Laboratories, Inc.) and a Ag/AgCl reference electrode (Sigma-Aldrich). EIS was measured from 1 – 10^5 Hz with 10 mV_{pp} driving voltage. Cyclic voltammetry was performed at a sweep rate of 50 mV/s. Safe voltage limits for MXtrodes were determined by incrementally increasing the negative limit of the CV scan until water reduction was observed (beginning at −1.9 V), then the positive limit of the CV scan until a linear, resistive behavior was observed (beginning at +0.7 V) beyond which the MXtrode showed current loss with subsequent scans. CSC_c was determined from the CV scans by taking the time integral of the cathodal current. Current pulsing was performed using chronopotentiometry with biphasic, charge-balanced current pulses with t_c = t_a = 500 μs and t_{ip} = 250 μs for currents ranging from 600 μA to 5 mA for N=3 electrodes of each size. For CIC_c calculations, E_{mc} was determined as the instantaneous voltage 10 μs after the end of the cathodal current pulse. E_{mc} values were plotted as a function of injected current amplitude, and the linear relation was determined to estimate the current limit at which the electrode would reach its cathodal limit (−1.8 V for MXtrodes, −0.6 V for Pt). Any series of measurements in which current amplitude vs. E_{mc} was not linear with $R^2 < 0.95$ were excluded. CIC_c was defined as: $CIC = \frac{I_{lim} \times t_c}{GSA}$, where I_{lim} is the cathodal current limit, t_c is the cathodal pulse width, and GSA is the electrode geometric surface area. CSC and CIC scaling relations were determined by fitting power functions to the data, similar to work by M. Ganji et al [317].

EEG experiments

EEG experiments were conducted under a protocol approved by the Institutional Review Board of Drexel University (Protocol # 1904007140). One healthy human subject was seated in a comfortable chair with a head rest. Prior to placing electrodes, the subject's scalp was prepared with an alcohol swab and light abrasion (3M TracePrep abrasive tape), though the presence of hair may have limited the efficacy of the skin abrasion. Recordings were made using an 8-electrode MXtrode device with dry 3 mm-diameter 3D mini-pillar electrodes and 1 standard gelled Ag/AgCl EEG cup electrode (Technomed Disposable EEG cup) placed in the center of the MXtrode array. Recordings were obtained using a NeuroNexus SmartBox amplifier system with a sampling rate of 20 kHz. Standard gelled Ag/AgCl EEG cup electrodes were used for reference (placed on left mastoid) and ground (placed on forehead center). In the first set of recordings, electrodes were positioned on the parietal region, centered over 10-20 site P1. Pre-wrap (Mueller) was used to hold the electrodes in place, and a small hole was made in this wrapping to allow application of conductive gel (SuperVisc, EASYCAP GmbH) beneath the standard EEG cup electrode. To evoke identifiable changes in the alpha band[362], six 2-minute-long recordings were obtained, alternating between eyes open and eyes closed states. During resting state, the subject was instructed to remain relaxed but alert. For the eyes open state, the subject was asked to fixate on a cross on a computer monitor to reduce oculomotor saccades and maintain a consistent level of external vigilance. In the second set of recordings, the hand motor region was localized using single TMS pulses to isolate a location that evoked lateral finger movements [363] *via* induced contractions of the first dorsal interosseus, and the electrodes were positioned centered over this location, approximately at site C3. Six 2-minute-long recordings were obtained, cycling through a resting state, imagined hand flexion, and actual hand flexion. Signals were notch filtered at 60 Hz and bandpass filtered from 0.1 – 100 Hz. Bridging analysis was performed to ensure that gel did not leak from the cup electrode to contact any recording surface on the MXtrode array.

EMG experiments

EMG, ECG, and EOG human epidermal recordings were conducted under an experimental protocol approved by the Institutional Review Board of the University of Pennsylvania

(Protocol # 831802). For all EMG experiments, skin preparation prior to placing MXtrode arrays included an alcohol swab followed by light abrasion (3M TracePrep abrasive tape), and signals were recorded at a sampling rate of 20 kHz on an Intan RHS2000 Stimulation/Recording Controller (Intan Technologies). For recordings from abductor pollicis brevis (APB), a 5x4 grid of 3 mm planar MXtrodes with center-to-center spacing of 7.5 mm horizontal, 6.5 mm vertical, was placed over the APB at the base of the thumb. Reference was placed over the bony interphalangeal thumb joint and ground was placed on the back of the hand (Natus disposable adhesive electrodes). The median nerve was stimulated at the wrist using a VikingQuest handheld bipolar stimulator (Nicolet), starting at 10 mA and gradually increasing until supramaximal activation of the APB was achieved in the form of a thumb twitch (amplitude 38.8 mA for the subject shown). For localization of the NMJ of the APB, evoked responses recorded on each electrode in the array (no signal filtering was used) were averaged across all stim trials (N=10), the peak of the average evoked response was determined, and a map of the latency of this peak from the onset of the stimulation was created. The location of the NMJ was approximated as the location with the shortest latency in the peak evoked response. For recordings of the biceps, a 10x4 grid of 3 mm planar MXtrodes with center-to-center spacing of 8.5 mm horizontal, 8.5 mm vertical, was placed over the center of the biceps muscle. Reference was placed distal to the array just above the inner elbow and ground was placed proximal to the array on the deltoid (Natus disposable adhesive electrodes). The supraclavicular nerve was stimulated using the same VikingQuest handheld bipolar stimulator (Nicolet), starting at 30 mA and gradually increasing until clear submaximal activation of biceps was observed (amplitude 49.0 mA for the subject shown). As for the APB recordings, evoked responses recorded on each electrode were averaged across all stim trials (N=11), the peak of the average evoked response was determined, and a map of the latency of this peak from the onset of the stimulation was created. The IZ was determined as the area with the shortest latency in the peak evoked response. To further validate the IZ localization in the biceps, additional EMG recordings were made with the subject performing periods of isometric voluntary contractions. Signals were subtracted in bipolar configuration down the length of the MXtrode array, and MUAPs

were identified in the raw EMG signal. The IZ was determined as the region where the MUAP appears earliest and where the signal polarity inverts.

ECG recording

For ECG recording experiments, skin preparation prior to placing electrodes included an alcohol swab followed by light abrasion (3M TracePrep abrasive tape), and signals were recorded at a 20 kHz sampling rate on an Intan RHS2000 Stimulation/Recording Controller (Intan Technologies). Recordings were made in a 3-electrode configuration with reference placed just below the subject's right clavicle, ground placed just below the subject's left clavicle, and the working electrode placed on the lower left ribs. For comparison, recordings were made sequentially using either all 2 cm gelled Natus electrodes (Natus disposable adhesive electrodes) or all 1.3 cm dry MXtrodes, with electrodes placed in the same locations.

EOG recording

EOG recording experiments followed a similar protocol to ECG recording. Skin preparation prior to placing the electrodes included an alcohol swab followed by light abrasion (3M TracePrep abrasive tape), and signals were recorded at a 20 kHz sampling rate on an Intan RHS2000 Stimulation/Recording Controller (Intan Technologies). 1.3 cm-diameter dry MXtrodes were used for ground, (+) and (-) contacts. For tracking up-down eye movements, the (+) and (-) electrodes were placed below and above the right eye, respectively. The subject moved their eyes in a center-down-center-up-center pattern for 2 minutes. For tracking left-right eye movements, the (+) and (-) electrodes were placed just lateral to the left and right eyes, respectively. The subject moved their eyes in a center-left-center-right-center pattern for 2 minutes. The ground electrode was centered on the forehead for both EOG recording paradigms.

ECoG recording

Pigs were pair housed when possible and were always in a shared room with other pigs in a research facility certified by the Association for Assessment and Accreditation of Laboratory Animal Care International (AAALAC facility). All experiments were conducted according to

the ethical guidelines set by the Institutional Animal Care and Use Committee of the University of Pennsylvania and adhered to the guidelines set forth in the NIH Public Health Service Policy on Humane Care and Use of Laboratory Animals (2015). Prior to the procedures, animals were fasted for 16 hours with water remaining ad libitum. After induction with 20 mg/kg of ketamine (Hospira, 0409-2051-05) and 0.5 mg/kg of midazolam (Hospira, 0409–2596-05), anesthesia was provided with using 2–2.5% isoflurane (Piramal, 66794-013-25) via a snout mask and glycopyrrolate was given subcutaneously to curb secretions (0.01 mg/kg; West-Ward Pharmaceutical Corp., 0143-9682-25). The animals were intubated with a size 6.0 mm endotracheal tube and anesthesia was maintained with 2–2.5% isoflurane per 2 liters O_2. Animals were then moved to an operating room, where they were transferred onto a ventilator. The ventilator provided the same rate of isoflurane and O_2 for anesthesia maintenance at a rate of 20-25 breaths per minute. Heart rate, respiratory rate, arterial oxygen saturation, end tidal CO_2, blood pressure and rectal temperature were continuously monitored, while pain response to pinch was periodically assessed. All of these measures were used to maintain an adequate level of anesthesia. A forced air warming system was used to maintain normothermia. Prior to electrode insertion, the pig was placed in a stereotaxic frame described previously [364], and the surgical site was prepared and draped in the standard sterile fashion. After the skull was exposed, an 11 mm craniectomy was performed at the recording site, 7 mm lateral to midline and 4.5 mm posterior to bregma in order to expose the frontoparietal cortex. The dura was opened to expose the cortical surface and the MXtrode array was then placed in the subdural space for recording. Recordings were obtained using an HS-36 amplifier and collected continuously at 32 kHz using a Neuralynx Digital Lynx SX recording system. Raw data was collected and stored using Neuralynx's Cheetah recording software.

Cortical stimulation

An adult male Sprague Dawley rat (Crl:SD, 300 g) was used for the stimulation experiment. Anesthesia was induced with 5% isoflurane and the rat was placed in a stereotaxic frame. Depth of anesthesia was monitored by respiratory rate and pedal reflex and maintained at a surgical plane with 1.5–2.5% isoflurane. Whisker motor cortex (wM1) was exposed

bilaterally with a craniotomy centered on the midline. A durotomy was performed over right wM1. A stimulation return skull screw was placed in the left frontal bone. Trains of biphasic current pulses (300 μs/phase, 3 μs interpulse interval, 100 pulses, variable pulse amplitude from 1.0 to 1.4 mA) were delivered through a single electrode in the MXtrode array using the Intan RHS System (Intan Technologies). Stimulus-evoked contralateral whisker movement was quantified with a laser micrometer (IG-028, Keyence Corp.), which had a measurement range of 28 mm, a spatial resolution of 5 μm, and a temporal resolution of 490 μs. A 360 μm diameter polyimide tube was placed over a whisker with visually apparent stimulus evoked movement. Spatial sensitivity of the micrometer was adjusted to detect only the motion of the whisker in the tube [365]. At the conclusion of the experiment, the rat was killed with an intraperitoneal injection of sodium pentobarbital. These procedures were approved by the Institutional Animal Care and Use Committee of the University of Pennsylvania.

Evaluation of MRI and CT compatibility

A strip of six 3 mm-diameter MXtrodes were prepared with PDMS encapsulation to match the geometry of the comparison Pt clinical ECoG electrode strips (Adtec epilepsy subdural grid TG48G-SP10X-000). Both types of electrode arrays were placed in 0.6% agarose (IBI Scientific) prepared with 10 mM PBS (Quality Biological, pH 7.4) in a 15 mm inner-diameter glass test tube, with degassing to remove air bubbles. A 9.4 T Horizontal bore MRI scanner (Bruker, Erlangen) and 35 mm diameter volume coil (m2m Imaging, USA) were used to acquire T1-weighted gradient echo MR images of cross-sections of both electrode types. The acquisition parameters for T1-W MRI were: TE/TR = 7/150 ms, FOV = 30x30 mm^2, Matrix size = 256x256, Averages = 4, Flip angle = 30°, slice thickness = 0.7 mm. For CT imaging, a μCT50 specimen scanner (Scanco Medical, Bruttisellen, Switzerland) was used to scan the electrodes at 70 kV, 115 μA, and 10 μm isotropic resolution. 2D images in the axial plane of each electrode type were acquired for comparison.

Magnetic susceptibility measurements

Magnetic properties of Ti_3C_2 were measured with Quantum Design EverCool II physical property measurement system. A free-standing film of Ti_3C_2 with a mass of 4.820 mg was

packed in a plastic sample container. The sample was heated to 310 K and was allowed to reach thermal equilibrium for about 10 min. Magnetization was recorded with respect to the applied magnetic field up to 9 T. The measured data was subtracted from that of the plastic sample holder and normalized by sample mass.

5.8 Supplementary material: MXtrode stability

Given the promise of MXtrodes for numerous applications, there has already been considerable interest in commercializing the technology. One important factor to consider is the usable "shelf life" of MXtrodes stored in ambient conditions, given prior knowledge that Ti_3C_2 MXene is prone to oxidation. To assess the stability of MXtrodes in ambient conditions, I performed periodic EIS testing of two 10 channel MXtrode arrays stored in air over a period of 6 months.

Methods

Two, 10 channel planar MXtrode arrays with 3 mm-diameter contacts were fabricated for the evaluation. For device 1, EIS was performed in PBS for all 10 channels every two weeks. Following EIS, the device was rinsed with DI water, gently dried with a Kim Wipe, then baked at 70°C for 1 h. For device 2, EIS was performed in PBS for channels 1-6 every two weeks and for channels 7 and 8 at fewer selected time points. Channels 9 and 10 were not tested until the final time point. Care was taken not to expose the un-tested channels to PBS or to DI water. Following EIS, the channels which were tested were rinsed with DI water and gently dried with a Kim Wipe. Device 2 was not baked. Between tests, both devices were stored in a foil pouch in ambient conditions.

Results

Bode plots of the impedance magnitude and phase at a few selected time points are shown in **Figure 5.18** for Device 1 (all channels) and Device 2 (channels 1-6) and plots showing the progression of impedance values at 1 kHz and at 10 Hz are shown in **Figure 5.19**. Throughout the course of the study the impedance gradually increased, however the changes were most pronounced in the first 6 weeks. The changes were also more pronounced at low frequencies. By week 16, the MXtrodes stabilized, and they showed little change in the last 10 weeks of the study. Accompanying the rise in impedance magnitude, the phase behavior dramatically shifted, consistent with the formation of a porous oxide layer on the surface of the electrodes. Comparing between the two devices, Device 1 showed faster oxidation and

stabilized to a higher overall impedance value compared to Device 2, indicating that the baking step following the EIS testing likely contributed to oxidation, as expected.

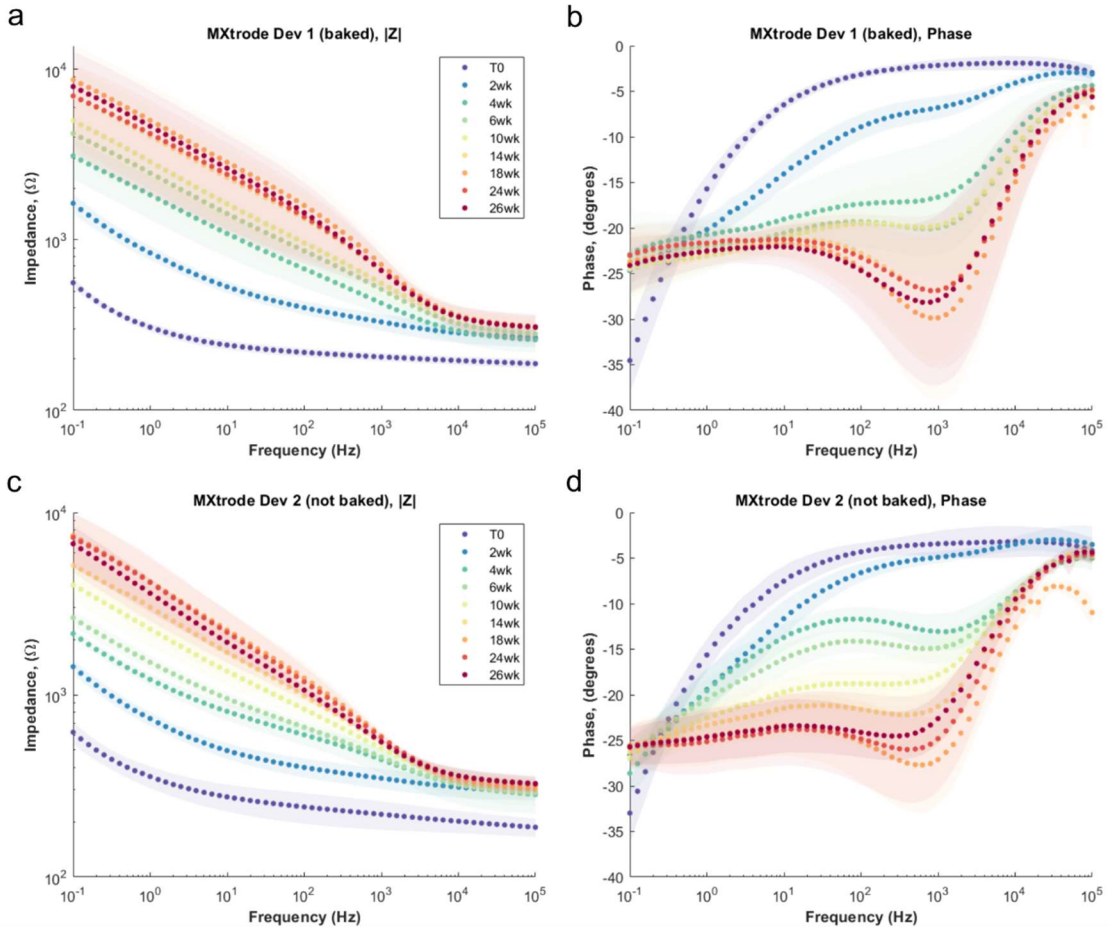

Figure 5.18 EIS spectra for two MXtrode devices over 26 weeks. (a-b) Impedance modulus (a) and phase (b) shown at selected time points for Device 1. All 10 channels were tested every 2 weeks and Device 1 was baked following each test. (c-d) Impedance modulus (c) and phase (d) shown at selected time points for Device 2. Only channels 1-6 were tested every 2 weeks, and no baking was performed following EIS testing.

An important concern in the test design is how much the periodic EIS testing contributed to accelerating the oxidation and degradation of the devices. Because the electrodes are exposed to PBS and DI water during each test, and because moisture is known to accelerate Ti_3C_2 oxidation, the results may not accurately represent the aging conditions of a device left in ambient air for a prolonged period, and thus may not give an accurate measure of the stable "shelf life" of the devices. To assess the contribution of the periodic EIS testing

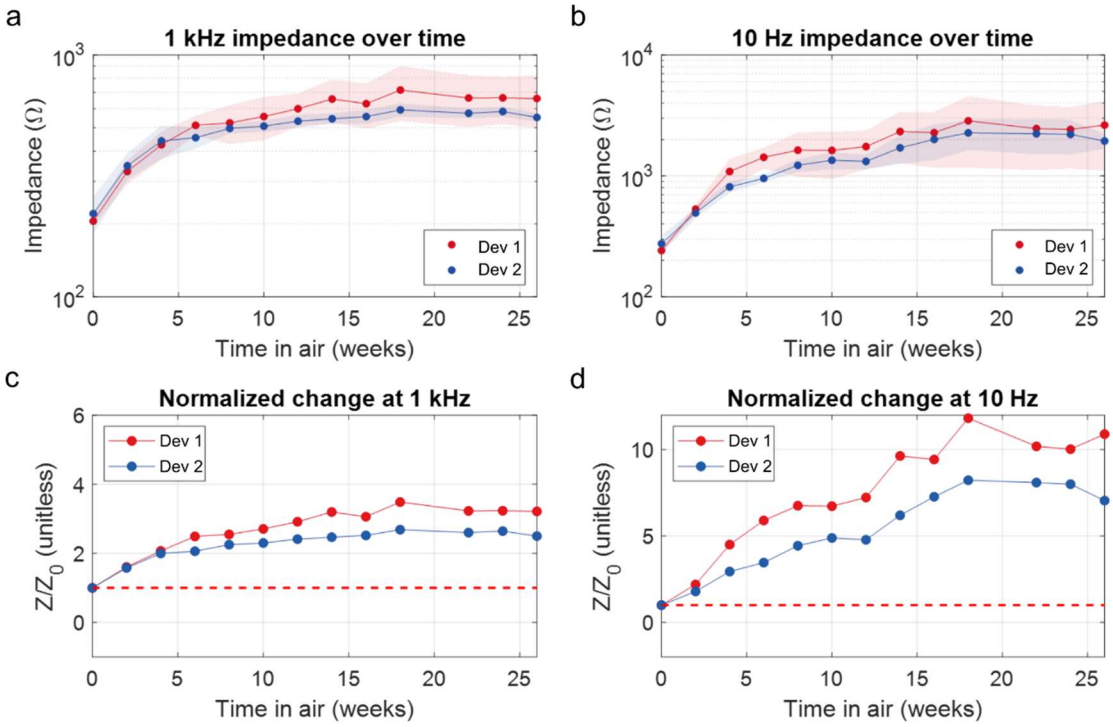

Figure 5.19 1 kHz and 10 Hz impedance values monitored over 26 weeks. (a) 1 kHz impedance values over time for Devices 1 and 2. Device 1 was baked following each test, while Device 2 was not. (b) 10 Hz impedance over time for Devices 1 and 2. (c-d) Normalized impedance change from initial value at (c) 1 kHz and (d) 10 Hz for each device.

to the rate of oxidation, 4 channels on Device 2 were held aside and tested at fewer time points: channels 7 and 8 were tested at four time points throughout the study, and channels 9 and 10 were only tested at the final time point. The results, shown in **Figure 5.20**, indicate that channels 7 and 8 had undergone significantly less oxidation by the final time point than the channels which were tested more frequently, suggesting that the EIS testing does accelerate the degradation. The behavior of channels 9 and 10, however, do not match expectations. These two channels were never exposed to PBS prior to testing at the final time point, thus we expected to see significantly less oxidation than any of the other channels, and phase behavior similar to that of un-aged MXtrodes at the initial time point. While the impedance at 1 kHz was lower than the other channels, the impedance in the low frequency regime was higher than expected. Furthermore, the phase behavior of these channels was unlike that of the other MXtrodes channels at any time point in the study.

Despite the formation of the oxide layer over the course of the study, even the aged MXtrodes that appear to have reached a stable state of oxidation still have low enough impedance that they may be able to record biosignals, though likely with reduced signal fidelity. Further evaluation will be needed to fully assess the useable shelf life of MXtrodes, and to determine an acceptable level of oxidation for functional devices.

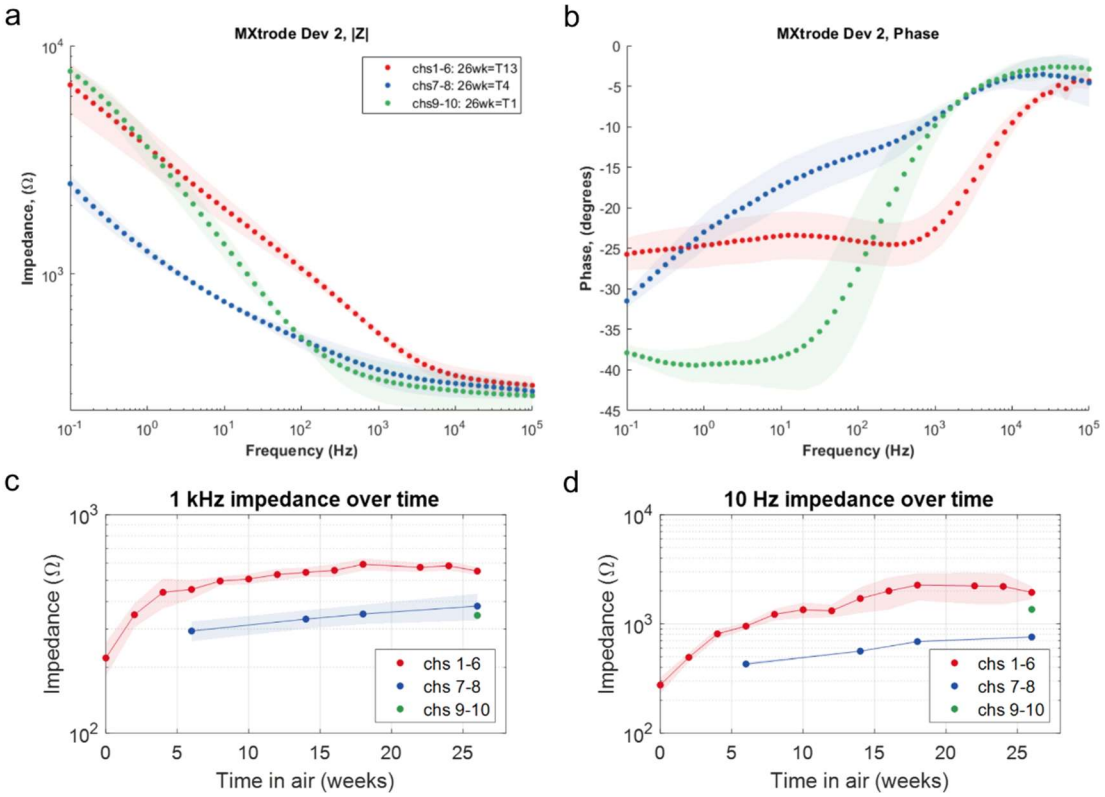

Figure 5.20 Effect of repeated impedance testing on device aging. (a-b) Impedance modulus (a) and phase (b) at the final 26 week time point for subsets of channels on Device 2, which were tested with varying frequencies. Channels 1-6 were tested every 2 weeks for a total of 13 tests by the final time point. Channels 7 and 8 were tested 4 times throughout the study. Channels 9 and 10 were tested only at the final time point. (c-d) 1 kHz (c) and 10 Hz (d) impedance values over time for each subset of channels.

Chapter 6: Conclusions and Future Directions

In this thesis, I have developed neurotechnologies that leverage unique properties of carbon nanomaterials to enable recording and modulating neural and neuromuscular activity across spatial scales. Starting at the microscale, I showed how transparent graphene microelectrodes could be used with simultaneous optical imaging to enable new insights into microscale brain dynamics. By optimizing the fabrication and processing of transparent graphene electronics, I improved the impedance and optical transparency properties of the electrodes beyond what had previously been reported. Still, such graphene-based transparent electrodes reach a fundamental limit in how far impedance can be reduced due to the quantum capacitance of graphene [144]. Thus, it remains challenging to scale transparent graphene electrodes down to the dimensions required for resolving neuronal spiking activity (~10s of μm) because their high impedance at these scales significantly degrades the recorded signal quality. New materials may soon enable transparent electrodes at these scales, however, and Ti_3C_2 MXene is a very promising candidate. A number of recent studies have shown that thin films of Ti_3C_2 MXene can achieve an optoelectronic figure of merit that meets or even exceeds that of CVD-grown graphene [21], [366], [367]. In Chapter 4 of this thesis, I showed that non-transparent Ti_3C_2 microelectrodes are highly sensitive for recording neural spiking activity. It would be a fairly simple matter to tune the processing conditions to fabricate similar Ti_3C_2 microelectrodes where the MXene films are optically transparent, and it seems plausible that such electrodes could achieve lower impedance than their graphene counterparts. In the future, Ti_3C_2 could push the bounds of transparent microelectrode density and spatial resolution beyond what is possible with graphene.

In Chapter 3, I also presented a new approach for combining multimodal data to harness the key advantages of electrophysiology and optical imaging, while accounting for their differences in temporal and spatial sampling. Such an approach can help elucidate the relation between individual cellular activity and network oscillations observed in neurologic phenomenon such as epileptogenesis. For example, high frequency oscillations (HFOs) have been proposed as a biomarker for identifying the seizure onset zone in epilepsy and for predicting epileptogenesis following cerebral insult or prolonged febrile seizures [183]–[185]. HFOs can also occur in the healthy brain, however, and distinguishing between normal and pathologic HFOs has been the subject of some debate [368]. It is now believed that

different cellular mechanisms give rise to normal and pathologic HFOs, however it has been challenging to study this phenomenon because the oscillations are too fast to be detected using optical imaging methods alone. The multimodal approach presented in Chapter 3 offers the necessary spatiotemporal resolution to begin to answer these questions. By using genetically-targeted optical reporter molecules, it may be possible to discern the individual contributions of specific neuronal and even glial sub-types to broader network oscillations such as HFOs.

In Chapter 4, I introduced Ti_3C_2 MXene as a new material for neural microelectrodes. I showed that Ti_3C_2 electrodes offered lower impedance, lower noise, and improved neural recording performance compared to gold electrodes. This was the first demonstration of any MXene for *in vivo* electrophysiology, and it identified the tremendous potential of MXenes for bioelectronics. Motivated by this success, I then developed a new class of MXene bioelectronics suitable for human-scale electrophysiology, with a focus on clinical translation. These MXtrodes, which are fast, simple, and low-cost to produce, have excellent electrochemical properties, outperforming current state-of-the-art electrode materials. In particular, their low electrode-skin interface impedance enables gel-free epidermal recording with high spatial resolution, which has been challenging for epidermal electronics.

Of the epidermal applications shown in Chapter 4, gel-free, high-density EEG with MXtrodes is one that has generated significant interest. In current clinical practice, recording an EEG requires a certified EEG technician to measure and individually place each gelled EEG electrode on the subject's scalp. This process is time-consuming, thus limiting the ability to rapidly obtain EEG in emergency situations, and it is costly to health systems to staff certified EEG technicians around-the-clock. The conductive gels used with current EEG electrodes leave unwanted residues in the hair, and in patients who require long-term EEG monitoring they can cause skin irritation and breakdown as well as impedance fluctuations over time as the gels dry out. This often necessitates periodic replacement of the gels, which is again a time-consuming process requiring an EEG technician. Given the success of MXtrodes in recording high-quality EEG signals without any conductive gel, it's possible that MXtrodes could be incorporated into an EEG cap or headband system that could be deployed rapidly without the need for a certified EEG technician. This could significantly improve access to

rapid EEG diagnostics in emergency and trauma situations. It could also enable simpler at-home monitoring for epilepsy patients, if they could put on the cap or headband system themselves at home and stream the data to a secure cloud-based platform where a clinician could monitor the EEG. More work is certainly needed to develop such a system, particularly in ensuring that the gel-free MXtrodes can achieve good scalp contact in subjects with long or thick hair, but initial results are promising.

In addition to clinical EEG applications, high-density EEG enabled by the mm-scale dry MXtrodes has also generated significant interest in the research community. High-density EEG can be used to study important phenomena in cognitive neuroscience and in sleep research, and can also be used as a non-invasive tool for epilepsy source localization [369]. It is also of great interest to the BCI community, where enhanced spatial resolution can improve decoding accuracy for non-invasive EEG-based BCIs [370]. So far, the spatial resolution of EEG has been limited because gelled electrodes can experience bridging when placed too close together, and because dry electrodes have so far required scalp contact areas >1 cm^2 in order to achieve sufficiently low interface impedance. Thus, it is not yet clear what the limit of scalp EEG resolution is, in part because there have not been electrodes capable of pushing the spatial sampling down to sub-cm scales. MXtrodes could enable studies to begin to answer this question. Spatial smearing from the skull and scalp as well as volume conduction surely limit the unique information content that can be obtained from closely adjacent scalp electrodes. However, techniques such as independent component analysis can help to detect subtle differences to leverage high spatial sampling [371].

Another key advantage of the MXtrodes is their compatibility with clinical imaging techniques. In clinical practice, inpatients requiring long-term EEG monitoring are often set up with MRI-compatible EEG leads so that they can be disconnected and taken for diagnostic imaging without requiring the EEG electrodes to be removed and replaced. Current MRI-compatible leads are very expensive, however, and MXtrodes may offer a significantly lower-cost solution. In research, the compatibility of MXtrodes with clinical imaging techniques opens new possibilities for multimodal studies combining EEG with imaging. Concurrent collection of EEG with fMRI or metabolic imaging such as GluCEST can yield complementary

information to enable new insights into brain activity, similar to the advantages of multimodal recording described in Chapter 3, albeit on a different scale.

Beyond epidermal recording applications, the MXtrodes were also found to possess exceptional electrochemical properties in saline, suggesting that they could outperform Pt and other noble metals in implantable electrodes. This observation matched the results shown for the Ti_3C_2 microelectrodes, which had ~4x lower impedance compared to size-matched Au electrodes. The MXtrodes have a slightly different morphology than the microelectrodes shown in Chapter 4, because the electrode contact is comprised of a MXene-coated textile composite rather than a pure thin film of Ti_3C_2. This is strong evidence that the unique properties of Ti_3C_2 are largely responsible for the exceptional electrochemical performance of MXene-based electrodes, though the electrode surface morphology and roughness certainly play a role.

One striking finding is that MXtrodes have significantly enhanced CSC_c and CIC_c compared to Pt and other common materials used for stimulation electrodes. The use of implantable neuromodulation systems to treat neurological conditions is rapidly expanding, with deep brain stimulation used to treat the motor symptoms of Parkinson's disease, vagus nerve stimulation used to treat depression and other conditions, and newer responsive neuromodulation systems developed for epilepsy seizure control such as the NeuroPace and Medtronic RC+S. These systems rely on safe, efficient charge transfer through their stimulation electrodes, and the efficiency of charge delivery has a significant effect on the battery life of the implanted system. While more work is needed to fully characterize the stimulation efficiency and safety of MXene-based electrodes, the results shown in this thesis suggest that they could offer more efficient stimulation performance, potentially prolonging the battery life of such implanted systems.

A notable caveat to any notion of using MXene for implantable electrodes is their poor oxidation stability in physiologic environments. Further optimization of the synthesis and processing conditions will be needed to realize stable MXene compositions for chronic bioelectronic applications. Significant progress toward oxidation-resistant MXene compositions has been made just in the past two years, however, so there is hope that this challenge can be overcome in the future.

The ultimate goal of this thesis was to develop new neurotechnologies that could expand our capabilities for recording and modulating neural and neuromuscular activity. Interfacing manmade electronics with biological tissues presents numerous challenges, and it is clear that new materials and fabrication methods can offer solutions to some of these challenges. In this work, I've shown that the unique properties of graphene and MXene can be harnessed to offer new capabilities for high-resolution neural recording and stimulation electrodes. Additionally, the fabrication methods developed here represent a significant step toward translating nanomaterial-based technologies beyond academic research by improving scalability. It is my hope that these technologies will enable future research studies aimed at unraveling complex neural dynamics, as well as advances in clinical monitoring and diagnostics to improve patient care.

Appendix A: Fabrication of Ti_3C_2 MXene microelectrode arrays for *in vivo* neural recording

Abstract

Implantable microelectrode technologies have been widely used to elucidate neural dynamics at the microscale to gain a deeper understanding of the neural underpinnings of brain disease and injury. As electrodes are miniaturized to the scale of individual cells, a corresponding rise in the interface impedance limits the quality of recorded signals. Additionally, conventional electrode materials are stiff, resulting in a significant mechanical mismatch between the electrode and the surrounding brain tissue, which elicits an inflammatory response that eventually leads to a degradation of the device performance. To address these challenges, we have developed a process to fabricate flexible microelectrodes based on Ti_3C_2 MXene, a recently discovered nanomaterial that possesses remarkably high volumetric capacitance, electrical conductivity, surface functionality, and processability in aqueous dispersions. Flexible arrays of Ti_3C_2 MXene microelectrodes have remarkably low impedance due to the high conductivity and high specific surface area of the Ti_3C_2 MXene films, and they have proven to be exquisitely sensitive for recording neuronal activity. In this protocol, we describe a novel method for micropatterning Ti_3C_2 MXene into microelectrode arrays on flexible polymeric substrates and outline their use for *in vivo* micro-electrocorticography recording. This method can easily be extended to create MXene electrode arrays of arbitrary size or geometry for a range of other applications in bioelectronics and it can also be adapted for use with other conductive inks besides Ti_3C_2 MXene. This protocol enables simple and scalable fabrication of microelectrodes from solution-based conductive inks, and specifically allows harnessing the unique properties of hydrophilic Ti_3C_2 MXene to overcome many of the barriers that have long hindered the widespread adoption of carbon-based nanomaterials for high-fidelity neural microelectrodes.

1. Synthesis of Ti_3C_2 MXene

NOTE: The reaction procedures described in this section are intended for use inside a chemical fume hood. Washing steps included in this procedure are intended to be used with balanced centrifuge tubes. All waste produced is considered hazardous waste and should be discarded appropriately following University guidelines.

CAUTION: Hydrofluoric acid (HF) is an extremely dangerous, highly corrosive acid. Consult the materials safety data sheets (MSDS) for the chemicals used to synthesize MXenes before use and implement and follow appropriate safety measures. Appropriate personal protective equipment (PPE) for handling HF includes a laboratory coat, acid resistant apron, close-toed shoes, long pants, goggles, full face shield, nitrile gloves, and HF resistant gloves made of butyl rubber or neoprene rubber.

1.1. **MAX phase synthesis**: The Ti_3AlC_2 MAX phase precursor used to synthesize MXenes has been shown to have direct implications on the resulting Ti_3C_2 MXene properties[372]. The Ti_3C_2 used to fabricate neural electrodes was selectively etched from MAX prepared following a previous procedure.[224] Ti_3AlC_2 was synthesized by ball milling TiC (2 μm), Ti (44 μm), and Al (44 μm) powders at a molar ratio (TiC:Ti:Al) of 2:1:1 for 18 h using zirconia balls. Then, the powders were placed in an alumina crucible and heated to 1380 °C (5 °C heating rate) and held for 2 h under argon. After the powders have been cooled, the MAX block was milled and sieved through a 200 mesh sieve (< 74 μm particle size).

1.2. **Etching: Removal of the Al layer in Ti_3AlC_2 in an acidic etchant solution.** Prepare the selective etching solution in a 125 mL plastic container by first adding 12 mL deionized water (DI H_2O) followed by the addition of 24 mL hydrochloric acid (HCl). Wearing all appropriate HF etching PPE, add 4 mL of hydrofluoric acid (HF) to the etchant container. Perform selective etching by slowly adding 2 g Ti_3AlC_2 MAX phase to the reaction container and stirring with a Teflon magnetic bar for 24 h at 35 °C at 400 rpm.

1.3. **Washing: Bringing the material to neutral pH.** Fill (2) 175 mL centrifuge tubes with 100 mL of deionized water. Split the etching reaction mixture into 175 mL centrifuge tubes and wash the material by repeated centrifugation at 3500 rpm (2550 rcf) for 5

min. Decant the acidic supernatant into a plastic hazardous waste container. Repeat until the pH reaches 6.

1.4. **Intercalation: Insertion of molecules between multilayer MXene particle to waken out-of-plane interactions.** Add 2 g lithium chloride (LiCl) to 100 mL of DI H_2O and stir at 200 rpm until dissolved. Mix 100 mL of LiCl/H_2O with the Ti_3C_2/Ti_3AlC_2 sediment and stir the reaction for 12 h at 25 °C.

1.5. **Delamination: Exfoliation from bulk multilayer particle into single- to few- layer Ti_3C_2 MXene.** Wash the intercalation reaction in 175 mL centrifuge tubes by centrifugation at 3500 rpm for 5 min. Decant the clear supernatant. Repeat until a dark supernatant is found. Continue to centrifuge for 1 h at 3500 rpm (2550 rcf). Decant the dilute-green supernatant. Re-disperse the swollen sediment with 150 mL of DI H_2O (re-dispersion will become difficult and will require agitation or manual shaking). Transfer supernatant to 50 mL centrifuge tubes and centrifuge at 3500 rpm for 10 min to separate remaining MAX (sediment) from MXene (supernatant). Collect supernatant as Ti_3C_2 MXene. Further size selection and optimization of the solution should be performed to isolate single- to few-layer flakes by collecting the supernatant following a centrifugation step at 3500 rpm for 1 h.

1.6. **Solution Storage: Packaging the MXene ink for long-term storage.** Solutions are Argon bubbled for 30 min prior to packaging in an Argon sealed headspace vial (transfer *via* a syringe). Solutions are stored at high concentrations (> 5 mg/mL), away from sunlight, and at low temperatures (≤ 5 °C) to ensure longevity.

2. Fabrication of Ti_3C_2 MXene Microelectrode Arrays

NOTE: The procedure described in this section is intended for use inside a standard university clean room facility, such as the Singh Center for Nanotechnology at the University of Pennsylvania. This facility, as well as similar facilities, are accessible to outside users as part of the National Nanotechnology Infrastructure Network (NNIN) supported by the National Science Foundation (NSF). In these facilities, many of the tools, equipment, and materials described in this section are provided along with access to the clean room facility and would not require separate purchase.

CAUTION: Many of the chemicals used in the fabrication of MXene electrodes are hazardous, including photoresists, RD6 developer, remover PG, aluminum etching solution, and buffered oxide etchant. Consult the materials safety data sheets (MSDS) for these chemicals before use and implement and follow appropriate safety measures at all times.

2.1. Deposit a 4 µm-thick bottom layer of parylene-C onto a clean Si wafer. (Figure A1a)

2.2. Use the first photomask (mask-1) to define the metal interconnects of the devices, as well as a metal ring around the edge of the wafer to aid in later lift-off steps. (Figure A1b)

2.2.1. Spin coat NR71-3000p onto the wafer at 3000 rpm for 40 s.

2.2.2. Soft bake the wafer on a hot plate for 14.5 min at 95 °C.

2.2.3. Load the wafer and mask-1 into a mask aligner. Position the wafer so that the ring on the photomask overlaps with all edges of the wafer.

2.2.4. Expose with i-line (365 nm wavelength) at a dose of 90 mJ/cm^2.

2.2.5. Hard bake the wafer on a hot plate for 1 min at 115 °C.

2.2.6. Immerse the wafer in RD6 developer for 2 min, continuously agitating the solution. Rinse thoroughly with DI and blow dry with an N_2 gun.

2.2.7. Use an electron beam evaporator to deposit 10 nm Ti, followed by 100 nm Au onto the wafer. NOTE: Typical deposition parameters are a base pressure of 5×10^{-7} Torr and a rate of 2 Å/s.

2.2.8. Immerse the wafer in remover PG for approximately 10 min until the photoresist has dissolved and the excess metal has fully lifted off, leaving Ti/Au only in the desired interconnect traces and the ring around the edge of the wafer. Once lift-off appears complete, sonicate for 30s to remove any remaining traces of unwanted metal. Rinse wafer first in clean remover PG solution, then thoroughly rinse in DI H_2O and dry the wafer with an N_2 gun.

2.3. Deposit the sacrificial parylene-C layer. (Figure A1c)

2.3.1. Expose the wafer to O_2 plasma for 30 s to render the underlying parylene-C layer hydrophilic.

2.3.2. Spin coat 2% Micro-90 in DI H_2O solution onto the wafer at 1000 rpm for 30 s. This dilute soap solution acts as an anti-adhesive, allowing the sacrificial parylene-

C layer to be peeled up later in the process. Allow wafer to air dry for at least 5 mins.

2.3.3. Deposit 3 μm of parylene-C onto the wafer

2.4. Use the second photomask (mask-2) to define the MXene patterns and a ring around the edge of the wafer. (Figure A1d)

2.4.1. Repeat steps 2.2.1 through 2.2.6, this time using mask-2 and carefully aligning the alignment marks between the wafer and photomask before exposure.

2.4.2. Use O_2 plasma reactive ion etching (RIE) to etch through the sacrificial parylene-C layer in the areas not covered by the photoresist to define the MXene electrodes and traces, which should partially overlap with the Ti/Au interconnects, as well as the ring around the edges of the wafer. Confirm complete etching of the sacrificial parylene-C layer by using a profilometer to measure the profile between the exposed Ti/Au interconnects and the bottom parylene-C layer. When etching is complete, the profile across the exposed metal surface will be smooth, while the bottom parylene-C layer will be rough and partially etched. NOTE: This etch step should be completed in a planar etch RIE system, not a barrel asher, and etch times and parameters will be highly dependent on the RIE system.

2.5. Spin-coat the MXene solution onto the wafer. (Figure A1e)

2.5.1. Pipette MXene solution onto each of the desired MXene patterns, then spin the wafer at 1000 rpm for 40 s.

2.5.2. Dry the wafer on a 120 °C hot plate for 10 mins to remove any residual water from the MXene film.

2.6. Use an electron beam evaporator to deposit 50 nm SiO_2 onto the wafer, to act as a protective layer over the MXene patterns for subsequent processing steps. NOTE: Typical deposition parameters are a base pressure of 5 x 10^{-7} Torr and a rate of 2 Å/s.

2.7. Remove the sacrificial parylene-C layer to pattern the MXene and SiO2 layers. (Figure A1f).

2.7.1. Apply a small drop of DI H_2O to the edge of the wafer and use tweezers to peel up the sacrificial parylene-C layer, beginning where its edges are defined in the ring

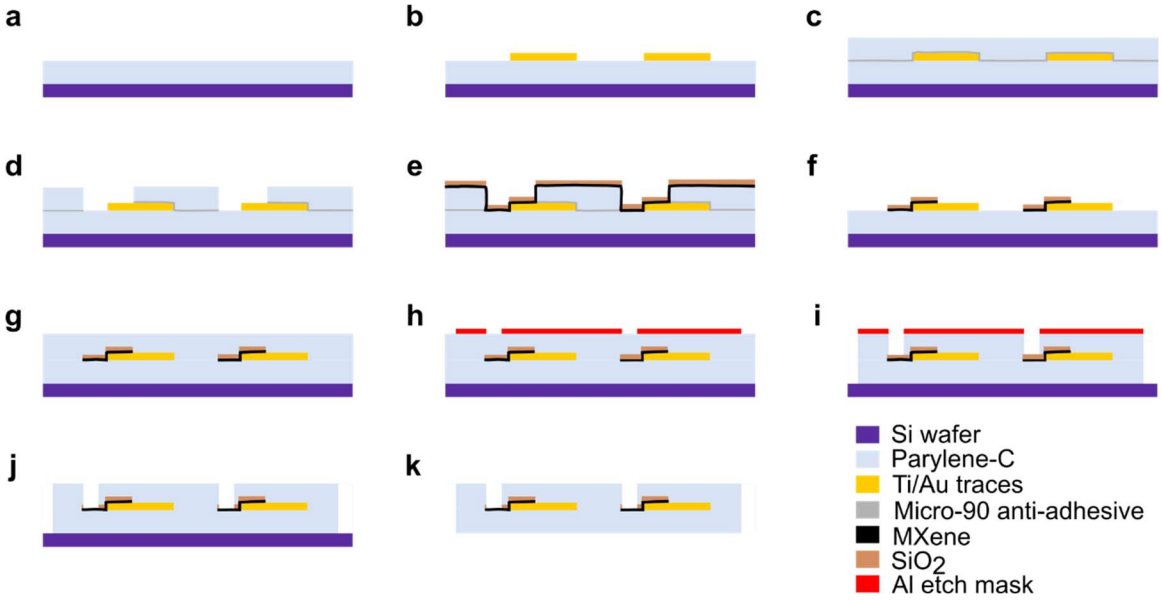

Figure A1. Schematics of the fabrication procedure for MXene microelectrode arrays. (a) Bottom parylene-C layer is deposited on a clean Si wafer. (b) Ti/Au (10 nm/100 nm) conductive traces are patterned through photolithography, e-beam deposition, and lift-off. (c) An anti-adhesive layer of 1% Micro-90 in DI H2O is applied, followed by deposition of a sacrificial parylene-C layer. (d) The sacrificial parylene-C layer is patterned through photolithography and O2 RIE etching. (e) Ti3C2 MXene is spin-coated onto the wafer, followed by e-beam deposition of 50 nm of SiO2. (f) The sacrificial parylene-C layer is lifted off, residues of Micro-90 are rinsed off, and the wafer is baked dry. (g) Top parylene-C layer is deposited. (h) An Al etch mask layer is patterned through photolithography, e-beam deposition, and lift-off to define VIAs and device outline. (i) Parylene-C over electrode contacts and surrounding devices is etched away through O2 RIE. (j) Al etch mask and SiO2 protective layer over MXene are etched away through wet etch processes. (k) Finished device is lifted off wafer.

around the outside of the wafer. The water will combine with the soap residue beneath the sacrificial parylene-C layer to enable this lift-off.

2.7.2. Rinse the wafer thoroughly in DI H_2O to remove any remaining Micro-90 residue. Dry the wafer with an N2 gun, then place on a 120 °C hot plate for 1 h to remove any residual water from the patterned MXene films.

2.8. Deposit the 4 µm-thick top layer of parylene-C. (Figure A1g)

2.9. Use the third photomask (mask-3) to define device outline and openings over electrodes and Au bonding pads (VIAs) (Figure A1h)

2.9.1. Repeat steps 2.2.1 through 2.2.6, this time using mask-3 and carefully aligning the alignment marks between the wafer and photomask before exposure.

2.9.2. Use an electron beam evaporator to deposit 100 nm Al onto the wafer. NOTE: Typical deposition parameters are a base pressure of 5 x 10^{-7} Torr and a rate of 2 Å/s.

2.9.3. Immerse the wafer in remover PG for approximately 10 min until the metal has fully lifted off, leaving Al covering the devices with openings for the electrodes and bonding pads. When lift-off is complete, sonicate for 30s to remove any remaining traces of unwanted metal. Rinse wafer first in clean remover PG solution, then thoroughly rinse in DI H_2O and dry the wafer with an N_2 gun.

2.10. Etch the parylene-C to pattern the device outline and openings over electrodes and Au bonding pads (VIAs) (Figure A1i)

2.10.1. Use O_2 plasma RIE to etch through the parylene-C layers surrounding the devices, and through the top parylene-C layer covering both the MXene electrode contacts and the Au bonding pads. Etching is complete when no parylene-C residue remains on the wafer between devices. The SiO_2 layer covering the MXene will act as an etch-stop layer, preventing the O_2 plasma from etching into or damaging the MXene electrode contacts.

2.11. Etch the Al layer covering the devices using a wet chemical etch in Al etchant Type A at 50 °C for 10 min, or for 1 min past when all visual traces of Al have been removed.

2.12. Etch the SiO_2 covering the MXene electrodes using a wet chemical etch in 6:1 buffered oxide etchant (BOE) for 30 s. (**Figure A1j**)

2.13. The MXene microelectrode arrays are now complete. They can be released from the Si substrate wafer by placing a small drop of DI H_2O water at the edge of a device, and gently peeling up the device as water is wicked underneath it by capillary action. (**Figure A1k** and **Figure A2**)

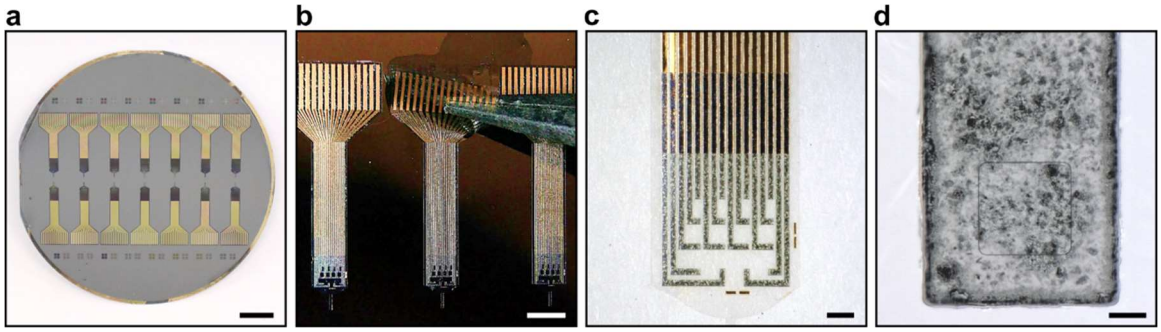

Figure A2. Photographs and optical microscopy images of MXene microelectrode arrays. (a) Photograph of a 3 inch Si wafer containing 14 completed MXene microelectrode arrays. Note the gold ring around the outer edge of the wafer, which is helpful for performing step 2.7 effectively. (b) Optical microscope image showing the peeling up of a completed device from the wafer using a small amount of DI H2O. (c) Optical microscope image showing the array of MXene microelectrodes. (d) Optical microscope image of an individual MXene electrode. Scale bars, left to right: 1 cm, 3 mm, 500 µm, 20 µm.

3. Adapter Construction and Interfacing

NOTE: At this point, the thin film microelectrode arrays must be interfaced with an adapter to connect to the electrophysiology recording system. In this protocol, we use the Intan 128ch Stimulation/Recording Controller with the RHS2000 16-ch stim/record headstage, which requires input *via* a connector compatible with the Omnetics 18-pin connector A79039-001. This section uses a printed circuit board (PCB, **Figure A3a**) with a zero-insertion force (ZIF) connector for interfacing with the Au bonding pads on the microelectrode array and Omnetics connector A79040-001 for interfacing with the head-stage of the recording system. Depending on the data acquisition system, different connectors can be used on the PCB to enable interfacing with the electrophysiology headstage.

3.1. **Solder the Omnetics and ZIF connectors to the PCB** by applying a thin film of solder paste to each of the contact pads on the PCB, placing the parts in their appropriate locations, and heating on a hot plate until the solder reflows to form connections (**Figure A3b**). NOTE: Reflow soldering can be done very easily on a hot plate or in a toaster oven and does not require the use of a costly reflow oven.

3.2. **Apply two layers of Kapton tape** to the back side of the Au bonding pad region of the MXene microelectrode array to give the device sufficient thickness to be secured in the

ZIF connector. After applying the tape, trim any excess beyond the edges of the parylene-C device using a razor blade or precision scissors (**Figure A3c**).

3.3. Either under an inspection scope or using magnifying glasses, **align the MXene microelectrode array in the ZIF connector** so that the Au bonding pads align with the pins inside the ZIF connector, then close the ZIF to form a secure connection (**Figure A3d,e**). NOTE: The ZIF connector used here is an 18-channel connector, while our device has 16 channels. The extra uncontacted channels are easily identified as an open circuit by means of impedance testing during recording sessions.

3.4. **Test the electrochemical impedance of the MXene electrodes** using a potentiostat to ensure successful fabrication and connection to the PCB adapter. Reasonable impedance values are given in the Discussion section to aid in troubleshooting.

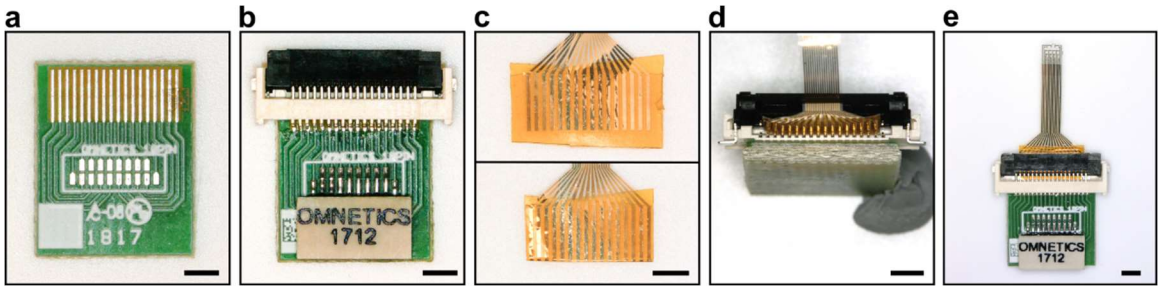

Figure A3. Interfacing the MXene microelectrode array with the adapter board. (a) PCB with pads for soldering Omnetics and ZIF connectors. (b) PCB after soldering of Omnetics and ZIF connectors. (c) Addition of Kapton layers to back side of Au bonding pads of device, to give sufficient thickness for the ZIF connector. Two layers of Kapton are added (top) and then trimmed around the edges (bottom). (d) MXene microelectrode array inserted into ZIF connector with proper alignment. (e) Top view of MXene microelectrode array connected to adapter board and ready for a recording experiment. Scale bars are 2 mm.

4. Acute Implantation and Neural Recording

NOTE: All *in vivo* procedures conformed to the National Institutes of Health (NIH) Guide for the Care and Use of Laboratory Animals and were approved by the Institutional Animal Care and Use Committee (IACUC) of the University of Pennsylvania. Rat surgeries were performed using sterile instruments and with aseptic technique. Respiratory rate, palpebral reflex, and

pedal pinch reflex were checked every 10 min to monitor depth of anesthesia. Body temperature was maintained with a heating pad.

4.1. Administer preemptive analgesia (subcutaneous injection of buprenorphine SR, 1.2 mg/kg).
4.2. Administer anesthesia (intraperitoneal injection of a mixture of 60 mg/kg ketamine and 0.25 mg/kg dexdomitor)
4.3. Secure rat in stereotaxic frame, apply ocular lubricant to the eyes, and clean shaved scalp with 10% povidone-iodine.
4.4. Expose the calvaria with single midline scalp incision and blunt dissection of underlying tissue.
4.5. Place a 00-90 screw into the skull to serve as the ground for recordings.
4.6. Using a dental drill with a small burr, make a craniotomy at the desired cortical recording site.
4.7. Secure the array connector to a stereotaxic manipulator and position the device over the craniotomy. Gently lower until the entire array is in contact with the exposed cortex.
4.8. Wrap the ground wire around the skull screw.
4.9. Connect the recording system headstage to the array and begin recording spontaneous activity.

Discussion

The MXene synthesis and delamination procedure described in this protocol (HF/HCl/LiCl) was built from the MILD etching approach which employed a LiF/HCl (*in situ* HF) etchant medium [224]. The MILD approach allows for large Ti_3C_2 flakes (several μm in lateral size) to be spontaneously delaminated during washing once pH ~5-6 has been attained. Compared to etching with HF alone, this results in material with higher quality and improved material properties, such as electronic conductivity and chemical stability. The HF/HCl/LiCl method takes advantage of the MILD synthesis improvements, while additionally separating each step (etching, intercalation, and delamination) allowing for more user control.

During step 1.1, the ratio of raw materials (TiC, Al, Ti), temperature, temperature ramp rate, and time are critical to achieving the correct MAX phase. Sieving of the MAX phase prior to etching will ensure more homogenous etching. Adding the MAX phase to the etchant media (step 1.2) must be conducted slowly to prevent overheating and a general rule of 5 min per 1 g of MAX is suggested. If overheating becomes a challenge, an ice bath should be employed during addition of the Ti_3AlC_2 MAX phase. When washing the etching reaction to neutral pH (step 1.3), each acidic supernatant after centrifugation should be transparent. If the supernatant after centrifugation is dark or dilute green, increase the centrifuge time and/or speed to sediment material. Because the addition of LiCl to H_2O is exothermic, some heating will occur (step 1.4). In this procedure, the intercalation time (step 1.4) is 12 h, although it can be modified or shortened to as little as 15 minutes. The quality of delamination (step 1.5) is specific to the quantity of water used during washing and the degree of agitation. The supernatants decanted during this step may be dilute instead of transparent. If sedimentation of material becomes a challenge, increasing the centrifuge speed/rcf should be used. It is critical to perform separation and size selection by centrifugation (step 1.5) to avoid polydisperse samples. Failure to perform this step will result in an ink that has both Ti_3AlC_2 MAX phase contamination and large multilayer Ti_3C_2 particles. During step 1.6, it is important that the headspace volume of the vial is minimized.

During the fabrication of the MXene microelectrode arrays, there are several critical steps which are essential for producing functioning, high-quality electrodes. It is important

to design the first photomask such that there is a metal ring patterned around the outer edge of the wafer (step 2.2) and the second photomask such that there is a corresponding, slightly larger diameter ring which will be etched through the sacrificial parylene-C (step 2.4) layer to aid in removing the sacrificial layer. Without this ring, it can be difficult to establish an edge to begin peeling up the sacrificial parylene-C layer in step 2.7. During step 2.3, it is critical to expose the wafer to O_2 plasma to allow the dilute Micro-90 solution to properly wet and adhere to the wafer. Failure to perform this step will result in areas of the wafer not accumulating a Micro-90 anti-adhesive layer, which renders the removal of the sacrificial parylene-C layer in step 2.7 impossible. During the removal of the sacrificial parylene-C layer in step 2.7, it is important to be careful to avoid scratching or damaging the bottom parylene-C layer, as this can lead to the formation of bubbles between the bottom parylene-C and the Si wafer, and subsequent delamination. If the sacrificial parylene-C layer does not peel up easily, a slightly more concentrated Micro-90 solution (4% in DI) can be used in step 2.3.2, or the O_2 plasma exposure in step 2.3.1 can be prolonged to improve hydrophilicity of the underlying parylene-C layer.

After the fabrication is completed, properly interfacing the MXene device with the connector board is essential. The addition of two layers of Kapton tape in step 3.2 is essential to ensure proper thickness for insertion into the ZIF connector, however care should be taken to avoid accidental folding or crumpling of the thin parylene-C device while the tape is added, as it is not possible to remove the tape without damaging the device. Subsequently, proper alignment of the Au bonding pads on the MXene device with pins inside the ZIF connector (**Figure A3d**) is essential for forming a robust connection (step 3.3). At this stage, measuring the impedance of the MXene electrodes is helpful for troubleshooting. A 50 μm x 50 μm square MXene electrode should have an impedance magnitude near 50 kΩ at a frequency of 1 kHz in 1x PBS, and a 25 μm diameter circular MXene electrode should have an impedance magnitude near 200 kΩ under the same parameters [312]. An impedance significantly larger than this can indicate that the electrode is not properly connected in the ZIF connector, or that the MXene electrode is not exposed, as may happen if either the top parylene-C layer was not completely etched in step 2.10.1 or the SiO_2 protective layer was not fully etched in step 2.12.

One limitation of this method is variability in MXene film thickness that is sometimes observed after spin-casting MXene onto the wafer. This variability can become more pronounced if electrodes are scaled up to larger areas. This limitation can be readily overcome by utilizing spray-coating instead of spin-coating to apply MXene to the wafer, representing another simple, low-cost solution processing method with which MXene, and this protocol, are compatible [307].

The protocol described here presents exciting new opportunities in neuroscience and in the larger field of bioelectronics. While there has long been interest in leveraging carbon-based nanomaterials for neural microelectrodes, the incorporation of Ti_3C_2 MXene into such electrodes has enabled significantly simpler and more high-throughput fabrication than has been possible with other carbon-based nanomaterials. Furthermore, the outstanding properties of Ti_3C_2 MXene endow the electrodes with remarkably low impedance for their size, thus improving sensitivity and signal quality. A growing body of literature also describes a number of methods for micropatterning MXene, which may be adapted for fabricating MXene microelectrodes in the future, including micro-contact printing [263], inkjet printing [274], [278], and automated scalpel engraving [276]. There exists great potential to extend this protocol to fabricate Ti_3C_2 MXene electrodes of arbitrary size and geometry for a range of biosensing applications.

References

[1] H. Bink *et al.*, "Spatiotemporal Evolution of Focal Epileptiform Activity from Surface and Laminar Field Recordings in Cat Neocortex," *J. Neurophysiol.*, p. jn.00764.2017, Feb. 2018.

[2] M. Stead *et al.*, "Microseizures and the spatiotemporal scales of human partial epilepsy," *Brain*, vol. 133, no. 9, pp. 2789–2797, Sep. 2010.

[3] C. A. Schevon *et al.*, "Microphysiology of Epileptiform Activity in Human Neocortex," *J. Clin. Neurophysiol.*, vol. 25, no. 6, pp. 321–330, Dec. 2008.

[4] O. Yizhar, L. E. Fenno, T. J. Davidson, M. Mogri, and K. Deisseroth, "Optogenetics in Neural Systems," *Neuron*. 2011.

[5] E. Yaksi and R. W. Friedrich, "Reconstruction of firing rate changes across neuronal populations by temporally deconvolved Ca2+ imaging," *Nat. Methods*, vol. 3, no. 5, pp. 377–383, May 2006.

[6] D. Kuzum *et al.*, "Transparent and flexible low noise graphene electrodes for simultaneous electrophysiology and neuroimaging," *Nat. Commun.*, vol. 5, no. May, p. 5259, Oct. 2014.

[7] D.-W. Park *et al.*, "Graphene-based carbon-layered electrode array technology for neural imaging and optogenetic applications.," *Nat. Commun.*, vol. 5, no. Di, p. 5258, Oct. 2014.

[8] M. Thunemann *et al.*, "Deep 2-photon imaging and artifact-free optogenetics through transparent graphene microelectrode arrays," *Nat. Commun.*, vol. 9, no. 1, p. 2035, Dec. 2018.

[9] Y. Qiang *et al.*, "Transparent arrays of bilayer-nanomesh microelectrodes for simultaneous electrophysiology and two-photon imaging in the brain," *Sci. Adv.*, vol. 4, no. 9, p. eaat0626, Sep. 2018.

[10] J. E. Ferguson, C. Boldt, and A. D. Redish, "Creating low-impedance tetrodes by electroplating with additives," *Sensors Actuators A Phys.*, vol. 156, no. 2, pp. 388–393, Dec. 2009.

[11] C. Boehler, T. Stieglitz, and M. Asplund, “Nanostructured platinum grass enables superior impedance reduction for neural microelectrodes,” *Biomaterials*, vol. 67, pp. 346–353, Oct. 2015.

[12] A. Petrossians, J. J. Whalen, J. D. Weiland, and F. Mansfeld, “Surface modification of neural stimulating/recording electrodes with high surface area platinum-iridium alloy coatings,” in *2011 Annual International Conference of the IEEE Engineering in Medicine and Biology Society*, 2011, pp. 3001–3004.

[13] R. D. Meyer, S. F. Cogan, T. H. Nguyen, and R. D. Rauh, “Electrodeposited iridium oxide for neural stimulation and recording electrodes,” *IEEE Trans. Neural Syst. Rehabil. Eng.*, vol. 9, no. 1, pp. 2–11, Mar. 2001.

[14] M. David Pur *et al.*, “All-carbon-nanotube flexible multi-electrode array for neuronal recording and stimulation,” *Biomed. Microdevices*, vol. 16, no. 1, pp. 43–53, 2014.

[15] H. Yoon, P. Hankins, S. Oh, R. E. Harbaugh, and V. K. Varadan, “Heterostructured IrO 2 / Au Nanowire Electrodes and Unit Recordings From Hippocampal Rat Brain,” 2010.

[16] Y. Lu, H. Lyu, A. G. Richardson, T. H. Lucas, and D. Kuzum, “Flexible Neural Electrode Array Based-on Porous Graphene for Cortical Microstimulation and Sensing,” *Sci. Rep.*, vol. 6, no. 1, p. 33526, Dec. 2016.

[17] X. Liang *et al.*, “Toward Clean and Crackless Transfer of Graphene,” *ACS Nano*, vol. 5, no. 11, pp. 9144–9153, Nov. 2011.

[18] B. Anasori, M. R. Lukatskaya, and Y. Gogotsi, “2D metal carbides and nitrides (MXenes) for energy storage,” *Nat. Rev. Mater.*, vol. 2, no. 2, p. 16098, Jan. 2017.

[19] F. Shahzad *et al.*, “Electromagnetic interference shielding with 2D transition metal carbides (MXenes).,” *Science*, vol. 353, no. 6304, pp. 1137–40, Sep. 2016.

[20] J. Yan *et al.*, “Flexible MXene/Graphene Films for Ultrafast Supercapacitors with Outstanding Volumetric Capacitance,” *Adv. Funct. Mater.*, vol. 27, no. 30, p. 1701264, Aug.

2017.

[21] C. J. Zhang *et al.*, “Transparent, Flexible, and Conductive 2D Titanium Carbide (MXene) Films with High Volumetric Capacitance,” *Adv. Mater.*, vol. 29, no. 36, p. 1702678, Sep. 2017.

[22] M. R. Lukatskaya *et al.*, “Ultra-high-rate pseudocapacitive energy storage in two-dimensional transition metal carbides,” 2017.

[23] S. Lee *et al.*, “Toward Bioelectronic Medicine—Neuromodulation of Small Peripheral Nerves Using Flexible Neural Clip,” *Adv. Sci.*, vol. 4, no. 11, p. 1700149, Nov. 2017.

[24] M. R. DeLong and T. Wichmann, “Basal ganglia circuits as targets for neuromodulation in Parkinson disease,” *JAMA Neurology*, vol. 72, no. 11. American Medical Association, pp. 1354–1360, 01-Nov-2015.

[25] H. Irisawa, H. F. Brown, and W. Giles, “Cardiac pacemaking in the sinoatrial node,” *Physiological Reviews*, vol. 73, no. 1. pp. 197–227, 1993.

[26] G. T. Hwang *et al.*, “Self-powered cardiac pacemaker enabled by flexible single crystalline PMN-PT piezoelectric energy harvester,” *Adv. Mater.*, vol. 26, no. 28, pp. 4880–4887, Jul. 2014.

[27] L. Ulloa, S. Quiroz-Gonzalez, and R. Torres-Rosas, “Nerve Stimulation: Immunomodulation and Control of Inflammation,” *Trends in Molecular Medicine*, vol. 23, no. 12. Elsevier Ltd, pp. 1103–1120, 01-Dec-2017.

[28] J. Cheng, H. Shen, R. Chowdhury, T. Abdi, F. Selaru, and J. D. Z. Chen, “Potential of Electrical Neuromodulation for Inflammatory Bowel Disease,” *Inflamm. Bowel Dis.*, vol. 26, no. 8, pp. 1119–1130, Jul. 2020.

[29] F. Vitale and B. Litt, “Bioelectronics: the promise of leveraging the body’s circuitry to treat disease,” *Bioelectron. Med.*, vol. 1, no. 1, pp. 3–7, Jan. 2018.

[30] G. Litscher, G. Kehl, G. Schwarz, and H. P. Soyer, “Inflammatory reactions of the skin caused by adhesive EEG electrodes,” *J. Neurosurg. Anesthesiol.*, vol. 9, no. 3, pp. 277–279, 1997.

[31] S. S. Barold, “Willem Einthoven and the birth of clinical electrocardiography a hundred years ago,” *Card. Electrophysiol. Rev.*, vol. 7, no. 1, pp. 99–104, Jan. 2003.

[32] J. D. Bronzino, “Principles of Electroencephalography,” in *Biomedical Engineering Fundamentals*, J. D. Bronzino and D. R. Peterson, Eds. CRC Press, 2014, pp. 47-1-47–12.

[33] K. Jeffrey, *Machines in Our Hearts*. Johns Hopkins University Press, 2001.

[34] J. Gardner, “A history of deep brain stimulation: Technological innovation and the role of clinical assessment tools,” *Soc. Stud. Sci.*, vol. 43, no. 5, pp. 707–728, Oct. 2013.

[35] J. Yang and J. H. Phi, “The present and future of vagus nerve stimulation,” *J. Korean Neurosurg. Soc.*, vol. 62, no. 3, pp. 344–352, May 2019.

[36] F. T. Sun, M. J. Morrell, and R. E. Wharen, “Responsive Cortical Stimulation for the Treatment of Epilepsy,” *Neurotherapeutics*, vol. 5, no. 1, pp. 68–74, Jan. 2008.

[37] F. G. Zeng, S. Rebscher, W. Harrison, X. Sun, and H. Feng, “Cochlear Implants: System Design, Integration, and Evaluation,” *IEEE Rev. Biomed. Eng.*, vol. 1, pp. 115–142, 2008.

[38] J. D. Weiland, W. Liu, and M. S. Humayun, “Retinal Prosthesis,” *Annu. Rev. Biomed. Eng.*, vol. 7, no. 1, pp. 361–401, Aug. 2005.

[39] L. R. Hochberg *et al.*, “Neuronal ensemble control of prosthetic devices by a human with tetraplegia,” *Nature*, vol. 442, no. 7099, pp. 164–171, Jul. 2006.

[40] R. Maskeliunas, R. Damasevicius, I. Martisius, and M. Vasiljevas, “Consumer-grade EEG devices: Are they usable for control tasks?,” *PeerJ*, vol. 2016, no. 3, 2016.

[41] M. Van Vliet, A. Robben, N. Chumerin, N. V. Manyakov, A. Combaz, and M. M. Van Hulle, “Designing a brain-computer interface controlled video-game using consumer grade EEG hardware,” in *2012 ISSNIP Biosignals and Biorobotics Conference: Biosignals and Robotics*

for Better and Safer Living (BRC), 2012, pp. 1–6.

[42] S. H. Liu, C. B. Lin, Y. Chen, W. Chen, T. S. Huang, and C. Y. Hsu, "An EMG patch for the real-time monitoring of muscle-fatigue conditions during exercise," *Sensors (Switzerland)*, vol. 19, no. 14, 2019.

[43] M. M. Merzenich, R. J. Nelson, M. P. Stryker, M. S. Cynader, A. Schoppmann, and J. M. Zook, "Somatosensory cortical map changes following digit amputation in adult monkeys," *J. Comp. Neurol.*, vol. 224, no. 4, pp. 591–605, Apr. 1984.

[44] G. Buzsaki, *Rhythms of the Brain*. Oxford Univ Press, 2006.

[45] G. Buzsáki, C. A. Anastassiou, and C. Koch, "The origin of extracellular fields and currents -- EEG, ECoG, LFP and spikes.," *Nat Rev Neurosci*, vol. 13, no. 6, pp. 407–420, 2012.

[46] H. Lindén, K. H. Pettersen, and G. T. Einevoll, "Intrinsic dendritic filtering gives low-pass power spectra of local field potentials," *J. Comput. Neurosci.*, vol. 29, no. 3, pp. 423–444, 2010.

[47] P. L. Nunez and R. Srinivasan, *Electric fields of the brain: the neurophysics of EEG*. Oxford University Press, 2006.

[48] L. Zhukov, D. Weinsfein, and C. Johnson, "Independent component analysis for EEG source localization an algorithm that reduces the complexity of localizing multiple neural sources," *IEEE Eng. Med. Biol. Mag.*, vol. 19, no. 3, pp. 87–96, 2000.

[49] C. Plummer, A. S. Harvey, and M. Cook, "EEG source localization in focal epilepsy: Where are we now?," *Epilepsia*, vol. 49, no. 2. John Wiley & Sons, Ltd, pp. 201–218, 01-Feb-2008.

[50] Ad-Tech Medical Instrument Corporation, "Epilepsy & Neurosurgery Product Guide." 2005.

[51] K. J. Miller, L. B. Sorensen, J. G. Ojemann, and M. Den Nijs, "Power-law scaling in the brain surface electric potential," *PLoS Comput. Biol.*, vol. 5, no. 12, p. 1000609, Dec. 2009.

[52] J. Parvizi and S. Kastner, “Promises and limitations of human intracranial electroencephalography,” *Nat. Neurosci.*, vol. 21, no. 4, pp. 474–483, 2018.

[53] J. C. Williams, R. L. Rennaker, and D. R. Kipke, “Long-term neural recording characteristics of wire microelectrode arrays implanted in cerebral cortex,” *Brain Res. Protoc.*, vol. 4, no. 3, pp. 303–313, 1999.

[54] J. Viventi *et al.*, “Flexible, foldable, actively multiplexed, high-density electrode array for mapping brain activity in vivo,” *Nat. Neurosci.*, vol. 14, no. 12, pp. 1599–605, Nov. 2011.

[55] D. Khodagholy *et al.*, “NeuroGrid: recording action potentials from the surface of the brain,” *Nat Neurosci*, vol. 18, no. 2, pp. 310–315, Jan. 2015.

[56] J. J. Jun *et al.*, “Fully integrated silicon probes for high-density recording of neural activity,” *Nature*, vol. 551, no. 7679, pp. 232–236, Nov. 2017.

[57] E. M. Maynard, C. T. Nordhausen, and R. A. Normann, “The Utah intracortical electrode array: a recording structure for potential brain-computer interfaces,” *Electroencephalogr. Clin. Neurophysiol.*, vol. 102, no. 3, pp. 228–239, 1997.

[58] L. R. Hochberg *et al.*, “Reach and grasp by people with tetraplegia using a neurally controlled robotic arm,” *Nature*, vol. 485, no. 7398, pp. 372–375, May 2012.

[59] C. A. Chestek *et al.*, “Long-term stability of neural prosthetic control signals from silicon cortical arrays in rhesus macaque motor cortex.,” *J. Neural Eng.*, vol. 8, no. 4, p. 045005, Aug. 2011.

[60] S. F. Cogan, “Neural stimulation and recording electrodes.,” *Annu. Rev. Biomed. Eng.*, vol. 10, pp. 275–309, 2008.

[61] S. F. Cogan, T. D. Plante, and J. Ehrlich, “Sputtered iridium oxide films (SIROFs) for neural stimulation electrodes,” in *Annual International Conference of the IEEE Engineering in Medicine and Biology - Proceedings*, 2004, vol. 26 VI, pp. 4153–4156.

[62] C. Grienberger and A. Konnerth, “Imaging Calcium in Neurons,” *Neuron*, vol. 73, no. 5, pp. 862–885, Mar. 2012.

[63] R. M. Paredes, J. C. Etzler, L. T. Watts, W. Zheng, and J. D. Lechleiter, “Chemical calcium indicators,” *Methods*, vol. 46, no. 3, pp. 143–151, 2008.

[64] M. Mank and O. Griesbeck, “Genetically encoded calcium indicators,” *Chem. Rev.*, vol. 108, no. 5, pp. 1550–1564, 2008.

[65] N. J. Sofroniew, D. Flickinger, J. King, and K. Svoboda, “A large field of view two-photon mesoscope with subcellular resolution for in vivo imaging,” *Elife*, vol. 5, no. JUN2016, Jun. 2016.

[66] W. Zong *et al.*, “Fast high-resolution miniature two-photon microscopy for brain imaging in freely behaving mice,” 2017.

[67] Y. Xu, P. Zou, and A. E. Cohen, “Voltage imaging with genetically encoded indicators,” *Curr. Opin. Chem. Biol.*, vol. 39, pp. 1–10, 2017.

[68] R. U. Kulkarni and E. W. Miller, “Voltage Imaging: Pitfalls and Potential,” *Biochemistry*, vol. 56, p. 26, 2017.

[69] S. Chamberland *et al.*, “Fast two-photon imaging of subcellular voltage dynamics in neuronal tissue with genetically encoded indicators,” *Elife*, vol. 6, pp. 1–35, 2017.

[70] E. S. Boyden, F. Zhang, E. Bamberg, G. Nagel, and K. Deisseroth, “Millisecond-timescale, genetically targeted optical control of neural activity,” *Nat. Neurosci.*, vol. 8, no. 9, pp. 1263–1268, 2005.

[71] E. S. Boyden, “Optogenetics and the future of neuroscience,” *Nat. Neurosci.*, vol. 18, no. 9, pp. 1200–1201, 2015.

[72] A. M. Packer, B. Roska, and M. Häuser, “Targeting neurons and photons for optogenetics,” *Nat. Neurosci.*, vol. 16, no. 7, pp. 805–815, 2013.

[73] D. R. Sparta, A. M. Stamatakis, J. L. Phillips, N. Hovelsø, R. Van Zessen, and G. D. Stuber, "Construction of implantable optical fibers for long-term optogenetic manipulation of neural circuits," *Nat. Protoc.*, vol. 7, no. 1, pp. 12–23, 2012.

[74] A. N. Zorzos, E. S. Boyden, and C. G. Fonstad, "Multiwaveguide implantable probe for light delivery to sets of distributed brain targets," *Opt. Lett.*, vol. 35, no. 24, p. 4133, Dec. 2010.

[75] J. W. Reddy *et al.*, "High density, double-sided, flexible optoelectronic neural probes with embedded µLEDs," *Front. Genet.*, vol. 10, no. JUL, pp. 1–15, 2019.

[76] M. G. Scopelliti and M. Chamanzar, "Ultrasonic Guiding and Steering of Light in Scattering Tissue," *2018 Conf. Lasers Electro-Optics, CLEO 2018 - Proc.*, pp. 19–20, 2018.

[77] E. Papagiakoumou *et al.*, "Scanless two-photon excitation of channelrhodopsin-2," *Nat. Methods*, vol. 7, no. 10, pp. 848–854, 2010.

[78] V. Busskamp, S. Picaud, J. A. Sahel, and B. Roska, "Optogenetic therapy for retinitis pigmentosa," *Gene Ther.*, vol. 19, no. 2, pp. 169–175, 2012.

[79] P. A. Bottomley and E. R. Andrew, "RF magnetic field penetration, phase shift and power dissipation in biological tissue: Implications for NMR imaging," *Phys. Med. Biol.*, vol. 23, no. 4, pp. 630–643, 1978.

[80] P. M. Matthews, G. D. Honey, and E. T. Bullmore, "Applications of fMRI in translational medicine and clinical practice," *Nat. Rev. Neurosci.*, vol. 7, no. 9, pp. 732–744, 2006.

[81] A. Thanh Vu *et al.*, "Tradeoffs in pushing the spatial resolution of fMRI for the 7T Human Connectome Project," *Neuroimage*, vol. 154, no. November 2016, pp. 23–32, 2017.

[82] S. G. Kim, W. Richter, and K. Uğurbil, "Limitations of temporal resolution in functional MRI," *Magn. Reson. Med.*, vol. 37, no. 4, pp. 631–636, 1997.

[83] M. Hallett, "Transcranial Magnetic Stimulation: A Primer," *Neuron*, vol. 55, no. 2, pp. 187–199, 2007.

[84] U. Herwig, F. Padberg, J. Unger, M. Spitzer, and C. Schönfeldt-Lecuona, “Transcranial magnetic stimulation in therapy studies: Examination of the reliability of ‘standard’ coil positioning by neuronavigation,” *Biological Psychiatry*, vol. 50, no. 1. pp. 58–61, 2001.

[85] M. Roet, S. A. Hescham, A. Jahanshahi, B. P. F. Rutten, P. O. Anikeeva, and Y. Temel, “Progress in neuromodulation of the brain: A role for magnetic nanoparticles?,” *Prog. Neurobiol.*, vol. 177, no. March, pp. 1–14, 2019.

[86] D. Gregurec *et al.*, “Magnetic Vortex Nanodiscs Enable Remote Magnetomechanical Neural Stimulation,” *ACS Nano*, vol. 14, no. 7, pp. 8036–8045, 2020.

[87] C. Rabut *et al.*, “Ultrasound Technologies for Imaging and Modulating Neural Activity,” *Neuron*, vol. 108, no. 1, pp. 93–110, 2020.

[88] A. Urban, C. Dussaux, G. Martel, C. Brunner, E. Mace, and G. Montaldo, “Real-time imaging of brain activity in freely moving rats using functional ultrasound,” *Nat. Methods*, vol. 12, no. 9, pp. 873–878, 2015.

[89] F. Munoz, C. Aurup, E. E. Konofagou, and V. P. Ferrera, “Modulation of Brain Function and Behavior by Focused Ultrasound,” *Curr. Behav. Neurosci. Reports*, vol. 5, no. 2, pp. 153–164, 2018.

[90] W. J. Tyler, “Noninvasive neuromodulation with ultrasound? A continuum mechanics hypothesis,” *Neuroscientist*, vol. 17, no. 1, pp. 25–36, 2011.

[91] A. Prasad *et al.*, “Comprehensive characterization and failure modes of tungsten microwire arrays in chronic neural implants,” *J. Neural Eng.*, vol. 9, no. 5, p. 056015, Oct. 2012.

[92] J. C. Barrese *et al.*, “Failure mode analysis of silicon-based intracortical microelectrode arrays in non-human primates.,” *J. Neural Eng.*, vol. 10, no. 6, 2013.

[93] S. M. Wellman and T. D. Y. Kozai, “Understanding the Inflammatory Tissue Reaction to Brain Implants To Improve Neurochemical Sensing Performance.” ACS Publications, 2017.

[94] T. D. Y. Kozai, A. S. Jaquins-Gerstl, A. L. Vazquez, A. C. Michael, and X. T. Cui, "Brain Tissue Responses to Neural Implants Impact Signal Sensitivity and Intervention Strategies," *ACS Chem. Neurosci.*, vol. 6, no. 1, pp. 48–67, Jan. 2015.

[95] C. S. Bjornsson *et al.*, "Effects of insertion conditions on tissue strain and vascular damage during neuroprosthetic device insertion," *J. Neural Eng.*, vol. 3, no. 3, pp. 196–207, Sep. 2006.

[96] K. Nakajima, S. Honda, Y. Tohyama, Y. Imai, S. Kohsaka, and T. Kurihara, "Neurotrophin secretion from cultured microglia," *J. Neurosci. Res.*, vol. 65, no. 4, pp. 322–331, Aug. 2001.

[97] V. S. Polikov, P. A. Tresco, and W. M. Reichert, "Response of brain tissue to chronically implanted neural electrodes," *J. Neurosci. Methods*, vol. 148, no. 1, pp. 1–18, Oct. 2005.

[98] Y. Zhong and R. V. Bellamkonda, "Dexamethasone-coated neural probes elicit attenuated inflammatory response and neuronal loss compared to uncoated neural probes," *Brain Res.*, vol. 1148, no. 1, pp. 15–27, 2007.

[99] S. P. Lacour, G. Courtine, and J. Guck, "Materials and technologies for soft implantable neuroprostheses," *Nat. Rev. Mater.*, vol. 1, no. 10, p. 16063, 2016.

[100] L. Luan *et al.*, "Ultraflexible nanoelectronic probes form reliable, glial scar–free neural integration," *Sci. Adv.*, vol. 3, no. 2, p. e1601966, Feb. 2017.

[101] A. Obaid, Y.-W. Wu, M. Hanna, W. Nix, J. Ding, and N. Melosh, "Ultra-sensitive measurement of brain penetration with microscale probes for brain machine interface considerations," *bioRxiv*, vol. 10, p. 454520, 2018.

[102] A. Lecomte *et al.*, "Silk and PEG as means to stiffen a parylene probe for insertion in the brain: Toward a double time-scale tool for local drug delivery," *J. Micromechanics Microengineering*, vol. 25, no. 12, 2015.

[103] A. M. Stiller *et al.*, "Chronic Intracortical Recording and Electrochemical Stability of Thiol-ene / Acrylate Shape Memory Polymer Electrode Arrays," *Macromachines*, no. 9, p. 500,

2018.

[104] F. Vitale *et al.*, “Fluidic microactuation of flexible electrodes for neural recording,” *Nano Lett.*, vol. 18, no. 1, pp. 326–335, 2017.

[105] N. V. Apollo *et al.*, “Gels, jets, mosquitoes, and magnets: a review of implantation strategies for soft neural probes,” *J. Neural Eng.*, vol. 17, no. 4, p. 041002, 2020.

[106] T. D. Y. Kozai *et al.*, “Mechanical failure modes of chronically implanted planar silicon-based neural probes for laminar recording,” *Biomaterials*, vol. 37, pp. 25–39, Jan. 2015.

[107] X. Liang and S. A. Boppart, “Biomechanical properties of in vivo human skin from dynamic optical coherence elastography,” *IEEE Trans. Biomed. Eng.*, vol. 57, no. 4, pp. 953–959, 2010.

[108] D. H. Kim *et al.*, “Epidermal electronics,” *Science (80-.).*, vol. 333, no. 6044, pp. 838–843, 2011.

[109] G. Ge *et al.*, “Highly stretchable and autonomously healable epidermal sensor based on multi-functional hydrogel frameworks,” *J. Mater. Chem. A*, vol. 7, no. 11, pp. 5949–5956, 2019.

[110] Y. Yang *et al.*, “Liquid-Metal-Based Super-Stretchable and Structure-Designable Triboelectric Nanogenerator for Wearable Electronics,” *ACS Nano*, vol. 12, no. 2, pp. 2027–2034, 2018.

[111] S. M. Lee *et al.*, “Self-adhesive epidermal carbon nanotube electronics for tether-free long-term continuous recording of biosignals,” *Sci. Rep.*, vol. 4, p. 6074, 2014.

[112] J. Heikenfeld *et al.*, “Wearable sensors: Modalities, challenges, and prospects,” *Lab Chip*, vol. 18, no. 2, pp. 217–248, 2018.

[113] R. S. Ochia and P. R. Cavanagh, “Reliability of surface EMG measurements over 12 hours,” *J. Electromyogr. Kinesiol.*, vol. 17, no. 3, pp. 365–371, 2007.

[114] R. S. Johnston, L. F. Dietlein, C. A. Berry, F. Parker, J. Vernon, and E. Larry, “Biomedical Results of Apollo,” 1975.

[115] J. Li, P. Wang, and H. J. Huang, “Dry Epidermal Electrodes Can Provide Long-Term High Fidelity Electromyography for Limited Dynamic Lower Limb Movements,” *Sensors (Basel).*, vol. 20, no. 17, p. 4848, 2020.

[116] G. Schiavone and S. P. Lacour, “Conformable bioelectronic interfaces: Mapping the road ahead,” *Sci. Transl. Med.*, vol. 11, no. 503, Jul. 2019.

[117] E. Forvi *et al.*, “Preliminary technological assessment of microneedles-based dry electrodes for biopotential monitoring in clinical examinations,” *Sensors Actuators, A Phys.*, vol. 180, pp. 177–186, 2012.

[118] D. Gao, K. Parida, and P. S. Lee, “Emerging Soft Conductors for Bioelectronic Interfaces,” *Advanced Functional Materials*, vol. 30, no. 29. p. 1907184, 29-Nov-2019.

[119] G. Acar, O. Ozturk, A. Jedari Golparvar, T. Alkhidir Elboshra, K. Böhringer, and M. Kaya Yapici, “Wearable and Flexible Textile Electrodes for Biopotential Signal Monitoring: A review,” *mdpi.comSign in*.

[120] L. Tian *et al.*, “Large-area MRI-compatible epidermal electronic interfaces for prosthetic control and cognitive monitoring,” *Nat. Biomed. Eng.*, vol. 3, no. 3, pp. 194–205, Mar. 2019.

[121] C. Boehler, S. Carli, L. Fadiga, T. Stieglitz, and M. Asplund, “Tutorial: guidelines for standardized performance tests for electrodes intended for neural interfaces and bioelectronics,” *Nat. Protoc.*, 2020.

[122] R. A. Green *et al.*, “Laser patterning of platinum electrodes for safe neurostimulation,” *J. Neural Eng.*, vol. 11, no. 5, p. 56017, 2014.

[123] R. A. Green, H. Toor, C. Dodds, and N. H. Lovell, “Variation in performance of platinum electrodes with size and surface roughness,” *Sensors Mater.*, vol. 24, no. 4, pp. 165–180,

2012.

[124] S. F. Cogan, K. A. Ludwig, C. G. Welle, and P. Takmakov, “Tissue damage thresholds during therapeutic electrical stimulation,” *J Neural Eng*, vol. 13, no. 2, p. 21001, 2016.

[125] A. Butterwick, A. Vankov, P. Huie, Y. Freyvert, and D. Palanker, “Tissue damage by pulsed electrical stimulation,” *IEEE Trans. Biomed. Eng.*, vol. 54, no. 12, pp. 2261–2267, 2007.

[126] E. W. Keefer, B. R. Botterman, M. I. Romero, A. F. Rossi, and G. W. Gross, “Carbon nanotube coating improves neuronal recordings,” *Nat. Nanotechnol.*, vol. 3, no. 7, pp. 434–439, Jul. 2008.

[127] T. Gabay *et al.*, “Electro-chemical and biological properties of carbon nanotube based multi-electrode arrays,” *Nanotechnology*, vol. 18, no. 3, 2007.

[128] L. Bareket-Keren, Y. Hanein, A. El Hady, G. W. Knott, and D. J. Margolis, “Carbon nanotube-based multi electrode arrays for neuronal interfacing: progress and prospects,” 2013.

[129] K. Wang, H. A. Fishman, H. Dai, and J. S. Harris, “Neural Stimulation with a Carbon Nanotube Microelectrode Array,” 2006.

[130] J. Zhang *et al.*, “Stretchable transparent electrode array for simultaneous electrical and optical interrogation of neural circuits in vivo,” *Nano Lett.*, p. acs.nanolett.8b00087, 2018.

[131] L. M. Ericson *et al.*, “Macroscopic , Neat , Single-Walled Carbon Nanotube Fibers,” vol. 305, no. September, pp. 1447–1451, 2004.

[132] N. Behabtu *et al.*, “Strong, light, multifunctional fibers of carbon nanotubes with ultrahigh conductivity,” *Science (80-.).*, vol. 339, no. 6116, pp. 182–186, 2013.

[133] F. Vitale, S. R. Summerson, B. Aazhang, C. Kemere, and M. Pasquali, “Neural Stimulation and Recording with Bidirectional, Soft Carbon Nanotube Fiber Microelectrodes,” *ACS Nano*, vol. 9, no. 4, pp. 4465–4474, Apr. 2015.

[134] L. C. Ong, F. F. L. Chung, Y. F. Tan, and C. O. Leong, “Toxicity of single-walled carbon

nanotubes," *Arch. Toxicol.*, vol. 90, no. 1, pp. 103–118, 2016.

[135] H. Hu, Y. Ni, V. Montana, R. C. Haddon, and V. Parpura, "Chemically functionalized carbon nanotubes as substrates for neuronal growth," *Nano Lett.*, vol. 4, no. 3, pp. 507–511, 2004.

[136] M. P. Mattson, R. C. Haddon, and A. M. Rao, "Molecular functionalization of carbon nanotubes and use as substrates for neuronal growth," *J. Mol. Neurosci.*, vol. 14, no. 3, pp. 175–182, 2000.

[137] G. Cellot *et al.*, "Carbon nanotubes might improve neuronal performance by favouring electrical shortcuts," *Nat. Nanotechnol.*, vol. 4, no. 2, pp. 126–133, 2009.

[138] O. A. Williams, "Nanocrystalline diamond," *Diam. Relat. Mater.*, vol. 20, no. 5–6, pp. 621–640, 2011.

[139] D. M. Gruen, "Nanocrystalline diamond films," *Annu. Rev. Mater. Sci.*, vol. 29, no. 1, pp. 211–259, Aug. 1999.

[140] D. Garrett, K. Ganesan, A. Stacey, K. Fox, H. Meffin, and S. Prawer, "Ultra-nanocrystalline diamond electrodes: optimization towards neural stimulation applications," *J. Neural Eng.*, vol. 9, no. 1, p. 16002, 2012.

[141] P. Ariano *et al.*, "Cellular adhesion and neuronal excitability on functionalised diamond surfaces," *Diam. Relat. Mater.*, vol. 14, no. 3–7, pp. 669–674, 2005.

[142] V. C. Sanchez, A. Jachak, R. H. Hurt, and A. B. Kane, "Biological interactions of graphene-family nanomaterials: An interdisciplinary review," *Chem. Res. Toxicol.*, vol. 25, no. 1, pp. 15–34, 2012.

[143] X. Liu, Y. Lu, E. Iseri, Y. Shi, and D. Kuzum, "A Compact Closed-Loop Optogenetics System Based on Artifact-Free Transparent Graphene Electrodes," *Front. Neurosci.*, vol. 12, p. 132, Mar. 2018.

[144] Y. Lu *et al.*, "Ultralow Impedance Graphene Microelectrodes with High Optical

Transparency for Simultaneous Deep Two-Photon Imaging in Transgenic Mice," *Adv. Funct. Mater.*, vol. 28, no. 31, 2018.

[145] A. Bourrier *et al.*, "Monolayer Graphene Coating of Intracortical Probes for Long-Lasting Neural Activity Monitoring," *Adv. Healthc. Mater.*, vol. 8, no. 18, pp. 1–13, 2019.

[146] Y. Xu, K. Sheng, C. Li, and G. Shi, "Self-assembled graphene hydrogel via a one-step hydrothermal process," *ACS Nano*, vol. 4, no. 7, pp. 4324–4330, 2010.

[147] W. Chen and L. Yan, "In situ self-assembly of mild chemical reduction graphene for three-dimensional architectures," *Nanoscale*, vol. 3, no. 8, pp. 3132–3137, 2011.

[148] R. Garg *et al.*, "Nanowire-Mesh-Templated Growth of Out-of-Plane Three-Dimensional Fuzzy Graphene," *ACS Nano*, vol. 11, no. 6, pp. 6301–6311, 2017.

[149] S. K. Rastogi *et al.*, "Three-dimensional fuzzy graphene ultra-microelectrodes for subcellular electrical recordings," *Nano Res.*, vol. 13, no. 5, pp. 1444–1452, 2020.

[150] M. Stead *et al.*, "Microseizures and the spatiotemporal scales of human partial epilepsy," *Brain*, vol. 133, no. 9, pp. 2789–2797, Sep. 2010.

[151] M. Wenzel, J. P. Hamm, D. S. Peterka, and R. Yuste, "Acute Focal Seizures Start As Local Synchronizations of Neuronal Ensembles," *J. Neurosci.*, 2019.

[152] S. A. Weiss *et al.*, "Ictal high frequency oscillations distinguish two types of seizure territories in humans.," *Brain*, vol. 136, no. Pt 12, pp. 3796–808, Dec. 2013.

[153] W. Truccolo *et al.*, "Single-neuron dynamics in human focal epilepsy," *Nat. Publ. Gr.*, vol. 14, no. 5, 2011.

[154] C. A. Schevon *et al.*, "Evidence of an inhibitory restraint of seizure activity in humans," *Nat. Commun.*, vol. 3, no. 1, p. 1060, Jan. 2012.

[155] S. Tumpa, R. Thornton, M. Tisdall, T. Baldeweg, K. J. Friston, and R. E. Rosch, "Interictal discharges spread along local recurrent networks between tubers and surrounding

cortex," *bioRxiv*, no. 691170, 2019.

[156] E. H. Smith *et al.*, "The ictal wavefront is the spatiotemporal source of discharges during spontaneous human seizures," *Nat. Commun.*, vol. 7, no. 1, p. 11098, Sep. 2016.

[157] L.-E. Martinet, O. J. Ahmed, K. Q. Lepage, S. S. Cash, and M. a. Kramer, "Slow Spatial Recruitment of Neocortex during Secondarily Generalized Seizures and Its Relation to Surgical Outcome," *J. Neurosci.*, vol. 35, no. 25, pp. 9477–9490, 2015.

[158] C. A. Schevon *et al.*, "Multiscale recordings reveal the dynamic spatial structure of human seizures," *Neurobiology of Disease*, vol. 127. Academic Press Inc., pp. 303–311, 01-Jul-2019.

[159] E. H. Smith *et al.*, "Dual mechanisms of ictal high frequency oscillations in rhythmic onset seizures," *medRxiv*, p. 2020.01.09.20017053, Jan. 2020.

[160] T. H. Kim *et al.*, "Long-Term Optical Access to an Estimated One Million Neurons in the Live Mouse Cortex," *Cell Rep.*, vol. 17, no. 12, pp. 3385–3394, Dec. 2016.

[161] C. Stringer, M. Pachitariu, N. Steinmetz, C. B. Reddy, M. Carandini, and K. D. Harris, "Spontaneous behaviors drive multidimensional, brainwide activity," *Science (80-.).*, vol. 364, no. 6437, Apr. 2019.

[162] M. Wenzel, J. P. Hamm, D. S. Peterka, and R. Yuste, "Acute Focal Seizures Start As Local Synchronizations of Neuronal Ensembles," *J. Neurosci.*, 2019.

[163] S. F. Muldoon, I. Soltesz, and R. Cossart, "Spatially clustered neuronal assemblies comprise the microstructure of synchrony in chronically epileptic networks," *Proc. Natl. Acad. Sci. U. S. A.*, vol. 110, no. 9, pp. 3567–3572, 2013.

[164] S. F. Muldoon *et al.*, "GABAergic inhibition shapes interictal dynamics in awake epileptic mice," *Brain*, vol. 138, no. 10, pp. 2875–2890, Oct. 2015.

[165] T. Shuman *et al.*, "Breakdown of spatial coding and interneuron synchronization in

epileptic mice," *Nat. Neurosci.*, vol. 23, no. 2, pp. 229–238, Feb. 2020.

[166] B. A. Flusberg *et al.*, "High-speed, miniaturized fluorescence microscopy in freely moving mice.," *Nat. Methods*, vol. 5, no. 11, pp. 935–8, Nov. 2008.

[167] T. D. Y. Kozai and A. L. Vazquez, "Photoelectric artefact from optogenetics and imaging on microelectrodes and bioelectronics: New Challenges and Opportunities.," *J. Mater. Chem. B*, vol. 3, no. 25, pp. 4965–4978, Jul. 2015.

[168] A. N. Khambhati, J. D. Medaglia, E. A. Karuza, S. L. Thompson-Schill, and D. S. Bassett, "Subgraphs of functional brain networks identify dynamical constraints of cognitive control," *PLoS Comput. Biol.*, vol. 14, no. 7, Jul. 2018.

[169] A. E. Sizemore and D. S. Bassett, "Dynamic graph metrics: Tutorial, toolbox, and tale," *NeuroImage*, vol. 180. Academic Press Inc., pp. 417–427, 15-Oct-2018.

[170] L. R. Chai *et al.*, "Evolution of brain network dynamics in neurodevelopment," *Netw. Neurosci.*, vol. 1, no. 1, pp. 14–30, Feb. 2017.

[171] Y. Chen, X.-L. Gong, and J.-G. Gai, "Progress and Challenges in Transfer of Large-Area Graphene Films," *Adv. Sci.*, vol. 3, no. 8, p. 1500343, Aug. 2016.

[172] D.-W. Park *et al.*, "Fabrication and utility of a transparent graphene neural electrode array for electrophysiology, in vivo imaging, and optogenetics," *Nat. Protoc.*, vol. 11, no. 11, pp. 2201–2222, Oct. 2016.

[173] L. Gao *et al.*, "Repeated growth and bubbling transfer of graphene with millimetre-size single-crystal grains using platinum," *Nat. Commun.*, vol. 3, no. 1, p. 699, Jan. 2012.

[174] L. D'Arsié *et al.*, "Stable, efficient p-type doping of graphene by nitric acid," *RSC Adv.*, vol. 6, no. 114, pp. 113185–113192, Nov. 2016.

[175] A. Kasry, M. A. Kuroda, G. J. Martyna, G. S. Tulevski, and A. A. Bol, "Chemical Doping of Large-Area Stacked Graphene Films for Use as Transparent, Conducting Electrodes," *ACS*

Nano, vol. 4, no. 7, pp. 3839–3844, Jul. 2010.

[176] S. Bae *et al.*, "Roll-to-roll production of 30-inch graphene films for transparent electrodes," *Nat. Nanotechnol.*, vol. 5, no. 8, pp. 574–578, Aug. 2010.

[177] F. Güneş *et al.*, "Layer-by-Layer Doping of Few-Layer Graphene Film," *ACS Nano*, vol. 4, no. 8, pp. 4595–4600, Aug. 2010.

[178] A. C. Ferrari, "Raman spectroscopy of graphene and graphite: Disorder, electron–phonon coupling, doping and nonadiabatic effects," *Solid State Commun.*, vol. 143, no. 1–2, pp. 47–57, Jul. 2007.

[179] S. Sahoo, R. Palai, and R. S. Katiyar, "Polarized Raman scattering in monolayer, bilayer, and suspended bilayer graphene," *J. Appl. Phys.*, vol. 110, no. 4, p. 044320, Aug. 2011.

[180] A. Das *et al.*, "Monitoring dopants by Raman scattering in an electrochemically top-gated graphene transistor," *Nat. Nanotechnol.*, vol. 3, no. 4, pp. 210–215, Apr. 2008.

[181] M. Thunemann *et al.*, "Deep 2-photon imaging and artifact-free optogenetics through transparent graphene microelectrode arrays," *Nat. Commun.*, vol. 9, no. 1, p. 2035, Dec. 2018.

[182] Y. Qiang *et al.*, "Transparent arrays of bilayer-nanomesh microelectrodes for simultaneous electrophysiology and two-photon imaging in the brain," *Sci. Adv.*, vol. 4, no. 9, p. eaat0626, Sep. 2018.

[183] M. Zijlmans, P. Jiruska, R. Zelmann, F. S. S. Leijten, J. G. R. Jefferys, and J. Gotman, "High-frequency oscillations as a new biomarker in epilepsy," *Ann. Neurol.*, vol. 71, no. 2, pp. 169–178, Feb. 2012.

[184] A. Bragin, C. L. Wilson, J. Almajano, I. Mody, and J. Engel, "High-frequency Oscillations after Status Epilepticus: Epileptogenesis and Seizure Genesis," *Epilepsia*, vol. 45, no. 9, pp. 1017–1023, Sep. 2004.

[185] M. Dümpelmann, J. Jacobs, and A. Schulze-Bonhage, “Temporal and spatial characteristics of high frequency oscillations as a new biomarker in epilepsy,” *Epilepsia*, vol. 56, no. 2, pp. 197–206, Feb. 2015.

[186] B. J. A. Gill *et al.*, “Ex vivo multi-electrode analysis reveals spatiotemporal dynamics of ictal behavior at the infiltrated margin of glioma,” *Neurobiol. Dis.*, vol. 134, no. November 2019, p. 104676, Feb. 2020.

[187] J. Kim and H. Park, “Toward Faster Nonnegative Matrix Factorization : A New Algorithm and Comparisons 2 Alternating Nonnegative Least Squares Framework for NMF,” *Proc. 2008 Eighth IEEE Int. Conf. Data Min.*, pp. 353–362, 2008.

[188] H. Kim and H. Park, “Sparse non-negative matrix factorizations via alternating non-negativity-constrained least squares for microarray data analysis,” *Bioinformatics*, vol. 23, no. 12, pp. 1495–1502, 2007.

[189] R. Pang, B. J. Lansdell, and A. L. Fairhall, “Dimensionality reduction in neuroscience,” *Curr. Biol.*, vol. 26, no. 14, pp. R656–R660, 2016.

[190] A. N. Khambhati, M. G. Mattar, N. F. Wymbs, S. T. Grafton, and D. S. Bassett, “Beyond modularity: Fine-scale mechanisms and rules for brain network reconfiguration,” *Neuroimage*, vol. 166, no. November 2017, pp. 385–399, 2017.

[191] Y. Lu *et al.*, “Ultralow Impedance Graphene Microelectrodes with High Optical Transparency for Simultaneous Deep Two-Photon Imaging in Transgenic Mice,” 2018.

[192] L. D’Arsié *et al.*, “Stable, efficient p-type doping of graphene by nitric acid,” *RSC Adv.*, vol. 6, no. 114, pp. 113185–113192, Nov. 2016.

[193] D.-W. Park *et al.*, “Fabrication and utility of a transparent graphene neural electrode array for electrophysiology, in vivo imaging, and optogenetics,” *Nat. Protoc.*, vol. 11, no. 11, pp. 2201–2222, Nov. 2016.

[194] F. Aeed, T. Shnitzer, R. Talmon, and Y. Schiller, “Layer- and Cell-Specific Recruitment

Dynamics during Epileptic Seizures In Vivo," *Ann. Neurol.*, vol. 87, no. 1, pp. 97–115, Jan. 2020.

[195] L. Mariotti *et al.*, "Interneuron-specific signaling evokes distinctive somatostatin-mediated responses in adult cortical astrocytes," *Nat. Commun.*, vol. 9, no. 1, pp. 1–14, Dec. 2018.

[196] C. a. Schevon *et al.*, "Evidence of an inhibitory restraint of seizure activity in humans.," *Nat. Commun.*, vol. 3, p. 1060, 2012.

[197] E. M. Merricks *et al.*, "Single unit action potentials in humans and the effect of seizure activity," *Brain*, p. awv208, 2015.

[198] T. Proix, V. K. Jirsa, F. Bartolomei, M. Guye, and W. Truccolo, "Predicting the spatiotemporal diversity of seizure propagation and termination in human focal epilepsy," *Nat. Commun.*, vol. 9, no. 17, p. 1088, Dec. 2018.

[199] D. D. Lee and H. S. Seung, "Learning the parts of objects by non-negative matrix factorization," *Nature*, vol. 401, no. October 1999, pp. 788–791, 1999.

[200] S. A. Weiss *et al.*, "Seizure localization using ictal phase-locked high gamma: A retrospective surgical outcome study," *Neurology*, vol. 84, no. 23, pp. 2320–2328, Jun. 2015.

[201] M. Breakspear, "A Unifying Explanation of Primary Generalized Seizures Through Nonlinear Brain Modeling and Bifurcation Analysis," *Cereb. Cortex*, vol. 16, no. 9, pp. 1296–1313, Nov. 2005.

[202] M. Goodfellow, K. Schindler, and G. Baier, "Self-organised transients in a neural mass model of epileptogenic tissue dynamics," *Neuroimage*, vol. 59, no. 3, pp. 2644–2660, Feb. 2012.

[203] O. Benjamin *et al.*, "A phenomenological model of seizure initiation suggests network structure may explain seizure frequency in idiopathic generalised epilepsy.," *J. Math. Neurosci.*, vol. 2, no. 1, p. 1, 2012.

[204] M. M *et al.*, "Solution-processed titanium carbide MXene films examined as highly transparent conductors," pp. 16371–16378, 10-Oct-2016.

[205] D. A. Dombeck, C. D. Harvey, L. Tian, L. L. Looger, and D. W. Tank, "Functional imaging of hippocampal place cells at cellular resolution during virtual navigation," *Nat. Neurosci.*, vol. 13, no. 11, pp. 1433–1440, Nov. 2010.

[206] L. Kandratavicius *et al.*, "Animal models of epilepsy: use and limitations.," *Neuropsychiatr. Dis. Treat.*, vol. 10, pp. 1693–705, 2014.

[207] H. Hirase, J. Creso, and G. Buzsáki, "Capillary level imaging of local cerebral blood flow in bicuculline-induced epileptic foci," *Neuroscience*, vol. 128, no. 1, pp. 209–216, Jan. 2004.

[208] P. Chauvel, O. Faugeras, J. Touboul, and F. Wendling, "Neural Mass Activity, Bifurcations, and Epilepsy," *Neural Comput.*, vol. 3286, pp. 3232–3286, 2011.

[209] S. J. Kiebel, J. Daunizeau, C. Phillips, and K. J. Friston, "Variational Bayesian inversion of the equivalent current dipole model in EEG/MEG," *Neuroimage*, vol. 39, no. 2, pp. 728–741, 2008.

[210] E. B. Geller *et al.*, "Brain-responsive neurostimulation in patients with medically intractable mesial temporal lobe epilepsy," pp. 1–11, 2017.

[211] R. C. Wykes, D. M. Kullmann, I. Pavlov, and V. Magloire, "Optogenetic approaches to treat epilepsy," *J. Neurosci. Methods*, vol. 260, pp. 215–220, 2016.

[212] R. C. Wykes *et al.*, "Optogenetic and potassium channel gene therapy in a rodent model of focal neocortical epilepsy.," *Sci. Transl. Med.*, vol. 4, no. 161, p. 161ra152, 2012.

[213] V. S. Polikov, P. A. Tresco, and W. M. Reichert, "Response of brain tissue to chronically implanted neural electrodes," *J. Neurosci. Methods*, vol. 148, no. 1, pp. 1–18, Oct. 2005.

[214] F. Patolsky *et al.*, "Detection, stimulation, and inhibition of neuronal signals with high-density nanowire transistor arrays.," *Science*, vol. 313, no. 5790, pp. 1100–4, Aug. 2006.

[215] N. A. Kotov *et al.*, "Nanomaterials for Neural Interfaces," *Adv. Mater.*, vol. 21, no. 40, pp. 3970–4004, 2009.

[216] Olga Matarredona, Heather Rhoads, Zhongrui Li, Jeffrey H. Harwell, and Leandro Balzano, and Daniel E. Resasco, "Dispersion of Single-Walled Carbon Nanotubes in Aqueous Solutions of the Anionic Surfactant NaDDBS," 2003.

[217] Sivarajan Ramesh *et al.*, "Dissolution of Pristine Single Walled Carbon Nanotubes in Superacids by Direct Protonation," 2004.

[218] S. W. Kim *et al.*, "Surface modifications for the effective dispersion of carbon nanotubes in solvents and polymers," *Carbon N. Y.*, vol. 50, no. 1, pp. 3–33, Jan. 2012.

[219] J. Wang *et al.*, "Removal of the Residual Surfactants in Transparent and Conductive Single-Walled Carbon Nanotube Films," *J. Phys. Chem. C*, vol. 113, no. 41, pp. 17685–17690, Oct. 2009.

[220] D. S. Hecht *et al.*, "High conductivity transparent carbon nanotube films deposited from superacid," *Nanotechnology*, vol. 22, no. 7, p. 075201, Feb. 2011.

[221] M. Wang, G. Mi, D. Shi, N. Bassous, D. Hickey, and T. J. Webster, "Nanotechnology and Nanomaterials for Improving Neural Interfaces," *Advanced Functional Materials*, vol. 28, no. 12. p. 1700905, 25-Jul-2018.

[222] X. Li *et al.*, "Transfer of Large-Area Graphene Films for High-Performance Transparent Conductive Electrodes," *Nano Lett.*, vol. 9, no. 12, pp. 4359–4363, Dec. 2009.

[223] M. Naguib *et al.*, "Two-Dimensional Nanocrystals Produced by Exfoliation of Ti3AlC2," *Adv. Mater.*, vol. 23, no. 37, pp. 4248–4253, Oct. 2011.

[224] M. Alhabeb *et al.*, "Guidelines for Synthesis and Processing of Two-Dimensional Titanium Carbide (Ti3C2Tx MXene)," *Chem. Mater.*, vol. 29, no. 18, pp. 7633–7644, Sep. 2017.

[225] M. Ghidiu, M. R. Lukatskaya, M.-Q. Zhao, Y. Gogotsi, and M. W. Barsoum, "Conductive two-

dimensional titanium carbide ‘clay’ with high volumetric capacitance,” *Nature*, vol. 516, no. 7529, pp. 78–81, Nov. 2014.

[226] T. Mathis *et al.*, “Modified MAX Phase Synthesis for Environmentally Stable and Highly Conductive Ti_3C_2 MXene Modified MAX Phase Synthesis for Environmentally Stable and Highly Conductive Ti_3C_2 MXene,” *ChemRxiv*, no. 2, 2020.

[227] Y. Zhu *et al.*, “Carbon-Based Supercapacitors Produced by Activation of Graphene,” *Science (80-.).*, vol. 332, no. 6037, pp. 1537–1541, Jun. 2011.

[228] M. Heon *et al.*, “Continuous carbide-derived carbon films with high volumetric capacitance,” *Energy Environ. Sci.*, vol. 4, no. 1, pp. 135–138, Dec. 2011.

[229] X. Yang, C. Cheng, Y. Wang, L. Qiu, and D. Li, “Liquid-mediated dense integration of graphene materials for compact capacitive energy storage.,” *Science*, vol. 341, no. 6145, pp. 534–7, Aug. 2013.

[230] O. Mashtalir *et al.*, “Intercalation and delamination of layered carbides and carbonitrides,” *Nat. Commun.*, vol. 4, pp. 1–7, 2013.

[231] C. E. Shuck *et al.*, “Scalable Synthesis of $Ti_3C_2T_x$ MXene,” *Adv. Eng. Mater.*, vol. 22, no. 3, p. 1901241, Mar. 2020.

[232] M. Alhabeb *et al.*, “Guidelines for Synthesis and Processing of Two-Dimensional Titanium Carbide ($Ti_3C_2T_x$ MXene),” *Chem. Mater.*, vol. 29, no. 18, pp. 7633–7644, 2017.

[233] A. Lipatov, M. Alhabeb, M. R. Lukatskaya, A. Boson, Y. Gogotsi, and A. Sinitskii, “Effect of Synthesis on Quality, Electronic Properties and Environmental Stability of Individual Monolayer Ti3C2 MXene Flakes,” *Adv. Electron. Mater.*, vol. 2, no. 12, p. 1600255, Dec. 2016.

[234] M. Li *et al.*, “Element Replacement Approach by Reaction with Lewis Acidic Molten Salts to Synthesize Nanolaminated MAX Phases and MXenes,” *J. Am. Chem. Soc.*, vol. 141, no. 11, pp. 4730–4737, Mar. 2019.

[235] J. L. Hart *et al.*, "Control of MXenes' electronic properties through termination and intercalation," *Nat. Commun.*, vol. 10, no. 1, 2019.

[236] X. Han, J. Huang, H. Lin, Z. Wang, P. Li, and Y. Chen, "2D Ultrathin MXene-Based Drug-Delivery Nanoplatform for Synergistic Photothermal Ablation and Chemotherapy of Cancer," *Adv. Healthc. Mater.*, vol. 7, no. 9, p. 1701394, May 2018.

[237] S. Kumar, Y. Lei, N. H. Alshareef, M. A. Quevedo-Lopez, and K. N. Salama, "Biofunctionalized two-dimensional Ti3C2 MXenes for ultrasensitive detection of cancer biomarker," *Biosens. Bioelectron.*, vol. 121, no. June, pp. 243–249, 2018.

[238] A. Saleh *et al.*, "Inkjet-printed Ti3C2Tx MXene electrodes for multimodal cutaneous biosensing," *J. Phys. Mater.*, vol. 3, no. 4, p. 044004, 2020.

[239] H. Lin, S. Gao, C. Dai, Y. Chen, and J. Shi, "A Two-Dimensional Biodegradable Niobium Carbide (MXene) for Photothermal Tumor Eradication in NIR-I and NIR-II Biowindows," *J. Am. Chem. Soc.*, vol. 139, no. 45, pp. 16235–16247, Nov. 2017.

[240] H. Lin, X. Wang, L. Yu, Y. Chen, and J. Shi, "Two-Dimensional Ultrathin MXene Ceramic Nanosheets for Photothermal Conversion," *Nano Lett.*, vol. 17, no. 1, pp. 384–391, 2017.

[241] C. Dai *et al.*, "Two-Dimensional Tantalum Carbide (MXenes) Composite Nanosheets for Multiple Imaging-Guided Photothermal Tumor Ablation," *ACS Nano*, vol. 11, no. 12, pp. 12696–12712, Dec. 2017.

[242] H. Lin, Y. Wang, S. Gao, Y. Chen, and J. Shi, "Theranostic 2D Tantalum Carbide (MXene)," *Adv. Mater.*, vol. 30, no. 4, p. 1703284, Jan. 2018.

[243] K. Chaudhuri, M. Alhabeb, Z. Wang, V. M. Shalaev, Y. Gogotsi, and A. Boltasseva, "Highly Broadband Absorber Using Plasmonic Titanium Carbide (MXene)," *ACS Photonics*, vol. 5, no. 3, pp. 1115–1122, 2018.

[244] L. Wu *et al.*, "Few-layer Ti3C2Tx MXene: A promising surface plasmon resonance biosensing material to enhance the sensitivity," *Sensors Actuators, B Chem.*, vol. 277, no.

June, pp. 210–215, 2018.

[245] W. Feng *et al.*, "Ultrathin Molybdenum Carbide MXene with Fast Biodegradability for Highly Efficient Theory-Oriented Photonic Tumor Hyperthermia," *Adv. Funct. Mater.*, vol. 29, no. 22, pp. 1–15, 2019.

[246] J. Zhang *et al.*, "Scalable Manufacturing of Free-Standing, Strong $Ti_3C_2T_x$ MXene Films with Outstanding Conductivity," *Adv. Mater.*, vol. 32, no. 23, 2020.

[247] Y. Gogotsi and B. Anasori, "The Rise of MXenes," *ACS Nano*, vol. 13, no. 8. American Chemical Society, pp. 8491–8494, 27-Aug-2019.

[248] F. Wang, C. Yang, C. Duan, D. Xiao, Y. Tang, and J. Zhu, "An Organ-Like Titanium Carbide Material (MXene) with Multilayer Structure Encapsulating Hemoglobin for a Mediator-Free Biosensor," *J. Electrochem. Soc.*, vol. 162, no. 1, pp. B16–B21, Nov. 2014.

[249] R. B. Rakhi, P. Nayak, C. Xia, and H. N. Alshareef, "Novel amperometric glucose biosensor based on MXene nanocomposite," *Sci. Rep.*, vol. 6, no. 1, p. 36422, Dec. 2016.

[250] C. Dai, H. Lin, G. Xu, Z. Liu, R. Wu, and Y. Chen, "Biocompatible 2D Titanium Carbide (MXenes) Composite Nanosheets for pH-Responsive MRI-Guided Tumor Hyperthermia," *Chem. Mater.*, vol. 29, no. 20, pp. 8637–8652, Oct. 2017.

[251] G. Liu *et al.*, "Surface Modified Ti_3C_2 MXene Nanosheets for Tumor Targeting Photothermal/Photodynamic/Chemo Synergistic Therapy," *ACS Appl. Mater. Interfaces*, vol. 9, no. 46, pp. 40077–40086, 2017.

[252] Z. Liu *et al.*, "2D magnetic titanium carbide MXene for cancer theranostics," *J. Mater. Chem. B*, vol. 6, no. 21, pp. 3541–3548, May 2018.

[253] A. Gazzi *et al.*, "Photodynamic therapy based on graphene and MXene in cancer theranostics," *Frontiers in Bioengineering and Biotechnology*, vol. 7, no. OCT. Frontiers Media S.A., p. 295, 25-Oct-2019.

[254] L. Zong, H. Wu, H. Lin, and Y. Chen, “A polyoxometalate-functionalized two-dimensional titanium carbide composite MXene for effective cancer theranostics,” *Nano Res.*, vol. 11, no. 8, pp. 4149–4168, Aug. 2018.

[255] F. Meng *et al.*, “MXene Sorbents for Removal of Urea from Dialysate: A Step toward the Wearable Artificial Kidney,” *ACS Nano*, vol. 12, pp. 10518–10528, 2018.

[256] S. Seyedin *et al.*, “MXene Composite and Coaxial Fibers with High Stretchability and Conductivity for Wearable Strain Sensing Textiles,” *Adv. Funct. Mater.*, vol. 30, no. 12, p. 1910504, Mar. 2020.

[257] Y.-Z. Zhang *et al.*, “MXenes stretch hydrogel sensor performance to new limits,” 2018.

[258] Y. Cai *et al.*, “Stretchable $Ti_3C_2T_x$ MXene/Carbon Nanotube Composite Based Strain Sensor with Ultrahigh Sensitivity and Tunable Sensing Range,” *ACS Nano*, vol. 12, no. 1, pp. 56–62, 2018.

[259] X. Chen *et al.*, “Ratiometric photoluminescence sensing based on Ti_3C_2 MXene quantum dots as an intracellular pH sensor,” *Nanoscale*, vol. 10, no. 3, pp. 1111–1118, Jan. 2018.

[260] Y. Lei *et al.*, “A MXene-Based Wearable Biosensor System for High-Performance In Vitro Perspiration Analysis,” *Small*, vol. 15, no. 19, p. 1901190, May 2019.

[261] K. Rasool, M. Helal, A. Ali, C. E. Ren, Y. Gogotsi, and K. A. Mahmoud, “Antibacterial Activity of $Ti_3C_2T_x$ MXene,” *ACS Nano*, vol. 10, no. 3, pp. 3674–3684, 2016.

[262] K. Rasool, K. A. Mahmoud, D. J. Johnson, M. Helal, G. R. Berdiyorov, and Y. Gogotsi, “Efficient Antibacterial Membrane based on Two-Dimensional Ti3C2Tx (MXene) Nanosheets,” *Sci. Rep.*, vol. 7, no. 1, p. 1598, Dec. 2017.

[263] B. Xu *et al.*, “Ultrathin MXene-Micropattern-Based Field-Effect Transistor for Probing Neural Activity,” *Adv. Mater.*, vol. 28, no. 17, pp. 3333–3339, 2016.

[264] L. Mao *et al.*, “Biodegradable and Electroactive Regenerated Bacterial Cellulose/MXene

($Ti_3C_2T_x$) Composite Hydrogel as Wound Dressing for Accelerating Skin Wound Healing under Electrical Stimulation," *Adv. Healthc. Mater.*, vol. 9, no. 19, p. 2000872, 2020.

[265] G. K. Nasrallah, M. Al-Asmakh, K. Rasool, and K. A. Mahmoud, "Ecotoxicological assessment of $Ti_3C_2T_X$ (MXene) using a zebrafish embryo model," *Environ. Sci. Nano*, vol. 5, no. 4, pp. 1002–1011, 2018.

[266] X. Yu, X. Cai, H. Cui, S. W. Lee, X. F. Yu, and B. Liu, "Fluorine-free preparation of titanium carbide MXene quantum dots with high near-infrared photothermal performances for cancer therapy," *Nanoscale*, vol. 9, no. 45, pp. 17859–17864, 2017.

[267] C. J. Zhang *et al.*, "Oxidation Stability of Colloidal Two-Dimensional Titanium Carbides (MXenes)," *Chem. Mater.*, vol. 29, no. 11, pp. 4848–4856, Jun. 2017.

[268] Y. Chae *et al.*, "An investigation into the factors governing the oxidation of two-dimensional Ti 3 C 2 MXene," *Nanoscale*, vol. 11, no. 17, pp. 8387–8393, May 2019.

[269] X. Zhao *et al.*, "Antioxidants Unlock Shelf-Stable $Ti_3C_2T_x$ (MXene) Nanosheet Dispersions," *Matter*, vol. 1, no. 2, pp. 513–526, 2019.

[270] V. Natu, J. L. Hart, M. Sokol, H. Chiang, M. L. Taheri, and M. W. Barsoum, "Edge Capping of 2D-MXene Sheets with Polyanionic Salts To Mitigate Oxidation in Aqueous Colloidal Suspensions," *Angewandte Chemie - International Edition*, vol. 58, no. 36. pp. 12655–12660, 10-Jul-2019.

[271] Y. Lee *et al.*, "Oxidation-resistant titanium carbide MXene film," *J. Mater. Chem. A*, 2019.

[272] M. Vural *et al.*, "Inkjet Printing of Self-Assembled 2D Titanium Carbide and Protein Electrodes for Stimuli-Responsive Electromagnetic Shielding," *Adv. Funct. Mater.*, vol. 28, no. 32, p. 1801972, 2018.

[273] X. Jiang *et al.*, "Inkjet-printed MXene micro-scale devices for integrated broadband ultrafast photonics," *npj 2D Mater. Appl.*, vol. 3, no. 1, pp. 1–9, 2019.

[274] C. Zhang *et al.*, “Additive-free MXene inks and direct printing of micro-supercapacitors,” *Nat. Commun.*, vol. 10, no. 1, p. 1795, Dec. 2019.

[275] B. Lyu *et al.*, “Large-Area MXene Electrode Array for Flexible Electronics,” *ACS Nano*, vol. 13, no. 10, pp. 11392–11400, Sep. 2019.

[276] P. Salles, E. Quain, N. Kurra, A. Sarycheva, and Y. Gogotsi, “Automated Scalpel Patterning of Solution Processed Thin Films for Fabrication of Transparent MXene Microsupercapacitors,” *Small*, vol. 14, no. 44, p. 1802864, Nov. 2018.

[277] V. Kedambaimoole *et al.*, “Laser-Induced Direct Patterning of Free-standing Ti3C2-MXene Films for Skin Conformal Tattoo Sensors,” *ACS Sensors*, vol. 5, no. 7, pp. 2086–2095, Jun. 2020.

[278] E. Quain *et al.*, “Direct Writing of Additive-Free MXene-in-Water Ink for Electronics and Energy Storage,” *Adv. Mater. Technol.*, vol. 4, no. 1, p. 1800256, Jan. 2019.

[279] B. L. McNaughton, J. O’Keefe, and C. A. Barnes, “The stereotrode: A new technique for simultaneous isolation of several single units in the central nervous system from multiple unit records,” *J. Neurosci. Methods*, vol. 8, no. 4, pp. 391–397, Aug. 1983.

[280] M. Sessolo *et al.*, “Easy-to-Fabricate Conducting Polymer Microelectrode Arrays,” *Adv. Mater.*, vol. 25, no. 15, pp. 2135–2139, Apr. 2013.

[281] Y. Dall’Agnese, M. R. Lukatskaya, K. M. Cook, P.-L. Taberna, Y. Gogotsi, and P. Simon, “High capacitance of surface-modified 2D titanium carbide in acidic electrolyte,” *Electrochem. commun.*, vol. 48, pp. 118–122, Nov. 2014.

[282] M. D. Levi *et al.*, “Solving the Capacitive Paradox of 2D MXene using Electrochemical Quartz-Crystal Admittance and In Situ Electronic Conductance Measurements,” *Adv. Energy Mater.*, vol. 5, no. 1, p. 1400815, Jan. 2015.

[283] A. G. Richardson *et al.*, “Hippocampal gamma-slow oscillation coupling in macaques during sedation and sleep,” *Hippocampus*, vol. 27, no. 11, pp. 1125–1139, Nov. 2017.

[284] D. Pal *et al.*, "Propofol, Sevoflurane, and Ketamine Induce a Reversible Increase in Delta-Gamma and Theta-Gamma Phase-Amplitude Coupling in Frontal Cortex of Rat," *Front. Syst. Neurosci.*, vol. 11, p. 41, Jun. 2017.

[285] C. Dai *et al.*, "Two-Dimensional Tantalum Carbide (MXenes) Composite Nanosheets for Multiple Imaging-Guided Photothermal Tumor Ablation," *ACS Nano*, p. acsnano.7b07241-17, Nov. 2017.

[286] R. Q. Quiroga, Z. Nadasdy, and Y. Ben-Shaul, "Unsupervised Spike Detection and Sorting with Wavelets and Superparamagnetic Clustering," *Neural Comput.*, vol. 16, no. 8, pp. 1661–1687, Aug. 2004.

[287] J. P. Harris, L. A. Struzyna, P. L. Murphy, D. O. Adewole, E. Kuo, and D. K. Cullen, "Advanced biomaterial strategies to transplant preformed micro-tissue engineered neural networks into the brain," *J. Neural Eng.*, vol. 13, no. 1, p. 016019, Feb. 2016.

[288] J. A. Rogers, T. Someya, and Y. Huang, "Materials and mechanics for stretchable electronics," *Science (80-.).*, vol. 327, no. 5973, pp. 1603–1607, 2010.

[289] Y. Liu, M. Pharr, and G. A. Salvatore, "Lab-on-Skin: A Review of Flexible and Stretchable Electronics for Wearable Health Monitoring," *ACS Nano*, vol. 11, no. 10, pp. 9614–9635, 2017.

[290] J. J. S. Norton *et al.*, "Soft, curved electrode systems capable of integration on the auricle as a persistent brain-computer interface," *Proc. Natl. Acad. Sci. U. S. A.*, vol. 112, no. 13, pp. 3920–3925, 2015.

[291] J. W. Jeong *et al.*, "Materials and optimized designs for human-machine interfaces via epidermal electronics," *Adv. Mater.*, vol. 25, no. 47, pp. 6839–6846, Dec. 2013.

[292] B. Xu *et al.*, "An Epidermal Stimulation and Sensing Platform for Sensorimotor Prosthetic Control, Management of Lower Back Exertion, and Electrical Muscle Activation," *Adv. Mater.*, vol. 28, no. 22, pp. 4462–4471, 2016.

[293] D. J. McFarland and J. R. Wolpaw, “EEG-based brain–computer interfaces,” *Curr. Opin. Biomed. Eng.*, vol. 4, pp. 194–200, 2017.

[294] M. H. Granat, A. C. B. Ferguson, B. J. Andrews, and M. Delargy, “The role of functional electrical stimulation in the rehabilitation of patients with incomplete spinal cord injury observed benefits during gait studies,” *Paraplegia*, vol. 31, no. 4, pp. 207–215, 1993.

[295] P. H. Peckham and J. S. Knutson, “Functional Electrical Stimulation for Neuromuscular Applications,” *Annu. Rev. Biomed. Eng.*, vol. 7, no. 1, pp. 327–360, Aug. 2005.

[296] C. Ethier, E. R. Oby, M. J. Bauman, and L. E. Miller, “Restoration of grasp following paralysis through brain-controlled stimulation of muscles,” *Nature*, vol. 485, no. 7398, pp. 368–371, May 2012.

[297] R. A. Nawrocki, H. Jin, S. Lee, T. Yokota, M. Sekino, and T. Someya, “Self-Adhesive and Ultra-Conformable, Sub-300 nm Dry Thin-Film Electrodes for Surface Monitoring of Biopotentials,” *Adv. Funct. Mater.*, vol. 28, no. 36, p. 1803279, 2018.

[298] D. Khodagholy *et al.*, “Highly conformable conducting polymer electrodes for in vivo recordings,” *Adv. Mater.*, vol. 23, no. 36, pp. H268–H272, 2011.

[299] A. Searle and L. Kirkup, “A direct comparison of wet, dry and insulating bioelectric recording electrodes,” *Physiol. Meas.*, vol. 21, no. 2, pp. 271–283, 2000.

[300] G. C. Jensen, C. E. Krause, G. A. Sotzing, and J. F. Rusling, “Inkjet-printed gold nanoparticle electrochemical arrays on plastic. Application to immunodetection of a cancer biomarker protein,” *Phys. Chem. Chem. Phys.*, vol. 13, no. 11, pp. 4888–4894, Mar. 2011.

[301] G. Mattana, A. Loi, M. Woytasik, M. Barbaro, V. Noël, and B. Piro, “Inkjet-Printing: A New Fabrication Technology for Organic Transistors,” *Advanced Materials Technologies*, vol. 2, no. 10. Wiley-Blackwell, p. 1700063, 2017.

[302] N. Lewinski, V. Colvin, and R. Drezek, “Cytotoxicity of nanopartides,” *Small*, vol. 4, no. 1. pp. 26–49, Jan-2008.

[303] M. Gao, L. Li, and Y. Song, “Inkjet printing wearable electronic devices,” *Journal of Materials Chemistry C*, vol. 5, no. 12. Royal Society of Chemistry, pp. 2971–2993, 2017.

[304] U. Kraft, F. Molina-Lopez, D. Son, Z. Bao, and B. Murmann, “Ink Development and Printing of Conducting Polymers for Intrinsically Stretchable Interconnects and Circuits,” *Adv. Electron. Mater.*, vol. 6, no. 1, p. 1900681, Jan. 2020.

[305] S. Park, J. An, J. R. Potts, A. Velamakanni, S. Murali, and R. S. Ruoff, “Hydrazine-reduction of graphite- and graphene oxide,” *Carbon N. Y.*, vol. 49, no. 9, pp. 3019–3023, Aug. 2011.

[306] C. Mattevi *et al.*, “Evolution of electrical, chemical, and structural properties of transparent and conducting chemically derived graphene thin films,” *Adv. Funct. Mater.*, vol. 19, no. 16, pp. 2577–2583, Aug. 2009.

[307] K. Hantanasirisakul *et al.*, “Fabrication of Ti3C2Tx MXene Transparent Thin Films with Tunable Optoelectronic Properties,” *Adv. Electron. Mater.*, vol. 2, no. 6, p. 1600050, Jun. 2016.

[308] M. Mariano *et al.*, “Solution-processed titanium carbide MXene films examined as highly transparent conductors,” *Nanoscale*, vol. 8, no. 36, pp. 16371–16378, 2016.

[309] S. J. Kim *et al.*, “Interfacial assembly of ultrathin, functional MXene films,” *ACS Appl. Mater. Interfaces*, vol. 11, no. 35, pp. 32320–32327, 2019.

[310] F. Vitale, N. Driscoll, and B. Murphy, “Biomedical applications of MXenes,” in *2D Metal Carbides and Nitrides (MXenes): Structure, Properties and Applications*, B. Anasori and Y. Gogotsi, Eds. Cham: Springer International Publishing, Cham, 2019, pp. 503–524.

[311] L. Li *et al.*, “Hydrophobic and Stable MXene−Polymer Pressure Sensors for Wearable Electronics,” *Cite This ACS Appl. Mater. Interfaces*, vol. 12, pp. 15362–15369, 2020.

[312] N. Driscoll *et al.*, “Two-Dimensional Ti_3C_2 MXene for High-Resolution Neural Interfaces,” *ACS Nano*, vol. 12, no. 10, pp. 10419–10429, Oct. 2018.

[313] N. Driscoll *et al.*, "Fabrication of Ti3C2 MXene Microelectrode Arrays for In Vivo Neural Recording," *J. Vis. Exp.*, vol. 15, no. February, pp. 1–9, 2020.

[314] B. B. Murphy *et al.*, "A Gel-Free Ti3C2Tx-Based Electrode Array for High-Density, High-Resolution Surface Electromyography," *Adv. Mater. Technol.*, vol. 5, no. 8, pp. 1–10, 2020.

[315] S. Uzun *et al.*, "Knittable and Washable Multifunctional MXene-Coated Cellulose Yarns," *Adv. Funct. Mater.*, vol. 29, no. 45, p. 1905015, Sep. 2019.

[316] M. Ganji, A. T. Elthakeb, A. Tanaka, V. Gilja, E. Halgren, and S. A. Dayeh, "Scaling Effects on the Electrochemical Performance of poly(3,4-ethylenedioxythiophene (PEDOT), Au, and Pt for Electrocorticography Recording," *Adv. Funct. Mater.*, vol. 27, no. 42, p. 1703018, Nov. 2017.

[317] M. Ganji, A. Tanaka, V. Gilja, E. Halgren, and S. A. Dayeh, "Scaling Effects on the Electrochemical Stimulation Performance of Au, Pt, and PEDOT:PSS Electrocorticography Arrays," *Adv. Funct. Mater.*, vol. 27, no. 42, p. 1703019, Nov. 2017.

[318] X. Luo, C. L. Weaver, D. D. Zhou, R. Greenberg, and X. T. Cui, "Highly stable carbon nanotube doped poly(3,4-ethylenedioxythiophene) for chronic neural stimulation," *Biomaterials*, vol. 32, no. 24, pp. 5551–5557, Aug. 2011.

[319] J. D. Weiland, D. J. Anderson, and M. S. Humayun, "In vitro electrical properties for iridium oxide versus titanium nitride stimulating electrodes," *IEEE Trans. Biomed. Eng.*, vol. 49, no. 12 I, pp. 1574–1579, Dec. 2002.

[320] C. Jiang, L. Li, and H. Hao, "Carbon nanotube yarns for deep brain stimulation electrode," *IEEE Trans. Neural Syst. Rehabil. Eng.*, vol. 19, no. 6, pp. 612–616, 2011.

[321] W. Franks, I. Schenker, P. Schmutz, and A. Hierlemann, "Impedance characterization and modeling of electrodes for biomedical applications," *IEEE Trans. Biomed. Eng.*, vol. 52, no. 7, pp. 1295–1302, 2005.

[322] S. F. Cogan, P. R. Troyk, J. Ehrlich, T. D. Plante, and D. E. Detlefsen, "Potential-biased,

asymmetric waveforms for charge-injection with activated iridium oxide (AIROF) neural stimulation electrodes," *IEEE Trans. Biomed. Eng.*, vol. 53, no. 2, pp. 327–332, 2006.

[323] W. M. Grill and J. T. Mortimer, "Stimulus Waveforms for Selective Neural Stimulation," *IEEE Eng. Med. Biol. Mag.*, vol. 14, no. 4, pp. 375–385, 1995.

[324] L. Lorencova *et al.*, "Highly stable Ti3C2Tx (MXene)/Pt nanoparticles-modified glassy carbon electrode for H2O2 and small molecules sensing applications," *Sensors Actuators, B Chem.*, vol. 263, pp. 360–368, 2018.

[325] Z. Ling *et al.*, "Flexible and conductive MXene films and nanocomposites with high capacitance," *Proc. Natl. Acad. Sci. U. S. A.*, vol. 111, no. 47, pp. 16676–16681, Nov. 2014.

[326] D. J. Hewson, Y. Langeron, and J. Duche, "Evolution in impedance at the electrode-skin interface of two types of surface EMG electrodes during long-term recordings," *J. Electromyogr. Kinesiol.*, vol. 13, pp. 273–279, 2003.

[327] G. Li, S. Wang, and Y. Y. Duan, "Towards gel-free electrodes: A systematic study of electrode-skin impedance," *Sensors Actuators, B Chem.*, vol. 241, no. April, pp. 1244–1255, 2017.

[328] Y. H. Chen *et al.*, "Soft, comfortable polymer dry electrodes for high quality ECG and EEG recording," *Sensors*, vol. 14, no. 12, pp. 23758–23780, 2014.

[329] T. C. Ferree, P. Luu, G. S. Russell, and D. M. Tucker, "Scalp electrode impedance, infection risk, and EEG data quality," *Clin. Neurophysiol.*, vol. 112, no. 3, pp. 536–544, Mar. 2001.

[330] E. S. Kappenman and S. J. Luck, "The effects of electrode impedance on data quality and statistical significance in ERP recordings," *Psychophysiology*, vol. 47, no. 5, pp. 888–904, Mar. 2010.

[331] W. Klimesch, "EEG alpha and theta oscillations reflect cognitive and memory performance: A review and analysis," *Brain Research Reviews*, vol. 29, no. 2–3. Elsevier, pp. 169–195, 01-Apr-1999.

[332] S. W. Hughes and V. Crunelli, “Thalamic mechanisms of EEG alpha rhythms and their pathological implications,” *Neuroscientist*, vol. 11, pp. 357–372, 2005.

[333] Y. Li *et al.*, “An EEG-based BCI system for 2-D cursor control by combining Mu/Beta rhythm and P300 potential,” *IEEE Trans. Biomed. Eng.*, vol. 57, no. 10 PART 1, pp. 2495–2505, Oct. 2010.

[334] H.-J. Hwang, K. Kwon, and C.-H. Im, “Neurofeedback-based motor imagery training for brain-computer interface (BCI),” *J. Neurosci. Methods*, vol. 179, pp. 150–156, 2009.

[335] G. Drost, D. F. Stegeman, B. G. M. van Engelen, and M. J. Zwarts, “Clinical applications of high-density surface EMG: A systematic review,” *Journal of Electromyography and Kinesiology*, vol. 16, no. 6. pp. 586–602, Dec-2006.

[336] E. Martinez-Valdes, C. M. Laine, D. Falla, F. Mayer, and D. Farina, “High-density surface electromyography provides reliable estimates of motor unit behavior,” *Clin. Neurophysiol.*, vol. 127, no. 6, pp. 2534–2541, 2016.

[337] E. Chang, N. Ghosh, D. Yanni, S. Lee, D. Alexandru, and T. Mozaffar, “A Review of Spasticity Treatments: Pharmacological and Interventional Approaches,” *Crit. Rev. Phys. Rehabil. Med.*, vol. 25, no. 1–2, pp. 11–22, 2013.

[338] A. P. Yelnik, O. Simon, B. Parratte, and J. M. Gracies, “How to clinically assess and treat muscle overactivity in spastic paresis,” *Journal of Rehabilitation Medicine*, vol. 42, no. 9. pp. 801–807, Oct-2010.

[339] S. Wynter and L. Dissabandara, “A comprehensive review of motor innervation of the hand: variations and clinical significance,” *Surg. Radiol. Anat.*, vol. 40, no. 3, pp. 259–269, 2018.

[340] T. Masuda and T. Sadoyama, “Distribution of innervation zones in the human biceps brachii,” *J. Electromyogr. Kinesiol.*, vol. 1, no. 2, pp. 107–115, 1991.

[341] T. L. Morris and J. C. Miller, “Electrooculographic and performance indices of fatigue during

simulated flight," *Biol. Psychol.*, vol. 42, no. 3, pp. 343–360, Feb. 1996.

[342] A. B. Usakli, S. Gurkan, F. Aloise, G. Vecchiato, and F. Babiloni, "On the use of electrooculogram for efficient human computer interfaces," *Comput. Intell. Neurosci.*, vol. 2010, p. 135629, 2010.

[343] J. I. Berman, M. S. Berger, P. Mukherjee, and R. G. Henry, "Diffusion-tensor imaging-guided tracking of fibers of the pyramidal tract combined with intraoperative cortical stimulation mapping in patients with gliomas," *J. Neurosurg.*, vol. 101, no. 1, pp. 66–72, 2004.

[344] M. J. Morrell, "Responsive cortical stimulation for the treatment of medically intractable partial epilepsy," *Neurology*, vol. 77, no. 13, pp. 1295–1304, 2011.

[345] B. Lee *et al.*, "Engineering artificial somatosensation through cortical stimulation in humans," *Front. Syst. Neurosci.*, vol. 12, p. 24, Jun. 2018.

[346] J. F. Schenck, "The role of magnetic susceptibility in magnetic resonance imaging: MRI magnetic compatibility of the first and second kinds," *Med. Phys.*, vol. 23, no. 6, pp. 815–850, 1996.

[347] J. H. Duyn, "The future of ultra-high field MRI and fMRI for study of the human brain," *NeuroImage*, vol. 62, no. 2. Academic Press, pp. 1241–1248, 15-Aug-2012.

[348] K. A. Davis *et al.*, "Glutamate imaging (GluCEST) lateralizes epileptic foci in nonlesional temporal lobe epilepsy," *Sci. Transl. Med.*, vol. 7, no. 309, p. 309ra161, 2015.

[349] H. Wei *et al.*, "Exceedingly small iron oxide nanoparticles as positive MRI contrast agents," *Proc. Natl. Acad. Sci. U. S. A.*, vol. 114, no. 9, pp. 2325–2330, 2017.

[350] W. Neumann, T. P. Pusch, M. Siegfarth, L. R. Schad, and J. L. Stallkamp, "CT and MRI compatibility of flexible 3D-printed materials for soft actuators and robots used in image-guided interventions," *Med. Phys.*, vol. 46, no. 12, pp. 5488–5498, 2019.

[351] Z. Fan *et al.*, "Modified MXene/Holey Graphene Films for Advanced Supercapacitor

Electrodes with Superior Energy Storage," *Adv. Sci.*, vol. 5, no. 10, p. 1800750, Oct. 2018.

[352] H. Daley, K. Englehart, L. Hargrove, and U. Kuruganti, "High density electromyography data of normally limbed and transradial amputee subjects for multifunction prosthetic control," *J. Electromyogr. Kinesiol.*, vol. 22, no. 3, pp. 478–484, Jun. 2012.

[353] D. Farina, T. Lorrain, F. Negro, and N. Jiang, "High-density EMG E-Textile systems for the control of active prostheses," *32nd Annu. Int. Conf. IEEE Eng. Med. Biol.*, pp. 3591–3593, 2010.

[354] M. Murphy *et al.*, "Propofol anesthesia and sleep: A high-density EEG study," *Sleep*, vol. 34, no. 3, pp. 283–291, Mar. 2011.

[355] M. Massimini, G. Tononi, and R. Huber, "Slow waves, synaptic plasticity and information processing: insights from transcranial magnetic stimulation and high-density EEG experiments," *Eur. J. Neurosci.*, vol. 29, no. 9, pp. 1761–1770, May 2009.

[356] C. Guger, H. Ramoser, and G. Pfurtscheller, "Real-time EEG analysis with subject-specific spatial patterns for a brain-computer interface (BCI)," *IEEE Trans. Rehabil. Eng.*, vol. 8, no. 4, pp. 447–456, 2000.

[357] B. Blankertz *et al.*, "The BCI competition 2003: Progress and perspectives in detection and discrimination of EEG single trials," *IEEE Transactions on Biomedical Engineering*, vol. 51, no. 6. pp. 1044–1051, Jun-2004.

[358] M. Jochumsen, I. K. Niazi, K. Dremstrup, and E. N. Kamavuako, "Detecting and classifying three different hand movement types through electroencephalography recordings for neurorehabilitation," *Med. Biol. Eng. Comput.*, vol. 54, no. 10, pp. 1491–1501, Oct. 2016.

[359] K. Cai *et al.*, "Magnetic resonance imaging of glutamate," *Nat. Med.*, vol. 18, no. 2, pp. 302–306, 2012.

[360] F. Shahzad, A. Iqbal, S. A. Zaidi, S. W. Hwang, and C. M. Koo, "Nafion-stabilized two-dimensional transition metal carbide ($Ti_3C_2T_x$ MXene) as a high-performance

electrochemical sensor for neurotransmitter," *J. Ind. Eng. Chem.*, vol. 79, pp. 338–344, Nov. 2019.

[361] J. Zhang, H. Yang, G. Shen, P. Cheng, J. Zhang, and S. Guo, "Reduction of graphene oxide via l-ascorbic acid," *Chem. Commun.*, vol. 46, no. 7, pp. 1112–1114, 2010.

[362] R. J. Barry, A. R. Clarke, S. J. Johnstone, C. A. Magee, and J. A. Rushby, "EEG differences between eyes-closed and eyes-open resting conditions," *Clin. Neurophysiol.*, vol. 118, no. 12, pp. 2765–2773, 2007.

[363] Z. D. Jonker *et al.*, "TMS motor mapping: Comparing the absolute reliability of digital reconstruction methods to the golden standard," *Brain Stimul.*, vol. 12, no. 2, pp. 309–313, 2019.

[364] A. V. Ulyanova *et al.*, "Electrophysiological signature reveals laminar structure of the porcine hippocampus," *eNeuro*, vol. 5, no. 5, pp. e0102-18.2018, 2018.

[365] M. A. Attiah, J. de Vries, A. G. Richardson, and T. H. Lucas, "A Rodent Model of Dynamic Facial Reanimation Using Functional Electrical Stimulation," *Front. Neurosci.*, vol. 11, no. APR, p. 193, Apr. 2017.

[366] G. Ying, A. D. Dillon, A. T. Fafarman, and M. W. Barsoum, "Transparent, conductive solution processed spincast 2D $Ti_3C_2T_x$ (MXene) films," *Mater. Res. Lett.*, vol. 5, no. 6, pp. 391–398, 2017.

[367] Y. Yang, S. Umrao, S. Lai, and S. Lee, "Large-Area Highly Conductive Transparent Two-Dimensional $Ti_3C_2T_x$ Film," *J. Phys. Chem. Lett.*, vol. 8, no. 4, pp. 859–865, 2017.

[368] J. Engel Jr, A. Bragin, R. Staba, and I. Mody, "High-frequency oscillations: What is normal and what is not?," *Epilepsia*, vol. 50, no. 4, pp. 598–604, Apr. 2009.

[369] A. Sohrabpour, Y. Lu, P. Kankirawatana, J. Blount, H. Kim, and B. He, "Effect of EEG electrode number on epileptic source localization in pediatric patients," *Clin. Neurophysiol.*, vol. 126, no. 3, pp. 472–480, Mar. 2015.

[370] F. Cincotti *et al.*, "High-resolution EEG techniques for brain-computer interface applications," *J. Neurosci. Methods*, vol. 167, no. 1, pp. 31–42, 2008.

[371] J. T. Gwin and D. Ferris, "High-density EEG and independent component analysis mixture models distinguish knee contractions from ankle contractions," in *Proceedings of the Annual International Conference of the IEEE Engineering in Medicine and Biology Society, EMBS*, 2011, pp. 4195–4198.

[372] C. E. Shuck *et al.*, "Effect of Ti_3AlC_2 MAX Phase on Structure and Properties of Resultant $Ti_3C_2T_x$ MXene," *ACS Appl. Nano Mater.*, vol. 2, no. 6, pp. 3368–3376, Jun. 2019.

[373] M. Naguib *et al.*, "Two-Dimensional Transition Metal Carbides," *ACS Nano*, vol. 6, no. 2, pp. 1322–1331, Feb. 2012.

[374] B. Anasori and Y. Gogotsi, *2D Metal carbides and nitrides (MXenes): Structure, properties and applications*. SPRINGER NATURE, 2019.

[375] T. J. Sejnowski, P. S. Churchland, and J. A. Movshon, "Putting big data to good use in neuroscience," *Nat. Neurosci.*, vol. 17, no. 11, pp. 1440–1441, 2014.

[376] N. V Thakor, "Translating the Brain-Machine Interface," *Sci. Transl. Med.*, vol. 5, no. 210, pp. 1–8, 2013.

[377] T. Kozai, Kozai, and T. D. Y., "The History and Horizons of Microscale Neural Interfaces," *Micromachines*, vol. 9, no. 9, p. 445, Sep. 2018.

[378] D. Khodagholy *et al.*, "Organic electronics for high-resolution electrocorticography of the human brain," *Sci. Adv.*, vol. 2, no. 11, 2016.

[379] P. E. Deal, R. U. Kulkarni, S. H. Al-Abdullatif, and E. W. Miller, "Isomerically Pure Tetramethylrhodamine Voltage Reporters," *J. Am. Chem. Soc.*, vol. 138, no. 29, pp. 9085–9088, 2016.

[380] S. K. Rastogi, A. Kalmykov, N. Johnson, and T. Cohen-Karni, "Bioelectronics with

nanocarbons," *J. Mater. Chem. B*, vol. 6, no. 44, pp. 7159–7178, 2018.